Solid Oxide Electrolysis Cells

Performance and Durability

Hauch, Anne; Bilde-Sørensen, Jørgen; Mogensen, Mogens Bjerg; Jacobsen, Torben

Publication date:
2008

Solid Oxide Electrolysis Cells

- Performance and Durability

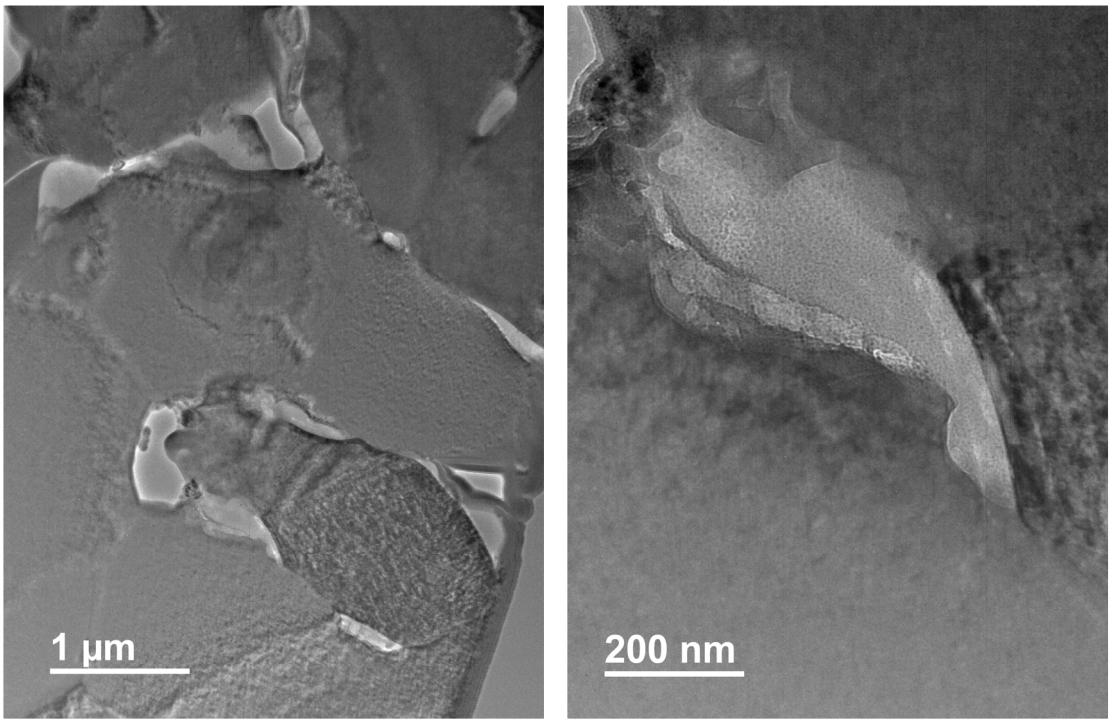

Anne Hauch

Risø National Laboratory & Department of Chemistry
Technical University of Denmark

Cover: Images from transmission electron microscopy investigation of the H_2 electrode for the solid oxide cell used for 3test22 (see chapter 6 and appendix A). Left image: A Ni particle adjacent to the electrolyte and further one YSZ particle and two Ni particles. Nine silicon containing impurity phases can be observed in this image. Right image: A high magnification image of one of the impurity phases at a triple-phase-boundary at the Ni-electrolyte interface.

Preface

This thesis is submitted to the Technical University of Denmark as a partly fulfilment of the requirements for the Ph.D. degree. The work presented in this thesis is the product of three years of work with solid oxide electrolysis cells (SOEC) and has mainly been carried out at the Fuel Cells and Solid State Chemistry Department at Risø National Laboratory. The Ph.D. project was financed by the EC via the project "Hi2H2", contract no. FP6-503765.
The work in this Ph.D. project deals with the use of solid oxide cells (SOC) as electrolysis cells for high temperature electrolysis of steam for hydrogen production. The focus has been H_2O electrolysis tests using state-of-the-art hydrogen electrode supported SOCs produced at Risø National Laboratory. Performance and durability of the SOCs and post-mortem analyses have been employed to map the problems and challenges for the further development of SOECs
The first two years of this Ph.D. work was done in close cooperation with Dr. Søren H. Jensen, who worked on his Ph.D. project at the time and I am very grateful to Søren for the many interesting discussions we had – and still have. We shared the work on cell testing including DC and AC characterisation approx. 50/50 during those two years. Søren had rebuilt the test rig for electrolysis testing before I started at Risø. He focused on modelling of impedance data and economic simulations, whereas I have focused on cell testing, electron microscopy & microanalysis (SEM, TEM, STEM and EDS) and the correlation between cell test results and post-mortem results.

I would like to thank my supervisors:
- Senior scientist Jørgen Bilde-Sørensen, Materials Research Department, Risø National Laboratory, for introducing me to the world of electron microscopy.
- Associated Professor Torben Jacobsen, Department of Chemistry, Technical University of Denmark, for suggestions, advice and pedagogical answers.
- Research Professor Mogens Mogensen, Fuel Cells and Solid State Chemistry Department, Risø National Laboratory, for the daily supervision, for rewarding discussions and a never failing willingness to let me draw from his enormous knowledge within the field of SOC R&D.

Senior Scientist Karin Vels Hansen did a proof-reading of the thesis and not only corrected the worst grammar mistakes but also came with useful suggestions for improvement of the manuscript, for which I am grateful. I would also like to thank the many colleagues in the Fuel Cells and Solid State Chemistry Department, who assisted me in this Ph.D. project, and especially thanks to the "*Jungle-office*" and Klaus Rasmussen.

Anne Hauch, Roskilde, Denmark, 15th of October 2007

Abstract

It has been known for decades that solid oxide fuel cells (SOFC) can be operated in reverse mode as solid oxide electrolysis cells (SOEC) to perform electrolysis of H_2O and/or CO_2 for hydrogen or synthesis gas (H_2+CO) production. In recent years SOECs have received a renewed interest in line with the increasing oil price, the general interest in H_2 based energy technologies and the possibilities of optimising the use of surplus electricity from renewable sources.

In this work H_2 electrode supported solid oxide cells (SOC) produced at Risø National Laboratory, DTU. SOCs optimised for SOFC conditions have been used for steam electrolysis. SOEC tests have been performed at temperatures from 650°C to 950°C, $p(H_2O)/p(H_2)$ from 0.99/0.01 to 0.30/0.70 and current densities from -0.25 A/cm^2 to -2 A/cm^2. The SOECs have been characterised by iV curves and electrochemical impedance spectroscopy (EIS) at start and end of tests and by EIS under current load during electrolysis testing. The tested SOECs have shown excellent initial electrolysis performance and have the best initial electrolysis performance reported in literature to date. Area specific resistances of 0.26 Ωcm^2 at 850°C and 0.17 Ωcm^2 at 950°C were obtained from electrolysis iV curves and a current density of -3.6 A/cm^2 has been reached at a cell voltage of only 1.49 V and 950°C.

The general trend for the SOEC tests was: 1) a short-term passivation in first few hundred hours, 2) then an activation and 3) a subsequent and underlying long-term degradation. The transient phenomenon (passivation/activation) was shown to be a set-up dependent artefact caused by the albite glass sealing with a $p(Si(OH)_4)$ of ~$1 \cdot 10^{-7}$ atm. Upon reduction of H_2O in the H_2 electrode, in the few microns closest to the electrolyte, the equilibrium between $Si(OH)_4$ and silica is shifted towards formation of silica leading to a contamination of the triple-phase boundaries (TPBs) of the electrode. The long-term degradation for the SOECs was more pronounced than for fuel cell testing of similar cells. Long-term degradation of 2%/1000 h was obtained at 850°C, $p(H_2O)/p(H_2)$ = 0.5/0.5 and -0.5 A/cm^2, whereas the degradation rate increased to 6%/1000h at 950°C, $p(H_2O)/p(H_2)$ = 0.9/0.1 and -1.0 A/cm^2. Both the short-term passivation and the long-term degradation appear mainly to be related to processes in the H_2 electrode.

Substantial post-mortem analysis of the H_2 electrodes of tested SOECs is reported in this work. Scanning electron microscopy micrographs show that only limited changes occur in the Ni particle size distribution. These changes were shown not to be the main degradation mechanism for the SOECs. Micro and nano analysis using energy dispersive spectroscopy in combination with transmission electron microscopy (TEM) and scanning TEM reveals that glassy phase impurities have accumulated at the TPBs as at result of testing the SOECs. The impurities have been observed both as “rims” around Ni particles and as more regularly shaped phases at the TPBs, typically in the size of 50-500 nm. The impurities are silicates, alumina silicates and in some cases sodium alumina silicates. It is believed that the degradation of the SOECs relates strongly to these impurity phases.

Dansk resumé

I årtier har det været velkendt at fastoxidbrændselsceller (SOFC) kan køres i modsat retning og anvendes som fastoxidelektrolyseceller (SOEC) til elektrolyse af vanddamp og/eller CO_2 for at producere hhv. brint eller syntesegas (H_2+CO). I løbet af de seneste par år er der opstået fornyet interesse for SOEC i takt med de stigende oliepriser og en general øget interesse for H_2-baserede energiteknologier samt mulighederne for optimeret anvendelse af overskudselektricitet fra vedvarende energikilder.

I dette ph.d.-projekt er der anvendt H_2-elektrodebårne fastoxidceller (SOC) til elektrolyse af vanddamp. Cellerne er produceret på Forskningscenter Risø, DTU og optimeret som SOFC'er. Elektrolysetest blev udført ved temperaturer fra 650°C til 950°C, $p(H_2O)/p(H_2)$ fra 0.3/0.7 til 0.99/0.01 og strømtætheder fra -0.25 A/cm^2 til -2.0 A/cm^2. SOEC'erne blev karakteriseret vha. iV-kurver og elektrokemisk impedansspektroskopi (EIS) ved start og afslutning af elektrolysetest og med EIS under strømtræk under test. De testede SOEC'er har vist optimal elektrolyseydeevne ved opstart, og bedre startydeevne ved elektrolyse er fundet ikke rapporteret i litteraturen. Areal specifikke modstande på 0.26 Ωcm^2 ved 850°C og 0.17 Ωcm^2 ved 950°C er opnået ved elektrolyse iV-kurver og en strømtæthed helt op til -3.6 A/cm^2 er opnået ved en cellespænding på kun 1.49 V ved 950°C.

Den generelle tendens for SOEC-testene var: 1) en korttidspassivering i de første par hundrede timer, 2) dernæst en aktivering og 3) en efterfølgende og underliggende langtidsdegradering. Det transiente fænomen (passivering/aktivering) viste sig at være et fænomen, der var afhængigt af test set-up og forårsaget af glasforseglinger af albit, som giver et $p(Si(OH)_4)$ på $\sim 1 \cdot 10^{-7}$ atm. Ved reduktion af H_2O i H_2-elektroden i de få mikrometer tættest på elektrolytten vil ligevægten mellem $Si(OH)_4$ og silika forskydes mod dannelse af SiO_2 og forårsage blokering af trefasegrænserne (TPB) i elektroden. Langtidsdegraderingen for SOEC'er er større end for brændselscelletest af lignende celler. Langtidsdegraderingen var ved 850°C, $p(H_2O)/p(H_2)$ = 0.5/0.5 og -0.5 A/cm^2 på 2%/1000 h, mens degraderingsraten steg til 6%/1000 h ved 950°C, $p(H_2O)/p(H_2)$ = 0.9/0.1 og -1.0 A/cm^2. Både korttidspassiveringen og langtidsdegraderingen synes hovedsagelig at skyldes processer i H_2-elektroden.

Omfattende post-mortem-analyser af H_2-elektroder af testede SOEC'er er beskrevet i denne afhandling. Skanningelektronmikroskopi billeder har vist, at elektrolysetestene kun har ført til begrænsede ændringer i Ni-partikelstørrelsesfordelingen, og at disse ændringer ikke er hovedårsagen til degraderingen. Mikro- og nanoanalyse ved anvendelse af energidispersiv spektroskopi i kombination med transmissionelektronmikroskopi (TEM) og skanning-TEM har vist, at glasfaseurenheder akkumuleres ved TPB'erne i løbet af elektrolysetestene af SOC'erne. Urenhederne er både observeret som kanter omkring Ni-partikler og som faser med mere regulære former ved TPB'erne, og typisk er de 50-500 nm. Urenhederne består af silikater, aluminosilikater og nogle gange aluminosilikater med natrium. Degraderingen af SOEC'erne menes at hænge nøje sammen med urenhederne ved TPB'erne.

Table of contents

1. Introduction

A fuel cell is an electrochemical device that can convert chemical energy directly into electrical energy. In that sense the fuel cell is much like a battery though it does need a continuous supply of fuel. As the conversion of chemical to electrical energy in a fuel cell does not include thermal and mechanical steps, the efficiency of a fuel cell is not restricted by the Carnot cycle. The fuel cell technology therefore has the potential of high fuel-to-electricity conversion efficiency. Furthermore, fuel cells enable an environmentally friendly conversion of chemical energy to electrical energy. The emission of pollutant gasses such as SO_2, NO_x and CO_2 pr. kWh produced are order(s) of magnitude(s) lower for fuel cells than for conventional power generation from burning of coal and oil [1]. These are some of the main reasons why fuel cells are seen as a promising future energy technology.
There are several different types of fuel cells operating at different temperatures. In general they are named after the type of material for the electrolyte. This thesis only addresses the high temperature solid oxide cells (SOC). The SOC can be used as fuel cells, a solid oxide fuel cell (SOFC) but the cells can work reversibly and be used as electrolysis cells, solid oxide electrolysis cells (SOEC), for hydrogen production using for instance surplus energy from wind turbines and nuclear power plants. This thesis will be focused on SOCs operated as SOECs. It is possible to use SOECs for production of synthesis gas ($CO + H_2$) by electrolysis of a mixture of CO_2 and steam but the work presented here will only be on high temperature steam electrolysis.
This chapter aims at giving a short introduction to the operation principle of the SOFCs and SOECs including a resume of SOC performance and polarisation losses [2], a short review of the SOC development and finally some aspects of the advantages of SOECs and the perspectives for SOECs in future energy systems.

1.1. Principle of operation SOFC and SOEC

Basically a fuel cell consists of an anode, at which the oxidation reaction occurs, an ion conducting electrolyte and a cathode, at which the reduction reaction occurs. An SOC is build up of a ceramic oxide ion conducting electrolyte, which is sandwiched between a porous electron conducting anode and cathode. This is sketched in Figure 1-1. When the cell is operated as a fuel cell gasses such as hydrogen, methane and even ammonia can be used as fuels. In the SOFC the hydrogen electrode works as the anode where e.g. H_2 is oxidized to H_2O. The oxygen electrode is fed with O_2 or air and works as the cathode. At the cathode/electrolyte interface oxygen molecules are reduced to oxide ions. Oxide ions are conducted through the electrolyte and the total reaction in fuel cell mode when using hydrogen as fuel is: $2H_2 + O_2 \rightarrow 2H_2O$ + heat + electrical energy. This is illustrated in Figure 1-1-A. Operating the cell in electrolysis mode demands an external power supply and the processes are reversed compared to fuel cell operation of the SOC. The steam electrolysis reaction is: $2H_2O$ + heat + electrical energy $\rightarrow 2H_2 + O_2$. In electrolysis mode the hydrogen electrode works as the cathode and the oxygen electrode works as the anode. This is shown in Figure 1-1-B. The hydrogen electrode is the negative electrode and the

oxygen electrode is the positive electrode. In fuel cell mode (anodic current load) the electrolyte will be polarised and have its more positive potential in the indirection of the hydrogen electrode. In electrolysis mode (cathodic current load) the electrolyte will have its more positive potential in the indirection of the oxygen electrode

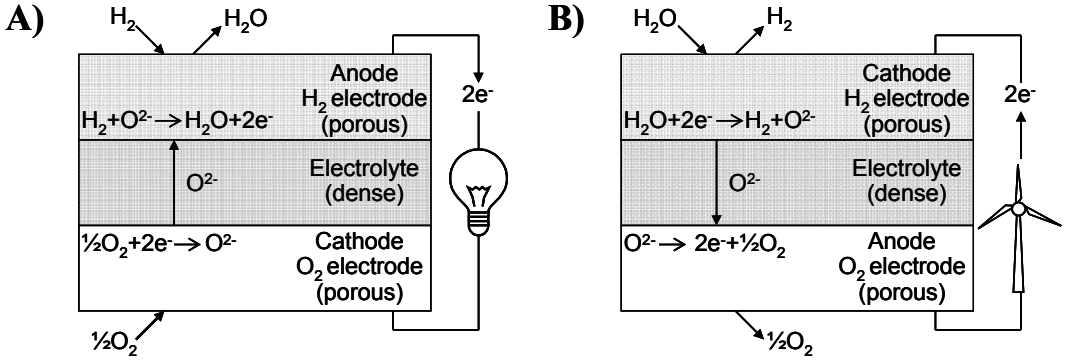

Figure 1-1: Basic operation principle for a Solid Oxide Cell (SOC). When the cell is operated in fuel cell mode (SOFC - part A) the total reaction is: $H_2 + ½O_2 \rightarrow H_2O$ + heat + electric energy. When the cell is operated in electrolysis mode (SOEC - part B) the total reaction is: H_2O + heat +electric energy $\rightarrow ½O_2 + H_2$.

The SOCs are typically operated in the temperature range from 700°C to 1000°C. The most widely used materials are: yttria stabilised zirconia (YSZ) for the electrolyte, a nickel-YSZ cermet for the hydrogen electrode and a composite of YSZ and strontium doped lanthanum manganite (LSM) for the oxygen electrode. The YSZ electrolyte has fluorite structure; it is gastight, electron insulating and ion conducting. Maximum ion conductivity is found for ZrO_2 doped with 8 mol% Y_2O_3 for which $\sigma = 0.1$ S/cm at 1000°C [3].The porous Ni/YSZ is electron conducting and Ni is a catalyst for the H_2/H_2O reaction. The LSM is stable in oxidizing atmosphere and electron conducting. The strontium doping of the $LaMnO_3$ perovskite enhances the electronic conductivity and modifies the thermal expansion coefficient (TEC) [1]. Besides these specific requirements for the different constituents of the cell, there are also requirements regarding match of TEC, undesirable reactions, sintering, durability, material costs and degree of purities etc. that needs to be considered in the choice of materials and processing techniques.

The potential over an SOC at open circuit voltage (OCV) is given by the Nernst equation [4] and is approximately 1 V. To obtain higher voltages the cells are connected in series to form a stack. In a stack an interconnect layer is added between the hydrogen electrode of one cell and the oxygen electrode of the next cell. The ferrite steel based interconnect provides a path for current collection while keeping the gasses from the electrodes of two cells apart.

1.2. Polarisation losses and SOC performance

At open circuit voltage the reversible cell potential, E_r, is given by the Nernst equation at the given operation conditions, assuming that there are no side reactions, gas leakage etc. When a load is applied to the cell the measured cell voltage, E, is influenced by polarisation losses. The cell potential can be expressed as:

$$E = E_r - \eta_\Omega - \eta_D - \eta_R - \eta_{ct} \quad (1\text{-}1)$$

The polarisation losses are functions of the applied current density (i) and for FC operation of a cell the potential E will always be less than E_r whereas EL operation of the cell leads to a cell potential, E, larger than E_r. The different losses can be described as [1; 5; 6]:

η_Ω: is the ohmic polarisation, sometimes called "ohmic losses" or "IR drop". It is caused by the resistance to conduction of ions in the electrolyte, conduction of electrons in the electrode and contact resistances.

η_D: is the diffusion or concentration polarisation. It appears when electrode reactions are hindered by mass transport effects. The effect of η_D will of course increase with increasing current density. Contributions from η_D will be smaller for a coarser electrode microstructure.

η_R: is the reaction polarisation. It appears when the supply of reactants or removal of products (in the vicinity of the electrode before/after the cell) is slow and is therefore in its nature similar to η_D.

η_{ct}: is the charge transfer polarisation, also called the activation polarisation. It is the overpotential or voltage drop necessary to "overcome" the energy barrier for the rate determining step in the electrochemical reaction. It describes the "sluggishness" of the electron transfer reaction at the electrolyte-electrode interface. Contributions from η_{ct} will be smaller for a finer electrode microstructure.

The electrochemical reactions in an SOC are believed to occur within the inner most (closest to the electrolyte) few microns of the electrode [7]. Therefore it can be advantageous to produce cells with a fine microstructure for the electrode layer closest to the electrolyte and a more coarse structure in the "outer" layer of the structures to stabilise polarisation losses and thereby improve the performance of the cell.
The availability of reaction sites to the electrochemical reaction is an important feature for the electron transfer reaction to occur and therefore in turn critical for the performance of the SOCs. The electron transfer reaction is believed to occur at the three phase boundaries (TPB) in the electrode. At the TPB the electron conducting material borders with the ion conducting material and a pore via which the gaseous reactants/products can enter/leave the electrode. An illustration of such TPBs in an SOC electrode is given in Figure 1-2. The importance of the TPB for the performance of the SOC and the effect of impurities at the TPB will be discussed in combination with the results presented in chapter 4 and 6-8.

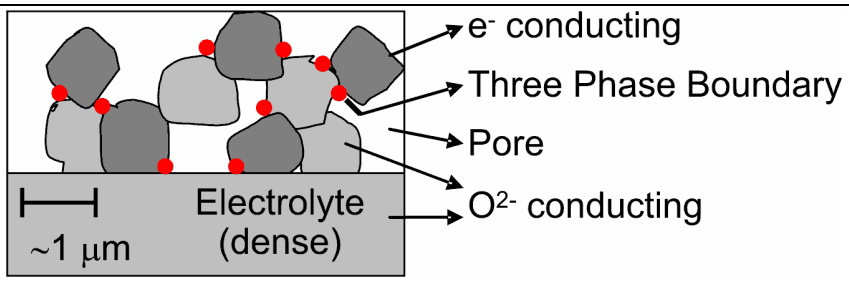

Figure 1-2: Illustration of three phase boundaries (TPB) in a porous SOC electrode near the electrode/electrolyte interface. At the TPB an ion conducting particle borders with an electron conducting particle and a pore via which the gaseous reactants/products can enter/leave the electrode.

The polarisation losses for an SOC, and thereby the performance of the SOC, can be measured by recording iV curves simply by measuring coupled pairs of cell voltage and current densities. From an iV curve the area specific resistance (ASR) can be obtained as the slope of the curve, which represents the cell performance over a full polarisation range. In some cases, especially convenient for concave iV curves, fuel utilisation corrected ASR (FUASR) at a specific current density is given instead [8]. As discussed by Mogensen and Hendriksen [8] there is a lack of consensus regarding the concept "ASR", so it is advisable to specify the conditions for the obtained ASR. Another way of measuring the performance of the SOC is to use the AC-method, electrochemical impedance spectroscopy (EIS, see chapter 4 for details), which enable separation of the different polarisation losses in an SOC [9-13].

1.3. SOC development

A strongly increased interest in hydrogen, energy sources alternative to oil and coal, and CO_2 neutral energy production has aroused during the last couple of decades. This has also lead to an increased interest - and R&D activities - within the SOC technology. The next two paragraphs give a short overview of the SOFC development in general and at Risø in specific. Both paragraphs use the initial performance of single cells to give a perspective on the development of SOFCs.

1.3.1. SOFC development in general

Basically there are two different geometries for SOFCs, tubular and planar. In Figure 1-3 three typical designs for the planar type of cells are shown: electrolyte supported, ceramic H_2 electrode supported and the metal H_2 electrode supported. The electrolyte supported cells have a 100-300 µm thick electrolyte – typically YSZ – and electrodes of 10-30 µm thickness [2]. Due to the lowering of the ion conductivity for YSZ with temperature, the electrolyte supported cells are designed for operating at ~1000°C [14]. If the operation temperature can be lowered it enables the use of cheaper materials e.g. for interconnects and manifolds for stacks. This has lead to the development of H_2 electrode supported cells, which have a thin (10-30 µm) O_2 electrode, electrolyte, and active H_2 electrode supported

by a 200-300 μm thick support of material similar to the H_2 electrode. The operation temperature for the H_2 electrode supported cells is typically 750-850°C. This is at the moment the most prevalent type of SOCs. The third and most recently developed type of cells aims for an even lower operating temperature at approximately 600°C and is a metal supported cell. Not only will lowering of the temperature compared to operation of H_2 electrode supported cells lead to lower cost of materials for interconnects and manifolds, the expenses for the raw materials for the cells themselves can be lowered approximately a factor of seven for metal supported cells compared to raw materials for electrode supported cells [15].

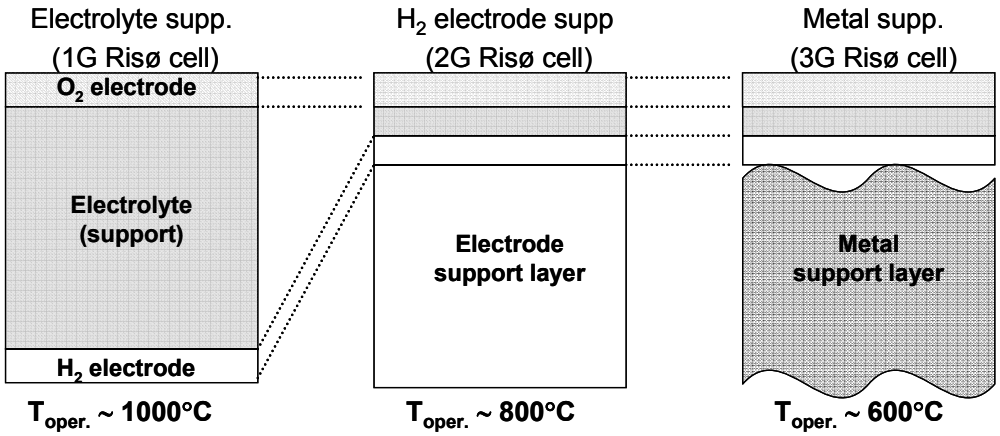

Figure 1-3: Sketch of three planar cell designs: electrolyte supported, H_2 electrode supported and metal supported, and the corresponding operations temperatures.

One way to monitor the results of the development of the SOFCs over the last two decades is by the reported initial performance for single cells over the years. The amount of literature on SOFC performance is tremendous. In order to give an extract of the results on SOFC performance *Proceedings of The Electrochemical Society SOFC-I to SOFC-IX* from 1989 to 2005 has been used to generate Table 1-1. Here the initial performance obtained via iV curves for single SOFCs are given to illustrate the increase in performance over the years for cells from institutions/countries that have contributed to SOFC-I to SOFC-IX over several years. The results in Table 1-1 are only a few examples to illustrate the development of SOFCs.

Table 1-1: Initial single cell SOFC performance obtained via iV curves and published in *Proceedings of The Electrochemical Society, SOFC-I to SOFC-IX*. The results are grouped after country and then year of publication.

Institution/ Country	Year	ASR [a] (Ωcm^2)	Temp (°C)	Type of cell [b] (p=planar, t=tubular)	Ref.
ECN /Netherlands	1993	0.82	930	p, electrolyte supp.	[16]
	1993	0.53	933	p, electrolyte supp.	[16]
	1995	0.31	904	p, electrolyte supp., up-scaled production	[17]
	1995	0.62	803	p, 60 μm electrolyte	[17]
	1999	0.41	800	p, H_2 electrode supp.	[18]
	1999	0.57	700	p, H_2 electrode supp.	[18]
Westinghouse /USA	1991	0.80	950	t, O_2 electrode supp.	[19]
	1991	1.10	875	t, O_2 electrode supp.	[19]
	2005	0.33	1000	t, O_2 electrode supp.	[20]
	2005	1.06	900	t, O_2 electrode supp.	[20]
Dornier & Jülich /Germany	1991	0.48	1000	t, electrolyte supp.	[21]
	1999	0.28	900	p, H_2 electrode supp.	[22]
	1999	0.56	800	p, H_2 electrode supp.	[22]
	2005	0.38	700	p, H_2 electrode supp. LSCF O_2 electrode	[23]
Cerametec /USA	1989	1.6	1000	p, electrolyte supp., ZrO_2 instead of YSZ	[24]
	1995	0.73	950	p, support ? [c]	[25]
	1997	0.40	800	p, electrolyte supp., LSCO/CeO_2-Sm_2O_3/Ni-CeO_2	[26]
Nat. Chem. Lab. for Industry, Murata Mfg. Co Ltd., Tokio Gas Co Ltd., Toho Gas Co Ltd. /Japan	1989	8	1000	p, electrolyte supp. LSCrM O_2 electrode	[27]
	1991	0.56	1000	p, electrolyte supp.,	[28]
	1993	0.32 [d]	1000	p, electrolyte supp.,	[29]
	2003	0.65	800	p, H_2 electrode supp.	[30]
	2003	0.27	950	p, H_2 electrode supp.	[30]
	2003	0.17	800	p, H_2 electrode supp., LSCF O_2 electrode	[30]

a) From the linear region of presented iV curves.

b) If nothing else is stated the cells are based on the composition LSM-YSZ/YSZ/Ni-YSZ.

c) The cell materials were not specified in [25] for the CPn design from Cerametec

d) For a 21 cm^2 cell. For a 91 cm^2 cell they reported an ASR of 0.84 Ωcm^2 in [29].

From Table 1-1 and similar literature studies it can be observed that:

- the ASR for SOFCs is lowered significantly over the last couple of decades
- the operation temperature has been lowered still with reasonable performance
- a shift from electrolyte supported to hydrogen electrode supported cells as the dominating design has occurred.
- institutions/companies in countries such as the Netherlands, Germany, USA, Japan and Denmark (see Table 1-2) have had continuous long-term R&D in SOFCs

The results in Table 1-1 should naturally be seen in a broader perspective. When it comes to the R&D of SOFC aspects such as the following should be addressed as well:

- durability of the SOFCs under operation, that is to keep the internal cell resistance low after thousands of hours of operation
- ability to cope with thermal and redox cycling
- development of improved materials for electrodes, electrolytes, sealing and interconnect
- optimisation of microstructure of the electrodes
- improvement/development of effective low cost processing techniques
- relation between cost of raw material, degree of purity and its effect on performance and durability of the cells

1.3.2. SOFC development at Risø National Laboratory

The SOFC project was started at Risø National Laboratory in 1987, see e.g. http://www.risoe.dk/Afd-abf/sofc/. Table 1-2 summarises the development of the SOFCs produced at Risø in a similar way as in Table 1-1, by reporting the initial ASR for single SOFCs as they have been reported in the *Proceedings of The Electrochemical Society SOFC-III to SOFC-IX*. The first generation (1G) of SOFCs produced at Risø were electrolyte supported cells (see Figure 1-3). In the late 1990ies the design was changed to H_2 electrode supported cells, 2G cells. Over the years the initial performance of these 2G cells has been improved and in 2002 a pre-pilot production line was built for larger scale production of these cells. Besides the studies of initial performance of the 2G cells produced on the pre-pilot scale, important studies of durability and reproducibility of such cells have also been reported [31; 32].

Development of 2.XG cells with LSFC/CGO oxygen electrodes [33], experiments with scandia and yttria doped ZrO_2 electrolyte materials, development of new full-ceramic hydrogen electrodes [34], optimisation of processing techniques [35], development of ferrite steel supported 3G cells [36] etc. is undertaken in parallel with the optimisation of 2G cells. Furthermore, the expertise within high temperature ceramic materials and electrochemistry is used in the Fuel Cells and Solid State Chemistry Department at Risø National Laboratory for research in related subjects such as oxygen diffusion membranes, ceramics cells for gas purification and high temperature electrolysis using SOECs.

Table 1-2: Initial single cell SOFC performance for cells produced at Risø National Laboratory. Results are obtained via iV curves and published in *Proceedings of The Electrochemical Society, SOFC-III to SOFC-IX.*

Year	ASR[a)] (Ωcm^2)	Temp (°C)	Notes	Ref.
1993	0.37	1000	Disk-formed cell, 10 cm^2. ASR at the rim: 0.46 Ωcm^2. ASR at the centre: 0.25 Ωcm^2 of the cell. Figure 6.	[37]
1993	1.14	1000	Poor performing electrolyte supported (1G) cell. Table 1.	[37]
1999	0.42	860	15 μm electrolyte, H_2 electrode supported. Figure 5.	[38]
1999	0.80	750	15 μm electrolyte, H_2 electrode supported	[38]
1999	0.30	1000	Electrolyte supported (1G) cell. Routine production, 180 μm YSZ electrolyte.	[39]
2001	0.30	850	2G cell, H_2 electrode supported. Figure 3.	[40]
2001	0.70	750	2G cell, H_2 electrode supported. Figure 1.	[41]
2005	0.18	850	2G cells produced on pre-pilot scale. ASR @850°C = 0.24±0.05 Ωcm^2 based on 20 cells produced on pre pilot scale before 2004 [31]. Table 1.	[42]
2005	0.61	750	2G cells produced on pre-pilot scale. Table 1.	[42]

1.3.3. SOEC R&D in the 1980's and 1990's

Promising results on high temperature electrolysis of steam using SOCs were reported already in 1980 by Dönitz et al. [43]. The results reported here were some of the first SOEC results from Dornier System GmbH obtained within the HotElly project[1]. During the 1980's SOEC results for the HotElly project were frequently reported in literature [21; 44-48], and a summary of the results can be found in [45]. The HotElly project was stopped around 1990 at a time at which the initial performance measured by the ASR from an iV curve was 0.8 Ωcm^2 at 995°C for their electrolyte supported tubular SOEC according to figure 21 in [45]. Also Westinghouse Electric Corporation Research and Development Centre contributed to the SOEC R&D in the 1980's. They reported SOEC stack performance and obtained an ASR of ~0.6 Ωcm^2 per cell in a 7 cell stack at 1003°C according to figure 4 in [49]. Not much R&D within the field of SOEC was conducted during the 1990's – most likely due to lower oil prices.

1.3.4. Present SOEC status

During the last few years the fossil fuel prices have increased. This is, in combination with the general interest in renewable energy and hydrogen based energy technologies, a

[1] HotElly was the acronym for "High Operating Temperature Electrolysis" – a project supported financially by the German Federal Ministry for Research and Technology BMFT.

plausible reason for the renewed interest in the SOEC technology that has appeared within the last couple of years. Some of the latest SOEC results are now reported from research groups in e.g. USA [50-55], Japan [56-58], Korea [59], Sweden [60] and Denmark [61-63]. Details on the initial performance for SOECs in some of these references and comparison with results obtained at Risø National Laboratory can be found in chapter 3.

1.4. Perspectives of SOECs

Looking at the perspectives of using SOECs for high temperature electrolysis (HTE) of steam, the technology clearly has the potential for highly efficient hydrogen production. Already in the HotElly project, Dönitz reported a Faradic efficiency for the SOECs above 100% using the higher heating value (HHV) of H_2, i.e. there are no "parasitic" reactions [45]. Such results of course form a basis for further research in SOEC and in the following paragraphs 3 different aspects of the perspectives of SOECs are dealt with briefly, that is: 1) the thermodynamics and kinetics for HTE of steam, 2) SOECs in energy systems and 3) H_2 production prices using SOECs.

1.4.1. Thermodynamics and kinetics for HTE versus low temperature electrolysis.

The thermodynamics of steam electrolysis is given in Figure 1-4 at ambient pressure and at 100 atm. The overall steam electrolysis reaction, $H_2O \rightarrow H_2 + ½O_2$, becomes increasingly endothermic with increasing temperature. From a thermodynamic point of view HTE is therefore favourable compared to low temperature electrolysis. Part of the energy demand for the electrolysis process to proceed can be obtained as heat (Joule heat) produced within the cell as consequence of the passage of electrical current through the cell. Utilizing the produced Joule lowers the electrical energy demand for production of a given quantity of hydrogen and thereby decreases the H_2 production price. In this perspective, it is favourable to operate the SOEC at thermoneutral potential, E_{tn}, which is the potential at which the generated Joule heat in the cell equals the heat consumption for the endothermic electrolysis reaction. For steam electrolysis, e.g. at 950°C, then the thermoneutral potential at 1 atm is:

$$E_{tn,950C} = H^{\theta}_{reac.,950C} \big/ nF = 1.29V \qquad (1\text{-}2)$$

where n is the number of transferred electrons per reaction and F is Faradays constant. In case H_2O is fed to the system as water, and heat for evaporation of the water in a heat exchanger should be provided by the heat generated in the SOEC as well, the thermoneutral potential at 950°C is:

$$E_{tn,950C} = (H^{\theta}_{reac.,950C} + H^{\theta}_{eva.,100C}) \big/ nF = 1.48V \qquad (1\text{-}3)$$

Furthermore, the kinetics of the reactions involved in steam electrolysis is increased at increased temperature and the conductivity increases as well [14]. The internal polarisation resistance follows an Arrhenius expression [1] and the measured ASR for SOECs is

lowered significantly at increased temperature (see chapter 3). Hence for a given constant cell voltage (electrical input) and steam partial pressure, increasing the temperature will increase the current density and therefore the hydrogen production rate. The materials typically used for the SOECs and the test set-up limits the SOEC test temperature to ~1000°C.

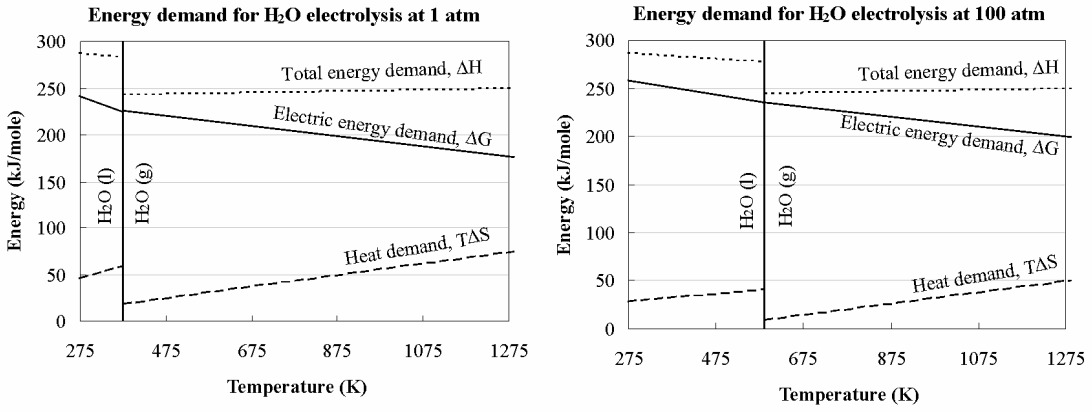

Figure 1-4: Thermodynamics for H_2O electrolysis at 1 atm and 100 atm. Data from [64]. Electrolysis of H_2O becomes increasingly endothermic with increased temperature.

1.4.2. SOECs in energy systems

Integrating SOECs in already existing energy systems are often described in the context of combining HTE with nuclear power plants as reported especially by research groups in USA [50; 65] and France [66]. Such combined SOEC/nuclear power systems obviously have the potential of improving the efficiency of the nuclear power plants, which are operated most efficiently at constant power output. Furthermore, high temperature waste heat from the nuclear power plants can be utilised in the HTE process. Even though several papers have been published concerning system analysis and the potential of combining SOEC systems with nuclear power plants, no literature on actual testing of such integrated systems seems to have appeared yet.

Seen from the "non-nuclear-power" countries, SOEC fit into a future energy system in combination with renewable energy sources such as solar, geothermal and wind energy. These energy sources typically do not provide a power output in agreement with the variation in consumption. Therefore SOECs to produce fuels (H_2 and/or CH_4) from surplus energy will be advantageous. Seen from a Danish perspective especially the possible use of SOECs to convert surplus wind energy is of interest [67]. Even with the existing number of wind turbines there have been windy times at which wind turbines have produced surplus

electrical energy as the electricity production from wind turbines exceeded the electricity consumption[2].

This thesis and most of the literature on SOECs deals with steam electrolysis and hydrogen production. Nevertheless, it is also possible to use SOECs to electrolyze a mixture of carbon dioxide and steam to produce synthesis gas, a mixture of carbon monoxide and hydrogen [68]. Synthesis gas can, by use of well known catalysts, be used for production of fuels such as methane or methanol. A system for methane production via CO_2 electrolysis has been reported by Jensen et al. [69] and is indeed interesting as the carbon containing fuels typically are easier to handle and have a higher energy density than hydrogen.

1.4.3. Estimated hydrogen production prices from high temperature electrolysis

From a commercial point of view an estimate of the hydrogen production price using SOEC is an utmost relevant subject to consider. The H_2 production price will of course vary considerably depending on the choice of values for input parameters such as SOC stack price, performance and lifetime of the cells, interest rate and in particularly on the electricity price [70]. Applying input parameters as reported by Mogensen et al.[71], a hydrogen production price of 30 US$/barrel equivalent crude oil was found using the HHV. This is indeed a very promising result when compared with crude oil prices of today. Especially two parameters in this calculation tend to attract attention: 1) the electricity price of only 1.3 US$/GJ was applied and 2) a cell performance of -3.6 A/cm^2 at 950°C, operating at the thermoneutral potential E_{tn} = 1.48V. Regarding the first parameter, the electricity price contributes approximately ¾ of the expenses for H_2 production; hence the calculated H_2 production price is indeed very sensitive towards higher electricity prices. Regarding the cell performance parameters, it is based on experimental results from an iV curve at 950°C [70]. Though considering the long-term testing of theses SOECs a more realistic performance of the cell would be approximately -1.5 A/cm^2 at 950°C and E_{tn} = 1.48 V (chapter 3 and appendix A). Using this cell performance as input parameter but otherwise use the input parameters given in [71], the estimated H_2 production price will increase as there will be increased stack investment costs. These calculations are only estimates of possible H_2 production price using SOECs. Nevertheless the calculations are important in order to illustrate the potential of the SOEC technology – also in a perspective of commercialisation.

1.5. Objective and lay-out of the thesis

Even though there has been an increase in the number of publications on SOEC during the last couple of years, there are still only a limited number of SOEC studies that include long-term durability of SOECs and investigation of passivation and/or degradation phenomena. The main objective of this Ph.D. project has been to study the performance and durability

[2] As an example; the electricity price was according to the Nordic Electric Power Market (Nord Spot Pool A/S, http://www.nordpoolspot.com) 0 Euro in Denmark from 1 to 5 am during the stormy weather on October 28th 2006. See also http://www.dr.dk/Nyheder/Indland/2006/10/27/104937.htm .

of the SOECs produced at Risø National Laboratory and to obtain an understanding of the passivation and/or degradation mechanisms in the SOECs especially by means of post mortem analysis of tested cells.
Chapter 2 gives a quite detailed description of the experimental set-up, whereas the experimental part in the following 6 chapters only describes variations from or additions to the description in chapter 2. Chapter 3-8 deal with the main results and each chapter contains its own discussion and conclusion. Chapter 3 describes the performance and durability of the Risø SOCs at different operation conditions. In chapter 4 analyses of impedance spectra is used to verify that the main passivation of the SOECs (shown in chapter 3) is caused by processes in the Ni/YSZ electrode. Microscopy results for H_2 electrodes of tested SOECs are presented in chapter 5-7, that is the microstructure (chapter 5), SEM/EDS investigation of impurity segregation in the electrodes (chapter 6) and focused ion beam (FIB) preparation of a TEM lamellae and TEM/STEM/EDS investigation of impurities in the electrode/electrolyte interface (chapter 7). The results presented in chapter 3-7 led to investigation of the effect of the glass sealing used for the electrolysis tests and this is presented in chapter 8. Overall discussion, conclusion and outlook are found in chapter 9, 10 and 11 respectively.
23 SOEC tests form the basis for the results presented in chapter 3-8 and not all tests are described in particular in these chapters. Therefore an overview of the electrolysis tests, test conditions and development of cell voltage and resistance during electrolysis testing is given in appendix A.

2. Experimental

2.1. Cell manufacturing

The electrolysis test results reported in this thesis have all been obtained on hydrogen electrode supported planar SOCs produced at Risø National Laboratory on a pre-pilot scale [32; 40]. The cells used for testing originate from 2 different production batches.

2.1.1. Raw materials and processing

TZ8Y (ZrO_2, 8 mol% Y_2O_3, Tosoh) was used for the electrolyte and the active hydrogen electrode. For the Ni/YSZ support layer TZ3Y (ZrO_2, 3 mol% Y_2O_3, Tosoh) was used. For both the active electrode and the support layer the NiO for the Ni/YSZ cermet was supplied by Alfa Aesar®, Johnson Matthey Company, see chapter 6 for details). The ratio between Ni and YSZ is 40/60 vol % both for the support layer and the active electrode layer [72]. For the LSM-YSZ composite electrode the composition was $(La_{0.75}Sr_{0.25})_{0.95}MnO_3$ supplied by Haldor Topsøe A/S and the YSZ was TZ8Y (ZrO_2, 8 mol% Y_2O_3, Tosoh). The ratio between LSM and YSZ in the composite electrode was LSM/YSZ = 50/50 vol % [73].
The NiO/YSZ support was made by tape casting [40] and both the active hydrogen electrode layer and the YSZ electrolyte was spray painted on the support layer. Half cells were stamped out and sintered. The oxygen electrode was spray painted on the half cells and the cells were sintered again [74]. LSM-YSZ and NiO/YSZ based contact layers were sprayed on the oxygen electrode and NiO/YSZ support layer respectively.

2.1.2. Electrode microstructure and dimensions

The planar SOCs are 5x5 cm^2, though using the test set-up described in this chapter the active electrode area is only 4x4 cm^2. Larger cells e.g. 12x12 cm^2 can easily be produced on the pre-pilot plant as well. Figure 2-1-A shows a scanning electron micrograph of a whole cross section of a cell. The cells have a 300 μm Ni/YSZ support layer, a 10–15 μm thick Ni/YSZ cermet hydrogen electrode, a 10–15 μm thick YSZ electrolyte and a 15–20 μm thick LSM-YSZ composite oxygen electrode. The different layers of the cell are remarkably even. Figure 2-1-B shows the NiO/YSZ electrode before reduction and Figure 2-1-C shows the microstructure of the porous hydrogen electrode after reduction of the NiO. The microstructure of the oxygen electrode is shown in Figure 2-1-D. The electrode microstructures (particle sizes, porosity and adhesion to the electrolyte) shown in Figure 2-1-C and Figure 2-1-D are representative for the cells used for electrolysis testing in this work.

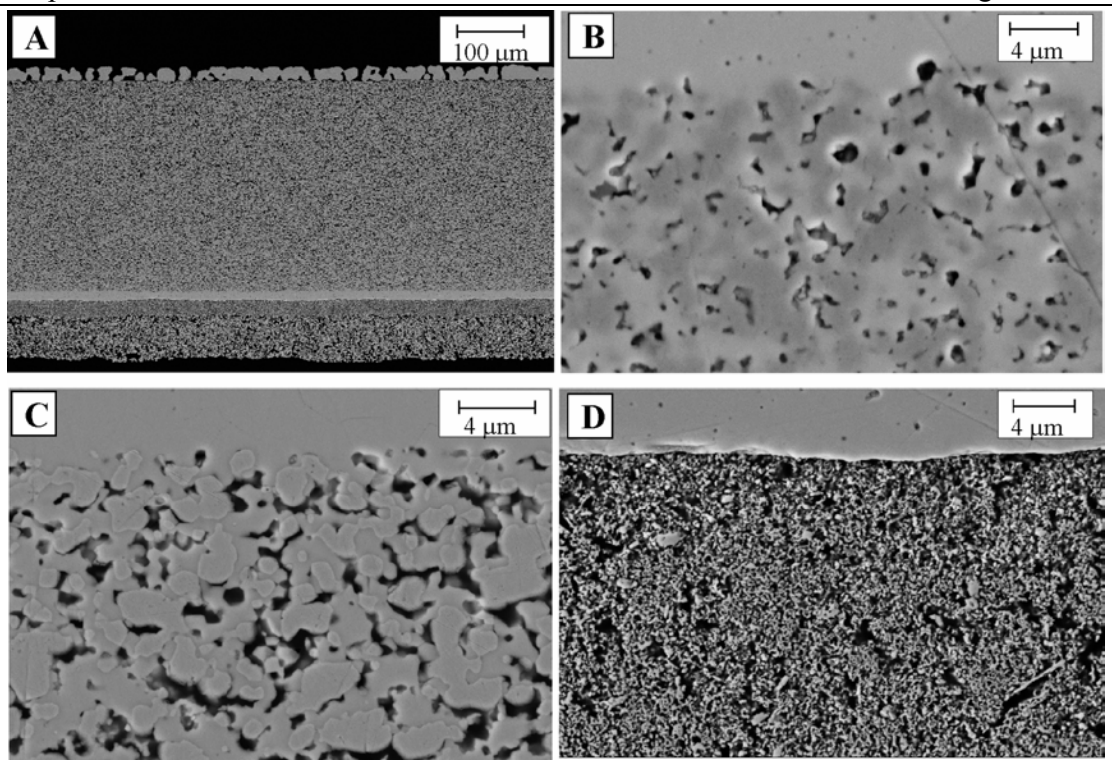

Figure 2-1: SEM images of cross sections of hydrogen electrode supported Risø SOCs. A: Overview over an entire cross section. See text for description of the different layers. B: Microstructure of a NiO/YSZ electrode prior to reduction. C: Microstructure of a Ni/YSZ electrode after reduction. D: Microstructure of a LSM-YSZ electrode.

2.2. Set-up for cell testing

A schematic drawing of the planar cells used for electrolysis testing is shown in Figure 2-2 (left) and an image of one half of the cell test set-up is shown in right part of Figure 2-2; this include the alumina housing, current collector (Ni foil), glass sealing and Ni/YSZ based gas distributor and the cell. The air distributor (LSM based), current collector (gold foil) and top part of the alumina cell housing is then placed on top to give a cross flow for the gasses. A schematic drawing of "sandwiching" of current collector foils, gas distributor plates and the cell can be found in [8]. The cell set-up in the furnace is shown in Figure 2-3A and a sketch of the configuration for the different probing and gas inlet and outlet in the set-up for single cell tests is shown in Figure 2-3B.

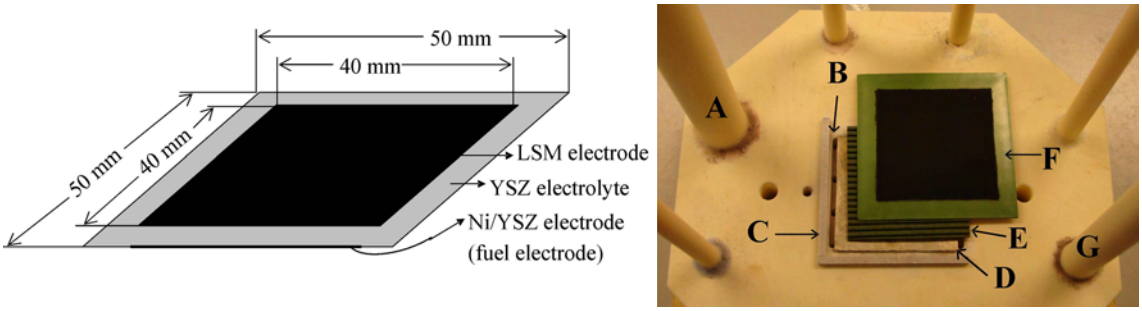

Figure 2-2: A schematic sketch of the cells used for electrolysis testing (left) Schematic drawing of the SOCs for the electrolysis tests (top) and an image of the one half of the test set-up in an alumina cell house (bottom). A: H_2O/H_2 tube inlet, B: Gas inlet holes for H_2O/H_2, C: Glass sealing, D: Current collector (Ni foil), E: Gas distributor, F: The cell and G: Gas outlet tube. Schematic drawing of the test set-up is given in [8].

Zirconia based oxygen sensors have been inserted in the gas tubing to and from the cell house (see Figure 2-3) to measure the partial pressure of oxygen in the fuel inlet and outlet gas and thereby monitor the H_2O/H_2 ratio in the gas mixtures. The single ended sensor tube is purged with air and two Pt wires are used to measure the potential difference over the zirconia tube wall. As the gas composition inside the sensor tube is known (air) the partial pressure of oxygen in the inlet and outlet gasses can be calculated from the Nernst equation. The potential measured using these ZrO_2 based sensors are referred to as VpO_2(in) and VpO_2(out). Furthermore a Pt/Rh(10%) wire is welded together with the Pt wire in the zirconia tube and used as a thermocouple to measure the temperature of the hot gas just before it enters/leaves the cell house.

The glass sealing used to keep the gasses to and from the two electrodes apart is a stoichiometric albite glass mixed with YSZ. The albite glass becomes viscous at 1000°C (mp. = 1118°C) and seals the cell set-up when a load of 8-10 kg is added on the top part of the alumina cell house (Figure 2-3). Even though the design of the alumina housing for single cell tests allows for the use a sweep gas, this has not been used for the electrolysis testing in the project.

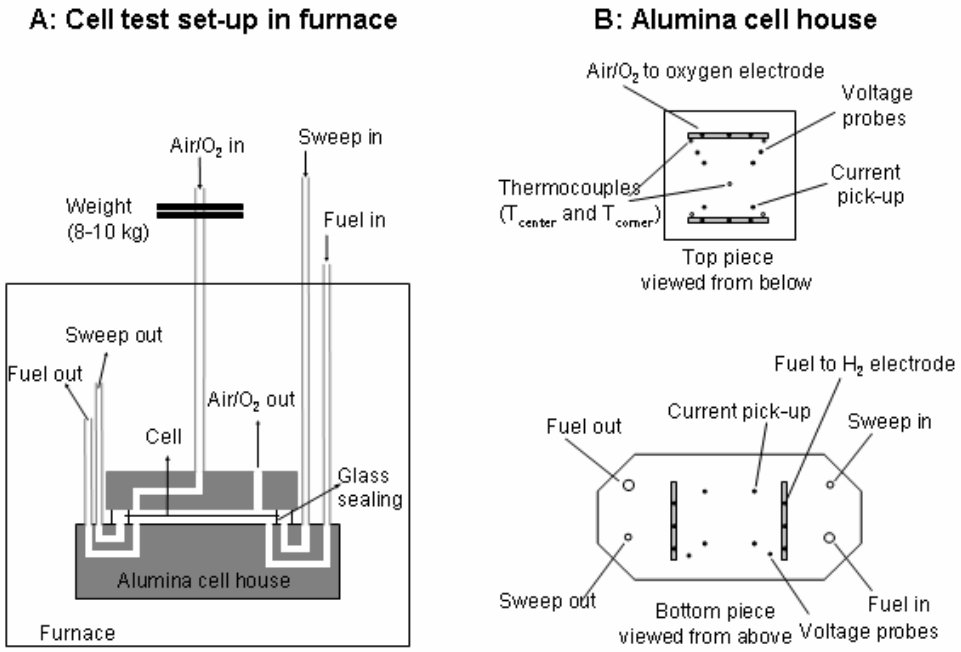

Figure 2-3: A: The cell test set-up in the furnace. B: Alumina housing including the configuration for voltage probes, current pick-up, thermocouples and gas inlet and outlet [75].

2.2.1. Reduction of NiO and start-up procedure

After mounting the cell in the test house and the test house in the furnace (see Figure 2-2 and Figure 2-3), the cell tests are started by heating up the test house to ~1000°C using a heating rate of 1°C/minute and applying 40 l/h of air to the oxygen electrode. To seal the cell a load of 8-10 kg is added on top of the test house for 2 hours prior to reduction of the nickel oxide. The reduction of the NiO is obtained by passing 18 l/h humidified (4% H_2O) diluted hydrogen 9% H_2 in N_2 over the hydrogen electrode for two hours, followed by passing 18 l/h humidified H_2 with 4% H_2O over the hydrogen electrode, still at ~1000°C. When the cell voltage is constant and close to the Nerstian emf (1049 mV) after approximately 1 hour, the temperature is decreased 1°C/minute to 850°C and the gas flows are changed to 140 l/h air to the oxygen electrode and 24 l/h humidified H_2 to the hydrogen electrode. The cells are then characterised by iV curves and impedance spectroscopy at 850°C and 750°C applying $p(H_2O)/p(H_2)$ = 0.04/0.96 and $p(H_2O)/p(H_2)$ = 0.20/0.80. Furthermore, iV curves are recorded at $p(H_2O)/p(H_2)$ = 0.50/0.50 in both fuel cell and electrolysis mode at both temperatures. Prior to starting electrolysis testing the gas to the oxygen electrode is changed to 10 l/h or 20 l/h oxygen. Thereby $p(O_2)$ is kept constant at 1 atm when switching from open circuit voltage (OCV) to electrolysis operation of the cell. This is advantageous for subsequent analysis of the possible changes in the oxygen electrode response observed in the electrochemical impedance spectra recorded during

testing. The $p(H_2O)/p(H_2)$ is then increased to the desired value prior to increasing the current density for electrolysis testing.

2.3. Test rig, test operation and data acquisition

2.3.1. Test rig specifications, data communication and data logging

The test rig for electrolysis testing of single SOCs is a re-build SOFC test rig and the gas flow system and safety control is described in general in [8]. The rebuilding of the SOFC test rig has enabled the use of the following gasses to the hydrogen electrode: H_2, H_2O, N_2, CO and CO_2 and the gasses: air, O_2, H_2O and N_2 to the oxygen electrode. The test rig is placed in a ventilated hood equipped with sensors for H_2, CO and level of ventilation that are connected to a safety box. In case a measured level at one of the sensors exceeds the predefined safety range, voltage supply from the safety box will ensure that magnet valves are triggered and the test rig will be left at OCV with gas mixture of 9% H_2 in N_2 to the hydrogen electrode. This mixture keeps the Ni in the hydrogen electrode reduced while being a non-explosive gas mixture. A cell can be operated again in fuel cell or electrolysis mode after a triggering of the safety box.

A schematic overview of the data communication for the test rig is given in Figure 8 in [76]. The gasses are operated by digital flow controllers of the type Brooks 5850S and connected via an RS485 bus. The $H_2O(l)$ flow controller is a Bronkhorst Liqui® L20 connected via an RS232 protocol. An ICP-DAS I7520 RS232-to-RS485 converter is used to bridge the communication between the flow controllers and the computer. The furnace temperature is controlled by a Eurotherm 2416e controller unit and connected to the RS-485 bus.

Thermocouples are used to log temperatures such as T_{center} and T_{corner} (Figure 2-3) and they are connected via Pt-Pt/Rh wires to a screw terminal. Pt wires for cell and in-plane voltages and Pt wires from the zirconia oxygen sensors are also connected to the screw terminal. Furthermore Pt-R1000 wires for cold junction measurement, Pt-R100 for water bottle temperature measurements and a Cu wire for the current shunt for impedance measurements (Figure 2-4) are connected to the screw terminal. The data communication for these probes is obtained via a Keithley7001 switch that is connected to a Keithley2000 multi meter and then to the PC. The DC current load to the cell is controlled by a Delta Electronika Power Supply SM15-100 galvanostat (0-15 V) which is connected to a Delta Electronika PSC 232 communication unit that communicates via an RS-232 bus to the computer.

Data, such as temperatures (T_{center}, T_{corner}, $T_{furnace}$, gas inlet and outlet etc.), voltages (cell voltage, in-plane voltages and VpO_2's) and gas flows, is logged and stored on a Linux system every 10 minutes or on demand from the user of the test rig. The programming for data logging, storing and a matching HTML interface available via Risø's intranet has been developed in-house by the developing engineers Bjørn Sejr Johansen and Søren Koch.

2.3.2. Steam generation and handling

Steam for the electrolysis testing has been generated in two different ways in this project: 1) combustion of H_2 in the furnace and 2) a liquid flow controller combined with an evaporator box. Using method (1) the humidified H_2 is fed to the cell via the gas manifold for gas mixing that is mounted on top of the alumina tubes outside the furnace. A smaller alumina tube is placed inside this H_2-inlet alumina tube and O_2 is fed via the small alumina tube. The O_2 and humidified H_2 meet in the lowest part of the alumina tube close to alumina cell house and auto ignite to form additional steam. The drawback of this method for the steam generation is that the process is highly exothermic and the maximum flow rate of steam will be approximately 12 l/h H_2O(g) in this test set-up. The advantage of steam generation by combustion of H_2 is a very stable flow rate of H_2O(g) which results in cell voltage variations of only ±0.1 mV. The test rig for electrolysis testing is also equipped with an evaporator box (model DV2MK), a control unit and heated transfer line from aDROP Feuchtemesstechnik GmbH. To avoid steam condensation when using the evaporator system, a pre-heater was added around the gas manifold. Using the evaporator box for steam generation has the advantage that H_2O(g) flows up to ~40 l/h can be obtained but it lacks stability in the flow rate of H_2O to the cell. At optimal operating conditions i.e. a flow between 5-15 l/h, the instability in H_2O(g) flow rate lead to a fluctuation of the cell voltage of approximately ±2 mV. Furthermore the nozzle in the evaporator box is easily blocked by impurities and demineralised water need to be further purified by a Millipore® system. The nozzle can be cleaned using citric acid. For most of the test reported in this thesis the combustion of H_2 in the furnace was applied for steam generation.

2.3.3. iV curves

DC characterisation of the SOCs has been performed by recording iV curves for each of the cells before and after the long-term electrolysis tests at various temperatures and $p(H_2O)/p(H_2)$ ratios. The polarisation curves were measured using controlled current method stepping 62.5 mA/(s·cm^2), and the iV curves presented in this work are almost linear over a large polarisation range (~ 2 A/cm^2) and no discontinuity across OCV has been observed. The current and voltage limits for the iV curves can be edited in the script used for controlling the recording of the iV curves. Voltage limits of typically 1.4 V for electrolysis iV curves and 0.6 V for fuel cell iV curves were applied.

The reported area specific resistance (ASR) values are calculated as the chord from OCV to the maximum current density for which fuel utilisation effect is not observed in the iV curve, typically to at least ±0.75 A/cm^2. If fuel utilisation corrected ASR (FUASR) values are given the method described by Mogensen and Hendriksen [8] is used for the iterative calculation of the FUASR and the minimum FUASR value for the specific iV curve is given.

2.3.4. Electrochemical impedance spectroscopy (EIS)

AC characterisation has been performed by recording electrochemical impedance spectra (EIS). The spectra were recorded applying AC current amplitude of 42 mA (root-mean-

square) and typically in the frequency range from 82 kHz to 0.82 Hz or 0.08 Hz recording 6 points per decade and 60 to 100 cycles. A Solartron 1260 frequency analyser was used for the impedance measurements. To obtain EIS to during electrolysis operation of the cells the Solartron was used in combination with an external shunt to measure the AC-current through the cell [3] [76; 77]. A diagram showing the basics of the set-up is shown in Figure 2-4. The DC current through the cell is measured by the voltage drop (V_{DC}) across a 1 mΩ shunt. Before impedance measurement on the SOC can be obtained, the impedance $Z_{50m\Omega}(f)$ was recorded in a normal impedance spectrum. Hereafter, it is possible to determine the time resolved AC current (I_{AC}) through the cell and the 50 mΩ shunt from the time resolved AC voltage drop V_1 as $I_{AC}=V_1/ Z_{50m\Omega}(f)$, where V_1 is measured using the Solartron 1260 (Figure 2-4). Measuring the time resolved AC voltage drop V_2 with the Solartron combined with the AC current (I_{AC}) obtained from measuring the voltage drop V_1 now leads to determination of the cell impedance: $Z_{cell}(f)=(V_2 \cdot Z_{50m\Omega}(f))/V_1$.
From the measured EIS, the ohmic resistance (R_s) is found as the value of the real part of the impedance measured at the highest frequency. The polarisation resistance (R_p) is determined as the real part of the impedance at the lowest frequency minus the real part of the impedance measured at the highest frequency.

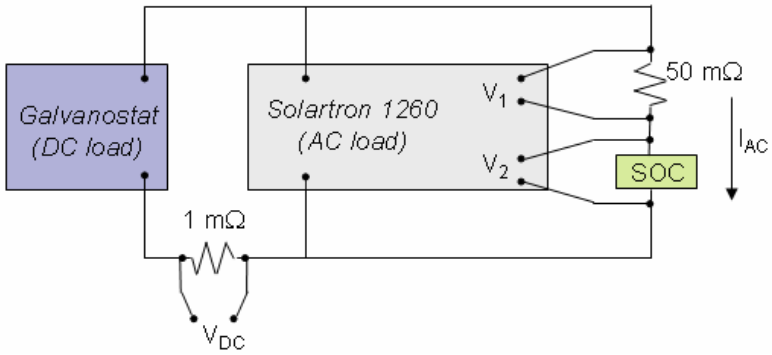

Figure 2-4: Set-up for recording impedance spectra during electrolysis testing using a Solartron 1260 galvanostat and external shunt [76; 77]. See text for details.

2.4. Electron microscopy

2.4.1. SEM sample preparation

Pieces (~1 cm long) of reference cells and electrolysis tested cells have been prepared for SEM investigations. The cell pieces were cold vacuum embedded in the epoxy mixture EpoFix from Struers®, grinded using SiC-paper and polished using diamond suspensions from Struers with diamond grains of 9, 3 and 1 μm. Subsequently the non-conductive samples were coated with carbon. It has been shown previously that the presence of epoxy

[3] This set-up for EIS during current load was developed by Jørgen Poulsen and Søren Højgaard Jensen, Fuel Cells and Solid State Chemistry Department, Risø National Laboratory, DTU.

as mounting material does not interfere with the quantitative analysis obtained by SEM/EDS [78].

2.4.2. Microscopes – hardware and software

A Zeiss SUPRA-35 thermal field emission gun SEM (FESEM) was used for the SEM investigation of the SOCs. The Zeiss SUPRA-35 is furthermore equipped with an energy dispersive X-ray spectrometer from Thermo Electron Corporation (Noran System Six Model 300) and the software Noran System Six X-ray microanalysis tool is used for the analysis of the obtained energy dispersive spectra (EDS). For a few of the SEM investigations of cell pieces a JEOL-840 SEM with a LaB_6 filament combined with an energy dispersive X-ray spectrometer from Noran Instruments was used. All EDS data were converted to the EMSA file format and analysed using the Noran System Six X-ray microanalysis tool.Quantification of the EDS were made by standardless analysis and the results should therefore be considered semi-quantitative. The ZAF correction (Atomic number Z, absorption A and fluorescence F) method was applied for the analyses. It should be noticed that for area spectra (see chapter 6) of inhomogeneous areas the conditions for ZAF corrections are not strictly fulfilled. Nevertheless, when the quantitative results from such area spectra are used to compare relative concentrations for example for comparison of different areas of a cell or a tested cell and a reference cell, the obtained quantitative EDS analysis of inhomogeneous areas applying the ZAF corrections still provide valuable information.

2.4.3. Monte Carlo simulations and peak resolution

To ensure proper excitation of X-rays an acceleration voltage of at least ~2.5 times the energy for the characteristic X-rays used for analysis should be applied. As the optimal working distance (WD) is 13 mm on the SUPRA-35 an acceleration voltage of 10-12 kV has typically been used to in order to do imaging and recording of EDS without change in microscope settings and thereby enable relatively fast combined SEM and EDS investigation of SOCs. In certain cases lower WD and acceleration voltage has been applied for SEM work.

The interaction and sampling volumes for ZrO_2 and SiO_2 at an acceleration voltage of 10 kV and for Ni at 10 and 12 kV are shown in Figure 2-5. The sampling volumes indicate the volumes from which detected X-rays can be expected in the different materials. The FWHM of the peaks are typically ~100 eV for the K-lines and ~200 eV for the L-lines [79]. Figure 2-6 is an example of an experimental EDS of a silica-containing impurity in an electrolysis tested cell (3test24, see details in chapter 6). The FWHM for Si_K is here 80 eV and 150 eV for Zr_L. The most significant effect of overlapping peaks will be in the quantification of yttrium and zirconium, and only a limited effect of overlap of the yttrium and silicon peak can be expected when analyzing silicon containing impurities in the Ni/YSZ electrode. In case of silicon in the oxygen electrode an overlap of the Si_K and Sr_L peaks will render a satisfactory quantitative EDS analysis of Si and Sr in the same spectrum. In such case it will be necessary or at least advantageous to use wavelength dispersive spectroscopy (WDS) or obtain EDS on a thin lamella of the sample (see chapter

7) to be able to minimise the volume of the sample from which detected X-rays originate and thereby avoid analysis of both silicon and strontium in same EDS.

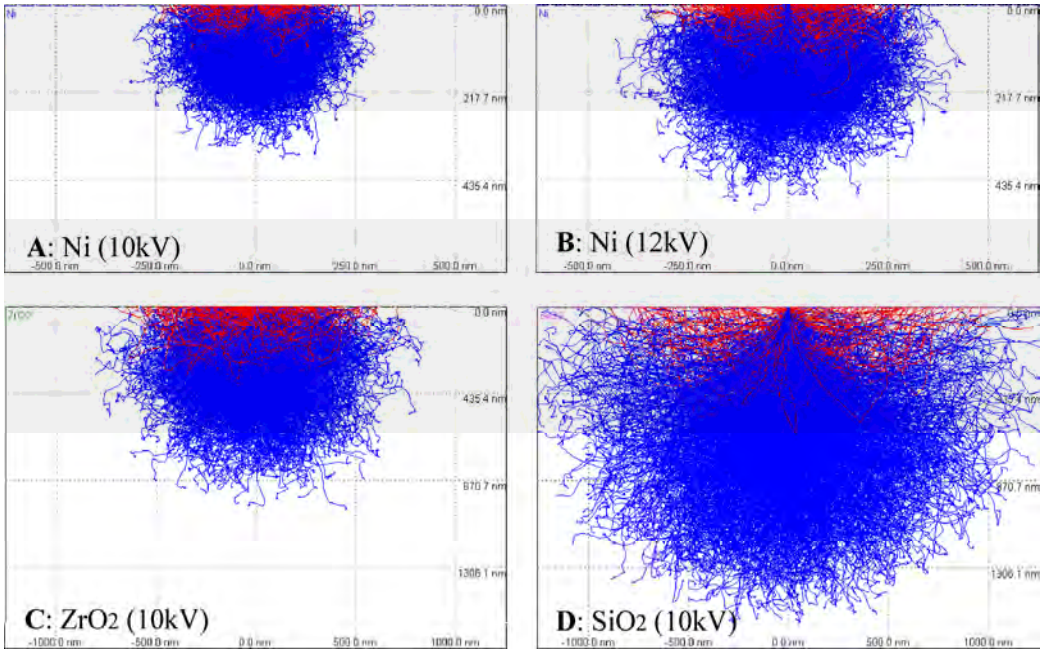

Figure 2-5: Monte Carlo simulations of the interaction (blue) and sampling (red) volumes in A) Ni at an acceleration voltage of 10 kV, B) Ni at 12 kV, C) ZrO_2 at 10 kV and D) SiO_2 at 10 kV. The program Casino v2.42 was used for the simulations [80].

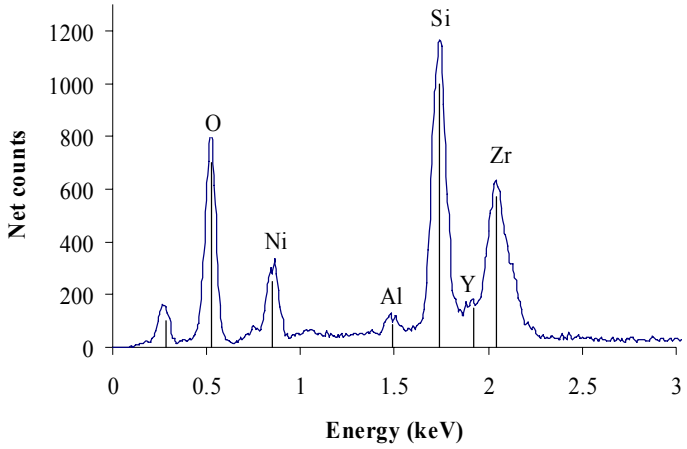

Figure 2-6: EDS of a silica containing impurity in the Ni/YSZ electrode of the cell used for 3test24 (see Appendix A and chapter 6 for details). The FWHM of K-lines are less than 100 eV and less than 200 eV for L-lines.

3. Performance, durability and effect of operating conditions

3.1. Introduction

For SOECs to become interesting from a commercial point of view a low internal resistance of the cell is important, not only at start-up but also during thousands of hours of electrolysis operation as the hydrogen and synthetic fuel production prices are proportional to the resistance of the cell. So far, only few results on durability of high performing SOECs have been reported in literature and even though the operation of the SOCs is reversible and can have comparable initial performance in electrolysis and fuel cell mode, the degree of passivation[4] of the cells during long-term testing in fuel cell and electrolysis operation mode respectively can be dramatically different [32]. Therefore it is necessary not only to produce high performing SOECs but also long-term stable electrolysis cells.
Results on initial performance, durability and effect of operation conditions for Risø SOECs are presented in this chapter[5]. Polarisation curves (iV curves) at various test conditions have been recorded to monitor the initial performance for both fuel cell and electrolysis operation of the SOCs produced at Risø National Laboratory. Results from galvanostatic long-term electrolysis tests for 8 SOCs[6] are given, and the electrolysis testing was shown to lead to a significant passivation of the cells within the first few hundred hours. A partial activation of an electrolysis tested cell by fuel cell operation is reported as well.

3.2. Experimental

The SOCs used for long-term electrolysis tests, the test set-up, test operation and procedure for data logging was described in detail in chapter 2. The test parameters (current density, $p(H_2O)/p(H_2)$, fuel utilisation and temperature) are shown in Table 3-1 for the tests described in this chapter. For all the reported results, except 3test27, steam was generated by combustion of hydrogen. The flow of steam to the fuel inlet of the cell was in all the tests, but 3test27, 12 l/h and the hydrogen flow rate was adjusted to meet the desired ratio of $p(H_2O)/(p(H_2)$. For 3test27 a steam flow of 45.5 l/h was applied. Measuring the $p(O_2)$ at inlet by the zirconia based oxygen sensors gives the ratio $p(H_2O)/(p(H_2)$ of the gas mixture close to the inlet of the cell and thereby check if a satisfying mixing and combustion of H_2 is obtained and that the desired $p(H_2O)$ is fed to the cell. Oxygen was led to the oxygen electrode during electrolysis operation of the cells, while air was applied to the oxygen electrode during OCV operation of the cells. Impedance spectra were recorded during electrolysis testing as described in chapter 2. The area specific resistances (ASRs) obtained from the iV curves presented here are calculated as described in chapter 2. The ASR values

[4] Passivation is a reversible and degradation is an irreversible loss in performance for the SOC.
[5] Parts of this chapter has been published as ”Performance and Durability of Solid Oxide Electrolysis Cells”, Hauch, A., Jensen, S.H, Ramousse, S. and Mogensen, M., *J. Electrochem. Soc.*, **153(9)** A1741-A1747 (2006).
[6] The long-term electrolysis tests presented in this chapter is only a selection. For an overview of all the electrolysis tests performed within this ph.d.-project see Appendix A.

therefore reflect the cell performances over a large polarisation range. A general "time line" for the tests is given in Figure 3-1. The AC and DC characterisation at OCV prior to electrolysis testing is used to monitor the initial performance of the cell. Passivation, degradation and/or activation during electrolysis testing are monitored by EIS under current load and the development of the cell voltage. Finally the cell is characterised again at OCV before cooling down and ending the test.

Table 3-1: Operation conditions for the galvanostatic long-term electrolysis tests. For all electrolysis tests, oxygen was passed over the oxygen electrode during electrolysis operation. The steam conversion is the number of converted water molecules (Faradays law) divided by the total number of H_2O molecules led to the cell.

Test	Current density	Steam conversion	$p(H_2O)/p(H_2)$	Temp.
3test14	- 0.25 A/cm^2	14%	0.7/0.3	750°C
3test19	- 0.25 A/cm^2	14%	0.7/0.3	850°C
3test21	- 0.50 A/cm^2	28%	0.7/0.3	850°C
3test22	- 1.00 A/cm^2	56%	0.7/0.3	850°C
3test23	- 0.50 A/cm^2	28%	0.7/0.3	950°C
3test26	- 0.50 A/cm^2	28%	0.99/0.01	850°C
3test27	- 2.0 A/cm^2	32%	0.9/0.1	950°C
3test30	- 0.50 A/cm^2	28%	0.5/0.5	850°C

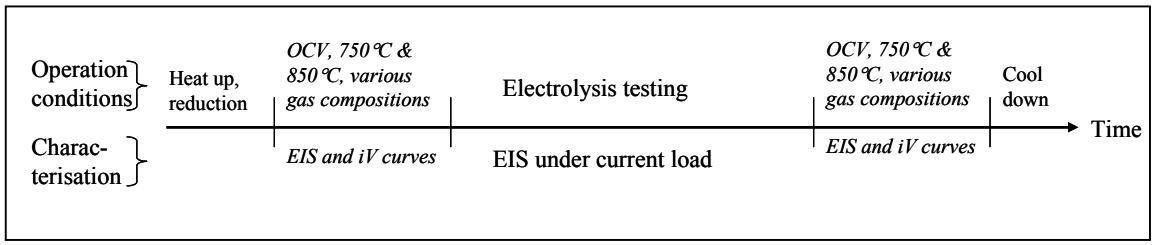

Figure 3-1: Time line for a typical electrolysis durability test. Italic text indicates initial and end characterisation of the cells. Passivation and/or degradation during electrolysis operation are monitored by EIS and the cell voltage development.

3.3. Results

3.3.1. Initial performance of SOECs and reversibility across OCV

The initial performance of all the cells was measured by recording iV curves at various temperatures and partial pressures of steam to the Ni/YSZ electrode prior to electrolysis testing. Figure 3-2 shows a comparison of representative initial iV curves for two cells, one with a high and one with a lower performance, 3test23 and 3test21. The iV curves shown were recorded at 850°C and $p(H_2O)/p(H_2) = 1$ and air to the oxygen electrode.

From the iV characteristic shown in Figure 3-2, it is observed that no discontinuity occurs in the shift from fuel cell to electrolysis operation. The ASR at varying $p(H_2)/p(H_2O)$ ratios at 850°C for the cells used for 3test23 and 3test21 is given in Table 3-2 together with the ASR values from 3test34 which is from another production batch but nevertheless have comparable initial performance. Even though the slopes of the iV curves in Figure 3-2 appear identical for positive and negative current densities, the numbers in Table 3-2 reveal that the ASR is larger when running the cells in electrolysis mode than in fuel cell mode. For one of the tested cells (3test24, app. A) a max current density record breaking electrolysis iV curve was performed where a current density of -3.58 A/cm^2 was obtained at 1.48 V, 950°C, 70% H_2O and for an active electrode area of 8 cm^2 [71]. The initial performance for this 3test24 was ASR(850°C) = 0.26 Ωcm^2 and ASR(950°C) = 0.167 Ωcm^2, which is the exact same initial performance as for 3test34 at both 850°C and 950°C.

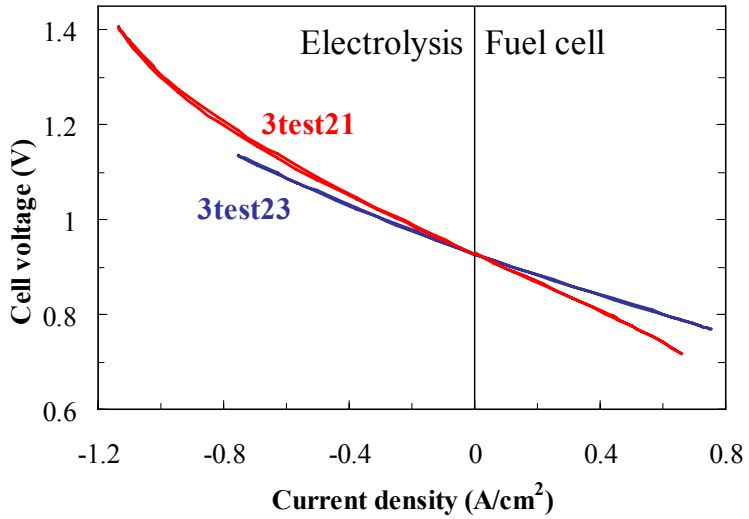

Figure 3-2: Comparison of iV curves recorded at 850°C before the electrolysis testing for 3test23 and 3test21, the cells with a high and lower performance. Air was passed over the oxygen electrode and the gas composition to the hydrogen electrode was $p(H_2O) = p(H_2) = 0.5$ atm.

The effect of temperature on the initial performance of the SOCs has also been investigated. Figure 3-3 shows an example of the effect of lowering the temperature from 850°C to 750°C for the high performing cell used for 3test23. Both curves were recorded at $p(H_2O)/p(H_2) = 1$. There is still continuity across OCV for the iV curve at 750°C but the ASR has more than doubled compared with the ASR values at 850°C (Table 3-2). For the iV curve at 750°C in fuel cell mode the ASR is 0.44 Ωcm^2. For the iV curve at 750°C in electrolysis mode the ASR is 0.65 Ωcm^2 if the data to -0.75 A/cm^2 is included and the chord is used for the calculation of the ASR. The ASR value "hides" the observed hysteresis effect. Calculating the ASR value as the chord from OCV to the voltage measured at a current density of -0.50 A/cm^2 for the start and end part of the iV curve leads

to ASR values of 0.60 Ωcm^2 and 0.70 Ωcm^2 respectively. The last part of this iV curve represents the more stable system.

Table 3-2: Area specific resistances (ASR) for the cell with a high (3test23) and a lower (3test21) performance at 850°C at varying steam content to the hydrogen electrode. The ASR values are calculated as the chord from OCV to the voltages measured at current densities of ± 0.75 A/cm^2. 3test34 is a typical and high performing cell from the 2005 production batch. For 3test21 at $p(H_2O)$ = 0.5 atm, fuel cell mode, only data to 0.67 A/cm^2 was available.

$p(H_2O)$	0.05 atm	0.20 atm	0.50 atm (fuel cell)	0.50 atm (electrolysis)
ASR_{3t21}	0.40 Ωcm^2	0.35 Ωcm^2	0.32 Ωcm^2	0.34 Ωcm^2
ASR_{3t23}	0.28 Ωcm^2	0.22 Ωcm^2	0.21 Ωcm^2	0.27 Ωcm^2
ASR_{3t34}	0.23 Ωcm^2	0.20 Ωcm^2	0.18 Ωcm^2	0.26 Ωcm^2

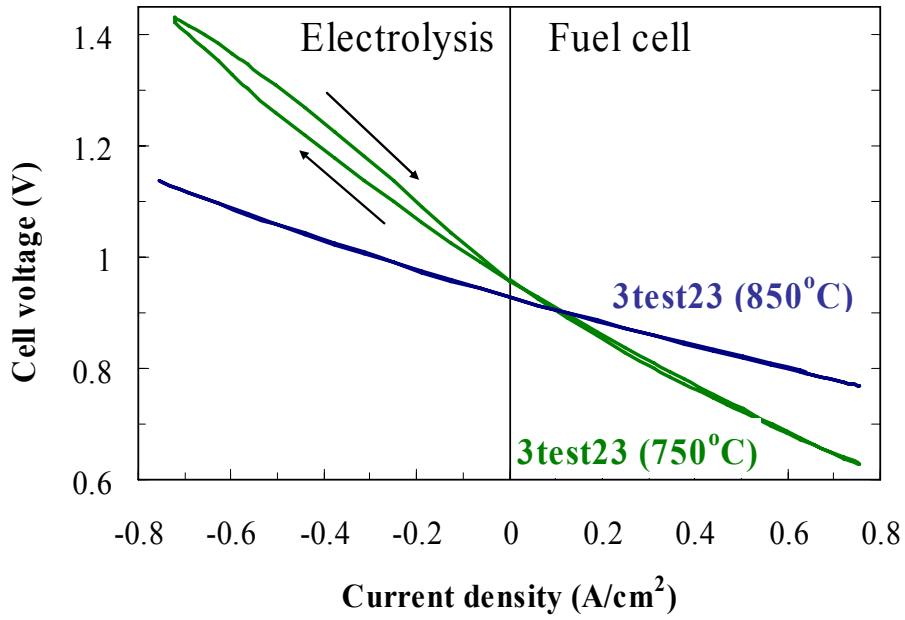

Figure 3-3: Initial iV curves at $p(H_2O)/p(H_2)$ = 0.5 atm/0.5 atm at 850°C and 750°C for 3test23. Arrows indicate direction of time when recording the iV curve at 750°C.

The same four trends for the initial characterisation have been observed for all cells tested in this work, namely 1) iV curves at 850°C and 950°C only have minor differences in ASR for fuel cell and electrolysis operation of the cell, 2) no passivation of the cell is observed to take place during electrolysis iV curves at 850°C and 950°C, 3) for electrolysis iV curves recorded at 750°C a passivation of the cell is observed and 4) the initial performance of the cells is improved at increasing temperatures.

3.3.2. Durability of SOECs – overview

The course of the cell voltage, the area specific ohmic resistance (R_s) and polarisation resistance (R_p) are used to monitor the durability and passivation of the SOECs during electrolysis testing. An overview of the changes in cell voltage, R_s and R_p during 7 electrolysis tests, for which cell voltage history graphs are presented in this chapter, is given in Table 3-3. The data with subscript "start" and "end" is the first and last measurement during constant electrolysis conditions for the long-term galvanostatic tests for data shown this chapter. A partly reactivation was observed for some of the tests; for example 3test19 after 116 h of test which is described in detail in [61] and 3test30 after 250 h of test (chapter 8). Durability tests over several – up to 15 – hundred hours reveal at least two different processes leading to the loss of performance for the SOECs: 1) an initial passivation within the first few hundred hours which is treated in this chapter and 2) a long-term degradation, see chapter 8. The development of cell voltage (ΔU), ohmic resistance (ΔR_s) and polarisation resistance (ΔR_p) in Table 3-3 is not normalised to e.g. 100 h or 1000 h as the observed passivation histories over the first few hundred hours are far from linear. ΔU, ΔR_s, ΔR_p should therefore be seen in relation to the given electrolysis test time in column 2 of Table 3-3.

Table 3-3: Development of cell voltage, ohmic resistance and polarisation resistance for the electrolysis test results presented in graphs in this chapter. R_s and R_p are determined as defined in chapter 2.

Test	Time*) (h)	ΔU (mV)	$R_{s,start}$ (Ωcm^2)	$R_{s,end}$*) (Ωcm^2)	$\Delta R_s / R_{s,start}$	$R_{p,start}$ (Ωcm^2)	$R_{p,end}$*) (Ωcm^2)	$\Delta R_p / R_{s,start}$
3t14	82	226	0.120	0.122	2%	0.267	1.477	453%
3t19	116	58	0.131	0.133	2%	0.163	0.456	179%
3t21	140	129	0.109	0.107	-2%	0.180	0.587	226%
3t22	92	184	0.168	0.282	68%	0.600	0.707	18%
3t23	135	23	0.067	0.109	63%	0.081	0.079	-2%
3t26	248	147	0.143	0.140	-2%	0.188	0.757	303%
3t30	247	122	0.170	0.190	12%	0.173	0.519	193%

*) Time and resistances at "end" refer to the last measurement of the test which is included in the figures in this chapter. 3t19, 3t22, 3t23 and 3t30 were tested further in electrolysis mode than the data presented here, see appendix A.

3.3.3. Durability of SOECs – effect of temperature

The development of the cell voltages during electrolysis test at three different temperatures and two different current densities is shown in Figure 3-4. For all tests, the cell voltage increased due to an increase in the internal resistance of the cells. The increase in cell voltage had a tendency to take the form of an "S" shaped curve and level off after approximately 100 hours of electrolysis. The least pronounced passivation over 135 hours of electrolysis was observed for the high temperature 3test23, which actually started out with a minor activation of the cell. The most significant passivation occurred for 3test14 where the cell voltage increased from 1055 mV to 1275 mV within only 82 hours of electrolysis. As the cell voltage seems to have stabilised at 1275 mV electrolysis 3test14 was stopped. The development of the polarisation resistance monitored by EIS recorded during the pronounced passivation observed for 3test14 is described and analysed in detail elsewhere [76]. The cell voltage curves for 3test14 and 3test19 illustrate the effect of increasing the temperature. At 750°C the cell voltage of 3test14 increased 226 mV (22%) while the similar 850°C test only had a cell voltage increase of 58 mV (6%). A similar effect of temperature change is observed by comparing 3test21 and 3test23, which had a cell voltage increase of 12% and 2%, respectively.

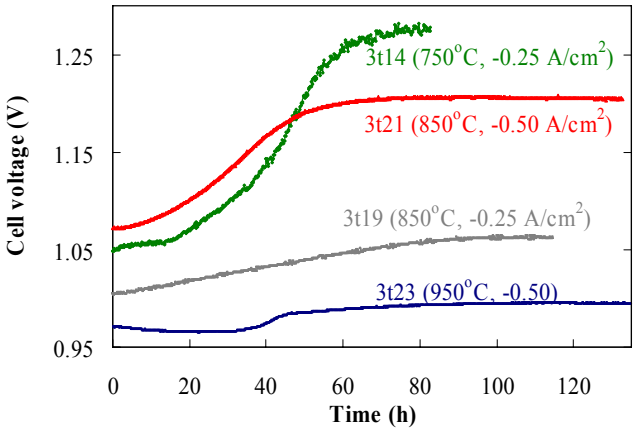

Figure 3-4: Cell voltage as a function of time at constant electrolysis conditions (Table 3-1). O_2 was passed over the oxygen electrode and the gas composition to the hydrogen electrode was $p(H_2O) = 0.7$ atm and $p(H_2) = 0.3$ atm for all 4 tests.

3.3.4. Durability of SOECs – Effect of current density/cell polarisation

The effect of increased current density is illustrated in Figure 3-5 by comparison of 3test19, 3test21 and 3test22. Initially the cell voltages for the three tests were 1.004 V, 1.072 V and 1.431 V, respectively, and the Nernstian voltage at OCV at these conditions is 0.885 V.
For the "low" current density (low cell polarisation[7]) tests, 3test19 and 3test21, the ohmic resistances are constant during testing while the polarisation resistances increase in

[7] The term "cell polarisation" describes the potential difference between the theoretical Nernstian potential (OCV) and the measured cell voltage at a given current density.

accordance with the increase in cell voltage. This is a typical development of the R_s and R_p during "low cell polarisation" tests (see app. A). For the "high cell polarisation" test, 3test22, not only an increase in polarisation resistance but also in ohmic resistance was observed. This is typical for tests having a cell polarisation above ~400 mV. Representative examples of differences in cell polarisations at start-up of electrolysis testing and the corresponding development of R_s and R_p during electrolysis operation of the cells are given in Table 3-4.

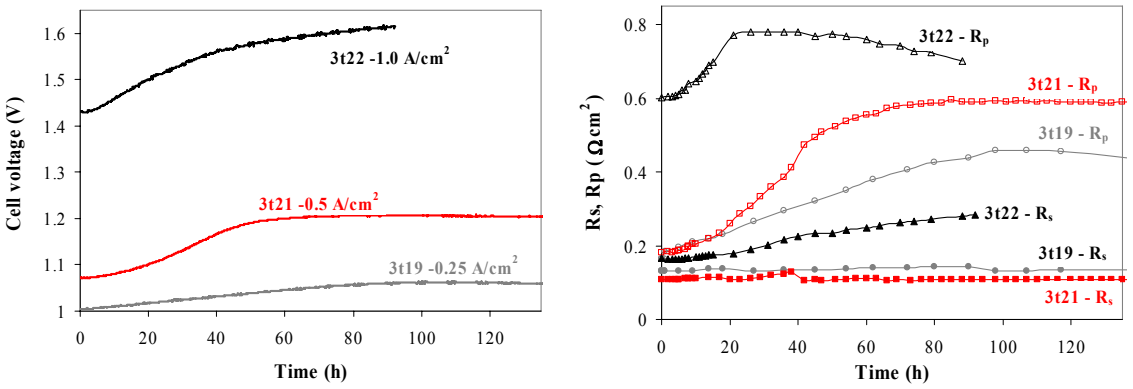

Figure 3-5: Cell voltage, R_s and R_p as a function of time at constant electrolysis conditions (Table 3-1). O_2 was passed over the oxygen electrode, and the gas composition to the hydrogen electrode was $p(H_2O) = 0.7$ atm and $p(H_2) = 0.3$ atm. The operation temperature was 850°C for all 3 tests.

Table 3-4: Development of cell voltage, ohmic resistance and polarisation resistance for long-term galvanostatic electrolysis tests. R_s and R_p are determined as defined in chapter 2. The given cell polarisation is measured at start of the electrolysis test period.

Test no	Time (h)	Temp. (°C)	i (A/cm^2)	H_2O-utiliza.	Cell Polarisation (mV)	$\Delta R_s / R_{s,start}$	$\Delta R_p / R_{s,start}$
3t21	140	850	-0.5	28%	184	-2%	226%
3t22	92	850	-1.0	56%	529	68%	18%
3t22*)	95	850	-0.5	28%	533	28%	30%
3t27	67	950	-2.0	32%	742	200%	-21%
3t32	620	950	-1.0	56%	281	-14%	173%

*) 2nd electrolysis test period after one electrolysis test and one fuel cell test period for 3test22

3.3.5. Durability of SOECs – Effect of p(H_2O)

The effect of increasing the partial pressure of steam at the inlet of the cell is illustrated in Figure 3-6. The operation temperature (850°C), current density (-0.5 A/cm^2) and steam flow rate (12 l/h) were identical for the 3 tests i.e. a steam utilisation of 28% applied for these three tests. For all three tests the ohmic resistances stayed constant during testing while the polarisation resistances increased in accordance with the increase in cell voltage. The increase in cell voltage is similar for the three tests but the rate at which the passivation occurs changes with the change in p(H_2O). Even though the rate for the initial passivation ("S-curve" for the cell voltage) is not identical for tests run at identical conditions, the general trend is still as illustrated by the cell voltage curves in Figure 3-6. Electrolysis tests that confirm this trend have been performed at p(H_2O) at 0.3 atm, 0.5 atm, 0.7 atm, 0.9 atm and 0.99 atm (see app. A), and they indicate a minimum time for the "S-curve" of the cell voltage is obtained for p(H_2O) between 0.7 atm and 0.9 atm.

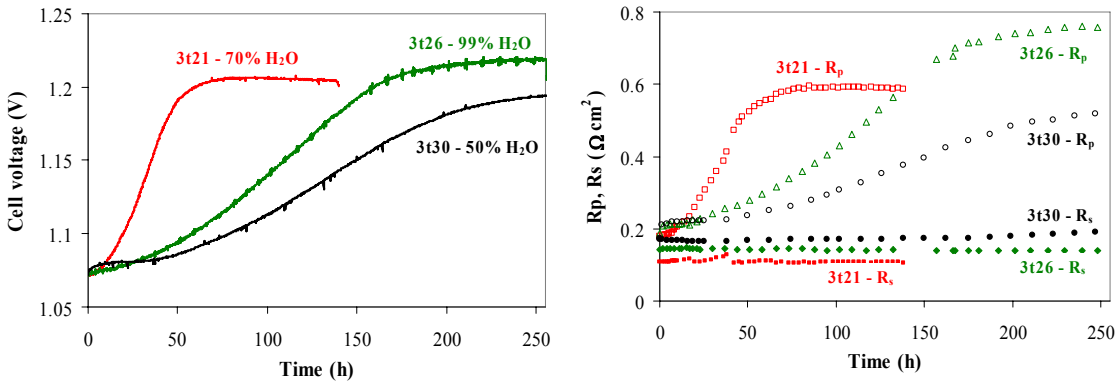

Figure 3-6: Cell voltage, R_s and R_p as a function of time at constant electrolysis conditions (Table 3-1). O_2 was passed over the oxygen electrode, the flow of H_2O was 12 l/h, and current density was -0.5 A/cm^2. The operation temperature was 850°C for all three tests. H_2 was used as buffer gas to achieve the different p(H_2O). The cell potential at start of 3test26 and 3test30 has been adjusted to the cell voltage of $3test21_{start}$ to ease the comparison of the cell voltage curves.

3.3.6. Activation of an SOC after passivation in electrolysis mode

A simple way to monitor the passivation of the cells used for electrolysis tests is by comparing iV curves recorded before and after electrolysis testing. A comparison of iV curves recorded before and immediately after electrolysis operation of 3test14 is shown in Figure 3-7. The passivation of the 3test14 cell has led to an increased slope of the iV curve. Data from the iV curves are applied to calculate the conversion corrected ASRs since the internal resistance of the cell depends on test conditions such as the reactant utilisation [81]. The over voltage will not be equal at the gas-inlet and gas-outlet and therefore a conversion correction has been made for the ASR using an iterative calculation method as discussed

elsewhere [8]. The conversion corrected ASRs are included in Figure 3-7. A significant hysteresis effect is observed for the iV curve recorded immediately after electrolysis operation of 3test14. This hysteresis effect corresponds to a partial activation of the cell obtained during the recording of the iV curve in fuel cell mode. In Figure 3-7, the direction of time is indicated by arrows.

After ending of the electrolysis test for 3test21, the cell was run at constant fuel cell conditions at 850°C, a current density of 0.5 A/cm^2 and p(H_2)/p(H_2O) = 0.95/0.05 as inlet gas composition to the hydrogen electrode and the development of the cell voltage during fuel cell operation is shown in Figure 3-8. The cell voltage increased by 49 mV during the 97 hours of constant fuel cell operation of the cell. This corresponds to a partial activation of cell used for 3test21 and both R_p and R_s decreased. Similar activation of a passivated SOEC by constant fuel cell operation has been obtained for 3test22 and 3test24 [82]. Furthermore, an activation of an SOEC passivated within the first couple of hundred hours can obtained by continued constant electrolysis operation of the cell (see chapter 8 and [61]).

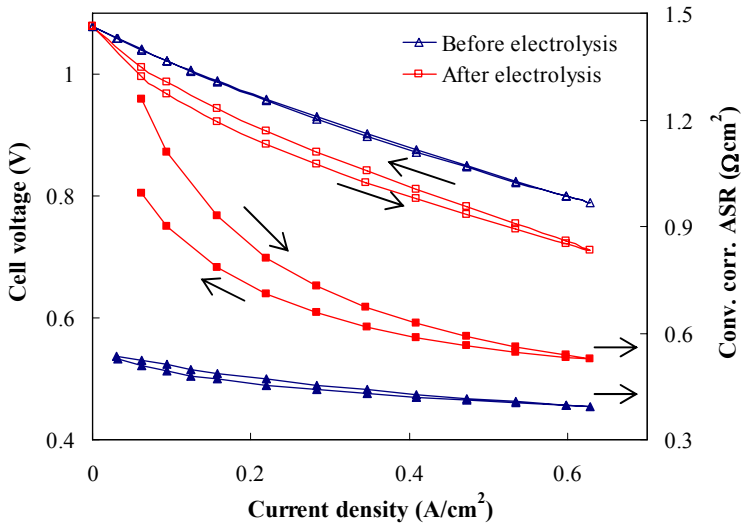

Figure 3-7: iV curve recorded before (Δ) and immediately after (□) electrolysis operation of 3test14. The iV curves were recorded at 750°C and with gas composition of p(H_2) = 0.95 atm and p(H_2O) = 0.05 atm to the hydrogen electrode. Arrows indicate direction of time. Open symbols show the cell voltages and closed symbols the calculated conversion corrected ASR values.

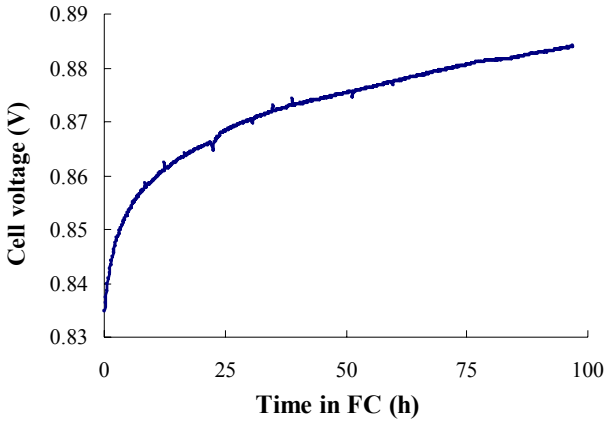

Figure 3-8: Cell voltage during constant fuel cell operation after electrolysis operation of 3test21. Operation conditions were: 850°C, 0.5 A/cm^2, p(H_2) = 0.95 atm and p(H_2O) = 0.05 atm.

3.4. Discussion

3.4.1. Initial electrolysis performance

The continuity of the iV curves (Figure 3-2) across OCV verifies that even though these cells were produced and optimised for fuel cell use, they can work as reversible SOCs. In general the initial ASR obtained from iV curves was lower in fuel cell mode than in electrolysis mode (Table 3-2).

A limiting factor when recording iV curves in electrolysis mode can be steam starvation at high current densities, especially if the inlet gas is not optimally distributed over the cell or if there is a leak in the cell test set-up. The highest current density for the 3test21 electrolysis iV curve (Figure 3-2) corresponds to a steam utilisation of 70%. Concentration polarisation is observed at the highest current densities for this iV curve, but no steam starvation problem occurred, which would have led to a more abrupt increase in cell voltage. For 3test34 (Table 3-2) the electrolysis iV curve at 850°C was run up to -1.45 A/cm^2 which gives a steam utilisation of 87% with no sign of steam starvation and only limited effect of concentration polarisation. This shows that the steam is satisfactorily distributed and large leaks are avoided. For properly sealed cells leak measurements at start-up show leaks of ~25 mA/cm^2 corresponding to a gas leak of ~0.2 l/h

Table 3-5 lists some initial performances obtained from iV curves in electrolysis mode for SOECs reported in literature. As discussed by Mogensen et al. [8], the concept of area specific resistance for SOFCs is often used, though no general accepted definition seems to exist. Since the ASR depends on fuel utilisation, a more direct and correct description of the cell performance is given by the conversion corrected ASRs (see Figure 3-7). Unfortunately, conversion corrected ASRs or information enabling the calculation of it, is not always reported in literature. The listed ASR values in Table 3-5 are therefore simply obtained by taken the slopes of the reported iV curves in the linear regions. The references in Table 3-5 have been selected as they represent results obtained at test conditions closest

to those applied for the iV curves presented here. Table 3-5 shows that the reversible SOCs produced at Risø National Laboratory have the best initial performance.

The "world record breaking" electrolysis iV curve reported in [71] for the cell used in 3test24 is in itself outstanding, and to the best of our knowledge a current density of -3.6 A/cm^2 has not been obtained for SOECs previously at a voltage of only 1.48 V. The significance of the "world record breaking" electrolysis iV curve is greatly enhanced by the following facts: 1) The cell is produced at the pre-pilot plant using inexpensive production methods and 2) other Risø SOECs have similar high initial electrolysis performance e.g. $ASR_{3test34,950°C}$ = 0.17 Ωcm^2 which is exactly the same as for the "world record breaking" electrolysis iV curve for 3test24. In other words, 3test24 used for the "world record breaking" electrolysis iV curve was not a unique single case of a high performing SOEC. Therefore the excellent initial performances for the Risø SOECs reported here demonstrate the large potential for the use of these cells for efficient and inexpensive hydrogen production – and in turn synthetic fuel production.

Table 3-5: Some reported initial performances of electrolysis cells. Comparison of ASRs obtained from iV curves. The ASRs are taken as the slopes in the linear regions of the electrolysis iV curves presented in the references sited. For each reference the ASR on full cells for systems and with the experimental conditions closest to the ones applied in this work is given.

T [°C]	p(H_2O) [atm]	p(H_2) [atm]	ASR [Ωcm^2]	Specifications	Ref.
850	0.50	0.50	0.27	Ni/YSZ-YSZ-LSM (planar 2G DK-SOFC)	[61]
950	0.50	0.50	0.15	Ni/YSZ-YSZ-LSM (planar 2G DK-SOFC)	[61]
1000	0.67	0.33	1.17	Ni/YSZ-YSZ-LSM (tubular cell)	[83]
908	0.67	0.33	2.7*	Ni/YSZ-YSZ-LSM. 32 cell stack – tubular cells.	[84]
1000	0.91	0.09	2	Ni/YSZ-YSZ-LSM	[85]
1000	0.50	0.50	0.7	Ni/YSZ-YSZ-LSM	[86]
850	0.50	0.50	0.45	Ni/YSZ-ScSZ(175 μm)-LSM	[87]
900	0.50	0.50	1.8	Figure 2 in [56] for calculation of ASR for full cell.	[56]
850	0.11	0.89	0.35	Ni/YSZ-ScSZ(125 μm)-LSM	[50]
800	0.11	0.89	0.50	Ni/YSZ-ScSZ(125 μm)-LSM	[88]
850	0.11	0.89	0.33	Ni/YSZ-ScSZ(125 μm)-LSM	[88]

*) The ASR given is the average per cell in the stacks. The numbers calculated from the iV curves have been reduced by 31% to correct for the resistance due to interconnect. The reduction by 31% was estimated by comparison of single cell and stack test at the same conditions as they were reported in [83].

3.4.2. Durability and effect of the different operation conditions

In literature the durability of SOFCs is often given by the change of the cell voltage in percentage per 1000 h [32] and/or the R_s and R_p values recorded at OCV before and after the test under current load. For the SOEC tests presented in this chapter the dominating passivation over the first few hundred hours is far from linear in time and only few electrolysis tests have been run for more than 1000 h. Therefore, the passivation measured by the cell voltage increase in these tests is here given as the change in cell voltage over the specific electrolysis test time and not per 1000 h. A more detailed observation of the durability during electrolysis testing is given by the development of R_s and R_p obtained from electrochemical impedance spectra under current load which is also given for the tests presented here. This set of data (R_s and R_p under current load) has two clear advantages over only monitoring durability via the change in cell voltage and EIS at OCV before and after test under current load: 1) EIS data separates the loss in performance of the cell into ohmic and polarisation losses and 2) the EIS is still recorded under conditions (i.e. current load/cell polarisation) at which the observed loss in performance occurs.

The issue of durability for SOECs is, as it is for SOFCs, important in the perspective of making the SOCs a reliable energy technology ready for commercialisation. To keep the investment costs low and in turn the hydrogen and synthetic fuel production price low using SOEC, future SOECs need to: 1) have high performance, 2) use inexpensive raw materials, 3) apply inexpensive productions methods and 4) have long-term durability.

Unfortunately long-term testing of SOECs has only been reported a very limited number of times in the literature. Therefore a comparison of the long-term electrolysis testing results presented here with results for similar electrolysis cells is difficult. One of the few successful long-term electrolysis tests was reported by Dönitz et al. [83]. They ran a 1000 hour single cell test at 1000°C and no notable passivation was observed. However, it should be pointed out that the microstructure of their electrodes was more coarse than for the SOECs tested in this project, and that the initial ASRs for their cells at 1000°C were larger than the ASR that was measured for a Risø cell at 850°C (3test19) after 766 hours of constant galvanostatic electrolysis testing.

Effect of temperature

Increasing the operating temperature will lead to improved kinetics for the SOECs, and as expected the ASRs of the SOECs decrease with increasing temperature (Figure 3-3). In view of the fact that different cells have very similar initial iV curves (Figure 3-2) and supplementary initial EIS characterisation gives comparable results, the development of the cell voltages in Figure 3-4 illustrates the effect of variation of temperature and current density for the electrolysis tests. A difference in temperature from 750°C to 850°C gives rise to a considerable difference in the increase of the cell voltage during electrolysis. While the cell voltage for 3test19 only increased by 58 mV over 116 hours (5%/100 h), the increase was 220 mV over 82 hours (27%/100 h) for 3test14. The same trend for the increase in cell voltages is seen when comparing 3test23 and 3test21, where the only difference in operation conditions was the temperature of 950°C and 850°C respectively.

For similar hydrogen electrode supported Risø SOCs tested as fuel cells a significant increase in the long-term degradation rate is also observed when shifting from testing at 850°C (and 950°C) to 750°C [32], but the degradation rates at the different temperatures for SOFCs are order(s) of magnitude(s) lower than for SOEC testing and the origin for the passivation/degradation is significantly different. Therefore a quantitative comparison of passivation/degradation rates for SOFC and SOEC is hardly appropriate.

As shown and discussed by Hagen et al. [32] an increase in temperature will lead to an increased mobility of Ni and Ni coarsening can be expected to increase with increasing operating temperature. An increase in the Ni particle size distribution for electrolysis tested SOCs has been observed [62], but coarsening of the Ni particles is not likely to be the main reason for the observed passivation during the first few hundred hours of electrolysis operation (see chapter 5). Changing the operating temperature will also lead to changes in the mobility and physical properties (viscosity, diffusion) of the glassy phase silica-containing impurities in the hydrogen electrode (see chapter 6 and 7), but more information about the chemical composition and properties of these glassy phase impurities is necessary, if the effect of operating temperature on these phases combined with their influence on cell performance shall be analysed.

Effect of current density and cell polarisation

The effect of changing the current density for SOECs is seen Figure 3-5. It should be noticed that the same flow rate of steam was applied and therefore a change in the current density from -0.25 A/cm^2 to -0.50 A/cm^2 and -1.0 A/cm^2 also changed the steam utilisation from 14% to 28% and to 56%. Therefore the increase in current density will also lead to an increase in the different gradients (potentials, p(H_2O) etc.) during electrolysis operation. As tests are operated galvanostatic, it is natural to see the observed development of the cell voltage, R_s and R_p at varying current densities as an effect of the current density. This is an incorrect simplification of the electrolysis test results. An increased passivation of the SOECs can be expected at higher loads; nevertheless the development of the ohmic resistances and the polarisation resistance seem more closely related to cell polarisation than the current density. This is illustrated by the numbers in Table 3-4, which is an extract of appendix A. Comparing the first electrolysis test for 3test22 with 3test32 which had the same current density and steam utilisation but with 3test32 having a considerably lower cell polarisation, it is observed that the "low cell polarisation" 3test32 does not suffer an increase in ohmic resistance as observed for "high cell polarisation" 3test22. Notice that the $\Delta R_p / R_{s,start}$ for 3test22 covers an increase in R_p of 0.18 Ωcm^2 over 92 h and $\Delta R_p / R_{s,start}$ for 3test32 covers an increase in R_p of 0.24 Ωcm^2 over 620 h. 3test27 was operated at the same temperature, p(H_2O)/p(H_2) as 3test32 and with a "conservative" choice of steam utilisation. Nevertheless, 3test27 had a cell polarisation of 742 mV at the start of electrolysis testing, and like the other "high-cell polarisation" tests an increase in R_s was observed. The general trend for tests that were run at cell polarisations less than ~400 mV at start of electrolysis operation is: 1) the ohmic resistance stays constant during long-term electrolysis testing and 2) R_p increase in accordance with the observed increase in cell voltage. The trends for

electrolysis tests run at large cell polarisations are: 1) the ohmic resistance increase and 2) R_p increase as well. The decrease in R_s for 3test32 can be due to improved contacting during testing at 950°C. Hagen et al. [32] also observed that SOFCs operated at higher cell polarisations experienced an increase in both R_s and R_p, whereas cells operated at lower cell polarisations only seemed to had an increase in the polarisation resistance.

Effect of partial pressure of steam

As seen from Figure 3-6 the change in $p(H_2O)$ changes the rate at which the passivation over the first few hundred hours occurs but it does not lead to any significant change in the degree of the passivation i.e. the increase in the cell voltage is very similar in the cases of $p(H_2O) = 0.5$ atm, $p(H_2O) = 0.7$ atm, $p(H_2O) = 0.99$ atm (Figure 3-6).

Previously Vels Jensen [89] found evidence for a build-up of impurities containing silicon at the triple phase boundary (TPB) for a Ni-YSZ model system and Liu and Jiao [90] found segregated silicon containing impurities in a tested half cell by scanning and transmission electron microscopy. Such a build-up of impurities could lead to an increase in cell voltage as observed in Figure 3-4, Figure 3-5 and Figure 3-6, where the cell voltage curves level off when the impurity build-up at the Ni-YSZ TPB stops. A subsequent decrease in the cell voltage could be due to a conversion of the impurity phase e.g. crystallization of the glass or evaporation, see chapter 8. The tendency for the course of the cell voltage for tests presented here to take the form of "S-curves" supports the explanation for the passivation of the electrolysis cells given by Jensen et al. [91]. By deconvolution of the EIS recorded during electrolysis, it was shown that the rate limiting step for the steam electrolysis using SOCs was due to a process at the TPB in the Ni/YSZ electrode, and it was argued that it is related to an increase in the diffusion path length during the passivation of the electrolysis cell. This phenomenon was explained as impurities building up at the TPB in the Ni/YSZ which is supported by the results in [82]. If this initial passivation as observed for the cell voltage curves presented in this chapter relates to the evaporation of $Si(OH)_4$ from glass sealing (see chapter 6 and 8), the increase in $p(H_2O)$ will lead to an increase in $p(Si(OH)_4)$ which will most likely affect the rate at which the passivation occur. At a certain point the evaporation of $p(Si(OH)_4)$ can be expected to end as a consequence of depletion of Si-species in the surface layers of the glass sealing. As the tests shown in Figure 3-6 were run at the same current density (i.e. the reduction of steam affects the equilibrium $Si(OH)_4 \leftrightarrow SiO_2 + 2H_2O$ to the same extent, chapter 6) and with the same type of glass sealing (same amount of Si-species available in the surface layer); the degree of passivation observed can be expected to be independent of a change in $p(H_2O)$. This is in good agreement with the observed effect of increasing the $p(H_2O)$ for the electrolysis tests, though it does not provide an explanation for the decreased rate of passivation observed when the $p(H_2O)$ is increased to 0.99 atm (3test26).

3.4.3. Reactivation of an SOEC

The partial activation of the cell by running an iV curve in fuel cell mode (Figure 3-7) after the electrolysis test has been observed for several tests. For the iV curve recorded after

electrolysis 3test14 (Figure 3-7), the conversion corrected ASR decreased by 20% at a current density of -62.5 mA/cm^2 and this activation occurred within the 22 minutes it took to record the entire iV curve. This activation of the cell is most likely of a nature different from that of the activation observed at constant electrolysis testing e.g. 3test19 and 3test30 (app. A and [61]). The activation due to fuel cell operation is governed by the change in current direction e.g. a change in the direction of O^{2-} ions conducted in the electrolyte and a change in the p(H_2O) gradient in the Ni/YSZ electrode. Impurities can be removed from the TPB and transported towards the bulk of the composite Ni-YSZ electrode, i.e. away from the electrolyte/electrode interface where the electrochemical reactions occur. Considering the partial activation of the cell for 3test14 by running an iV curve in fuel cell mode after electrolysis passivation, it is not surprising that a partial activation of an SOC after electrolysis testing can also be obtained by operating the cell at constant fuel cell conditions as observed for the cell for 3test21 (Figure 3-8). For the activation of the cell at constant fuel cell operation, the time scale is again shorter than for the activation observed for 3test19 [61] at constant electrolysis conditions.

3.5. Conclusion

From the results presented here using hydrogen electrode supported SOCs produced at Risø National Laboratory for high temperature electrolysis of steam it can be concluded that:

- The cells were produced on a pre-pilot scale and optimised for fuel cell use. These cells can be operated both as fuel cells and electrolysis cells. The cells can be shifted directly from fuel cell to electrolysis operation without discontinuity across OCV.
- The area specific resistance obtained from the iV curves run in electrolysis mode was higher than for fuel cell mode iV curves for the same cells.
- The electrolysis iV curves show that the SOECs tested in this work performs very well compared with similar SOEC results reported in literature. The excellent initial electrolysis performance can be obtained not only for a single cell but for the main part of the tested SOCs
- At constant galvanostatic electrolysis conditions, the internal resistance of the cells increased significantly during the first ~100-200 hours, after which the cell voltage stabilised or even decreased (chapter 8).
- For heavily passivated cells a partial activation of the cell can be obtained by running an iV curve in fuel cell mode immediately after long-term electrolysis test.
- Cells that have been passivated during electrolysis can be partly activated by operating the cell at constant fuel cell conditions over hundred(s) of hours.
- Decreasing the operating temperature leads to an increase in the degree of passivation of the SOEC.
- Changing the inlet p(H_2O) does not significantly change the degree of passivation but up to p(H_2O) = 0.7 atm the rate at which the SOEC passivate (in this initial passivation over the first ~100-200 h) increase with increasing p(H_2O) and for p(H_2O) above ~ 0.8 atm it decreases for increasing p(H_2O).

- The development of the ohmic and polarisation resistances during electrolysis testing is more closely related to the cell polarisation than to the actual current density for the tests. For tests operated at cell polarisation below ~400 mV, the ohmic resistance, R_s, is more or less constant while the polarisation resistance, R_p, increase in accordance with the cell voltage increase. For tests operated at cell polarisations above <400 mV, the ohmic resistance – and typically also the polarisation resistance – increases.

4. Electrochemical Impedance Spectroscopy for SOECs

4.1. Introduction

Electrochemical impedance spectroscopy (EIS) has previously led to valuable information for the characterisation of SOFCs. EIS has increased the understanding of the limiting processes for different materials as well as effects of processing and microstructure of materials in tests applying electrode pellets, half cells and full SOFCs [13; 92-95]. The EIS is sensitive to the design of the cells and the exact microstructure of the electrodes. Therefore, it is advantageous to compare the obtained impedance spectra for SOECs with EIS results and analyses for similar cells tested in fuel cell mode, as it has been reported by Barfod et al. [11; 13; 95]. In this chapter impedance results and analyses for three representative tests are given. The purpose of the selected EIS results and analyses presented here is to illustrate that: 1) the ohmic resistance (R_s) is not affected significantly by the "short-term" passivation (in the first few hundreds of hours of SOEC testing) but the polarisation resistance (R_p) is, 2) change in impedance spectra due to gas variation experiments before and after electrolysis operation verifies that the main passivation of the SOECs is caused by processes in the H_2 electrode, 3) analyses of impedance spectra recorded during the "short-term" passivation strongly point towards that this passivation is caused by solid-state or surface diffusion related process(es) in the H_2 electrode.

4.2. Experimental

The SOCs used for long-term electrolysis tests, the test set-up, test operation, procedure for data logging and recording impedance spectra were described in chapter 2. The operating conditions for the electrolysis tests described in this chapter are given in Table 4-1. Steam at a flow of 12 l/h was generated by combustion of hydrogen. The three tests, 3test14, 3test19 and 3test30, have been exposed to one electrolysis test period each. The electrolysis testing has been stopped at three different parts of the passivation/activation/degradation course. 3test14 was stopped at the maximum passivated state during the "short-term" passivation. 3test19 was stopped after passivation and partly activation during electrolysis operation. 3test30 was operated in constant electrolysis mode long enough to show "short-term" passivation, activation and the underlying and subsequently long-term degradation (Figure 4-10).

Table 4-1: Operating conditions during electrolysis testing. O_2 was passed over the O_2 electrode during electrolysis operation. Steam conversion is the number of converted water molecules divided by the total number of H_2O molecules supplied to the cell.

Test	Current density	Steam conv.	$p(H_2O)/p(H_2)$	Duration	Temp.
3test14	- 0.25 A/cm^2	14%	0.7/0.3	82 h	750°C
3test19	- 0.25 A/cm^2	14%	0.7/0.3	767 h	850°C
3test30	- 0.50 A/cm^2	28%	0.5/0.5	1316 h	850°C

4.3. Analysis of impedance spectra

Basic elements in equivalent circuits for EIS analysis

The basic elements used in the equivalent circuits for analysis of the impedance spectra are shown in Figure 4-1. In Figure 4-1 a resistor (R1) is in series with a parallel connection of a constant phase element (CPE1) and a resistance (R2), a so-called Cole-element. The series resistance R1 can describe the ohmic resistance and R2 can describe the polarisation resistance of a cell. The CPE is used instead of capacitor to compensate for the distribution/ non-homogeneity of the system. For porous SOCs a frequency exponent (n) of ~0.8 to 1 can be expected and the Cole-element will appear as a depressed semicircle. The summit frequency, f_s, for the Cole-element is given by [96]:

$$f_s = \frac{1}{2\pi}(RY_0)^{-1/n} \qquad (4\text{-}1)$$

where R is the resistance and Y_0 is amplitude of the admittance.

To describe a diffusion limited process a fractal shorted Warburg diffusion element (Ws) can be applied. This solves the one-dimensional diffusion equation. A simulated impedance spectrum for a resistance (R1) in series with a Ws-element is shown in Figure 4-1B. The impedance (Z_w) of the Ws was for instance described by Jacobsen and West [97]:

$$Z_W(\omega) = \frac{RT\nu}{F^2c}\cdot\frac{\delta}{D}\cdot\frac{\tanh((j\omega\delta^2/D)^p)}{(j\omega\delta^2/D)^p} \qquad (4\text{-}2)$$

where c is the concentration of the diffusing species, ν is the stoichiometric number, δ is the diffusion path length, D is the diffusion coefficient at the temperature T and p is the frequency exponent to describe the degree of distribution of the system. For a non-distributed system p equals 0.5 and values below 0.5 for systems having distributed finite diffusion path lengths. In the fitting programme Zview [98] the following parameters are used to optimise the fit of impedance spectra: $W_p = p$, $W_T = \delta^2/D$ and the resistance $W_R = RT\nu^2\delta/F^2cD$. The summit frequency ($f_{s,w}$) for the Ws-element is found by solving $\partial Z''(\omega)/\partial\omega = 0$ using the programme MathCad or similar programme and in the simple case of p = ½ the expression for the summit frequency reduces to:

$$f_{s,W}(p=0.5) = \frac{2\pi D}{\delta^2}\cdot 2.54 \qquad (4\text{-}3)$$

Modelling of impedance spectra of SOCs

Thorough modelling of impedance spectra obtained on half cells and full SOFCs, similar to the SOCs tested as electrolysis cells in this project, has led to the equivalent circuit model for H_2 electrode supported SOCs produced at Risø National Laboratory shown in Figure 4-2. As shown by Jensen et al. [91] and which will be evident from the results presented here, it is advantageous to replace the Cole-element $(R,CPE)_{Ni}$ in the equivalent circuit model (Figure 4-2) with a Ws-element in order to better describe the development of the impedance spectra recorded during electrolysis testing.

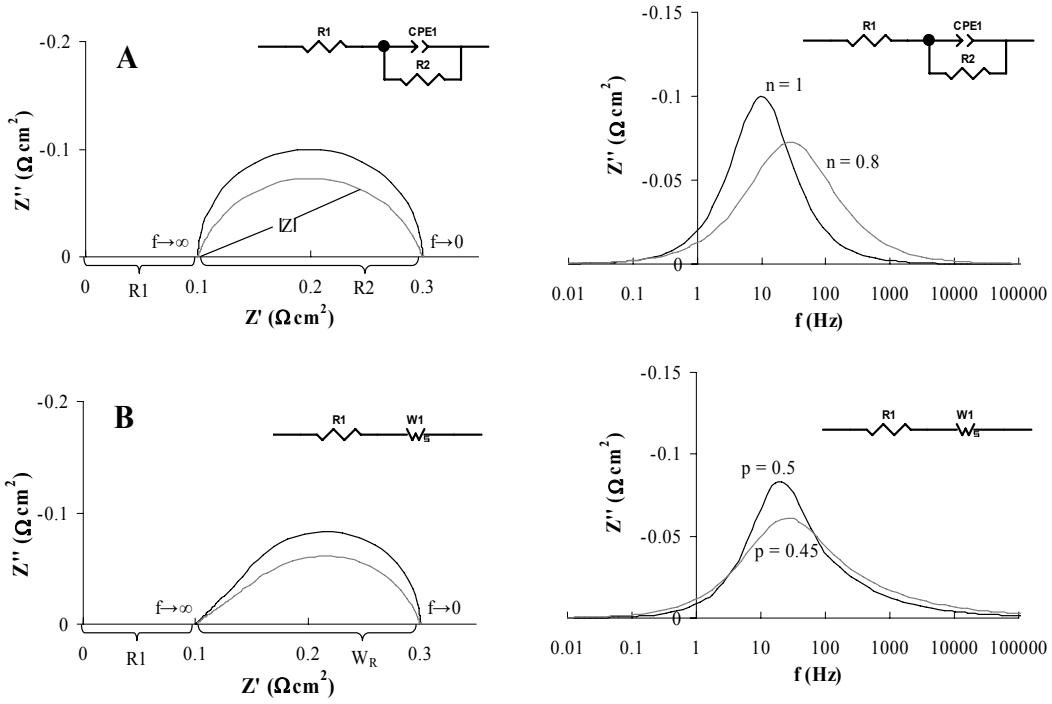

Figure 4-1: Equivalent circuit elements and resulting simulated spectra. A) Resistor (R1) in series with a Cole-element (R2 in parallel with a constant phase element, CPE1). B) Resistor (R1) in series with a fractal shorted Warburg element (Ws).

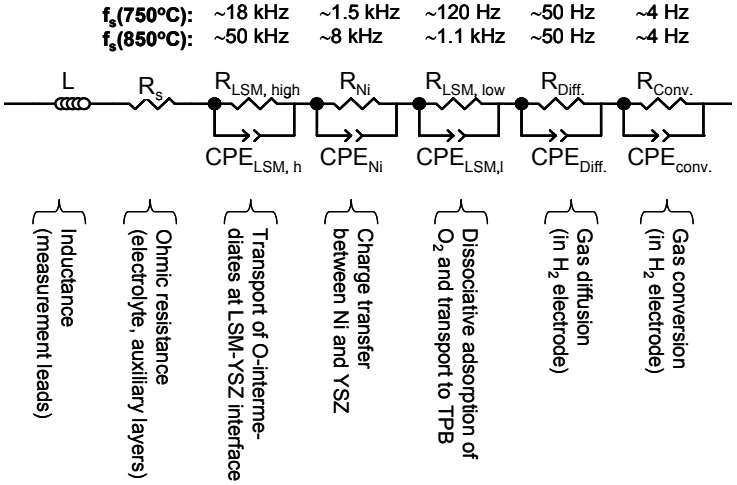

Figure 4-2: Equivalent circuit model to fit impedance spectra obtained on hydrogen electrode supported Risø SOCs [13; 95]. Summit frequencies for the (R,CPE)-circuits at 750°C and 850°C are approximate numbers.

Analysis of changes in impedance spectra due to gas variations

Changes in the impedance spectra due to variations in the gas mixture led to each of the electrodes have been used to analyse the passivation and degradation of the SOECs. Prior to electrolysis testing, spectra are recorded at OCV first keeping the gas to the oxygen electrode constant but recording a spectrum with 4% H_2O in H_2 and afterwards a spectrum with 20% H_2O in H_2 to the H_2 electrode. Hereafter two spectra are recorded keeping the gas to the H_2 electrode constant but recording first a spectrum applying pure O_2 and then a spectrum applying air to the O_2 electrode. A similar set of four impedance spectra is recorded at OCV after electrolysis testing. Subtraction of two spectra where a gas change has been made for one electrode only and comparing the "subtraction spectra" (ΔZ) obtained before and after electrolysis testing reveal at which electrode and in which frequency range the main changes have occurred. To enhance the frequency resolution of ΔZ it is advantageous to represent the change in the impedance spectra due to the gas variations by calculating the difference between the derivates of spectra obtained at two different gas compositions with respect to ln(f) and plot this versus frequency i.e. for the real part of the impedance spectra for the gas change at the O_2 electrode the expression is [99]:

$$\Delta\partial Z'(f)=\frac{\partial(Z'_{air}(f)-Z'_{O_2}(f))}{\partial \ln(f)} \qquad (4\text{-}4)$$

$\Delta\partial Z'(f)$ plotted versus the frequency will be referred to as a difference plot. The error limits for the difference plot method for these cells have been investigated by Jensen et al. [99]. It was shown that a difference plot at 750°C for a "H_2-H_2 shift", with a D_2 spectrum in between, resulted in $\Delta\partial Z'(f)$ ~0.1 $m\Omega cm^2$. The advantages of analysis using the changes in impedance spectra due to gas variation experiments combined with difference plots are: 1) the method is model independent; 2) it clearly separates contributions from each of the two electrodes to the change of the impedance spectra and 3) difference plots lead to increased frequency resolution for different arcs in the spectra. The disadvantages of this method as it has been applied in this project compared to analysis of impedance spectra recorded during electrolysis testing are: 1) the impedance spectra are not recorded at the conditions at which the passivation occurs i.e. under cathodic polarisation, and 2) it does not reveal whether the process leading to passivation/degradation is best described as limitation due to diffusion, charge transfer etc.

4.3. Results

4.3.1. Impedance spectra before and after electrolysis tests

The electrolysis testing of 3test14 was stopped at the maximum passivated state during the "short-term" passivation. Impedance spectra obtained at OCV before and after electrolysis testing of 3test14 at 750°C applying 20% H_2O in H_2 to the H_2 electrode is shown in Figure 4-3. R_s and R_p for the two spectra in Figure 4-3 are given in Table 4-2. R_s stayed constant while R_p increased 98%. The f_s for the arc which increased the most in resistance as a

consequence of electrolysis testing decreased from 2100 Hz to 80 Hz at 750°C (Figure 4-3B).

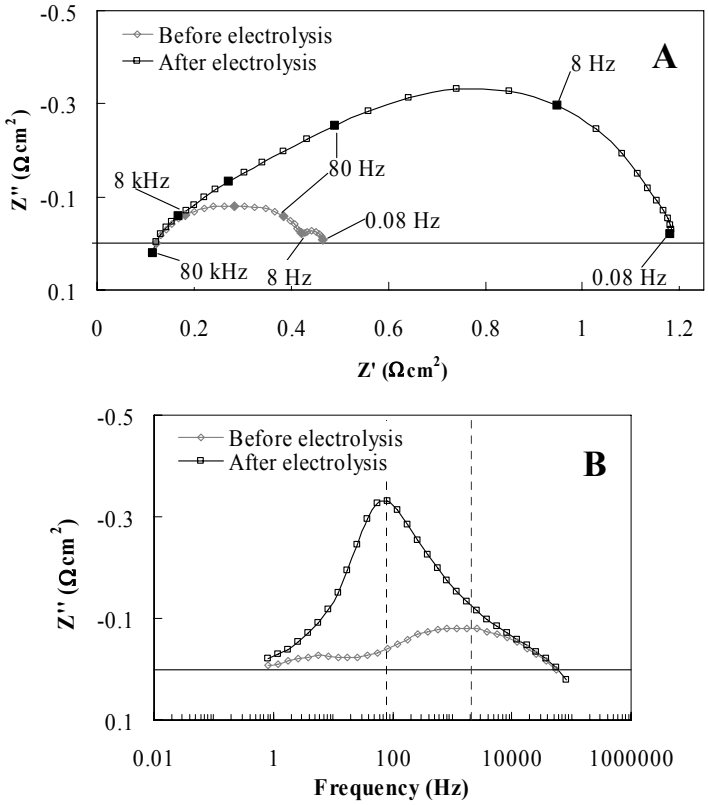

Figure 4-3: Impedance spectra obtained at OCV at 750°C, air to the oxygen electrode and 20% H_2O in H_2 to the H_2 electrode before and after electrolysis testing of 3test14. R_s and R_p are given in Table 4-2.

Table 4-2: R_s and R_p for spectra obtained at OCV at 750°C, air to the oxygen electrode and 20% H_2O in H_2 to the H_2 electrode for 3test14 (Figure 4-3) and 3test30 (Figure 4-4).

Test	$R_{s,\,before}$	$R_{s,\,after}$	$R_{p,\,before}$	$R_{p,\,after}$
3test14	0.11	0.11	0.36	1.07
3test30	0.27	0.34	0.46	0.59

3test30 was operated in electrolysis mode long enough to show the "short-term" passivation followed by almost complete re-activation and an underlying and subsequent long-term degradation. EIS obtained at OCV before and after electrolysis testing of 3test30

at 750°C applying 20% H_2O in H_2 to the H_2 electrode is shown in Figure 4-4. R_s and R_p for the two spectra in Figure 4-4 are given in Table 4-2. The relatively large $R_{s,before}$ for 3test30 was most likely caused by imperfect Ni current collector foil. R_s increased 26% and R_p increased 28%. The summit frequency for the arc for which the resistance increased the most as a consequence of electrolysis testing is 2100 Hz at 750°C (Figure 4-4).

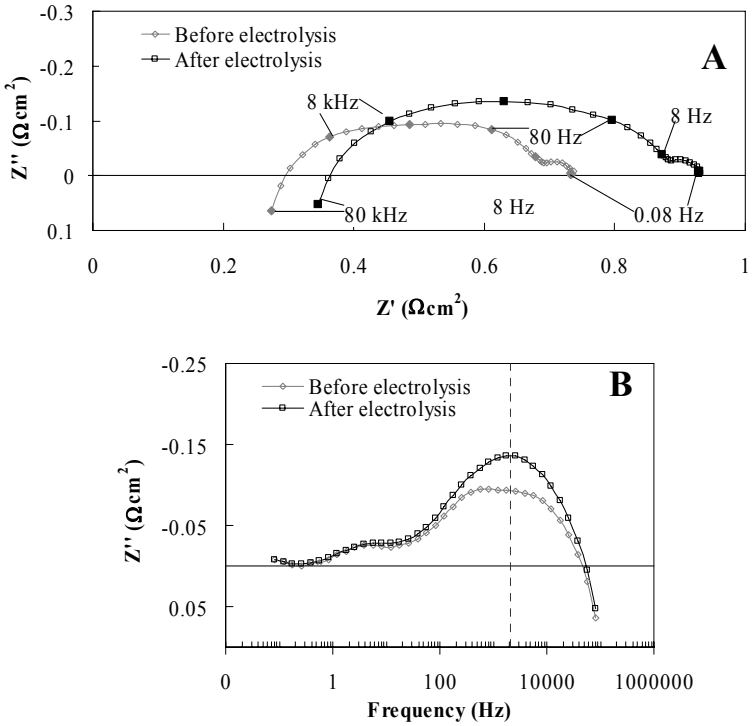

Figure 4-4: EIS obtained at OCV at 750°C, air to the oxygen electrode and 20% H_2O to the H_2 electrode before and after electrolysis testing of 3test30. R_s and R_p are given in Table 4-2.

4.3.2 Changes in impedance spectra due to gas variations

Difference plots obtained from impedance spectra at gas variations performed before and after electrolysis testing of 3test14, 3test19 and 3test30 are shown in Figure 4-5. The difference plots for 3test19 and 3test30 show that the gas variations for the H_2 electrodes changed significantly more than the gas variations for the O_2 electrodes. For 3test14 (Figure 4-5A) a peak due to gas conversion can be observed at $f_s \sim 3$ Hz and the main peak for the due to the gas variation for the H_2 electrode before electrolysis testing was at ~825 Hz. This peak was shifted to ~30 Hz after electrolysis testing. From the difference plot at 850°C for 3test19 (Figure 4-5C) which was partly reactivated during electrolysis testing, it is evident that the passivation "left" for 3test19 is caused by limiting processes in the Ni/YSZ electrode. The change in the difference plot due to gas variation at the H_2 electrode is considerable for 3test19, whereas it is almost non-existing for the O_2 electrode gas

variation. The difference plot at 750°C for the H_2 electrode of 3test30 (Figure 4-5D) shows a change before and after electrolysis testing of ~2 mΩcm^2 at 383 Hz. The changes in the difference plot for the gas variation for the O_2 electrode (Figure 4-5E) of 3test30 is very limited, in fact close to the error limits of this method.

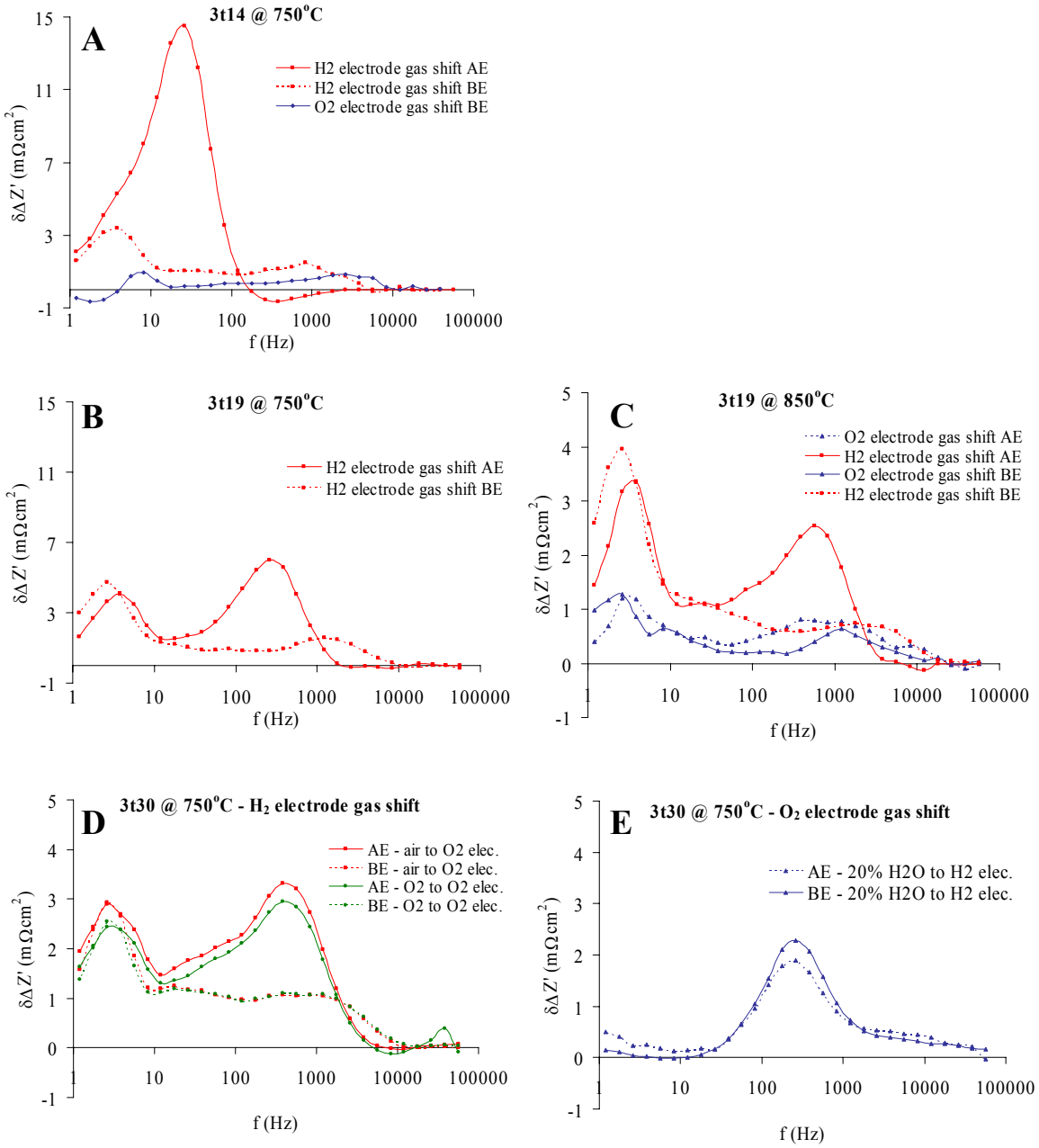

Figure 4-5: Difference plot of changes in impedance spectra due to gas variations for 3test14 (A), 3test19 (B and C) and 3test30 (D and E). "BE" is before electrolysis test and "AE" is after electrolysis testing. The gas variations for the hydrogen electrode were from 5% to 20% H_2O. The gas variations for the oxygen electrode were from 140 l/h air to 20 l/h O_2.

4.3.3 Impedance spectra during electrolysis operation

3test14 was operated for a total electrolysis time of 82 hours and the course of the cell voltage during the electrolysis test period is shown in Figure 4-6. The test was stopped when the maximum degree of passivation during the "short-term" passivation was reached. Impedance spectra were recorded during electrolysis testing. The values for R_p derived from these spectra are shown in Figure 4-6. The impedance spectra in Figure 4-7 are recorded with approximately equivalent time intervals; 1, 30, 56 and 82 hours of electrolysis testing. The spectra in Figure 4-7 have the R_p values indicated by the closed triangles in Figure 4-6. The spectra in Figure 4-7 show that R_s stays constant during electrolysis operation of 3test14. From Figure 4-7B it is observed that the frequency for the numeric maximum of Z'' decreases from ~2000 Hz after 1 hour of electrolysis to ~ 40 Hz after 82 hours of electrolysis. Detailed analysis of the impedance spectra recorded during electrolysis testing of 3test14 can be achieved as described for 3test30 (see text below) by substituting the $(R,CPE)_{Ni}$ with a Ws element in the equivalent circuit (Figure 4-2) to account for the increasing arc with a summit frequency of 40-2000 Hz. This has been described in detail by Jensen et al. [91].

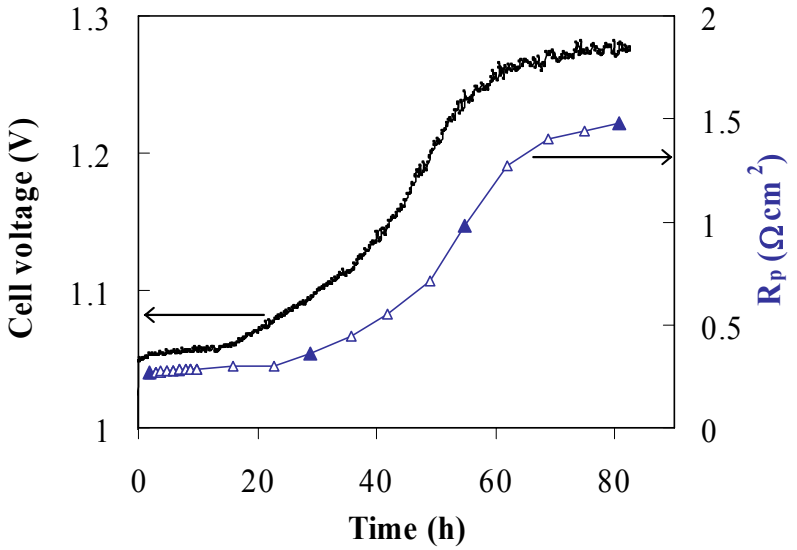

Figure 4-6: Cell voltage and R_p (Δ) for 3test14 as a function of time. Experimental conditions were: -0.25 A/cm^2, 750°C, p(H_2O) = 0.7 atm and p(H_2) = 0.3 atm to the hydrogen electrode and O_2 was passed over the oxygen electrode. The impedance spectra corresponding to the R_p marked by closed triangles are shown in Figure 4-7.

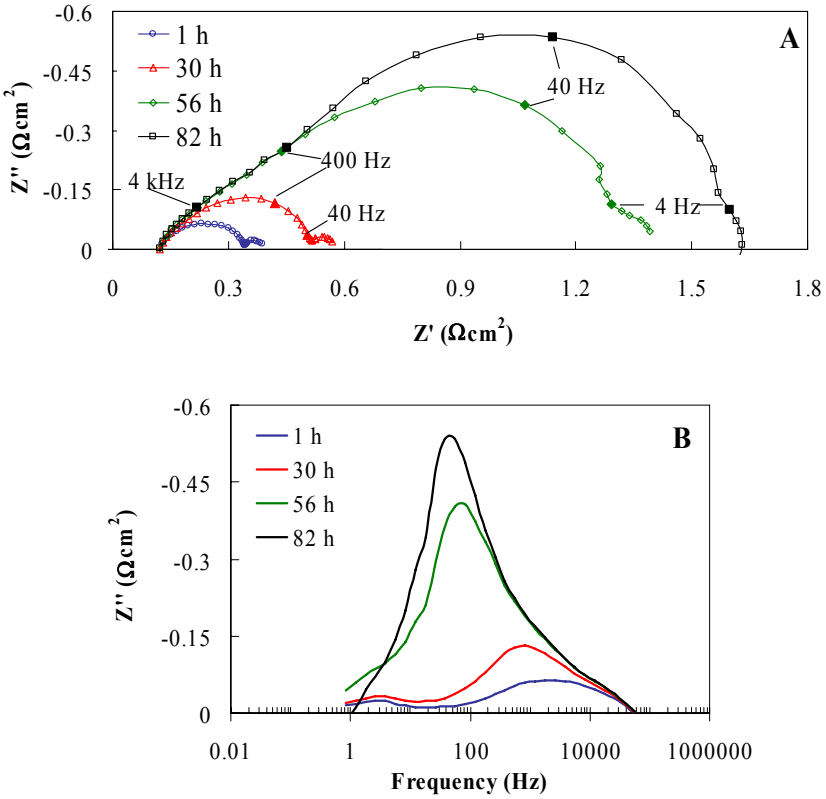

Figure 4-7: Impedance spectra recorded during electrolysis 3test14. Experimental conditions were: -0.25 A/cm^2, 750°C, p(H_2O) = 0.7 atm and p(H_2) = 0.3 atm to the hydrogen electrode and O_2 was passed over the oxygen electrode. A: Nyquist plot of the impedance spectra and B: Imaginary part of the Bode plot for the impedance spectra.

3test19 was operated in electrolysis mode for a total of 766 hours and the course of the cell voltage during electrolysis testing is shown in Figure 4-8. It is observed that the cell reactivated partly after the initial "short-term" passivation. Impedance spectra were recorded during electrolysis testing. The R_p values derived from these spectra are shown in Figure 4-8. The spectra in Figure 4-9 are recorded after 1, 45, 116 and 317 hours of electrolysis testing and these spectra have the R_p values indicated by the closed triangles in Figure 4-8. The spectrum after 45 hours of electrolysis is recorded during passivation of the cell and the spectrum after 317 hours of electrolysis testing is recorded during the subsequent activation of the cell. The maximum R_p was obtained after 116 hours of electrolysis. The complete overlap of the impedance spectra recorded after 45 and 317 hours of electrolysis testing at constant conditions should be noticed. The spectra in Figure 4-9 show that R_s stays constant during the entire electrolysis period of 3test19.

From the Bode plot (Figure 4-9B), it is observed that the frequency for the numeric maximum for Z'' decreases from ~ 7 kHz after 1 hour of electrolysis to ~ 2 kHz after 45 hours of electrolysis and down to ~ 400 Hz at the most passivated state after 116 hours of electrolysis testing. Furthermore, the impedance spectra for 3test19 (Figure 4-9B) show minor increase/decrease in Z'' at a frequency of 1-5 Hz, which is ascribed to gas conversion impedance [9]. Detailed analysis of the impedance spectra during electrolysis testing of 3test19 can be achieved as described for 3test30 (see below) by substituting the $(R,CPE)_{Ni}$ with a short circuited Ws-element in the equivalent circuit (Figure 4-2) to account for the increasing arc at with a summit frequency of 400-7000 Hz.

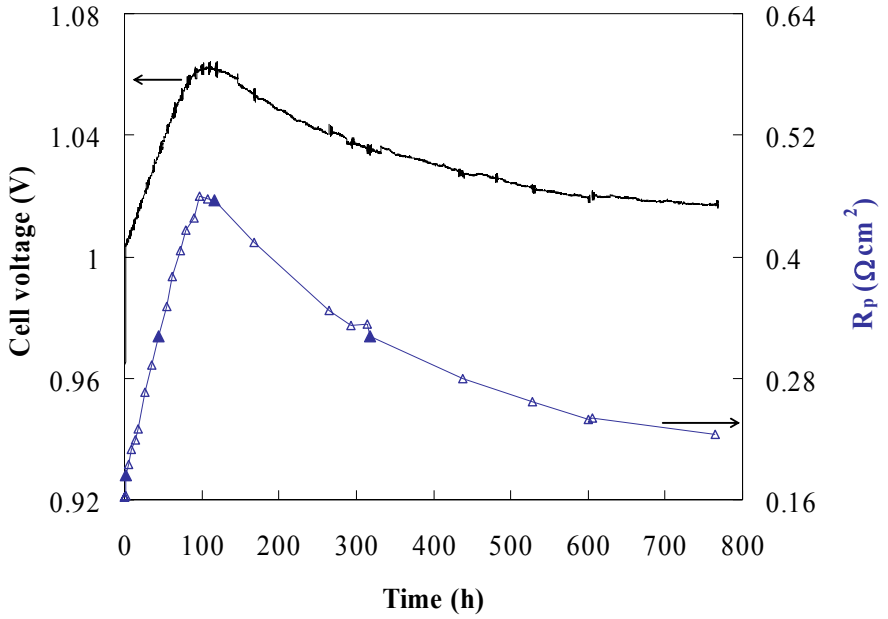

Figure 4-8: Cell voltage and R_p (Δ) for 3test19 as a function of time. Experimental conditions were: -0.25 A/cm^2, 850°C, p(H_2O) = 0.7 atm and p(H_2) = 0.3 atm to the hydrogen electrode and O_2 was passed over the oxygen electrode. Closed symbols for R_p were obtained from the impedance spectra in Figure 4-9.

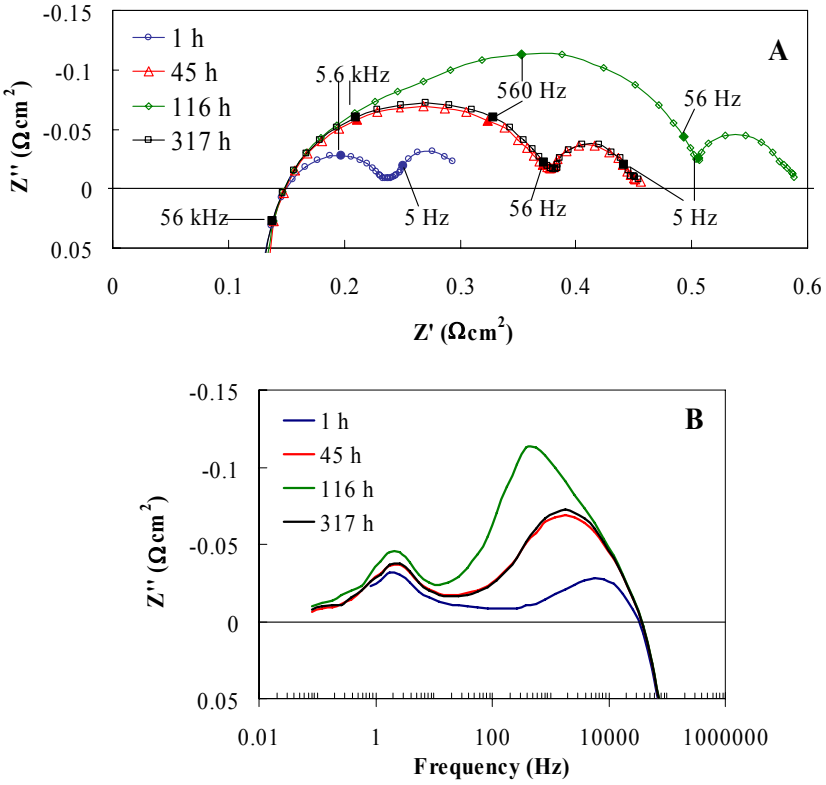

Figure 4-9: Impedance spectra recorded during electrolysis 3test19. Experimental conditions were: -0.25 A/cm^2, 850°C, p(H_2O) = 0.7 atm and p(H_2) = 0.3 atm to the hydrogen electrode and O_2 was passed over the oxygen electrode. A: Nyquist plot of the impedance spectra and B: Imaginary part of the Bode plot for the impedance spectra.

3test30 was operated for a total electrolysis time of 1316 hours and the course of the cell voltage during electrolysis testing is shown in Figure 4-10. It can be observed that the cell passivated, reactivated and had an underlying and subsequent long-term degradation for which the trend was an increase of 20 mV/1000 h as indicated by the dotted line in Figure 4-10. Impedance spectra were recorded during electrolysis testing. The values of R_p derived from these spectra are included in Figure 4-10. The impedance spectra in Figure 4-11 were recorded after 1, 264, 599 and 1217 hours of electrolysis. These spectra have the R_p values indicated by the closed triangles in Figure 4-10. The change in the impedance spectra from 1 to 264 h of electrolysis testing is mainly due to the "short-term" passivation. The change in the spectra from 264 to 599 h of electrolysis testing is mainly due to the re-activation of the cell. Comparing the impedance spectra recorded at 599 h and 1271 h of electrolysis testing illustrates the change in the spectra caused by the underlying and subsequent long-

term degradation. The ohmic resistance increased slightly throughout the electrolysis testing period.

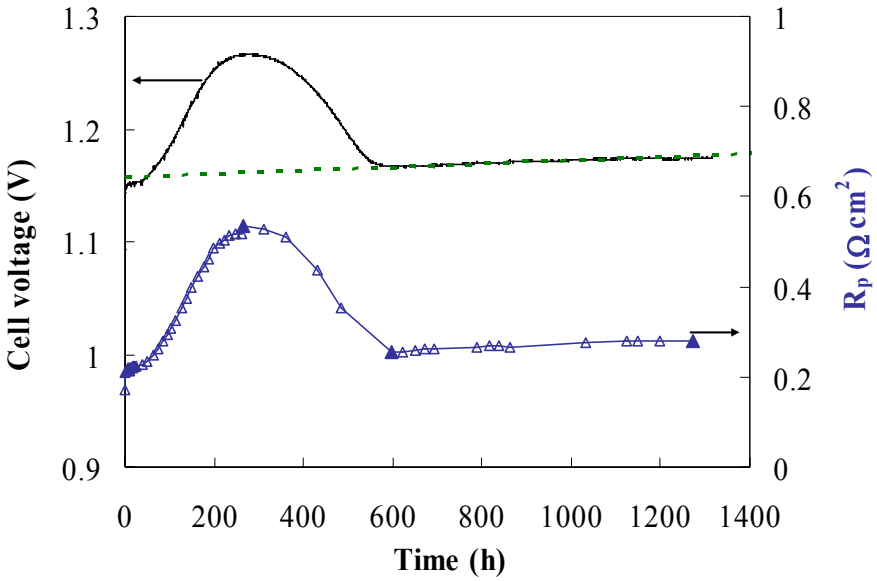

Figure 4-10: Cell voltage and R_p (Δ) for 3test30 as a function of time. Experimental conditions were: -0.5 A/cm^2, 850°C, p(H_2O) = 0.5 atm and p(H_2) = 0.5 atm to the H_2 electrode and O_2 was passed over the oxygen electrode. Closed symbols for R_p were found from the impedance spectra shown in Figure 4-11.

Analysis of the impedance spectra aquired during the "short-term" passivation of 3test30 has been performed. The experimental spectra after 1 h (Δ) and 264 h (O) of electrolysis testing of 3test30 are shown in Figure 4-12 together with the optimal fit (lines) for the two spectra. The optimal fits were obtained using the equivalent circuit given in Figure 4-2 with the Cole-element $(R,CPE)_{Ni}$ replaced by a Ws-element. The fitted values for the arcs describing processes at the O_2 electrode and the $(R,CPE)_{diff}$ arc were optimised for the first spectrum and kept constant at: $R_{diff.}$ = 0.02 Ωcm^2, n_{diff} = 1, $f_{s,diff}$ = 47 Hz, $R_{LSM,\ low}$ = 0.04 Ωcm^2, $n_{LSM,low}$ = 0.77, $f_{s,LSM,low}$ = 2040 Hz, $R_{LSM,\ high}$ = 0.09 Ωcm^2, $n_{LSM,high}$ = 0.68 and $f_{s,LSM,high}$ = 22 kHz for the optimisation of the second spectrum. The parameters describing the gas conversion arc and the Ws-element were optimised for both impedance spectra shown in Figure 4-12. The values for the optimal fit parameters are given in Table 4-3.
Good agreement between the modelled spectra and the experimental impedance spectra is observed in Figure 4-12. The errors $[Z_{measured}-Z_{fit}]/ Z_{measured}$ were below 10% over the entire frequency range for both fitted spectra. The χ^2 values were $1.0\cdot10^{-4}$ and $2.9\cdot10^{-4}$ for the spectrum after 1 h and 264 h when the parameters for the Warburg diffusion, gas conversion and ohmic resistance were left "free" for optimisation.

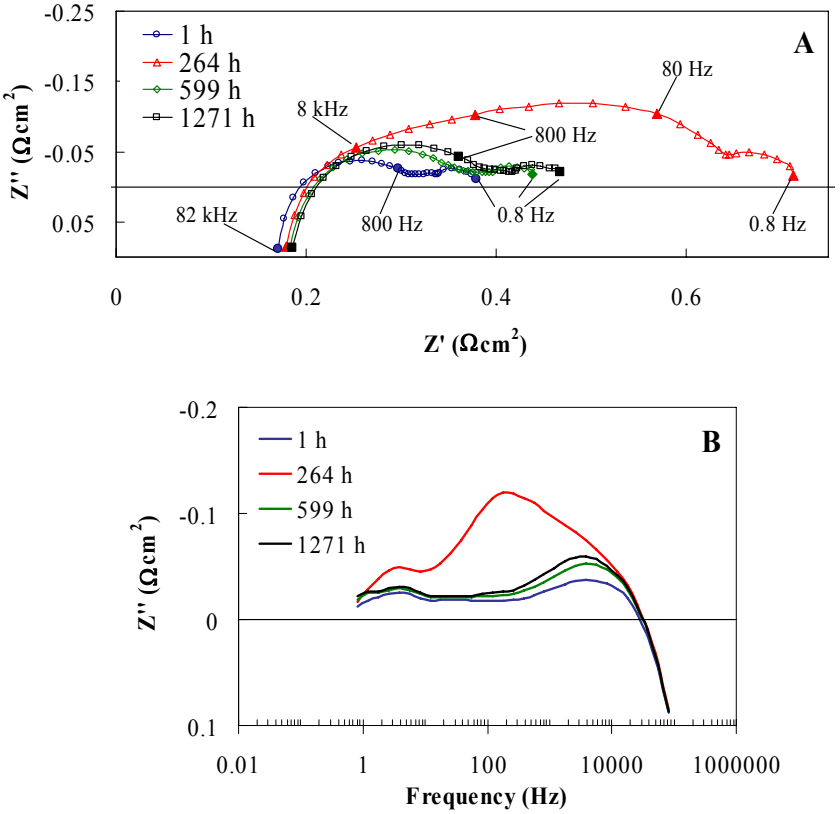

Figure 4-11: Impedance spectra recorded during electrolysis 3test19. Experimental conditions were: -0.50 A/cm^2, 850°C, p(H_2O) = 0.5 atm and p(H_2) = 0.5 atm to the hydrogen electrode and O_2 was passed over the oxygen electrode. A: Nyquist plot of the impedance spectra and B: Imaginary part of the Bode plot for the impedance spectra.

An attempt to fit the two spectra in Figure 4-12 using a $(R,CPE)_{Ni}$ circuit instead of a Ws-element and keeping the parameters describing processes at the O_2 electrode and $(R,CPE)_{diff.}$ constant at the values obtained for the spectrum after 1 h did not give satisfactory results. An optimal fit including a $(R,CPE)_{Ni}$ circuit and the same number of free parameters as for the Warburg-fit resulted in a χ^2 value of $1.0 \cdot 10^{-4}$ for fit of the spectrum after 1 h, but was less successful for the spectrum after 264 h which led to a χ^2 value of $6.7 \cdot 10^{-4}$. The relative errors for the $(R,CPE)_{Ni}$ –fit were up to 22% for the 264 h-spectrum.

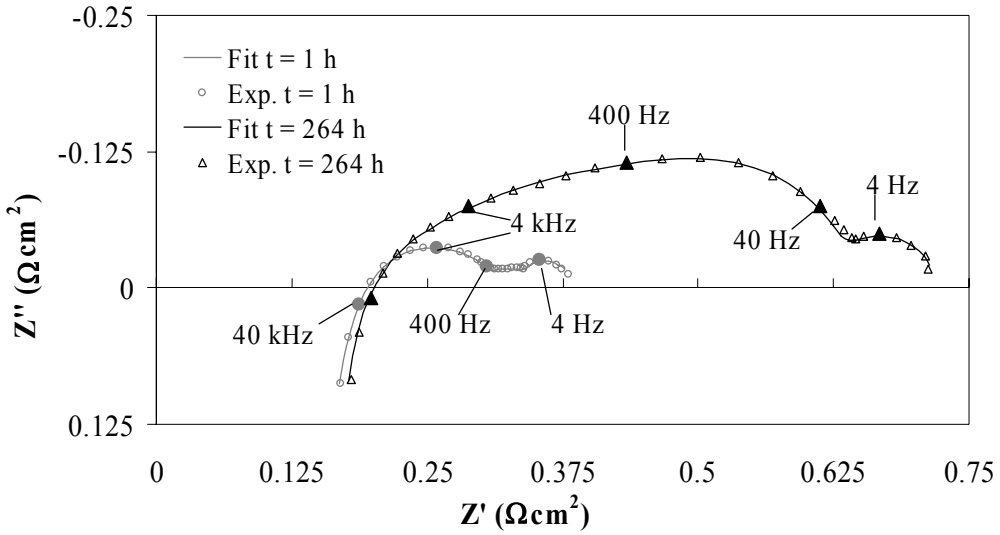

Figure 4-12: Experimental EIS after 1 h (Δ) and 264 h (O) of electrolysis testing for 3test30. The lines represent optimal fit of the spectra using the equivalent circuit given in Figure 4-2 with the Cole-element $(R,CPE)_{Ni}$ replaced by a Ws-element. The values for the arcs describing processes at the O_2 electrode and $(R,CPE)_{diff.}$ were optimised for the first spectrum and kept constant for the analysis of the second impedance spectrum. The values for the optimal fit parameters are given in Table 4-3.

Table 4-3: Optimal fit parameters for the ohmic resistance, gas conversion arc and the Ws-element to describe the diffusion process (surface or solid-state) in the Ni/YSZ electrode for the impedance spectra shown in Figure 4-12. The fitted values for the two arcs describing processes at the O_2 electrode and $(R,CPE)_{diff.}$ were kept constant at $R_{diff.} = 0.02\ \Omega cm^2$, $n_{diff} = 1$, $f_{s,diff} = 47$ Hz, $R_{LSM,\ low} = 0.04\ \Omega cm^2$, $n_{LSM,low} = 0.77$, $f_{s,LSM,low} = 2040$ Hz, $R_{LSM,\ high} = 0.09\ \Omega cm^2$, $n_{LSM,high} = 0.68$, $f_{s,LSM,high} = 22$ kHz.

Test time	$R_{conv.}$ (Ωcm^2)	$f_{s,conv.}$ (Hz)	W_R (Ωcm^2)	δ^2/D (s)	p	$f_{warb.}$ (Hz)	R_s (Ωcm^2)
1 h	0.04	3	0.05	$8 \cdot 10^{-5}$	0.35	7541	0.136
264 h	0.07	3	0.36	$2 \cdot 10^{-3}$	0.38	256	0.150

4.4. Discussion

4.4.1. Passivation of the H_2 electrode during electrolysis

"Short-term" passivation

The "short-term" passivation is most pronounced and best illustrated by the spectra obtained for 3test14 (Figure 4-7). The difference plots for 3test14 show large changes for the impedance changes upon gas variations for the H_2 electrode (Figure 4-5A). The difference plot for impedance changes due to gas variations for the H_2 electrode has a minor peak at ~825 Hz which shifts to ~30 Hz and the $\Delta\partial Z$' increases an order of magnitude. These results for the gas variation experiments for 3test14 are consistent with the development of the impedance spectra recorded during electrolysis testing of 3test14 (Figure 4-7). Unfortunately gas variation experiments were not performed for the oxygen electrode after electrolysis testing for 3test14. Nevertheless, combining the result for the impedance changes due to gas variations (Figure 4-5A) with the impedance spectra during electrolysis (Figure 4-7) and at OCV before and after electrolysis testing (Figure 4-3), it is evident that by far the most dominating change in the impedance spectra caused by electrolysis testing starts at a frequency of ~1-2 kHz and decrease to ~40-80 Hz at the end of electrolysis testing, and it can be concluded that for the "short-term" passivation the main change in cell performance is caused by rate limiting processes (decreased electrode kinetics) in the H_2 electrode. This is further confirmed by gas variation experiments on 3test26, 3test28 and 3test35 which were all stopped at the maximum passivation during the "short-term" passivation, see appendix A. The analyses of impedance spectra during the "short-term" passivation of 3test30 support the hypothesis that the "short-term" passivation stems from rate limiting processes in the H_2 electrode and not in the O_2 electrode. This is seen from the fact that the parameters describing the processes at the O_2 electrode could be kept constant at the value optimised for the spectrum after 1 h of electrolysis when analysing the spectrum recorded after 264 h of electrolysis for 3test30.

The "short-term" passivation for 3test19 most likely also originates from decreased electrode kinetics for the H_2 electrode. The difference plots of the change in the impedance spectra due to gas variations for 3test19 reveal that the passivation "left" for 3test19 at the end of electrolysis testing relates to the H_2 electrode. The differences observed in the difference plots for the H_2 electrode of 3test19 before and after electrolysis testing can be caused by at least two mechanisms or a mixture of them: 1) the cell has not fully re-activated after the "short-term" passivation i.e. the difference plot results in Figure 4-5B and Figure 4-5C is an effect of the "short-term" passivation or/and 2) an underlying long-term degradation has become the most dominating process when the electrolysis testing was stopped i.e. the difference plot results in Figure 4-5B and Figure 4-5C is an effect of the long-term degradation (next paragraph). Therefore Figure 4-5 B and Figure 4-5C does not provide sufficient evidence that the "short-term" passivation of 3test19 only originates from the H_2 electrode.

Long-term degradation

The long-term degradation for the SOECs was clearly observed by the course of the cell voltage and the impedance spectra for the last 700 hours of 3test30. From Figure 4-10 it is evident that there is an underlying long-term degradation of 20 mV/1000 h throughout the entire electrolysis test period and the activation after the "short-term" passivation is complete. Therefore the difference plots for the changes in impedance spectra due to gas variations for 3test30 show the effect of the long-term degradation. The main contribution to the degradation is therefore believed to be caused by limiting processes in the hydrogen electrode. This is supported by the fact that the arc evolving during long-term degradation of 3test30 has a summit frequency of ~8 kHz at 850°C (Figure 4-11) in line with the analyses of the Ni/YSZ contributions to the impedance spectra for similar SOFCs (Figure 4-2, [95]). Furthermore, the main change in the impedance spectra recorded at OCV and 750°C for 3test30 (Figure 4-4) occurred at ~2 kHz in accordance with the EIS equivalent circuit model given by Barfod and reproduced in Figure 4-2.

Previously Jensen [76] suggested that the long-term degradation was caused by coarsening of the Ni particles. This is hardly the case, see chapter 5 and [32; 62]

4.4.2. Diffusion related passivation processes during electrolysis testing

The impedance spectra recorded during 3test19 - and 3test30 as well - did not only lead to polarisation resistances being equal during passivation and the subsequent activation of the cell; the spectra with the same R_p recorded during passivation and activation are identical at each measured frequency (Figure 4-9). This strongly suggests that it is the same processes which are the rate limiting steps during the passivation and the following activation of the SOEC. The analysis of the impedance spectra during this passivation showed that the optimal fit can be obtained by applying a Ws-element in the equivalent circuit to describe the arc that increases during the "short-term" passivation of the SOEC. This strongly points towards surface or solid-state diffusion limitations for species (H^+ and O^{2-}) in the active H_2 electrode, most likely at the triple phase boundaries (TPB), being responsible for the for the "short-term" passivation of the cell for 3test30. For impedance analyses for 3test14 and 3test19 obtained in the same way as shown here for 3test30 (Figure 4-12 and Table 4-3) by Jensen et al. [91] showed that the increased diffusion resistance at the TPB was caused by an increased diffusion path length. This could be caused by a build-up of glassy phase impurities at the TPB of the hydrogen electrode. This hypothesis is supported by electron microscopy and energy dispersive spectroscopy results (see chapter 6 and 7) and has been reported previously for three electrode pellets and half cells [78; 89; 100]. If the "short-term" passivation is caused by a build-up of glassy phase impurities at the TPB of the H_2 electrode, then a plausible, but not yet completely experimentally verified, explanation for the subsequent activation of the cell could be a break-up of the glass caused by crystallisation of these glassy phases. Such break-up would lead to a decrease in the diffusion path length and enable the complete overlap of the impedance spectra recorded during passivation and activation of the cell as observed in Figure 4-9 and for 3test30. Another explanation for the activation of the SOECs could be evaporation of these glassy

phase impurities, but if this is the case then far from all impurities evaporate as several impurity particles have been detected in 3test30 (Na, Si and Al oxide containing, see chapter 7) – unless of course the long-term degradation also stems from build-up of glassy phase impurities at TPB in the H_2 electrode.
Analysis of changes in impedance spectra due to gas variation experiments applying a D_2/D_2O mixtures to the H_2 electrode before and after electrolysis testing has shown that surface and/or solid-state diffusion of protons play a role in the observed "short-term" passivation of the SOECs.Gas variations experiments applying CO/CO_2 mixtures to the hydrogen electrode before and after electrolysis testing reveal that it is not only proton diffusion but O^{2-} diffusion is also involved in the limiting processes observed during the passivation of the SOECs.

4.5. Conclusion

EIS results were obtained at OCV and under current load during electrolysis testing of SOECs. From the EIS results presented here it can be concluded that:

- During the "short-term" passivation R_s stays more or less constant while R_p increases
- The summit frequency for the arc increasing during the "short-term" passivation decreases more than one order of magnitude. The summit frequency increases again during the subsequent activation of the SOECs.
- Impedance spectra obtained during the "short-term" passivation and the subsequent activation completely overlap at each frequency. This indicates that it is the same process(es) responsible for both the passivation and the activation of the SOECs.
- Difference plots of the changes in the impedance spectra due to gas variations before and after electrolysis for 3test14 reveal that the "short-term" passivation is caused by one or more rate limiting process(es) in the H_2 electrode.
- Difference plots of the changes in the impedance spectra due to gas variations before and after electrolysis testing of 3test30 reveal that the long-term degradation is mainly caused by rate limiting process(es) in the H_2 electrode.
- Analyses of impedance spectra recorded during the "short-term" passivation can best be optimised by using an equivalent circuit including a fractal Warburg diffusion element to describe the arc with the most significant increase in resistance during electrolysis testing.
- The reactions in the O_2 electrode seem unaffected by the "short-term" passivation. Optimal fit of impedance spectra recorded during the "short-term" passivation (after e.g. 264 h of electrolysis testing of 3test30) can be obtained by leaving the parameters relating to the O_2 electrode constant at the values optimised for the impedance spectrum recorded after 1 h of electrolysis testing.

5. Microstructure of the Ni/YSZ electrode

5.1. Introduction

Based on the EIS results presented in chapter 4, the SEM work presented in this chapter has been focused on the microstructure of the Ni/YSZ electrode. From the technological point of view it is important that the electrodes of the SOCs can withstand thousands of hours of testing. Hagen et al. [32] found changes in the microstructure of the Ni/YSZ for tested SOFCs but this was reported not to be the main degradation factor. In this chapter it is shown that the H_2 electrodes of similar SOCs can withstand 1500 h of electrolysis testing with microstructural changes of the H_2 electrode comparable to the changes for SOFC anodes, but at more "harsh" electrolysis conditions significant changes in the Ni/YSZ microstructure occur and some of these relate to impurity findings.

It would be most convenient if SOECs are able to sustain periods of time at OCV with a high partial pressure of steam at the H_2 electrode without significant loss in performance. The high $p(H_2O)$ is a condition that the electrolysis cell will always be exposed to for shorter or longer periods of time during operation unless a major H_2 recycling is performed. In this chapter the effect of a $p(H_2O) = 0.98$ atm to the H_2 electrode for an SOC at OCV is shown[8]. Furthermore, the Ni particle size distributions for tested SOECs are related to the electrolysis test results, and it is shown that changes in the Ni size distributions can only play a minor role in the passivation and degradation of the SOECs.

Finally, the occurrence of aluminium in the active H_2 electrode of non-tested cells is presented as this relates to the analysis of impurities found in a TEM lamella of tested SOECs (chapter 7).

5.2. Experimental

The preparation of cell pieces for post-mortem analysis using SEM and EDS is described in chapter 2. The chemical compositions are obtained from quantification of energy dispersive X-ray spectra using standard-less analysis, and the results of the analyses should therefore be regarded as semi-quantitative. Two different reference cells have been investigated for comparison with electrolysis tested cells. The reference cells have been heated up, the NiO have been reduced and the cell performance has been checked by iV curves and impedance spectra before cooling down.

Ni particle size distributions have been determined for the active layer of the H_2 electrodes for several cells. A typical micrograph for analysis of the Ni particle size distribution is shown in Figure 5-1A. The size distributions of Ni particles were obtained by

[8] Parts of the results presented in this chapter has been published in "Ni/YSZ electrodes in solid oxide electrolyser cells", Hauch, A., Jensen, S. H., and Mogensen, M., in *Solid State Electrochemistry, Proceedings of the 26th Risø International Symposium on Materials Science*, Roskilde, Denmark; p. 203-208, edited by S. Linderoth et al. (2005)

superimposeing a grid on the SEM micrograph. The grid was a set of parallel lines with a distance of 1 μm from each other as shown in Figure 5-1B, where the innermost three lines are shown. The 10 μm of the Ni/YSZ electrode closest to the electrolytes are included in the grid for analyses. The fragments of the lines intercepting with Ni particles were measured (see bottom line in Figure 5-1B) and the size distributions for the Ni particles are given as frequencies over Ni intercept lengths. The uncertainty for the measured intercept lengths is estimated to be 0.05 μm for the micrographs used for the Ni particle size distributions given here.
Underwood [102] gave the mathematical foundation of quantitative stereology i.e. the quantitative characterisation of three dimensional structures by means of analysis of two dimensional sections through the solid. Assuming that the hydrogen electrode is isotropic and the Ni particles are randomly distributed in the active layer of the H_2 electrode, it can therefore be assumed that the 2D and 3D fractions of Ni are equal and the Ni particle size distributions presented in this chapter can be assumed to give a satisfying description of the three dimensional electrode as well.
For a couple of micrographs of both reference and tested cells analyses of the Ni particle sizes have also been obtained by encircling each Ni particle and calculating its area using an image analysis program. Assuming that the Ni particles are circular, this type of analysis gave the same mean Ni particle diameter as the mean Ni intercept length determined from the analysis method illustrated in Figure 5-1B.
An alternative way to obtain micrographs for Ni particle size distributions is to enhance the contrast difference between Ni and YSZ using low voltage SEM micrographs of uncoated samples as shown in Figure 5-1C [103] and apply a filter to the micrographs which should enable automatic measurement of the Ni particles (Figure 5-1D). Nevertheless, this procedure still needs optimisation before automatically generated size distributions give satisfactory results and the method shown in Figure 5-1B has therefore been applied for the Ni particle size distributions given in this chapter.

5.3. Results

5.3.1. Microstructure for long-term tested SOEC

Representative images of a reference cell and the cell from 3test33 are shown in Figure 5-2. 3test33 was operated for 1510 h at constant galvanostatic electrolysis conditions; -0.5 A/cm^2, 850°C, p(H_2O) = 0.5 atm, p(H_2) = 0.5 atm (Table 5-1). From the overview micrographs of the reference cell (Figure 5-2B) and the cell from 3test33 (Figure 5-2D) it is evident that the electrolysis testing has not given rise to changes such as cracks in the electrolyte, delamination of the electrodes from the electrolyte, and "large-scale" (> 5 μm) changes in the electrode microstructures. Difference plots of changes in impedance spectra due to gas variations before and after electrolysis testing of 3test33 were performed and

gave results similar to those for 3test30 (chapter 4). Therefore the microscopy emphasis has been on the H_2 electrode. Figure 5-2A and Figure 5-2C show representative micrographs of the microstructure of the H_2 electrode of a reference cell and the cell from 3test33, respectively.

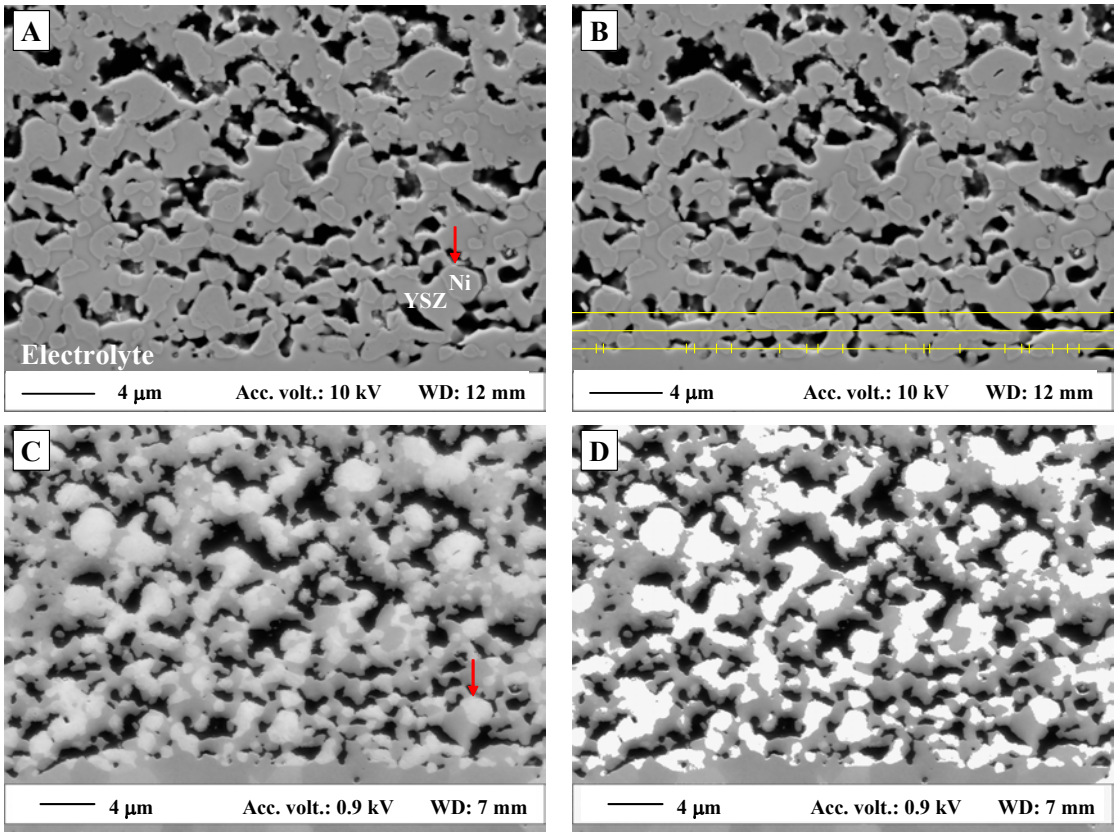

Figure 5-1: Secondary electron micrographs of the electrolyte/H_2 electrode interface of a reference cell. A: Micrograph of interface. B: Same image as A, but with illustration of the start of the grid for analysis of the Ni particle size distribution. C: Low voltage SEM of the same area of the H_2 electrode, see the arrow in image A and C. D: Filter applied to the Ni particles of micrograph C.

Qualitatively the microstructure (pores, particle sizes and shape) of 3test33 appear to be intact and the adhesion between the porous H_2 electrode and the dense YSZ electrolyte has not altered significantly for the tested cell compared to the reference cell. The qualitative SEM results shown in Figure 5-2 are representative for numerous of the investigated SOECs. At least two cell pieces of each of the following cells: 3test14, 3test15, 3test19, 3test21, 3test26, 3test28, 3test31 and 3test33 was investigated, see appendix A for test conditions and results for these tests.

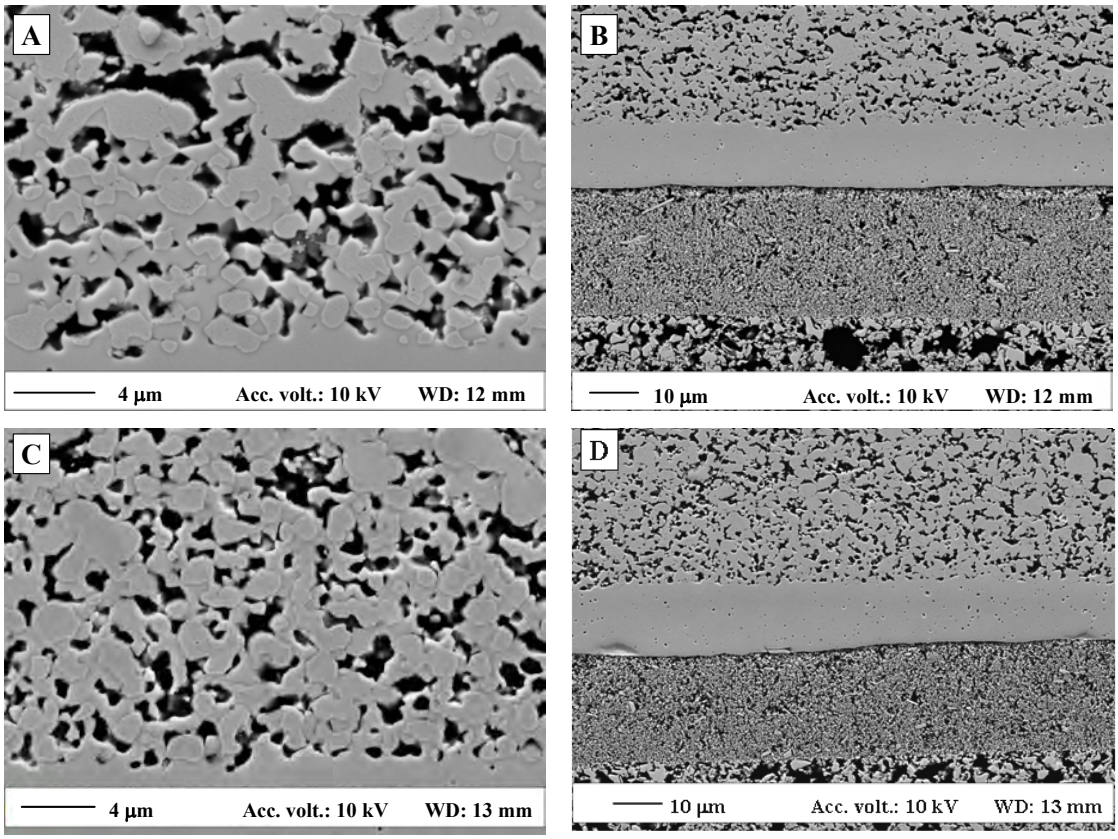

Figure 5-2: Secondary electron micrographs. A: The H_2 electrode of a reference cell. B: Overview of H_2 electrode (top), electrolyte (middle) and the O_2 electrode of a reference cell. C: The H_2 electrode of the cell from 3test33. D: Overview micrograph of the cell from 3test33 used for 1510 h of electrolysis.

5.3.2. Microstructural changes caused by "harsh" electrolysis testing conditions

Electrolysis testing at more "harsh" electrolysis conditions i.e. higher current density/cell polarisation and/or higher $p(H_2O)$ have led to changes in the microstructure of the H_2 electrodes. The most significant microstructural change for the H_2 electrodes was found for the cell from 3test27 (68 h at 950°C, -2 A/cm^2, $p(H_2O)$ = 0.9 atm, Appendix A). In some regions of the investigated cell pieces the Ni particles seem surrounded completely by YSZ and a densification of the YSZ seem to have been occurred in the innermost ~2 µm of the electrode as shown in Figure 5-3A. Furthermore, "dark spots" as shown in Figure 5-3B where found in 3test27. A point spectrum of one of the "dark spots" in the Ni particles is given in Figure 5-4A, which clearly shows that it is inclusions of silica in the Ni particles. This is only found in the few microns closest to the electrolyte. This is not an artefact of sample preparation as other cell pieces in the same embedding did not show this feature.

Significant microstructural changes were not observed for the O_2 electrode of the investigated pieces from 3test27.

Inclusion of silica impurities in the Ni particles of tested SOECs have been observed in a couple of other cells e.g. 3test24 (Figure 5-3C), but never to the same extent as for 3test27. In Figure 5-3C and Figure 5-3D the encircled areas show "dark rims" around Ni particles close to the electrolyte for cell pieces of 3test24 and 3test12, respectively. Such "rims" have been observed in different regions of the investigated cell pieces and for pieces of 3test22 (chapter 6). Figure 5-4B shows a point spectrum obtained in the "dark rim" that is encircled in Figure 5-3D. The spectrum reveals that the "dark rims" are not simply a detachment of the Ni particles from the YSZ. The "rims" (~50 nm) consist of silica-containing impurities that have built up during testing.

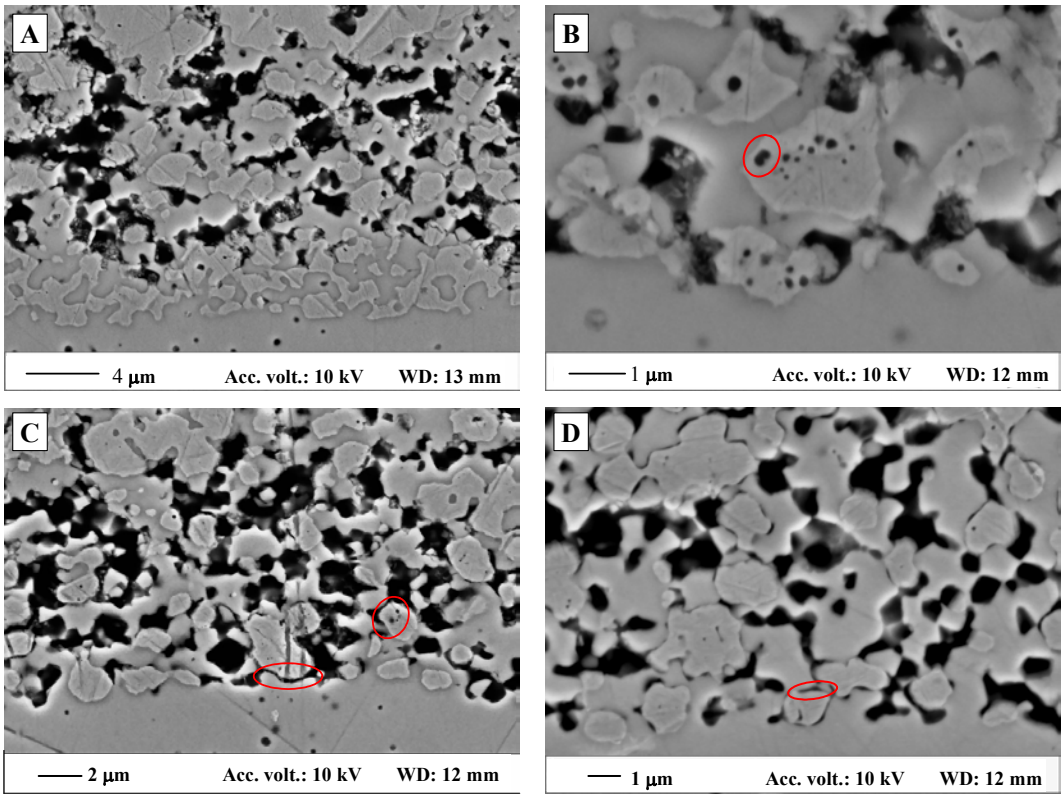

Figure 5-3: Secondary electron micrographs. A: Microstructural changes in the H_2 electrode/electrolyte interface of 3test27. B: Inclusion of impurities in Ni particles of 3test27. Energy dispersive X-ray spectrum from the encircled spot is given in Figure 5-4A. C: Microstructure of the H_2 electrode/electrolyte interface of 3test24. D: Microstructure of the H_2 electrode/electrolyte interface of 3test12. Energy dispersive X-ray spectrum obtained in the "dark rim" is given in Figure 5-4B.

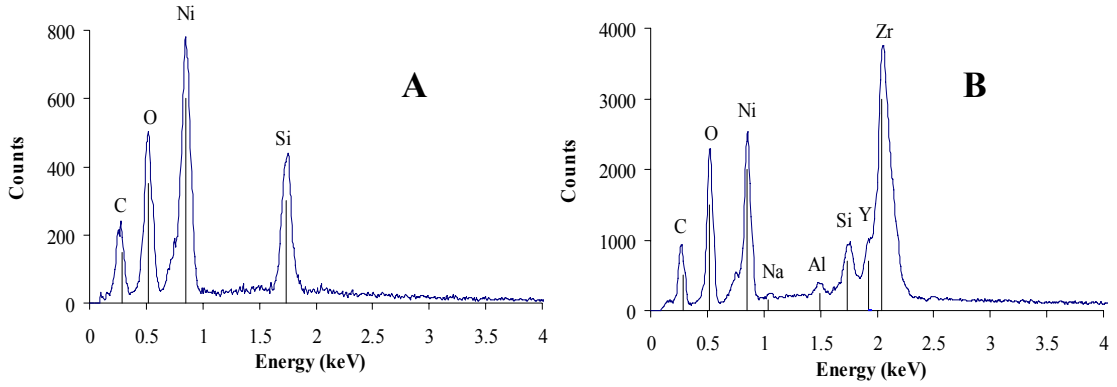

Figure 5-4: A: Point spectrum of impurity inclusion in a Ni particle in the cell from 3test27 (Figure 5-3B). B: Point spectrum of impurity "rim" around a Ni particle in the cell from 3test12 (Figure 5-3D).

5.3.3. Ni coarsening – effect of p(H_2O)

The effect of the steam content of 98% to the H_2 electrode at OCV and 850°C was tested on 3test12 prior to electrolysis testing. The effect of the high p(H_2O) at OCV was studied by recording impedance spectra during the entire testing period. The polarisation resistances (R_p) obtained from these impedance spectra are shown in Figure 5-5A.

The impedance spectra were analysed by deconvolution of the spectra as described by Barfod et al. [95]. Applying this model to selected impedance spectra it was observed that the increase in R_p is caused by an increase in the resistance, $R_{p,Ni}$ (see §4.3) from 0.04 Ωcm^2 to 0.17 Ωcm^2. This is ascribed to the charge transfer between YSZ and Ni/YSZ. The development of $R_{p,Ni}$ is shown in Figure 5-5B, where the fit of the type (1-exp(-t/τ)) leads to a characteristic time τ = 38 hours for the loss in performance relating to the charge transfer at the YSZ-Ni/YSZ interface at 98% to the H_2 electrode, OCV and 850°C.

Deconvolution of the two impedance spectra shown in Figure 5-6A were done applying the equivalent circuit shown in Figure 4-2. For the first spectrum recorded after 102 hours of test (3 hours with 98% steam) all 5 arcs in the equivalent circuit model were included in the fitting procedure. For the last spectrum (162 hours with 98% steam) the parameters relating to the contributions from the O_2 electrode were kept constant in the fitting procedure. Lines in the spectra in Figure 5-6A show the results of the fitting of the two impedance spectra. Dots and triangles show the experimental impedance spectra. The largest change in the impedance spectra in Figure 5-6A was found at a frequency of ~2000-3000 Hz and this relates to the Ni/YSZ electrode [95]. SEM micrographs of 3test12 support the EIS findings.

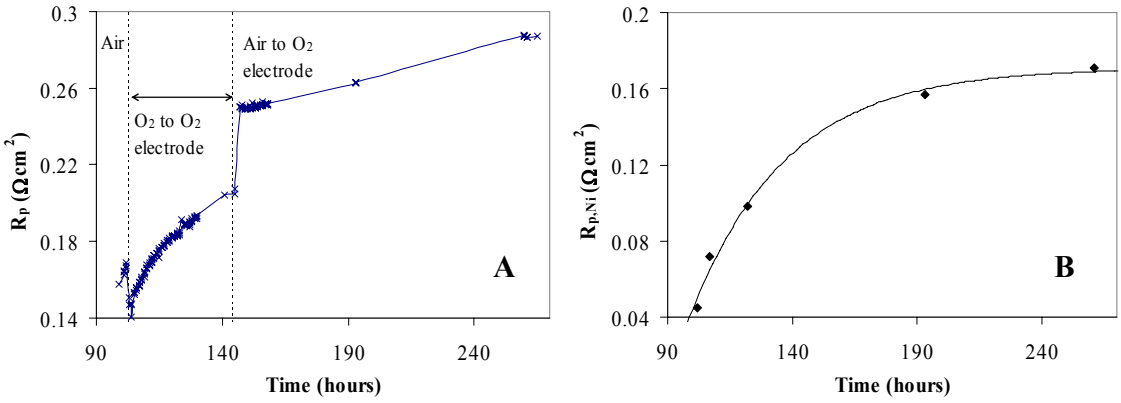

Figure 5-5: A: R_p, as function of time from recorded impedance spectra. Gas fed to the Ni/YSZ was 98% H_2O and 2% H_2, and gas passed over the O_2 electrode is given in the graph. The cell temperature was 850°C. B: The increase in $R_{p,Ni}$ as a function of time according to analysed impedance spectra. The fit of the type (1-exp(-t/τ)) shown gives a time constant, τ, of 38 hours. Errors for the obtained $R_{p,Ni}$ values are less than 10% and the equivalent circuit described by Barfod et al. was applied [95].

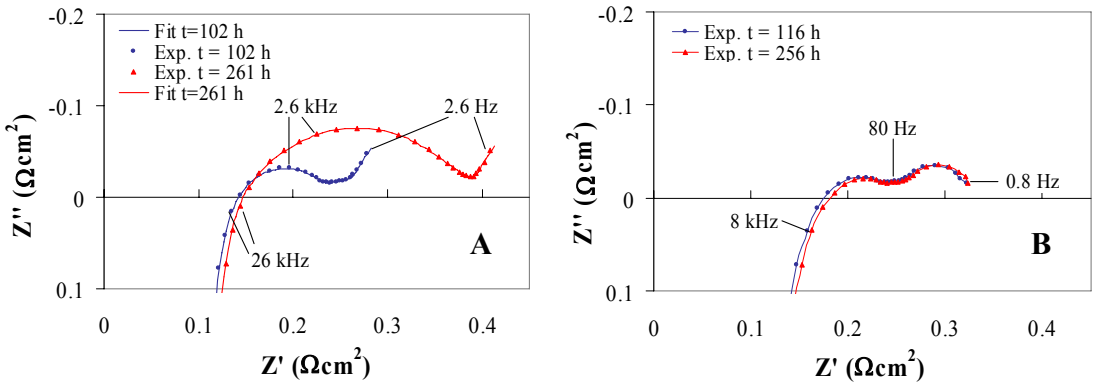

Figure 5-6: A: Development of impedance spectra for 3test12 constant at 850°C, OCV and p(H_2O) = 0.98 atm prior to any testing under current load. Impedance spectra recorded at t = 102 h and t = 261 h, see Figure 5-5. B: Impedance spectra for a cell left at 850°C, OCV and p(H_2O) = 0.04 atm before any testing under current load. The impedance spectra were recorded within 2 x 8 minutes and obtained at 20% H_2O at t = 116 h and t = 256 h.

For comparison a cell was left at OCV, 850°C and 4% H_2O in H_2 to the H_2 electrode. As shown in Figure 5-6B the impedance spectra recorded over 140 hours at these conditions show that the cell is stable. The $p(H_2O)$ was increased to 20% an left for a few minutes to stabilise before the impedance spectra in Figure 5-6B where recorded. The impedance spectra were recorded over 2x8 minutes at $p(H_2O) = 0.2$ atm.

5.3.4. Ni particle size distributions for differently tested SOECs

Ni particle size distributions have been obtained from SEM micrographs of several cells. Figure 5-7 shows the Ni particle size distributions for a reference cell and three differently tested SOECs. The reference cell has a more narrow size distribution and the mean Ni intercept length is smaller when compared to the size distributions for electrolysis tested cells. Furthermore, it is observed that the Ni particle size distributions for 3test21 and 3test22 are much alike.

Statistical tests have been applied to describe the differences in the Ni particle size distributions for 3test13, 3test21 and 3test22. Using an F-test to compare the variances of the Ni particle size distributions for 3test13 and 3test21 gave a probability of only $9 \cdot 10^{-10}$ that the two variances were identical, whereas a similar comparison of variances of 3test21 and 3test22 gave a probability of 0.04. A double tailored heteroscedastic t-test (confidence level of 95%) was applied for comparison of the mean Ni intercept lengths of the distributions for 3test13, 3test21 and 3test22. This gave a probability of only $2 \cdot 10^{-10}$ that the mean Ni intercept lengths of 3test13 and 3test21 are alike but a probability of 0.90 when comparing the mean Ni intercept lengths of 3test21 and 3test22.

Table 5-1 compares electrolysis test conditions and the loss in performance for SOECs cells with key parameters describing the Ni particle size distributions for very differently tested SOECs. The loss in performance (ΔASR) given in Table 5-1 was obtained from the first and last impedance spectrum at OCV and 850°C and calculated as $\Delta ASR = (ASR_{start}-ASR_{end})/ASR_{start}$. The ΔASR differs greatly for the tested cells but the mean Ni particle intercept lengths and the number of Ni particles per 300 μm line in the applied grids i.e. describing the number of Ni particles per active H_2 electrode area do not differ greatly for the differently tested SOECs. The characteristic numbers describing the Ni particle size distributions for electrolysis tested cells differ significantly from those obtained for the reference cells. The Ni particle size distributions for two different reference cells are very alike (2nd column, Table 5-1).

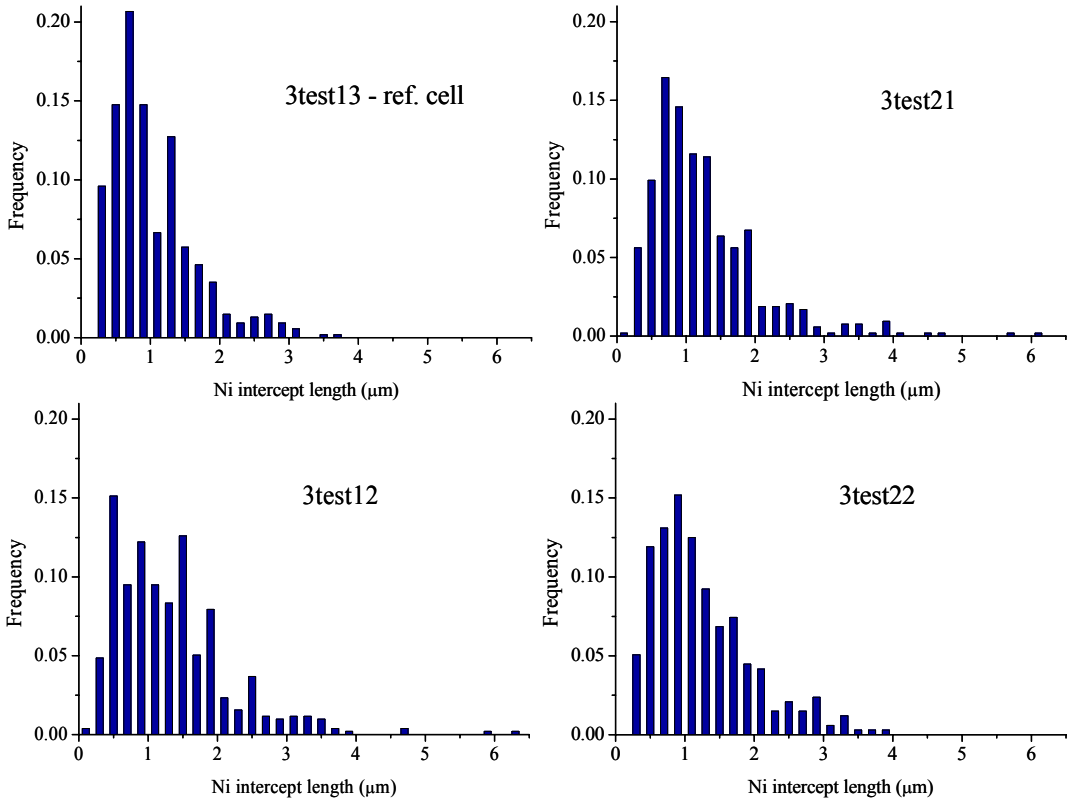

Figure 5-7: Ni particle size distributions for the active H_2 electrode for a reference cell (3test13) and three differently tested electrolysis cells (Table 5-1).

5.3.5. Aluminium occurrences in the H_2 electrode

SEM investigations of an "as-produced" half cell with a non-reduced NiO/YSZ electrode have been performed. A representative micrograph of the H_2 electrode/electrolyte interface is shown in Figure 5-8. Alumina (~ 0.25 w%) is added to the H_2 electrode support layer as a sintering aid. The spectrum in Figure 5-8 shows that Al can be found in the active layer of the H_2 electrode after sintering but prior to reduction of the NiO and testing of the cell. The cross in the inset marks the point at which the energy dispersive X-ray spectrum in Figure 5-8 was obtained. In this non-reduced half cell several similar particles were found. The EDS results show that the Al is most likely present as $NiAl_2O_4$ spinel particles. Some of these particles had Al/Ni ratios below the expected two for the spinel which is due to the large sampling volume and the surrounding Ni particles. None of the particles had Al/Ni ratio above two.

Table 5-1: Electrolysis test conditions, change in ASR and Ni particle size distributions for differently tested SOECs. ASR (R_s+R_p) obtained for the first and last impedance spectrum at OCV and 850°C are used to calculate ΔASR = (ASR_{start}-ASR_{end})/ASR_{start}. The last row gives the number of Ni particles counted for each size distribution. Numbers in brackets are for Ni particle size distribution for a reference cell from the same production batch as the cells for 3test26, 3test30 and 3test33.

Test no	Ref.	3t12	3t14	3t21*)	3t22*)	3t26	3t30	3t33
Temp. [°C]	-	850	750	850	850	850	850	850
i [A/cm^2]	-	-0.25	-0.25	-0.5	-1.0	-0.5	-0.5	-0.5
p(H_2O) [atm]	-	0.98	0.70	0.70	0.70	0.99	0.50	0.50
Duration [h]	-	459	82	140	358	300	1316	1510
ΔASR [%]	-	118	85	38	332	75	15	24
Mean Ni intercept length [μm]	1.04 (1.01)	1.29	1.21	1.25	1.24	1.27	1.26	1.22
No of Ni particles/300 μm line	86 (84)	67	67	63	66	68	63	66
Ni coverage [%]	29 (28)	25	27	26	27	29	26	27
No of Ni particles	542 (509)	516	395	535	336	560	512	536

*) For these tests, the main electrolysis test conditions are given. For test conditions during shorter electrolysis test periods see appendix A.

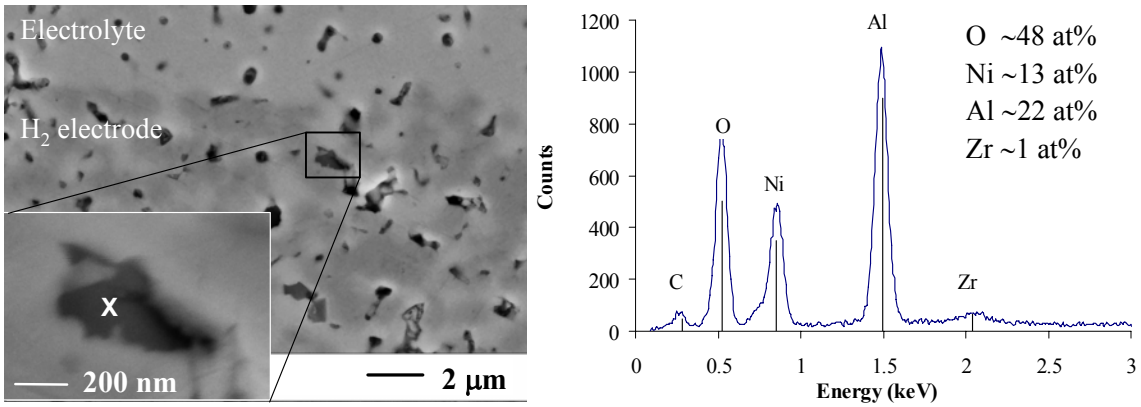

Figure 5-8: SEM micrograph of $NiAl_2O_4$ spinel in the active layer of the H_2 electrode of a non-reduced half cell. The cross in the inset marks the point at which the energy dispersive X-ray spectrum was obtained. The relative errors for the atom percentages for Ni and Al are below 10%.

The occurrence of $NiAl_2O_4$ spinel particles in the active H_2 electrode layer of a non-reduced, non-tested cell is supported by the phase diagram for the NiO-Al_2O_3 system given in Figure 5-9 where Al_2O_3 is observed to be slightly soluble in NiO. The sintering temperature for the SOCs is slightly above 1300°C.

Two different reference cells (NiO was reduced, but the cells were not tested under current load) have been investigated using SEM/EDS. Numerous Al-containing particles have been found in the active H_2 electrode layer of these reference cells. A typical micrograph of the H_2 electrode/electrolyte interface is shown in Figure 5-10 including an Al-containing particle only 2 µm from the electrolyte. For point spectra of Al-containing particles in the active H_2 electrode layer of the reference cells Al/Ni ratios above two are easily found. For the spectrum shown in Figure 5-10 an atom ratio of ~5 for Al/Ni were found. Therefore, the aluminium in the reduced H_2 electrodes of the reference cells is not present as $NiAl_2O_4$ spinel particles but rather as Al_2O_3 particles.

Al has also been detected by SEM/EDS in the H_2 electrode of electrolysis tested cells. Here Al was found in two types of compositions: 1) as "pure" Al_2O_3 particles or 2) in combination with silicon oxide containing impurities (chapter 6 and 7).

Whether or not the quantity of Al per volume of the active layer of the H_2 electrode equals the Al quantity per volume in the support layer has not yet been investigated.

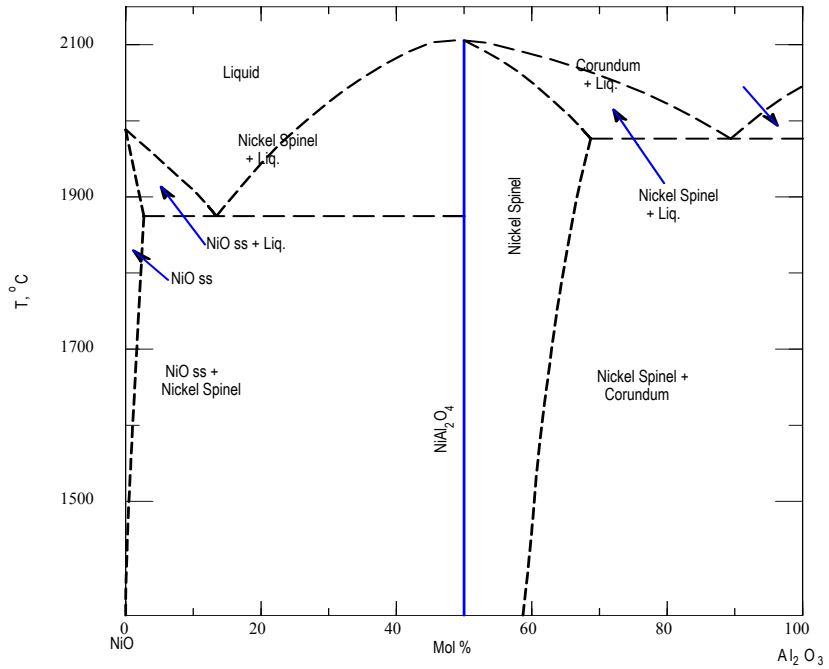

Figure 5-9: NiO-Al_2O_3 phase diagram adapted from [104] via NIST [105].

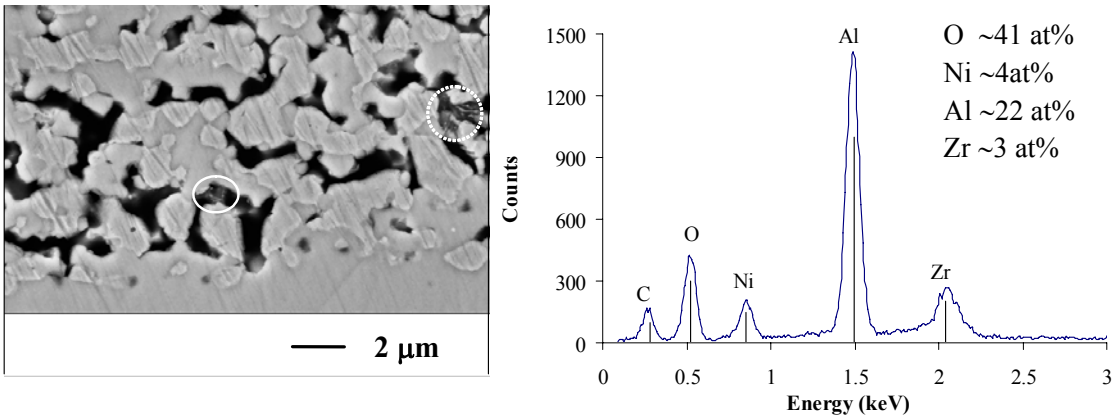

Figure 5-10: SEM micrograph of Al_2O_3 particle in the H_2 electrode of reduced cell that has not been exposed to electrolysis testing. The circle in the middle of the micrograph marks the point at which the energy dispersive X-ray spectrum (to the right) was obtained. The relative errors for the atom percentages of Ni and Al are below 10%. The circle with the dotted line is also an Al_2O_3 particle.

5.4. Discussion

5.4.1. Microstructure of tested SOECs

The performance of SOCs is very sensitive to the microstructure of the electrodes and cells having electrodes and electrolytes of raw materials with the same chemical composition can easily vary significantly in performance [11; 61; 106]. The microstructures of the SOCs are extremely dependent on the processing parameters (spraying, pore former, sintering temperatures etc.) and it is therefore difficult to compare the microstructures of the SOECs tested in this work with cells produced in other labs.

In general the microstructure of the tested SOEC seems to have been able to withstand 1510 hours of electrolysis at what can be considered "moderate" electrolysis test conditions (Figure 5-2). From the SEM investigations of the tested SOECs both the electrolyte and the O_2 electrode seem intact and so far no impurities have been found in the O_2 electrodes by SEM/EDS investigation of the SOECs. As the main passivation/degradation of the SOECs has been ascribed to the H_2 electrode (chapter 4, 6 and 7) a more thorough microscopic analysis of the O_2 electrode was not pursued. If/when the passivation/degradation processes for the H_2 electrode have been overcome or at least minimised it is advisable to perform a closer microscopy investigation of the O_2 electrode of tested SOECs that include: 1) search for impurities and undesirable zirconate compositions by EDS and WDS for long-term tested cells, 2) detailed microstructural investigation of the O_2 electrode/electrolyte interface and inhomogeneities in the composite electrode structure as obtained by Hagen et al. [32].

As illustrated in Figure 5-3 more harsh electrolysis conditions led to undesirable microstructural changes in the H_2 electrode. The electrolysis test conditions for 3test27 (950°C, 90% H_2O and -2 A/cm^2) led to a very high cell polarisation; nevertheless these test conditions can be relevant from a technological point of view. The fact that in some regions of this cell the Ni particles closest to the electrolyte were completely surrounded by densified YSZ must have caused a considerable decrease in the TPB and two phase boundary of the electrode, which will lead to an increase in both the ohmic and polarisation resistance. Furthermore, EDS mapping of the active H_2 electrode of 3test27 in the same manner as reported for 3test24 (chapter 6) show up to 1.2 w% SiO_2 in the innermost 2 μm closest to the electrolyte. If SOECs in the long-term are to be operated at electrolysis test conditions like the ones applied for 3test27 considerable changes, e.g. different microstructure and possibly also a different composition, of the H_2 electrode is necessary for it to withstand these conditions for long-term testing.

The impurity containing "dark rims" around the Ni particles were found in different regions of 2 different pieces of the cell used for 3test12. Even though the quantity of Si-containing impurities in these "rims" in the H_2 electrode of 3test12 is much smaller than quantities of impurities observed for H_2 electrodes from tests like 3test27, 3test22 and 3test24 (chapter 6) and 3test30 (chapter 7), the SEM micrograph in Figure 5-3D reveal that the Ni particles in the active H_2 electrode are "smeared" with the impurities. The impurities therefore cover

a significant quantity of the two and three phase boundaries, which in turn lead to a loss in performance for the cell as it hampers the electrochemical reactions at these sites.
The SiO_2 inclusions in the Ni particles (Figure 5-3B) are not believed to influence the performance of the H_2 electrode significantly as they block neither TPB nor two phase boundaries.

5.4.2. Coarsening of Ni particles

The procedure for obtaining the Ni particle size distributions was adapted from Hagen et al. [32] but it can be questionable for a variety of reasons e.g. at what point has enough Ni particles been included in a distribution for it to constitute a trustworthy description of the size distribution and are the Ni particles randomly and isotropically distributed in the investigated electrode areas? Furthermore, choices regarding the sample can be debatable e.g. how many microns from the electrode/electrolyte interface should be regarded as the active layer and included for the Ni size distributions? Is the microstructure in the selected SEM images representative for the cell and micrographs from how many different regions of a cell should be included to check this? Nevertheless, the resulting size distributions given here are all obtained in the same manner which justifies a comparison of the Ni size distributions for reference cells and differently tested SOECs.
For the Ni particle size distributions presented here a layer of 10 μm from the electrolyte was investigated as this constitutes the active electrode layer from a production point of view. Brown et al. [107] found a thickness of the electrochemically active layer of ~10 μm for Ni/YSZ cermet electrode at 1000°C. The thickness of the electrochemically active layer varies with temperature and microstructure of the electrode. The microstructure of the electrodes used by Brown et al. was coarser than those of the SOECs tested here and the thickness of the electrochemically active layer for the tested SOECs is presumably 5-10 μm.
A minimum of five micrographs from different regions of the cell have been investigated to calculate each of the Ni particle size distributions presented in Table 5-1. For electrolysis tested cells steam inlet parts of the cells were used for the Ni particle size distributions. Variations in the size distributions of different regions were observed and a thorough analysis of these variations will require a programme for image processing that can automatically distinguish the Ni and YSZ contrast and the borders between the particles in SEM micrographs.
From the characteristic numbers for the Ni particle size distributions (Table 5-1) it is evident that the tested SOECs have very similar Ni particle size distributions, even though the cells have been exposed to very different test conditions and suffer from extremely different degrees of passivation/degradation. 3test21 and 3test22 were both operated at 850°C and $p(H_2O)$ = 0.7 atm during electrolysis testing. The degree of passivation/degradation for 3test21 is almost an order of magnitude lower than for 3test22 but their Ni particle size distributions given in Figure 5-7 are very similar. The results of statistical tests for these distributions show that the two distributions have the same mean Ni intercept length. The large variation in the degree of passivation/degradation for 3test21

and 3test22 cannot be related to the Ni particle size distributions but seems more closely related to impurities in the H_2 electrodes (see chapter 6). EDS results for the H_2 electrode of 3test22 showed significant amounts of Si-containing impurities [82], whereas only "traces" of Si-containing impurities have been found in the H_2 electrode of 3test21.
In chapter 4 it was postulated that the long-term degradation observed for 3test30 was hardly caused by Ni coarsening. The Ni particle size distribution for 3test30 is similar to distributions for much shorter test e.g. 3test14 and 3test21. The higher $p(H_2O)$ for 3test21 compared to 3test30 can have accelerated the coarsening of the Ni particles, on the other hand lowering the temperature (3test14) will lead to a less pronounced effect of Ni coarsening [108]. Furthermore, 3test25 (appendix A) was tested at the exact same conditions as 3test30 but only for 596 h, and 3test25 had a Ni particle size distribution similar to 3test30 i.e. a mean Ni intercept length of 1.27 μm, 66 Ni particles/300 μm line in the grid and a Ni coverage of 28%. Therefore the Ni particle size distributions given in this chapter provides evidence that the long-term degradation observed over 1316 h of electrolysis testing for 3test30 is not mainly caused by Ni coarsening. In line with these results, Hagen et al. [32] found that the Ni size distribution for long-term fuel cell tested SOCs had changed compared to a reference cell but the change in the size distribution was not the main degradation cause in these tests either.
The results from the analyses of impedance spectra recorded during operation at OCV, 850°C and 98% steam to the H_2 electrode (Figure 5-5) are supported by the obtained Ni particle size distribution for 3test12. The observed loss in performance for 3test12 relates to a significant increase in the resistance at the YSZ-Ni/YSZ interface compared to a cell left at OCV, 850°C and 4% H_2O (Figure 5-6 and [75]). At the very high $p(H_2O)$ it does not have a significant effect on the Ni particle size distribution whether the test lasted more than 600 hours as for 3test12 or only 300 h as for 3test26 (Table 5-1). This supports the EIS findings that the effect of a high $p(H_2O)$ at OCV on an SOEC occurs on a relatively short time scale well below 300 h. From a technological point of view it will be relevant to develop H_2 electrodes for SOECs where particle agglomeration is avoided even at high $p(H_2O)$ at OCV and maintain its high performance. An alternative to the Ni/YSZ electrode could be an "all-ceramic" H_2 electrode e.g. a niobium doped strontium titanate electrode [34; 109] or titanate/ceria electrode [106], as oxides are not expected to agglomerate as metal particles do. However, it is noted that titanate/ceria based electrodes have been shown to have the drawback of decreased conductivity for increasing pO_2 i.e. at high $p(H_2O)/p(H_2)$ [110].

5.4.3. Diffusion of Al-species the H_2 electrode

From Figure 5-8 it is evident that even though alumina is added only to the support layer during production of the cells it can also be found as $NiAl_2O_4$ spinel in the active H_2 electrode layer of a sintered, but non-reduced and non-tested cell and after reduction it is found as Al_2O_3 particle. Based on the phase diagram of the NiO-Al_2O_3 and the applied sintering temperature, a plausible but not yet experimentally verified explanation is, that Al_2O_3 dissolves in NiO during sintering of the cells and diffuses (concentration gradient

driven) into the active layer of the H_2 electrode and $NiAl_2O_4$ spinel particles are formed in the non-reduced NiO/YSZ electrode upon cooling of the sample. The aluminium is subsequently precipitated as Al_2O_3 particles when the NiO is reduced to Ni. The Al_2O_3 have been observed to be located at TPB and thereby decrease the performance of the cell from the very start of a cell test. On the other hand the addition of alumina to stabilised zirconia in optimised quantities have been shown to improve the strength [111] and lower the thermal expansion coefficient [112], while there are contradicting results regarding the effect of Al_2O_3 addition on the conductivity of stabilised zirconia [113-116]. There are numerous of examples of detection of aluminium oxides in the active H_2 electrode of the tested SOECs (chapter 6) and in several cases (chapter 7) EDS for these aluminium oxide particles show peaks from silicon and sometimes sodium as well. This is not surprisingly as Al_2O_3 is known as a scavenger of Si in stabilized zirconia [113]. As described by Lybye and Liu [117] the optimal amount of Al-dopant for scavenger Si-impurities is a delicate balance and the optimal quantity of Al_2O_3 for scavenging does not scale proportionally to the quantity of Si impurities. Furthermore, the Al_2O_3 not only acts as a Si scavenger in stabilised zirconia but also slightly decreases the bulk conductivity and influences the grain boundary conductivity negatively or positively depending on the alumina addition relative to the amount of impurities present. In order to make use of Al_2O_3 as a Si-scavenger in SOECs a controlled addition of the optimal amount of Al-dopant should be obtained instead of the somewhat unintentional "addition" of Al_2O_3 to the active H_2 electrode that occurs due to solid-state diffusion of Al-species from the support layer during sintering. Furthermore, the size and distribution of Al_2O_3 in the active layer is probably also important for to obtain an optimal scavenger effect.
If SOEC H_2 electrodes with optimised Al_2O_3 addition shall be produced it is necessary to: 1) perform long-term electrolysis tests using a set-up where Si-contamination from the sealing/test set-up has been avoided or at least minimized (chapter 8) and 2) investigate the impurities in these tested SOECs in line with the results presented in chapter 7 i.e. SEM/EDS and TEM/EDS for the H_2 electrode/electrolyte interface.

5.5. Conclusion

From the SEM, EDS and EIS results presented in this chapter, it can be concluded that:

- The microstructure of the hydrogen electrode supported SOCs produced at Risø National Laboratory can withstand long-term (1500 h) galvanostatic electrolysis testing at moderate test conditions (850°C, $p(H_2O)$ = 0.5 atm, -0.5 A/cm^2)
- SEM micrographs of the tested SOECs did not show cracks in the electrolyte, significant delamination of the electrodes or similar damages.
- At more "harsh" electrolysis test conditions (850°C, $p(H_2O)$ = 0.9 atm, -2.0 A/cm^2) the microstructure in 2 μm of the H_2 electrode closest to the electrolyte has changed

significantly after only 68 h of electrolysis testing. In certain regions of the YSZ seem to have densified totally and surround the Ni particles completely in a ~2 μm layer closest to the electrolyte. Si-containing impurities were found in this H_2 electrode.

- What looks like a detachment of Ni particles from the adjacent YSZ in secondary electron SEM micrographs of several tested SOECs was found by EDS to be a build-up of Si-containing impurity "rims" covering significant parts of the two and three phase boundaries.
- The Ni particle size distributions have changed upon testing. The Ni size distributions have broadened and the mean Ni intercept lengths, i.e. the mean Ni particle sizes, have increased for tested SOECs (mean Ni intercept length ~ 1.24 μm) when compared to reference cells (~1.03 μm).
- Operating a cell constant at OCV, 850°C, and $p(H_2O) = 0.98$ atm led to an increase in the polarisation resistance originating from increased resistance for the charge transfer at the YSZ-Ni/YSZ interface. This part of the polarisation resistance increased from 0.04 Ωcm^2 to 0.17 Ωcm^2 within ~150 h.
- Comparing electrolysis test conditions (temperature, current density, $p(H_2O)$ and duration) and the resulting increase in ASR (start and end of test) with the Ni particle size distributions for the SOECs with very different test parameters and results, it is evident that the coarsening of the Ni particles is not the main passivation/degradation mechanism for the SOECs tested in this work.
- The long-term degradation (3test30, chapter 4) is hardly caused by Ni coarsening.
- Al_2O_3 from the support layer diffused into the active H_2 electrode during production of the cells and is found in both reference and tested cells. Al_2O_3 can be used as a Si-scavenger but a much more controlled Al-doping of the H_2 electrode is necessary if this is to be obtained.

6. Silica segregation in the Ni/YSZ electrode

6.1. Introduction

In this chapter test results from two different electrolysis tests are given[9]. The cells were tested at a variety of operation temperatures, current densities and gas flows to the electrodes. The cell voltages monitored during the electrolysis operation increased significantly during the first few days of testing. Electrochemical impedance spectroscopy (EIS) obtained before, during and after electrolysis operation shows that it is the Ni/YSZ electrode that passivates as it was described in chapter 4 for different electrolysis tests. Reference cells and the two tested cells were examined in a scanning electron microscope after test. These post-mortem analyses reveal a reason for the observed passivation, as results from energy dispersive spectroscopy (EDS) clearly show evidence that silica containing impurities have segregated to the hydrogen electrode/electrolyte interface during electrolysis testing. Examples of different microstructures and amounts of Si-containing impurities in the electrolyte/hydrogen electrode interface are presented and related to the electrolysis test conditions and the passivation histories of the electrolysis cells. This chapter focuses on microscopy investigations of impurities in the hydrogen electrode/electrolyte interface of these two cells, where the amount and microstructure of these impurities vary depending on the operation conditions during electrolysis. Si-containing impurities have been detected in the H_2 electrode of other tested SOECs as well. It is shown that substantial amounts of impurities can be found in the few microns of the hydrogen electrode closest to the electrolyte and this support the EIS results presented in chapter 4.

6.2. Experimental

6.2.1. Electrolysis tests and test set-up

Ni/YSZ supported SOFCs produced at Risø National Laboratory were used as SOECs for high temperature steam electrolysis. Detailed information about the composition of the electrodes and the dimension of the tested cells as well as detailed information about the cell test setup, reduction and start-up procedure, steam generation etc. is given elsewhere [61; 118; 119]. Reference cells were obtained by applying the usual heating up and NiO-reduction procedure to cells from the same production batch as the cells used for electrolysis testing. After obtaining a cell voltage close to the one expected from the calculated Nernst potential the cooling down of the reference cells was started. EIS was obtained as described in chapter 2.

[9] This chapter has been published as "Silica segregation in the Ni/YSZ electrode", Hauch, A., Jensen, S.H., Bilde-Sørensen, B. and Mogensen, M., in *Journal of the Electrochemical Society*, **154**(7), A619-A626 (2007).

6.2.2. Raw materials and sample preparation

TZ8Y (ZrO_2, 8 mol% Y_2O_3, Tosoh) was used for the electrolyte and the 10 µm thick active hydrogen electrode. For the 300 µm thick Ni/YSZ support layer TZ3Y (ZrO_2, 3 mol% Y_2O_3, Tosoh) was used. For both the active electrode and the support layer the NiO for the Ni/YSZ cermet was supplied by Alfa Aesar®, Johnson Matthey Company. The chemical composition of the raw materials according to the specifications from the suppliers together with impurity analysis by GDMS (Glow Discharge Mass Spectroscopy) is given in Table 6-1. The organic solutions used for the YSZ slurry for the production of the cells also contain impurities, but the amount of silicon originating from the organic compounds used in the cell production is only approximately $^1/_{10}$ of the amount of silicon from the YSZ.

Table 6-1: Chemical composition of raw materials for the YSZ electrolyte and the Ni/YSZ electrode and support layer according to the specifications from the supplier given as maximum content and content of impurities according to GDMS analysis. Numbers are given in ppm.

	TZ3Y Tosoh	TZ3Y GDMS	TZ8Y Tosoh	TZ8Y GDMS	NiO Alfa Aesar	NiO GDMS
Y_2O_3	40800	-	106600	-	-	-
Al	26	8.3±1.0	26	8.3±0.6	-	3.4±0.4
Si	33	13.0±1.5	9	13±1	-	12.0±1.0
Ni	-	0.53±0.06	-	3.0±0.2	786000	-
Fe	21	29±2	35	31±4	10.2	23.0±0.5
S	-	5.4±0.5	-	200±15	6	5.3±0.3
Cl	-	400±50	-	5700±200	-	0.78±0.10
Ca	-	14±1	-	11±1	0.4	1.6±0.2
Na	133	200±15	533	680±40	0.4	0.73±0.10
Co	-	0.30±0.05	-	0.38±0.04	0.3	0.27±0.07
Li	-	2.3±0.3	-	1.9±0.2	-	< 0.05
F	-	< 5	-	< 5	-	< 5
N	-	130±20	-	160±30	-	< 25
Zn	-	1.5±0.2	-	1.4±0.1	-	5.5±0.4
Ti	-	3.0±0.3	-	3.6±0.4	-	0.27±0.05
Cu	-	2.3±0.3	-	3.8±0.3	0.1	1.20±0.15
Pb	-	2.3±0.3	-	0.45±0.05	< 2	< 0.05
Cr	-	0.19±0.03	-	1.5±0.2	-	10.0±0.7
Mn	-	1.1±0.1	-	1.1±0.1	-	0.27±0.05
Mg	-	3.2±0.3	-	2.9±0.2	< 1	0.43±0.06
K	-	1.3±0.1	-	1.9±0.2	< 3	0.51±0.15

The cells were prepared for SEM investigation by vacuum embedding pieces of the cells in epoxy (EpoFix from Struers) followed by grinding and polishing. The samples were subsequently coated with carbon. It has been shown that the presence of epoxy as mounting material does not interfere with the impurity analysis [78].

6.2.3. SEM and EDS

Reference cells and the tested cells were examined in a Zeiss Supra 35 FE-SEM (Field Emission SEM) equipped with the Noran System SIX X-ray microanalysis system. The EDS was obtained at an acceleration voltage of 10-12 kV. Monte Carlo simulations show that at an acceleration voltage of 10 kV, the X-rays penetrate to a maximum depth in the material from ~ 400 nm for Ni(L_α) to ~ 750 nm for Zr(L_α) and a spatial resolution of approximately 1 μm can be expected for the elements of interest. A counting time of 60 s was used for the point EDS. For the line scan the distance between each individual spectrum was 0.06 μm and the counting time was 30 s for each point. EDS maps were recorded over 30 minutes with a resolution of 256x192 pixels corresponding to 10 pixels per μm at the selected magnification.

Quantification was made by standardless analysis. Element concentrations were calculated using the K_α-line for O, C, Al and Si. The L_α-line was used for Ni, Y and Zr. Peak overlap occurred for Y and Zr only. The detection limit for silicon and sodium is estimated to be 0.1 wt%. The relative uncertainty for the EDS analysis is generally ±5%, though it could be up to ±10% for analysis of elements which are only present at very low concentrations [78].

6.3. Results

6.3.1. 3test24 – electrolysis testing

A history plot for the cell voltage during the entire 3test24 is shown in Figure 6-1 and the different operation conditions during testing are given in Table 6-2. The two main electrolysis test periods are marked by the numbers 4 and 11 in Figure 6-1 and the electrolysis conditions were -0.5A/cm^2 at 850°C applying 90% steam and 10% hydrogen in the inlet gas to the Ni/YSZ electrode and later -1.0A/cm^2 at 950 °C applying 66% steam and 34% hydrogen in the inlet gas to the Ni/YSZ electrode. As observed previously for other test conditions [61; 91], the cell passivates[10] within the first few days. The cell voltage increased 49 mV over 161 hours during the first H_2O electrolysis test period and 221 mV over 474 hours during the last H_2O electrolysis test period. The short period of CO_2 electrolysis (marked 7 in Figure 6-1) led to an increase in the cell voltage of 29 mV.

[10] Passivation is a reversible loss and degradation is an irreversible loss of performance for the SOC.

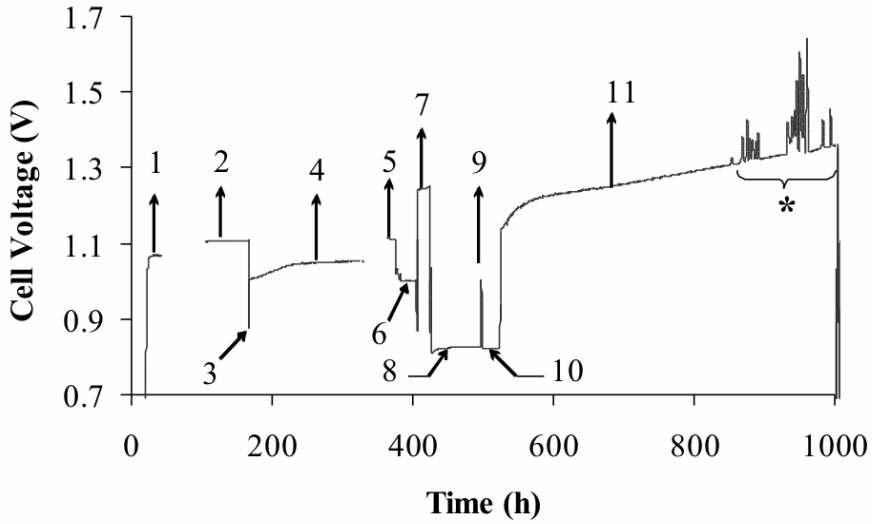

Figure 6-1: Cell voltage vs. time for 3test24. The numbers next to the cell voltage curve correspond to the numbers in the first column in Table 6-2 in which the operating conditions are given. Characterisation (iV curves, impedance spectra and gas shift experiments) of the cell was performed from 41-105 h and 329-360 h of testing. *) The observed instability was caused by temperature control problems.

Table 6-2: Operation conditions for cell 3test24. The numbers in the first column correspond to the numbers in Figure 6-1.

No	Time (h)	Gas to H_2 electrode (l/h)	Gas to O_2 electrode	Current density (A/cm^2)	Nernst potential (mV)	Temp. (°C)
1	34-40	1.0/18.0 H_2O/H_2	Air	0	1025	850
2	115-166	1.2/24.0 H_2O/H_2	O_2	0	1107	850
3	166-168	12.5/1.6 H_2O/H_2	O_2	0	824	950
4	168-329	12.5/1.6 H_2O/H_2	O_2	-0.5	863	850
5	368-388	1.3/24.0 H_2O/H_2	O_2	0	1104	850
6	388-406	2.3/10.0 CO_2/CO	O_2	0	990	950
7	406-424	30.2/10.0 CO_2/CO	O_2	-1.0	854	950
8	424-497	12.6/12.6 H_2O/H_2	O_2	1.0	932	950
9	497-498	5.0/20.0 H_2O/H_2	O_2	0	990	950
10	498-525	12.6/12.6 H_2O/H_2	O_2	1.0	932	950
11	525-1000	4.5/2.3 H_2O/H_2	O_2	-1.0	897	950

6.3.2. 3test24 – SEM/EDS results

It has not been possible to find delamination between the electrolyte and the electrodes, cracks in the electrolyte, or similar types of changes in the cell from 3test24. The upper part

of Figure 6-2 shows a SEM image of the electrolyte/hydrogen electrode interface for 3test24 after electrolysis testing. Point energy dispersive spectra were recorded at the three coloured points marked in the SEM image. The lower part of Figure 6-2 shows the spectra obtained at the three points. The colour of the lines in the spectra specifies where each spectrum was obtained on the sample. It is seen that Si and YSZ are present as oxides. On the contrary Ni is not oxidized. The calculated atom percentages and weight percentages of the oxides obtained for the three spectra in Figure 6-2 are given in Table 6-3. The main constituents for the "red spectrum" are Si and O, and only few atom percentages of Ni, Y, Z, Al and Na were detected. The Si/O ratio was close to 0.5 and silicon most likely exists as SiO_2 in this grain of impurity. Note that only the Si and O peak seems to be present in the point spectra recorded at the red mark, besides carbon from the mounting material. This reveals that even though it can be difficult to see the borders of the silica particle in the SEM image, the SiO_2 particle actually occupies the main part of the sampling volume and therefore has a diameter of approximately 1 μm. The presence of sodium in the red point (Figure 6-2) can be difficult to see in the spectrum given in Figure 6-2 because of the low counting time[11]. Point spectra with a counting time of 60 s also shows the presence of Na in the Si-containing grains of impurities. The Na/Si ratio is typically between 1/14 and 1/34 in the Si-containing impurities. Both sodium and silicon are most likely present as oxides.

An element map of the cell area in Figure 6-2 is shown in Figure 6-3. The rather large particles of alumina observed in Figure 6-3 originate from alumina that is added as sintering aid during the cell manufacturing and such alumina particles are also found in the reference cells. Area analysis using EDS data originating from the area between 0 and 2 μm from the electrolyte was obtained and the resulting spectrum is shown below the element map in Figure 6-3. The corresponding counting time for the spectrum in Figure 6-3 was 180 s for the area of 2x30 μm^2. Compound weight % were calculated based on the spectra from the energy dispersive spectroscopy originating from the regions 0-2 μm, 2-4 μm, 4-6 μm, 6-8 μm and 8-10 μm from the electrolyte[12]. The inset in Figure 6-3 shows the calculated concentrations as a function of distance from the electrolyte. Note how the SiO_2 concentration decreases with increasing distance from the electrolyte. Several mappings similar to the one shown in Figure 6-3 have been made for this cell and Si could not be detected in the spectra obtained at a distance of more than 8 μm from the electrolyte for any of them. Furthermore, the silica content in the innermost 2 μm close to the electrolyte varied along the electrode/electrolyte interface from no detectable silica to a maximum of ~8 wt% SiO_2 which is the interface region shown in Figure 6-3. The variation in SiO_2 content was examined along an electrode/electrolyte interface of 0.8 cm.

[11] The spectra for the points shown in the upper part of Figure 6-2 are extracted from the mapping (30 minutes) of the entire image using the "Spectral Imaging" feature in Noran System SIX. Therefore the EDS for these points only correspond to a counting time of approximately 5 s.

[12] Area spectra from an inhomogeneous area do not strictly fulfill the conditions for ZAF corrections. The absolute value of the Si content is therefore somewhat uncertain, but the curve in Figure 6-3 is expected to reflect the relative variation correctly.

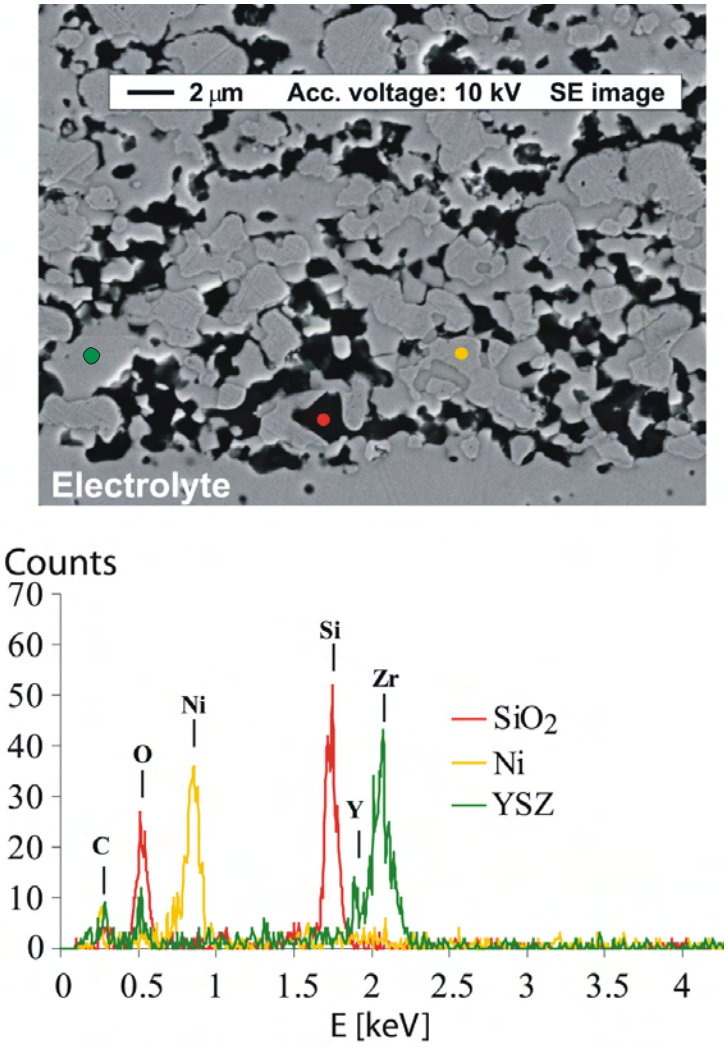

Figure 6-2: Post mortem SEM secondary electron (SE) micrograph of 3test24. Three coloured points are shown on the SE image. EDS for each point is shown in the same colour below the SEM micrograph.

Table 6-3: Chemical composition as atom percentages determined by point EDS. Colours in 1st column refer to points in Figure 6-2. Numbers in brackets give the calculated weight percentage for the corresponding oxides.

	Si	Ni	Zr	Y	Al	Na	O	C
Red	26 (81)	0.5 (1.5)	0.5 (3.1)	-	0.7 (1.9)	1.5 (2.5)	54	17
Yellow	-	55 (83)	1.1 (3.4)	0.5 (1.5)	-		3	40
Green	-	-	20 (77)	5.0 (17)	-		48	27

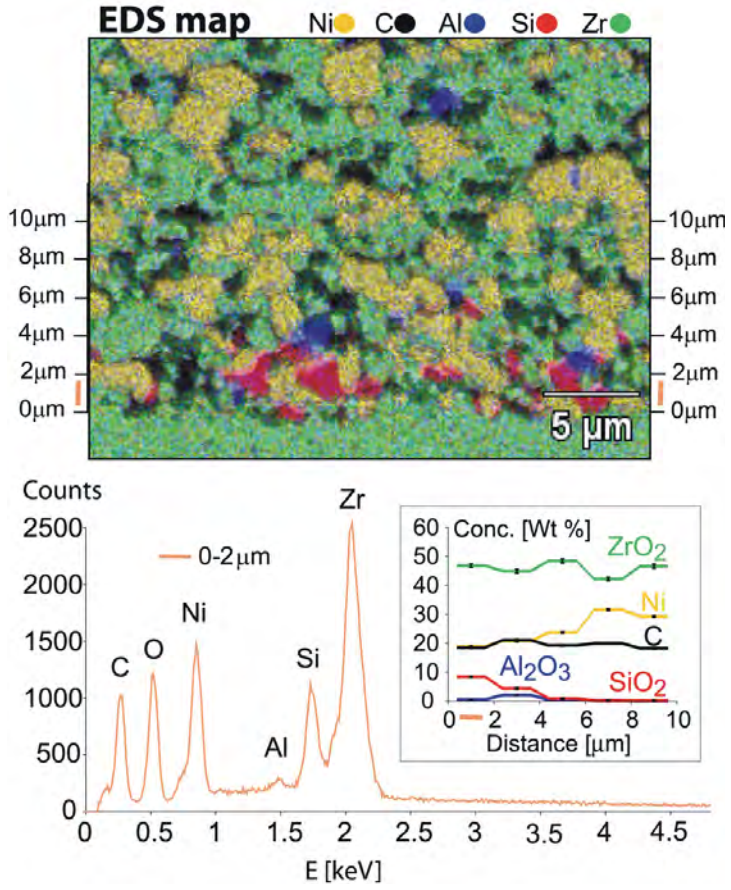

Figure 6-3: EDS mapping of Si (red), Al (blue), Zr (green), Ni (yellow) and C (black). The carbon comes from holes in the porous electrode filled with epoxy. The EDS shown below is an additive spectrum of all point EDS lying within a specified distance from the electrode/electrolyte interface. Concentrations of compounds are calculated based on the additive EDS. The concentration for each compound is given as a function of interval distance from the electrolyte in the inset.

6.3.3. 3test24 – EIS during testing

Figure 6-4A shows an impedance spectrum obtained just after the beginning of the first electrolysis test period for 3test24 and an impedance spectrum obtained just before ending the first electrolysis test period (see Table 6-2). Note that the real part of the impedance (Z') at 100 kHz is constant during this first electrolysis test period. This corresponds to a constant ohmic resistance while the polarisation resistance increases. The impedance spectra shown in Figure 6-4B were recorded just after starting and just before ending of the last electrolysis test period for 3test24. Here it is observed that both the polarisation and ohmic resistance increase. Part C of Figure 6-4 show two impedance spectra recorded at OCV, one recorded before the first electrolysis testing at t = 93 h and after ending the last electrolysis test period at t = 1001 h.

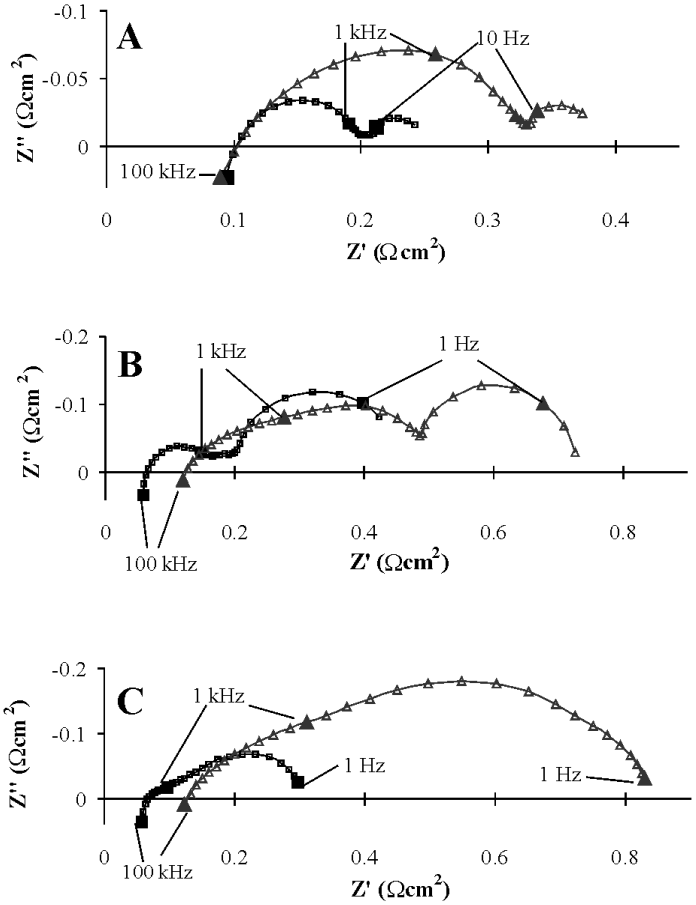

Figure 6-4: Impedance spectra recorded during 3test24. Impedance spectra marked by triangles are the last recorded spectra in each figure. A) During the first electrolysis test period at t = 166 h and t = 329 h. B) During the last electrolysis test period at t = 526 h and t = 999 h. C) At OCV (950°C, 5% H_2O and 95% H_2 to the Ni/YSZ electrode) before the first electrolysis test at t = 93 h and after the last electrolysis test at t = 1001 h. See Table 6-2 for operation condition for spectra recorded during electrolysis testing.

6.3.4. 3test22 – electrolysis testing

A history plot for the cell voltage during the entire 3test22 is shown in Figure 6-5 and the different operation conditions during testing is given in Table 6-4. The main electrolysis test period is marked by the number 2 in Figure 6-5 and the electrolysis conditions were -1.0 A/cm^2 at 850 °C applying 70% steam and 30 % hydrogen in the inlet gas to the Ni/YSZ electrode. During the main electrolysis test period, the cell voltage increased 479 mV over 351 h. Later during testing of 3test22 three shorter electrolysis test periods were run at a current density of -0.5 A/cm^2 (marked 5, 6 and 9 in Figure 6-5). 3test22 was also operated in fuel cell mode at 0.5 A/cm^2 at 850 °C with 5% steam and 95% hydrogen in the inlet gas to the Ni/YSZ electrode (marked 4 and 8 in Figure 6-5).

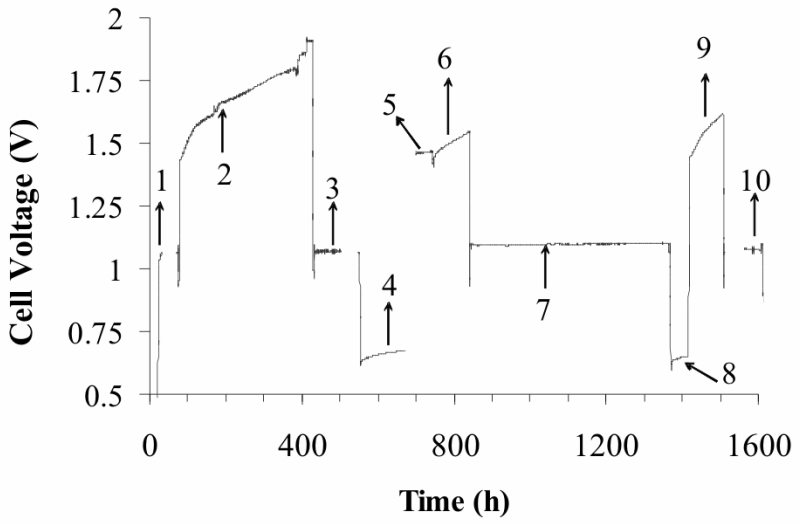

Figure 6-5: Cell Voltage vs. time for 3test22. The numbers next to the cell voltage curve correspond to the numbers in the first column in Table 6-4 in which the operating conditions are given. Characterisation (iV curves, impedance spectra and gas shift experiments) of the cell was performed from 32-76 h, 504-560 h and 670-713 h of testing.

Table 6-4: Operation conditions for cell 3test22. The numbers in the first column correspond to the numbers in Figure 6-5.

No	Time (h)	Gas to H_2 electrode (l/h)	Gas to O_2 electrode	Current density (A/cm^2)	Nernst potential (mV)	Temp. (°C)
1	30-32	1.0/18.0 H_2O/H_2	Air	0	1025	850
2	76-429	12.3/5.6 H_2O/H_2	O_2	-1.0	924	850
3	429-504	1.3/24.0 H_2O/H_2	Air	0	1067	850
4	560-671	1.3/24.0 H_2O/H_2	Air	0.5	1067	850
5	713-756	7.6/17.6 H_2O/H_2	O_2	-0.5	1003	850
6	756-840	12.3/5.6 H_2O/H_2	O_2	-0.5	924	850
7	840-1369	1.3/24.0 H_2O/H_2	O_2	0	1104	850
8	1369-1417	12.6/12.6 H_2O/H_2	O_2	0.5	962	850
9	1417-1508	7.6/17.6 H_2O/H_2	O_2	-0.5	1003	850
10	1508-1600	1.3/24.0 H_2O/H_2	O_2	0	1104	850

6.3.5. 3test22 – SEM/EDS results

A representative overview SEM micrograph is shown in Figure 6-6. Even though a significant increase in the ohmic resistance was measured during testing, it was not possible to find delamination between the electrolyte and the electrodes, cracks in the electrolyte or similar changes in the cell used for 3test22 that could be expected to lead to an increase in the ohmic resistance [42].

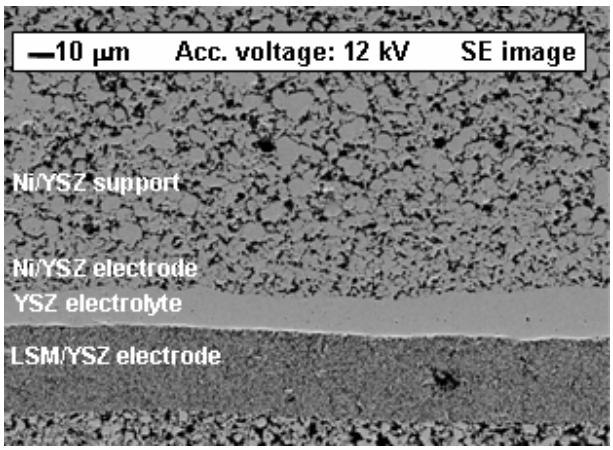

Figure 6-6: Low magnification SEM image of the cell used for 3test22. No cracks in the electrolyte or delamination between electrolyte and the electrodes could be found.

Figure 6-7A is a representative SEM image of a hydrogen electrode/electrolyte interface of the cell from 3test22 at a higher magnification. Note the dark rims between the Ni and the YSZ particles. The inset is a higher magnification image of one of the Ni particles adjacent to the electrolyte. The dark rim shown here has a width of approximately 50 nm. A line scan was made at the red line in the inset. Figure 6-7B shows the counts for Si(K_α), Ni(L_α) and Zr(L_α) as a function of position in the line scan. It is seen that the Si counts has a maximum where the dark rim between the Ni and the YSZ particles is located, whereas the Zr counts increases, and the Ni counts decreases from start to end point of the line scan.

6.3.6. 3test22 – EIS during testing

Figure 6-8A shows an impedance spectrum obtained just after the beginning of the first electrolysis test period for 3test22 and an impedance spectrum obtained just before ending the first electrolysis test period (see Table 6-4). The polarisation resistance as well as the real part of the impedance (Z') at 100 kHz (ohmic resistance) increases during the testing at -1 A/cm^2 in contrast to 3test24 where only the polarisation resistance increased during the first electrolysis period at -0.5 A/cm^2. Both the polarisation and ohmic resistance increased during the shorter 2nd and 3rd electrolysis test period (-½ A/cm^2) for 3test22. Figure 6-8B

shows two spectra recorded during the first fuel cell test period (0.5 A/cm^2) at t = 561 h and t = 679 h. During this fuel cell test period the real part of the impedance (Z') at 100 kHz (ohmic resistance) decreases. Figure 6-8C shows two spectra recorded at OCV, one recorded before the first electrolysis testing at t = 49 h and after ending the 3rd electrolysis test period at t = 1514 h.

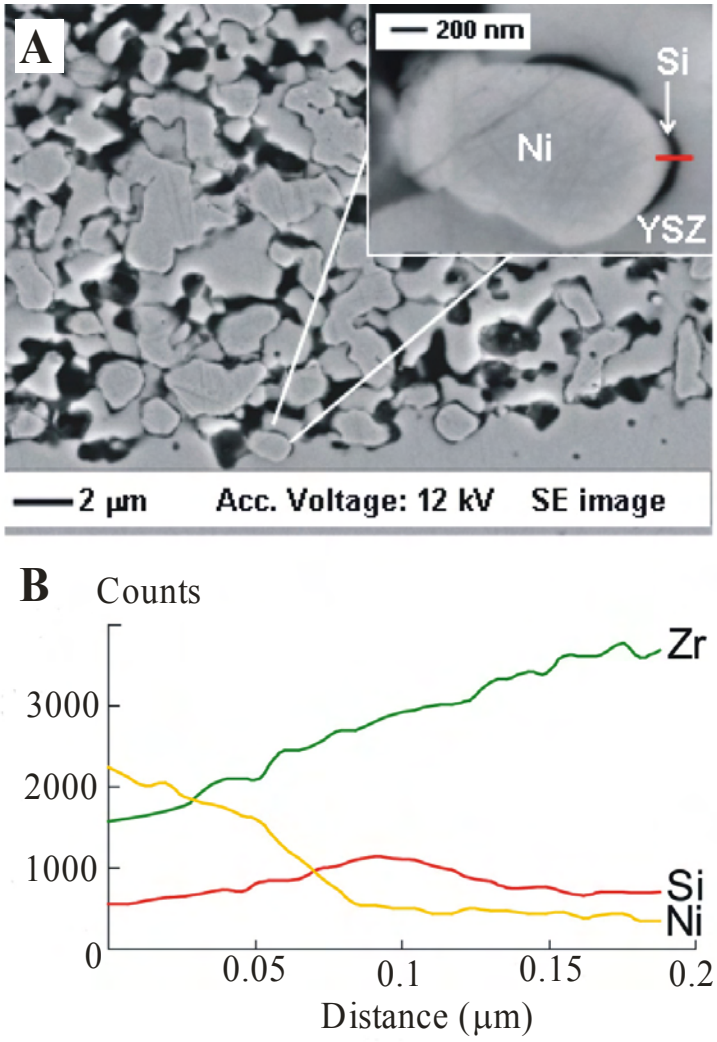

Figure 6-7: A) SEM micrograph of 3test22. Note the black "rims" between the Ni and YSZ particles. The inset is a zoom on a Ni particle adjacent to the electrolyte. The red line in the inset shows where the EDS line scan in part B was made.

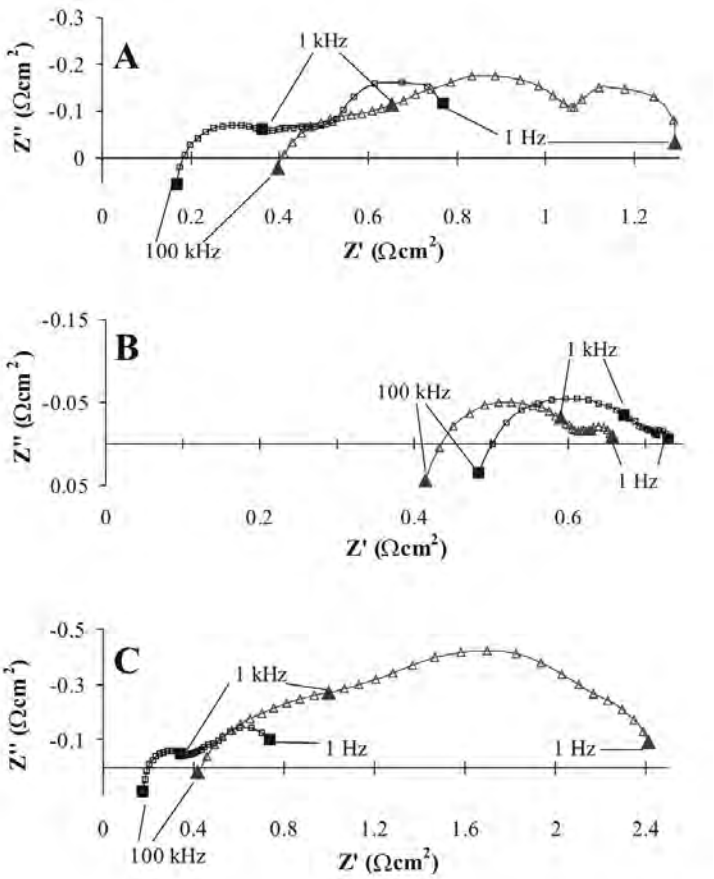

Figure 6-8: EIS recorded during 3test22. EIS marked by triangles are the last recorded EIS in each figure. Part A: During the first electrolysis test at t = 77 h and t = 380 h. Part B: During the first fuel cell test period at t = 561 h and t = 679 h. Part C: At OCV (850°C, 5% H_2O and 95% H_2 to the Ni/YSZ electrode) before the first electrolysis test period at t = 49 h and after the last electrolysis test period at t = 1514 h. See Table 6-4 for operation conditions for spectra recorded during electrolysis testing.

6.4. Discussion

The EIS results presented by Jensen [63; 91] verify that the observed passivation during electrolysis testing of these cells relates to processes in the Ni/YSZ electrode and the SEM/EDS analyses have therefore been focused on the Ni/YSZ-electrolyte interface. Si was found in the hydrogen electrode after test for both 3test24 and 3test22. In 3test24 the Si was shown to occur in an oxidized state. A few atomic % of sodium were detected in many of the Si-containing impurity particles. No Si was detected in two reference cells. This verifies that the accumulation of impurities at the hydrogen electrode/electrolyte interface is a result of the testing of the cell and not a result of the production method for the cells. Si-containing impurities have been found on half cells in set-ups with YSZ electrolyte pellets [78; 120]. In these cases it was believed that the Si-containing impurities segregated from

the Ni electrode and the YSZ electrolyte to the electrode/electrolyte interface. Long-term fuel cell testing of similar cells using the same test set-up as for the electrolysis testing has not led to Si segregation to the electrode/electrolyte interface to an extent that can be observed using EDS. In 3test24 the Si-containing impurities segregate to the triple phase boundary (TPB) at the electrode/electrolyte interface. In 3test22 the distribution of impurities is different from 3test24, and impurities tend to segregate to the two phase boundary (2PB) between the Ni and the YSZ. Several other electrolysis tested cells have been examined by SEM and EDS. For some of these cells it has not been possible to detect Si-containing impurities as those found in 3test24 and 3test22. The cells, for which no impurities were detected by SEM/EDS, where all tested at current densities of -0.5 A/cm^2 or below, and only the polarisation resistance and not the ohmic resistance increased during these electrolysis tests. The fact that no Si was detected by SEM/EDS for these cells does not necessarily mean that Si-containing impurities are absent at the electrolyte/electrode interface for these cells, but only that the amount of possible Si-impurities is below the detection limit of approximately 0.1 wt% for Si.

In general, SEM investigation of electrolysis tested cells shows that the microstructure of the Ni/YSZ have changed slightly when compared with a reference cell, but Ni/YSZ microstructures for heavily passivated (large cell polarisation) and only slightly passivated (small cell polarisation) electrolysis cells are alike (see chapter 5). On the other hand there is a relation between the degree of passivation during electrolysis testing and the findings of Si-containing impurities in the H_2 electrode of tested SOECs. An example of this is found by comparing the electrolysis test results (cell polarisation and EIS) with the SEM/EDS findings e.g. for 3test22 in this work and test C and D reported previously [61] which were all operated at 850°C and p(H_2O) = 0.7 atm but with current densities of -1 A/cm^2, -0.5 A/cm^2 and -0.25 A/cm^2, respectively. 3test22 was heavily passivated, test C was “medium” passivated and test D was only slightly passivated. They had similar Ni/YSZ microstructures. As shown here, a large amount of silica containing impurities was found in the Ni/YSZ electrode of 3test22, traces (close to the detection limit for EDS) of impurities were found in the Ni/YSZ electrode of test C, and no impurities were detected in the Ni/YSZ electrode of test D, i.e. the amount of impurities were below the detection limit for EDS. This combination of electrolysis test results and SEM/EDS investigations for electrolysis cells that were passivated to different degrees illustrates that if not solely, then at least the main reason for the passivation of the cells is the segregation of impurities in the hydrogen electrode of the SOECs.

6.4.1. Composition and properties of impurities

The chemical composition (Table 6-3) of the Si-containing particles in Figure 6-2 is typical for the analysis of impurity particles found close to the electrolyte/electrode interface for 3test24. Sodium and aluminium oxides are often found in small amounts in the Si-containing particles. The impurities detected at this interface are most likely a glassy phase. This is in good agreement with the TEM/EDS analysis results obtained by Liu and Jiao for the Si-glass found at the interface of a long-term tested Ni-YSZ(anode)/YSZ(electrolyte)

half cell [90]. In contrast to the work by Liu and Jiao, we have not been able to detect calcium oxide in the impurity particles in the electrolyte/electrode interface of 3test24.
Sodium is known to be a network modifier for silica glasses as it creates non-bridging oxygen atoms and thereby break up the silica network structure. At high temperatures the presence of Na_2O in the silica glass therefore decreases the viscosity of the glass compared with that of pure SiO_2 glass [121; 122]. The presence of alumina in a Si glass phase is known to increase the surface tension and the viscosity [123]. For this reason alumina has been suggested as a scavenger for SiO_2-impurities in YSZ [113]. To separate the effect of the Al_2O_3 found as an impurity in the raw materials and the Al_2O_3 added to the support layer as sintering aid, cells without additional alumina have been produced and will be tested as electrolysis cells. Not only sodium and alumina oxides influence the physical properties of silica glasses, also the H_2O content has a large effect on the viscosity of various silica glasses [122; 124-126]. The addition of only 0.12% H_2O to a SiO_2 glass has been shown to decrease the viscosity of the SiO_2 glass three orders of magnitude at 1000°C [122] and Shelby [126] reported that the viscosity of sodium trisilicate glasses decreases by factor of 9 at 440°C upon changing the water content from 110 ppm to 1850 ppm. 3test24 was operated at 850°C with a mixture of 0.9 atm H_2O and 0.1 atm H_2 to the hydrogen electrode throughout the first electrolysis test period, giving "water rich" conditions for the formation and segregation of Si glass phase impurities in the hydrogen electrode. For the longer electrolysis test periods the steam content was at least 66% for both tests. The glassy phase impurities therefore probably had very low viscosity at the electrolysis operation conditions. Liu et al. also reported a correlation between the water concentration profile and damages caused by the glassy phase [78].

6.4.2. Sources for the detected Si in tested cells

There are at least two obvious sources for the Si-containing impurities: 1) Impurities in the raw materials and 2) the glass sealing around the cell and gas distributors [61]. In the following a rough estimate of the total mass of Si in the cells coming from the raw materials is made. Since it has been reported that impurities such as Si, Na and Al from the bulk of YSZ can segregate to the grain boundaries, external surfaces and interfaces when annealed at 800-1500°C [127], the total amount and not only surfaces of the raw material used for the manufacture of one cell is applied in the calculation. With the cell dimensions and specifications given elsewhere for similar cells [61], the total mass of the electrolyte, the active hydrogen electrode and the support layer (before reduction) is approximately 3.6 g for one cell. According to the GDMS analysis of the raw materials (Table 6-1) this gives a maximum of ~0.1 mg SiO_2. As mentioned the Si-content at the electrolyte/electrode interface varies along the interface. Therefore adding up the SiO_2 content as shown in Figure 6-2, Figure 6-3 and Table 6-3 hardly give the correct total amount of impurity particles at the interface for the entire cell. However, if the SiO_2 content shown in the area of Figure 6-3 is used merely to give an estimate of the amount of SiO_2 in the cell used for 3test24, a SiO_2 content of 1.4 mg SiO_2 for the entire cell is found. The estimated values for the mass of SiO_2 from raw materials and from EDS results (Figure 6-3) indicates that only

a few percentages of the hydrogen electrode can be like the part shown in Figure 6-3. SEM work on different pieces of the tested cells does not support this. Therefore it is concluded that impurities in the raw materials are unlikely to be the only source for the detected Si-impurities in the tested cells.

The glass sealing surrounding the cell is another possible source for the Si-containing impurities. To clarify whether or not the albite ($NaAlSi_3O_8$) glass sealing can be expected to give a significant contribution of Si-species over the cell during testing, thermodynamic calculations were made using the FACTSAGE® software. As shown previously [128; 129] the main contributor to the vapour pressure of Si species is $Si(OH)_4$. At relevant conditions (950°C, 0.7 atm H_2O and 0.3 atm H_2) the vapour pressure of $Si(OH)_4$ over the albite glass is ~10^{-7} atm. For a 500 hour test a rough estimate for the upper limit for the Si contribution from the glass sealing is 3 mg SiO_2 at the chosen operation condition. For this estimate the calculated $p(Si(OH)_4)$ was used in combination with Ficks 1st law, a diffusion length through 1 mm of stagnant gas next to the glass sealing [10], the binary diffusion coefficient for water in water [10; 130] [13], and the geometry of the cell test set-up. The result of this estimate indicates that the vapour pressure of $Si(OH)_4$ over the glass sealing can be a source for the detected Si-containing impurities in the tested cells. The glass sealing is indeed a *possible* source for the impurities found in the Ni/YSZ electrodes but the experimental results presented here do not give the proof that the silica impurities do indeed origin from the glass sealing. Further tests for investigating the effect of the glass sealing on the passivation of the cells during electrolysis testing of similar cells are necessary and in progress. Visual inspection of the glass sealing after the tests show that especially the glass sealing at the steam inlet side of the set-up has become more porous as a result of testing.

If the origin of the main silicon source is $Si(OH)_4(g)$ from the sealing then the equilibrium:

$$Si(OH)_4(g) \rightleftharpoons SiO_2(l) + 2H_2O(g) \qquad (6\text{-}1)$$

will be forced towards the formation of glassy phase silica in the regions of the cell where the most steam is reduced to hydrogen, that is in the few microns of the hydrogen electrode closest to the electrolyte. This would lead to the highest silica content closest to the electrode/electrolyte interface. This is in agreement with the gradient for silica content found for the cell used for 3test24, where EDS results shown in Figure 6-3 led to ~8 w% SiO_2 in the electrode 0-2 μm from the electrolyte, ~4 w% SiO_2 for the electrode 2-4 μm from the electrolyte, and below the detection limit in a distance more than 4 μm from the electrolyte. In 3test22 (period 5, Figure 6-5) fuel cell operation of the cell led to 54 mV increase in the cell voltage corresponding to an activation of the cell. The ohmic resistance decreased 15% and the polarisation resistance decreased 20% (part B, Figure 6-8) during the 121 h of fuel cell mode operation of the cell. Similar reactivation by fuel cell operation of a cell passivated in electrolysis mode was observed for 3test24 (period 8 and 10, Figure

[13] The binary diffusion coefficient for H_2O in H_2O has been calculated and applied for the estimate of the flux of $Si(OH)_4$ from the glass sealing because the diffusion volume for $Si(OH)_4$ was not available.

6-1) and has been reported for other similar tests [61; 91]. These reactivation results combined with the lack of silica impurities in the Ni/YSZ electrodes of similar cells tested for hundreds of hours as fuel cells using the same type of test set-up [42], points towards that the fuel cell reactivation of the passivated electrolysis cells can be related to equilibrium (6-1). When the cells are used for oxidizing hydrogen, equilibrium (6-1) will be forced towards the formation of $Si(OH)_4$ and thereby evaporate some of the silica that hampers the reactions at the electrode/electrolyte interface. Another aspect to consider in relation to the activation of the cell used in 3test22 is phase changes for the impurities as gasses are changed to a drier H_2O/H_2 mixture. Leaving the cell for more than 500 h at OCV at $p(H_2O)/p(H_2) = 0.05/0.95$ (period 7, Figure 6-5) lead to 15% and 13% decrease in R_{ohmic} and R_p, respectively.

6.4.3. Passivation history for the tested cells

The passivation histories for 3test24 and 3test22 are more complex than for the simple tests of similar SOCs at constant electrolysis conditions as reported previously [61; 91]. The relative changes in both the ohmic and polarisation resistances for the two tests are comparable. The increase in the ohmic resistance was 115% and 139% for 3test24 and 3test22 respectively, and polarisation resistances increased 195% for 3test24 and 225% for 3test22. This is observed from the EIS recorded at OCV before and after the electrolysis testing of the two cells (part C in Figure 6-4 and Figure 6-8). The passivation histories for the two cells are very different. As illustrated (Figure 6-8), the EIS recorded during electrolysis testing shows that for 3test22 already the first electrolysis test period led to significant increases in both the polarisation and the ohmic resistance. Even though 2nd and 3rd electrolysis test periods were performed at a lower current density (-0.5 A/cm^2) both the polarisation resistance and the ohmic resistance kept increasing. The passivation history of 3test24 is somewhat reverse of that of 3test22. Here the first electrolysis test period is at a low current density (-0.5 A/cm^2), and only the polarisation resistance increases during this part of the test (Figure 6-4). During the last H_2O electrolysis operation at "harder" conditions (-1 A/cm^2) significant increases in both the polarisation and ohmic resistance are observed. The cell voltage increase during the short CO_2 electrolysis test period for 3test24 is approximately a factor of 10 lower than the total increase in cell voltage during the H_2O electrolysis test periods. The CO_2 electrolysis therefore hardly plays a key role in the overall passivation of the cell used for 3test24. The results from 3test24 cannot preclude the possibility of impurity segregation during CO_2 electrolysis but the impurity segregation in the Ni/YSZ electrode definitely occur during H_2O electrolysis as seen from 3test22 that was operated in a H_2O/H_2 atmosphere only. It is believed that these very different passivation histories for the two cells have led to the large differences in the microstructure of the impurities for the two cells. Even though there are large differences in the distribution, microstructure and amount of impurities found in these two cells and in other tested SOECs, there are some common trends for the tested cells: 1) Impurities have so far only been found in the hydrogen electrode. 2) The main constituent in the impurities is silica. 3)

The concentration of impurities is largest closest to the electrode/electrolyte interface and no impurities have been detected more than ~8 μm from the electrolyte.

In both tests presented in this chapter the polarisation resistance increased with time during electrolysis. This might be related to the segregation of Si-containing impurities to the TPB at the electrode/electrolyte interface. Even though a significant increase (especially compared with fuel cell testing of similar cells [42]) in the ohmic resistance was observed, it was not possible to detect delaminations between the electrolyte and the electrode or damages of the electrolyte. The contributions to the ohmic resistance (R_{ohmic}) can be written as:

$$R_{ohmic} = R_{ion,\ conduc.} + R_{e^-,\ conduc.} + R_{current\ constriction} \qquad (6\text{-}2)$$

The ionic and electronic conductivities for the materials used in these cells are well-known and at these operation temperatures the ion conductivity in the YSZ is ~0.1 S/cm which is approximately 3 orders of magnitude smaller than the electron conductivity of the electrode materials [1]. $R_{current\ constriction}$ include contributions from the resistance in the auxiliary layers of the cell test set-up i.e. gas distribution layers and current collector foils. It has been shown that the contributions from the auxiliary layers can be made insignificantly small using this test set-up [11] and using this test set-up it is possible to keep R_{ohmic} constant for 1500 h of fuel cell testing at 850°C [42]. We therefore believe that the observed increase in the ohmic resistance is strongly related to the segregation of Si-containing impurities to the Ni-YSZ interface and this leads to current constrictions for the current passage from the electrolyte to Ni/YSZ cermet electrode. Impurity containing rims between the Ni and YSZ with a shape similar to the ones in the cell from 3test22 (Figure 6-7) was found by Liu and Jiao in a tested SOFC half cell [90]. The rims were reported to consist of a sodium silicate glass phase, but they were thinner (10 nm) than those reported here (40-70 nm). The exact chemical composition and crystal structures of the impurity rims observed in the cell from 3test22 have been analyzed further by TEM of a thin lamella cut using the FIB (Focused Ion Beam) technique, similar to the work presented in chapter 7. Two TEM micrographs of impurities in the H_2 electrode of 3test22 are shown on the cover of this thesis.

The SEM and EDS results presented here provides the basis for the schematic presentation of the hydrogen electrode/electrolyte interfaces shown in Figure 6-9. The impurities in the sketch explain the reason for the observed electrode passivation and show the qualitative difference between the two tests. The Si segregation to the 2PB was only observed in 3test22 (Figure 6-7) and is probably caused by the higher cell voltage (cell polarisation) compared to 3test24. The increase in the ohmic resistance for 3test24 (Figure 6-4) might be caused by impurities that also cover the 2PB, since silica impurities have been shown to be present in significant amounts in the active layer of the Ni/YSZ electrode. The fact that impurities were not found in the 2PB by SEM/EDS investigation of 3test24 only means that they are below the detection limit for EDS at the SEM.

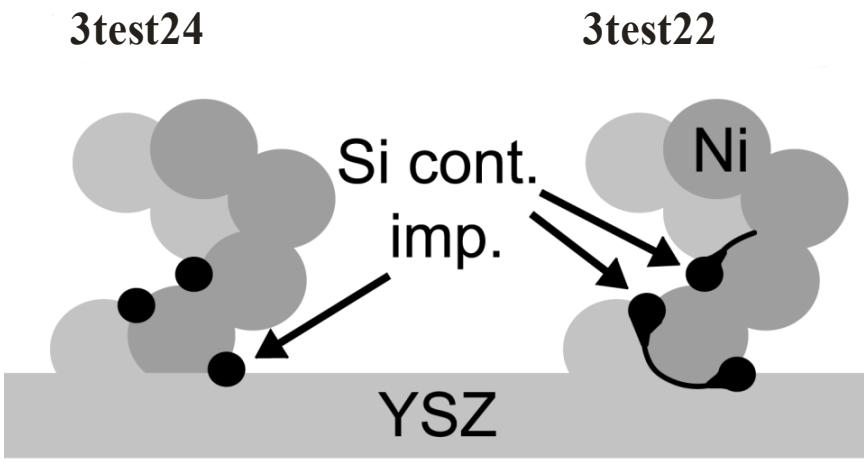

Figure 6-9: Schematic presentation of Si-containing impurities segregating to the hydrogen electrode/electrolyte interface during electrolysis as observed by SEM. In 3test24 the impurities tend to block the TPB. In 3test22 the impurities also segregate to the 2PB between the Ni and the YSZ. EIS results indicate that also the 2PB of 3test24 could contain impurities, but such impurities at the 2PB were not observed by SEM for 3test24.

6.5. Conclusion

SOECs used for high temperature steam electrolysis were found to passivate significantly within few days when operated at temperatures of 850-950°C, current densities from -0.5 to -1 A/cm^2 and partial pressures of steam from 0.3 to 0.9 atm. At low cell polarisation (3test24, 950°C, 90% H_2O and -0.5A/cm^2) only the polarisation resistance increased. At high cell polarisations/voltages both the polarisation resistance and the ohmic resistance increased.

A substantial amount of SiO_2 was detected in the Ni/YSZ electrode/electrolyte interface of the tested cells using EDS mapping whereas no Si was detected in two reference cells. For the test at the lowest cell voltage (3test24) the impurities had segregated to the triple phase boundary and were found by SEM/EDS as grains of impurities with diameters up to ~1 μm. For this test the innermost 2 μm of the electrode closest to the electrolyte contain the most silica and the Si-containing impurities are only detected within the innermost ~8 μm of this electrode. Point EDS results indicate that these impurity particles consist of a sodium silicate glass. For the test at the highest cell voltage (3test22) the impurities had segregated to the interface between the Ni and the YSZ particles where thin (40-70 nm) Si-containing rims had formed. A possible source for the detected silicon is the albite glass sealing used in the applied cell test set-up.

Impedance spectra recorded during testing reveals large differences in the passivation history for the two electrolysis tests presented here. The dissimilarities in the microstructure and amount of detected Si-containing impurities in the hydrogen electrode of the two tested cells are most likely related to the variation in the electrolysis operation conditions.

6.6. Acknowledgement

Thanks to senior scientist Karin Vels Hansen (Fuel Cells and Solid State Chemistry Department, Risø National Laboratory, Technical University of Denmark) for providing GDMS data for the raw materials.

7. Nanoscale chemical analysis and imaging of SOCs

7.1. Abstract

The demand for increased energy efficiency and decreased air pollution has accelerated the development of solid oxide cells (SOC) as an attractive energy conversion technology. The performance of SOCs is highly dependent on the nanostructure of the electrodes, especially at the triple-phase-boundaries (TPB) where the electrochemical reactions occur. Therefore detailed TPB characterisation of tested SOCs is crucial for their further development.

Here we demonstrate that it is possible to prepare a ~54 nm thin TEM lamella of the interface between the dense electrolyte and the porous mixed metallic/ceramic hydrogen electrode of an SOC using a focused ion beam (FIB). We show for the first time results from combined TEM/STEM/EDS investigations of the nanostructure at the TPB in a real, high performance SOC. The chemical composition of the nanoscale impurity phases that block the TPB in the H_2 electrode has been obtained with ~1 nm lateral resolution[14].

7.2. Introduction

Solid oxide cells are a promising and rapidly developing energy conversion technology due to factors such as high energy efficiency and reduced emission of CO_2 and NO_x [1]. SOCs can be operated both as solid oxide fuel cells (SOFC) to produce electrical energy and as solid oxide electrolysis cells (SOEC) to produce fuels such as H_2 or synthesis gas (H_2+CO). For SOCs to become a commercially mature technology it is necessary to produce low cost cells, with high reproducibility, high performance and long-term stability. Several studies [1; 2; 32; 131] of state-of-the-art SOCs have shown that the cell performance decreases with operation over hundreds of hours. A key parameter for the performance of the SOCs is the triple phase boundary (TPB) in the electrodes where the electrochemical reactions occur. At the TPB in, e.g. the H_2 electrode, an oxygen ion conducting particle (e.g. yttria-stabilised-zirconia, YSZ) is bordered by a catalytically active and electron conducting particle (e.g. Ni) and a pore through which the gasses can enter and leave the porous electrode structure [132]. A schematic illustration of a catalytically active TPB available for the electrode reaction in the H_2 electrode of a solid oxide fuel cell is shown to the left in Figure 7-1 and a catalytically inactive TPB blocked by the creation of an impurity phase is shown to the right. A simplified scheme for the reaction in an SOC hydrogen electrode is:

$$H_2(gas, pores) + O^{2-}(YSZ) \underset{SOEC}{\overset{SOFC}{\rightleftharpoons}} 2e^-(Ni) + H_2O(gas, pores) \qquad (7\text{-}1)$$

[14] This chapter has been submitted to *Electrochemical and Solid State Letters* as "Nanoscale chemical analysis and imaging of SOCs", Hauch, A, Bowen, J. R., Theil Kuhn, L. and Mogensen, M.. The structure of the chapter therefore varies slightly from the previous chapters. Supplementary information is found at the end of the chapter.

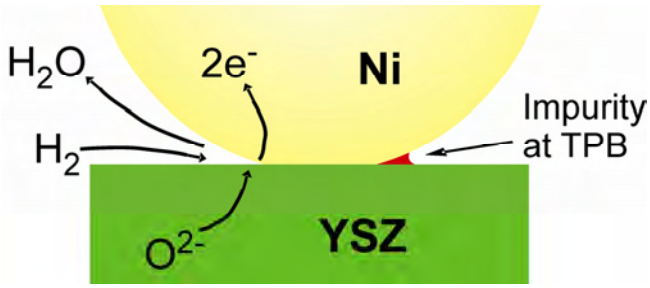

Figure 7-1: A schematic illustration of TPBs in a SOC H_2 electrode. A TPB accessible for the electrochemical reaction (left) and a TPB blocked by and impurity phase (right). A typical diameter for the Ni particles is ~1 µm.

Consequently, a decrease of the density of unblocked TPBs in an electrode structure will lead to an increase in the resistance of the cell and therefore a decrease in the cell performance. Initial results on a quantification of the TPB in an SOFC H_2 electrodes was reported by Wilson et al. [133] and for similar ceramic materials by Holzer et al. [134] by 3D reconstruction of the nanostructures using combined FIB/SEM, and others have reported on the effect of the TPB in the electrode nanostructure on the performance of the cell [131; 135; 136].

A loss of TPB may be caused by Ni coarsening and/or segregated impurities blocking the TPB. Studies of model systems and half cells have shown that the degree of impurities in the raw materials greatly influences the performance of a cell and the degree of passivation [78; 89; 90; 137], and it has been shown for model systems that impurities tend to segregate to and agglomerate at the TPB [127; 138; 139]. Therefore, a detailed characterisation of the interfacial structure on the nanometer scale and chemical analyses of the TPB in the SOC electrodes are necessary to understand - and in turn overcome - the observed loss in performance for the SOCs. This will be a crucial step towards development of high performing, long-term stable SOCs. Previously only few TEM studies of electrodes of full and half cells have been reported [140-143], but particularly interface TEM studies have been very limited due to difficulties in specimen preparation.

7.3. Experimental

The FEG-SEM imaging and FIB milling was performed on a Zeiss Crossbeam 1540X. The microscope is equipped with a field-emission electron gun and the ion Ga^+ gun was operated at 30 keV. Platinum was used as the protective layer on the sample surface prior to FIB milling and tungsten was used to attach the lamella to the TEM Cu Omniprobe holder prior to final polishing.

A JEM-3000F field-emission gun TEM/STEM microscope equipped with a Gatan imaging filter was used to perform the TEM, STEM and EELS analysis. In STEM mode a high angular annular dark-field detector was used and the beam diameter was 0.2 nm. The EDS

microanalysis system Oxford Instruments INCA was used for collecting energy dispersive X-ray spectra. The spectra were acquired with an acquisition time of 60 s and the EDS map in Figure 7-5 was acquired within 30 minutes. The quantification of the EDS was obtained by standardless analysis using the Cliff-Lorimer correction with absorbance. The calculations were made using the Thermo Fisher NoranSystemSix software version 1.5.
The TEM/STEM analysis was obtained at Lund University, Faculty of Engineering.

7.4. Results and discussion

To obtain such nanoscale characterisation of the TPBs we have used a combination of TEM, scanning transmission electron microscopy (STEM) and chemical analysis by EDS as these are advantageous analytical tools. The use of combined FIB and field-emission gun SEM (FEG-SEM) for preparation of TEM samples is advantageous as it allows TEM specimen preparation from site specific locations with submicron precision and furthermore, the heterogeneous and highly porous electrode structure can be uniformly thinned. To the best of our knowledge this paper is the first characterisation with a ~1 nm resolution of TPBs in an electrode of a high performing real SOC using a combination of FIB, TEM, STEM and EDS.
The hydrogen electrode supported SOC for the TEM/STEM/EDS study presented here was produced at Risø National Laboratory. This type of cell has shown excellent initial performance [61; 70]. Details on cell materials, electrode structure, test set-up etc. is described elsewhere [61]. The SOC was subjected to a galvanostatic 1300 h electrolysis test and was operated at 850 °C, a current density of -0.5 A/cm^2, with a gas mixture of $p(H_2)$ = 0.5 atm and $p(H_2O)$ = 0.5 atm supplied to the hydrogen electrode. The cell test results showed a decrease in the performance of the cell of 2% per 1000 h. This was largely caused by an increase in the polarisation resistance related to processes in the hydrogen electrode as reported elsewhere [63]. Based upon these cell test results, systematic investigation of the interface between the hydrogen electrode, which is a porous (~30%) Ni/YSZ cermet, and the dense oxygen ion conducting electrolyte made of YSZ was performed.
Firstly, a cell fragment with an H_2 electrode/electrolyte interface length of ~1 cm was investigated by FEG-SEM to confirm that the electrode nanostructure of the interface was representative over larger regions. Secondly, a combined FIB and FEG-SEM equipped with an energy dispersive X-ray spectrometer (EDS) was used to record X-ray spectra in different regions of the interface in order to select a representative interfacial area for FIB milling, including at least one impurity phase in the cross section of the sample (see Supplementary Information, S1). After deposition of a 3 μm protective layer of platinum at the area of interest, the dual-beam FIB was used to cut the lamella. The lift-out technique [144] was used to transfer the ~500 nm thick sample from the bulk of the SOC and attach it to a TEM holder for final thinning. Even though the H_2 electrode is highly porous and consists of materials of different hardness (Ni and YSZ), it was possible to thin a lamella of homogenous thickness suitable for TEM investigations. Figure 7-2 shows the lamella after final polishing prior to TEM investigation. A black line is added in Figure 7-2 to indicate the border between the protective Pt layer and the electrode. The lamella has an

electrode/electrolyte interface length of ~17 µm, which is marked by a white line in Figure 7-2. The thinned region of the electrode is ~275 µm^2, which provided us with a lamella including numerous TPBs. The lamella was thinned until significant 10 keV electron transparency in the SEM was obtained, as can be observed in Figure 7-2. For stability reasons the final milling was omitted for a ~2 µm bar of material parallel to the electrode/electrolyte interface in the middle of the electrode. The thickness of the lamella was measured to be ~60 nm in the thinned regions by imaging in the FEG-SEM and this was confirmed by electron energy loss spectroscopy (EELS) performed in the TEM (see Supplementary Information, S2). TEM imaging of the lamella indicated thickness variations across the lamella; nevertheless it contained several regions suitable for high resolution TEM. Examples of high resolution TEM is given in Supplementary Information, S3.

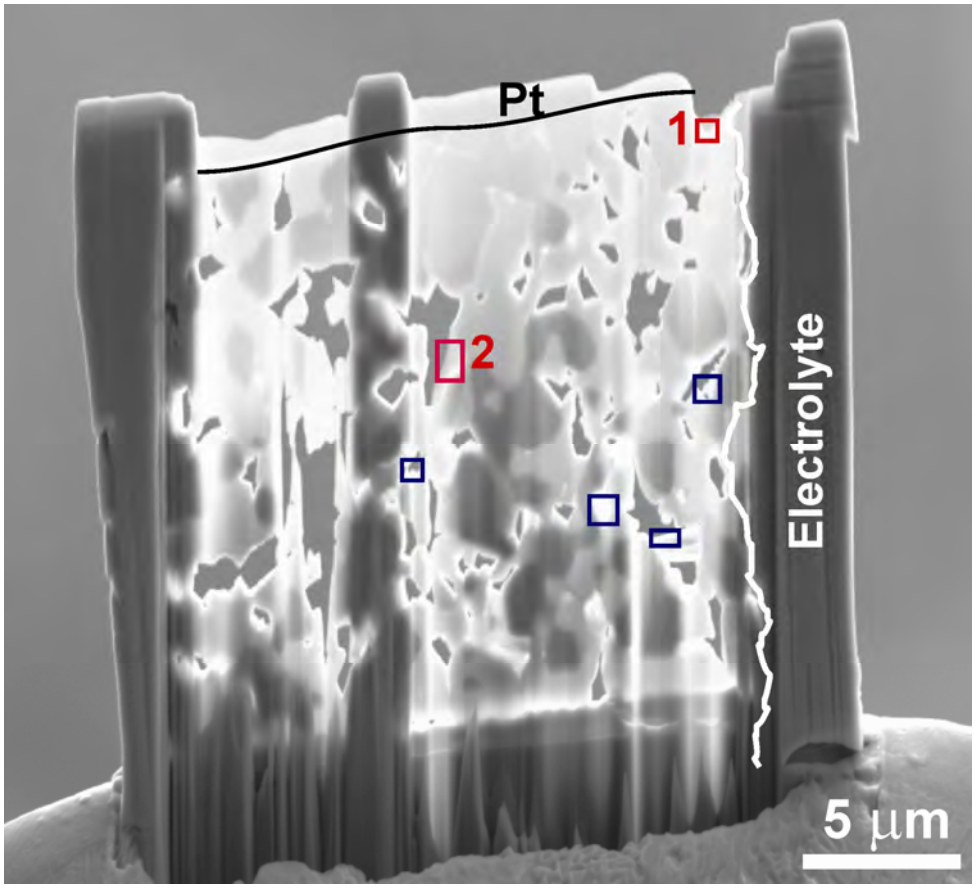

Figure 7-2: SEM micrograph of the TEM lamella obtained by FIB milling and lift-out technique for the H_2 electrode/electrolyte interface. TEM and STEM micrograph of the region marked by the red square (1) is shown in Figure 7-3. EDS mapping of the region marked by red rectangle (2) is shown in Figure 7-5. The blue rectangles mark regions where further impurity phases have been found.

Impurities containing oxides of Si, Al and occasionally Na were found at six different locations in the lamella and are marked by rectangles in Figure 7-2. All six impurity phases were found at locations in the electrode nanostructure that were TPBs prior to contamination with the impurity phase.

A typical example of a Si and Al oxide containing impurity phase at a TPB is shown in the bright field TEM micrograph in Figure 7-3a and its position in the lamellae is shown by the red square marked 1 in Figure 7-2. The alumina phase in Figure 7-3a most likely originates from the addition of Al_2O_3 as sintering aid during production of the cells. The glassy impurity phase surrounding the alumina particle is spread out along the original TPB where the oxygen ion conducting YSZ particle adjacent to the electrolyte and the electron conductive and catalytically active Ni particle meet. In this impurity phase FIB artefacts in form of re-deposited Ni was observed as crystalline particles with a diameter of a few nanometres (see Supplementary Information, S4) and similarly re-deposited material (Ni and Zr) was found at the interface of some of the Ni and YSZ particles in this lamella (see Supplementary Information, S5). A maximum of three metal atom percent of Ga from the FIB preparation of the sample was detected in some regions of the lamella.

A STEM micrograph using a high angular annular dark field detector (HAADF) of the same area as the TEM micrograph in Figure 7-3a is shown in Figure 7-3b. STEM mode has the following advantages when investigating the TPB in the hydrogen electrode: 1) The atomic contrast obtained using the HAADF detector facilitates the discrimination of impurity phases and thin films of re-deposited material at borders of the Ni and YSZ particles directly as the impurity phases consist of light elements, 2) the STEM beam is less harmful than a convergent TEM beam to the sample, e.g., when recording EDS and 3) the beam diameter is only 0.2 nm, thus providing a high lateral EDS resolution in STEM mode. The beam damage effect of recording energy dispersive X-ray spectra in TEM mode using a focused electron beam is seen in Figure 7-3b, where the beam has perforated the thin impurity phase; this is observed as a black spot in the centre of the impurity phase in the STEM micrograph. In STEM mode EDS was obtained for selected areas of the impurity phase and the Al/Si ratio was found to be 35/44 with a relative uncertainty of ~10% (see Supplementary Information, S6). Elements such as Na, Ca and V that are typically found in glassy impurities were not detected in this impurity phase.

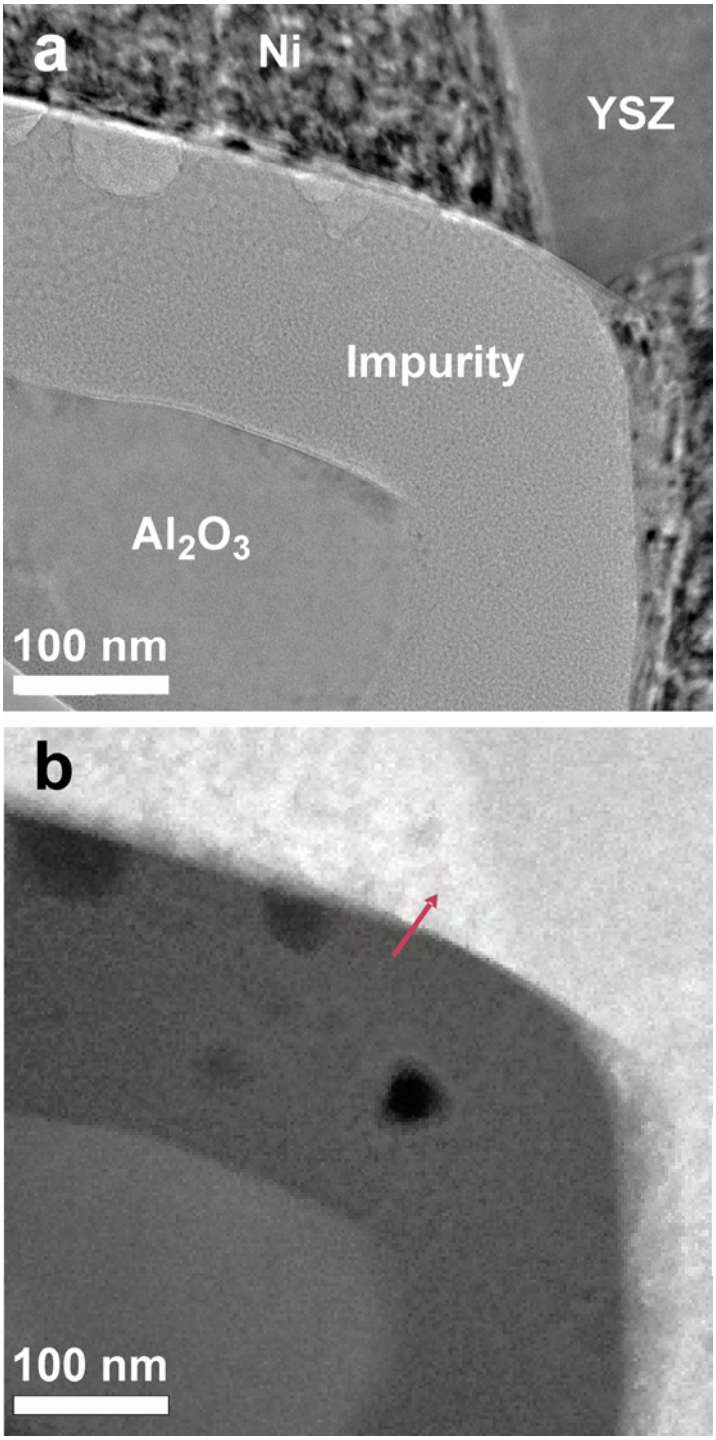

Figure 7-3: Bright field TEM micrograph (a) and HAADF STEM micrograph (b) of the impurity marked by the red square (1) in Figure 7-2. The arrow marks the position for the line scan from which results are given in Figure 7-4.

The arrow in Figure 7-3b marks the position for the EDS line scan from which results are shown in Figure 7-4. This line scan was performed in STEM mode with a beam diameter of only 0.2 nm. The thickness of the lamella in this region is estimated to be ~54 nm by electron energy loss spectroscopy using an average density of ~3 g/cm^3 for this phase, and a beam spread of ~1 nm was calculated for this region (see Supplementary Information, S7). This therefore provides chemical compositions of the imaged impurities with a sub-nanometre lateral resolution. From the EDS line scan results it is observed that there is a marked composition difference between the impurity phase and the Ni particle. The Si and Al oxide impurity phase is delineated by a distinct phase boundary without a diffusion gradient into the Ni particle. This was further confirmed by EDS in a selected area where "Ni" is written in Figure 7-3a. In this area, the only element detected was Ni (and background Cu). From Figure 7-4 it is also observed that the chemical composition, as evident from the Al/Si ratio, of the impurity phase varies greatly over a 30 nm range up to the phase interface. This difference in the Al/Si ratio observed from the line scan in Figure 7-4, has also been observed in other impurity phases in this lamella. Based upon the observed heterogeneity of the impurity phase it is assumed that nanocrystalline particles exist in the amorphous glassy phase impurity.

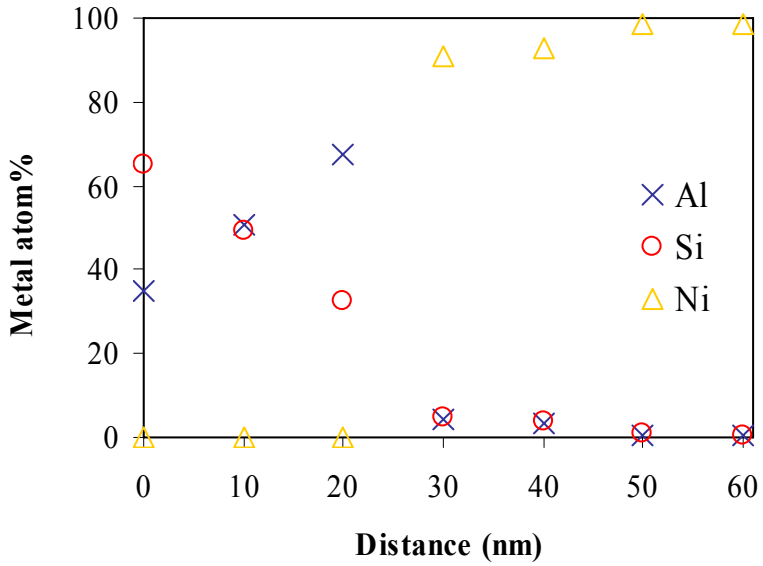

Figure 7-4: The metal atom percentages of Ni, Al and Si over the interface marked by the arrow in Figure 7-3b. The relative uncertainty for the metal atom percentages is ~10%. The applied beam diameter was 0.2 nm. Cu and re-deposited Ni has been omitted in the calculations (see details in Supplementary Information, S4).

Besides impurities of Si and Al oxides three of the six detected impurities in this TEM lamella also contained Na. One of these Na containing impurities at a TPB is shown by the EDS map given in Figure 7-5. A TEM micrograph of this region is supplied in Supplementary Information, S8. The chemical composition of the silicon containing impurity phase was found by standardless analysis and Cliff-Lorimer correction and the numbers are given below the EDS map in Figure 7-5. The atom ratio Na/Al/Si ~ 1/3/3 found for the impurity phase in Figure 7-5 is representative for the three Na containing impurity phases found in this TEM lamella.

Furthermore, the EDS mapping in Figure 7-5 illustrates how a site that, presumably, originally was a TPB (marked by the arrow in Figure 7-5) is now completely blocked by an impurity phase. The impurity phase seems to have started to build-up at the exact position of the TPB and grown to cover several hundred nanometres in the vicinity of the TPB and hereby block or at least significantly hamper the electrochemical reaction (eq. 7-1). This observation of impurities that build-up at the TPB is in agreement with model studies of impurity growth at the interface between a Ni wire and a YSZ electrolyte pellet [138] and confirms the results from electrochemical impedance spectroscopy characterisation of this cell during testing.

7.5. Conclusion

From the results presented here and supported by the Supplementary Information the following can be concluded that combining the following three techniques: 1) in-situ site specific FIB preparation of large area TEM lamella of the electrode/electrolyte interface, 2) TEM/STEM imaging of the TPB and 3) EDS for nanoscale chemical analysis of impurities and interfaces; we are able to obtain detailed information on the impurity phases accumulated at the TPB of an SOC H_2 electrode/electrolyte interface. Regarding both the lateral resolution of the analysis of the chemical composition and the structure, the information is obtained on the nanometer scale. Six impurity phases were found in the 275 μm^2 electrode area of the lamella. They all contained Al and Si oxides and three of them also contained sodium oxide. The ratio Na/Al/Si was approximately 1/3/3.

The present work therefore finally brings the evidence that Si-containing impurities build up in the H_2 electrode nanostructure at the TPB and thereby hamper the electrochemical reactions for initially high performing SOCs. Now having developed the necessary characterisation tools, it brings the possibility of finding mechanisms to hinder/limit the segregation of impurity phases to the TPBs of the SOC electrodes. Many ideas have been proposed regarding impurities in SOCs, but until now it has not been possible to actually observe the size and chemical composition of the impurity phases in the TPBs of tested SOCs. FIB/TEM/STEM/EDS investigations as presented here of the TPB of SOC electrodes will clearly be a key method to reach an understanding of the loss in performance of SOCs. This in turn is thereby expected to be a critical step in the development of SOCs from a promising energy technology to a market efficient technology.

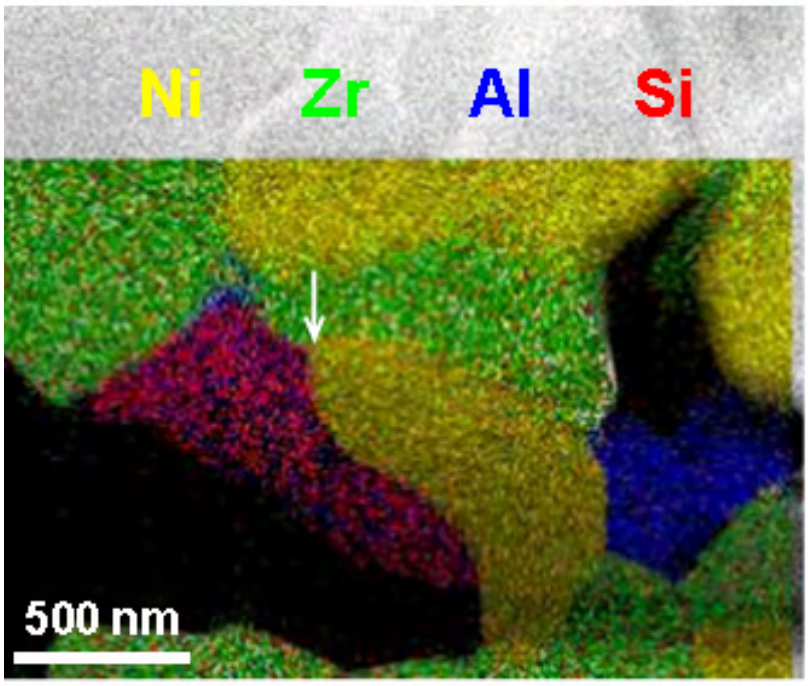

Element	Na	Al	Si	Ni	Cu	Zr
Metal atom%	13±2	36±2	41±3	2±1	7±1	1±1

Figure 7-5: EDS map of alumina-silicate impurity at a TPB. The area for this EDS map is marked by the red rectangle marked 2 in Figure 7-2. The arrow marks the TPB. The impurity phase is a Na containing alumina-silicate. Na is not visible in the map when both the Si and Al maps are overlaid, however Na is solely located within the alumina-silicate phase. Metal atom percentages for the alumina-silicate impurity phase are given below the EDS map. Dark regions are porosities.

7.6. Acknowledgement

We would like to acknowledge Dr. Jakob Wagner at Lund University, Faculty of Engineering for TEM assistance. This work was supported by the EC via the project "Hi2H2" contract no. FP6-503765 and Energinet.dk via project PSO2007-1-7124.

7.7. Supplementary information

The supplementary information below supports the result presented above.

S1: SEM and EDS prior to FIB milling to select area of interest

After thorough FEG-SEM and EDS investigation of ~1 cm of the H_2 electrode/electrolyte interface, the area of interest for the FIB cutting of a TEM lamella was located. This area of interest is shown in Figure 7-6. An impurity phase was found by EDS (Figure 7-6b) at the electrode/electrolyte interface (Figure 7-6a). After depositing a 2x30 μm and 3 μm thick protective Pt layer (Figure 7-6c), the FIB cutting of a TEM lamella at the area of interest was started (Figure 7-6d).

S2: Thickness of the lamella measured by electron energy loss spectroscopy (EELS)

Thickness measurement using EELS was performed in two regions of the lamella. The impurity phase marked by the blue retangle closest to the electrode/electrolyte interface shown in Figure 7-2 was subjected to EELS and the resulting electron energy loss spectrum is shown in Figure 7-7 together with a TEM micrograph of this area. From the ratio of the zero-loss peak intensity and the total intensity in the spectrum the thickness was calculated to be 54 nm using Digital Micrograph (convergence semi-angle = 30 mrad, collection semi-angle = 1.0 mrad, and Z-effective = 15).

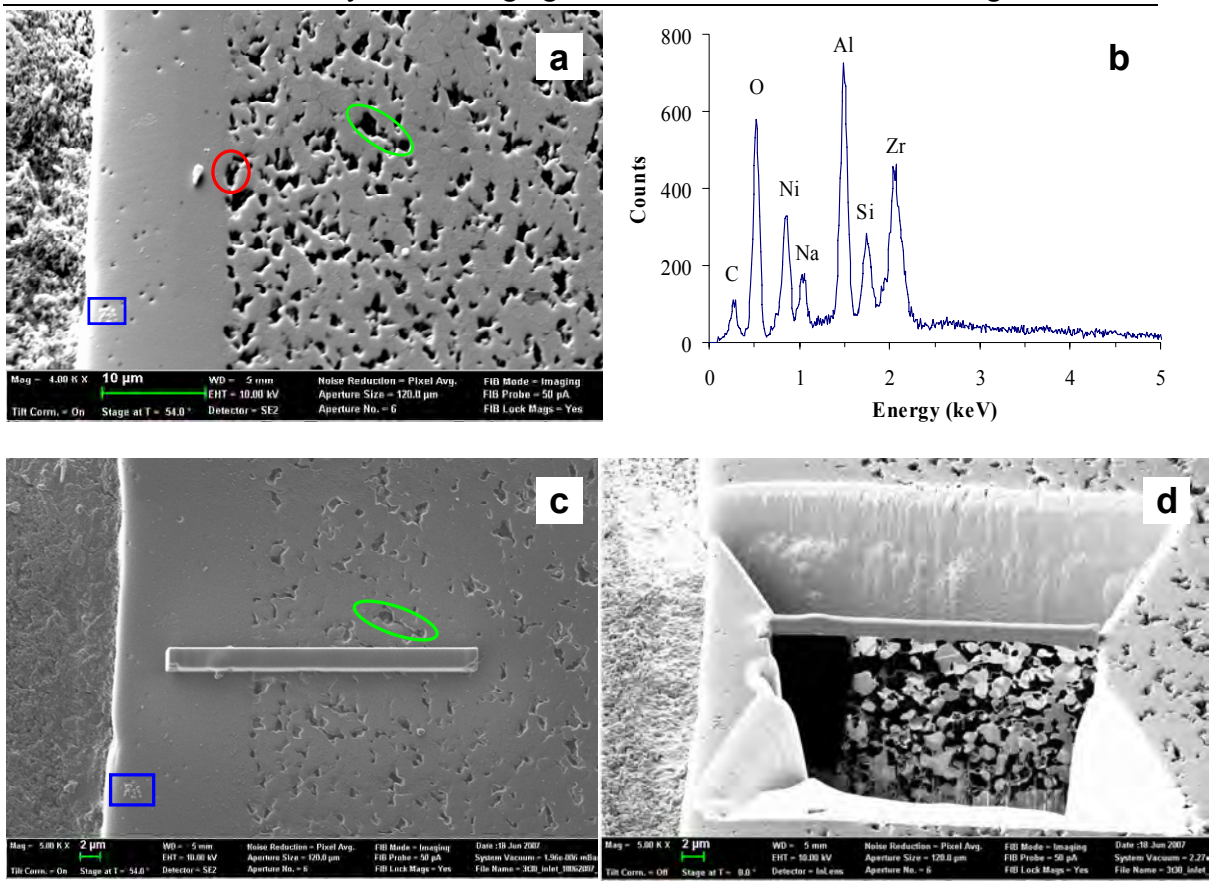

Figure 7-6: Area of interest for the TEM lift-out. a) SEM micrograph of the area of interest. The red circle is the spot for the point EDS in part b. b) Point EDS of impurity at the H_2 electrode/electrolyte interface. c) Area of interest after depositing of the Pt protective layer. The green and blue markings are the same spots as marked in part A. d) FIB milling started at the area of interest.

S3: Example of high resolution TEM micrograph

Two examples of high resolution TEM micrographs are given in Figure 7-8. Both micrographs are from the region shown in Figure 7-3. In A the lattice fringes in the alumina particle (left) are observed while the impurity phase (right) appears amorphous with crystalline "islands" of a few nanometres (see S4). In B the lattice fringes in the Ni particle (right) are clearly visible, as well as a distinct interface between the Ni particle and the impurity phase to the left.

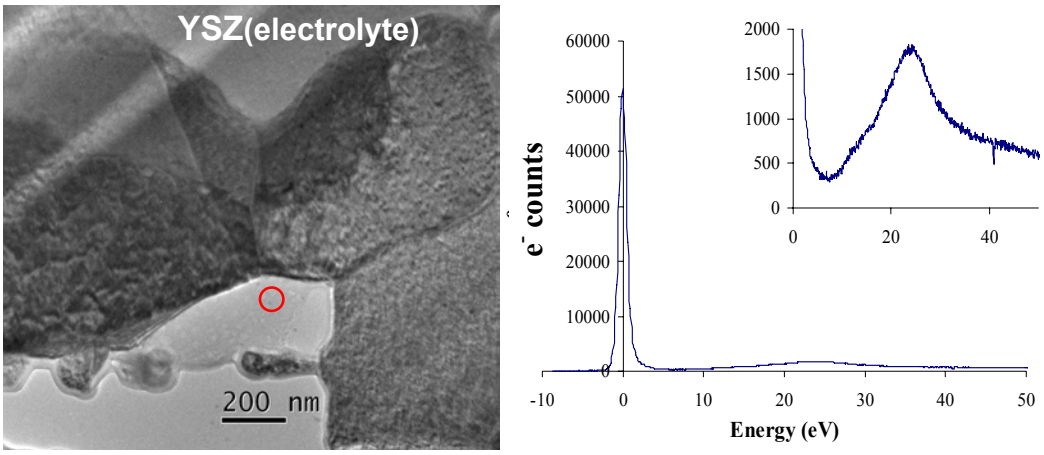

Figure 7-7: TEM micrograph of the impurity phase marked by the blue square closest to the electrolyte in Figure 7-2 and EELS obtained in the region marked by the circle in the micrograph.

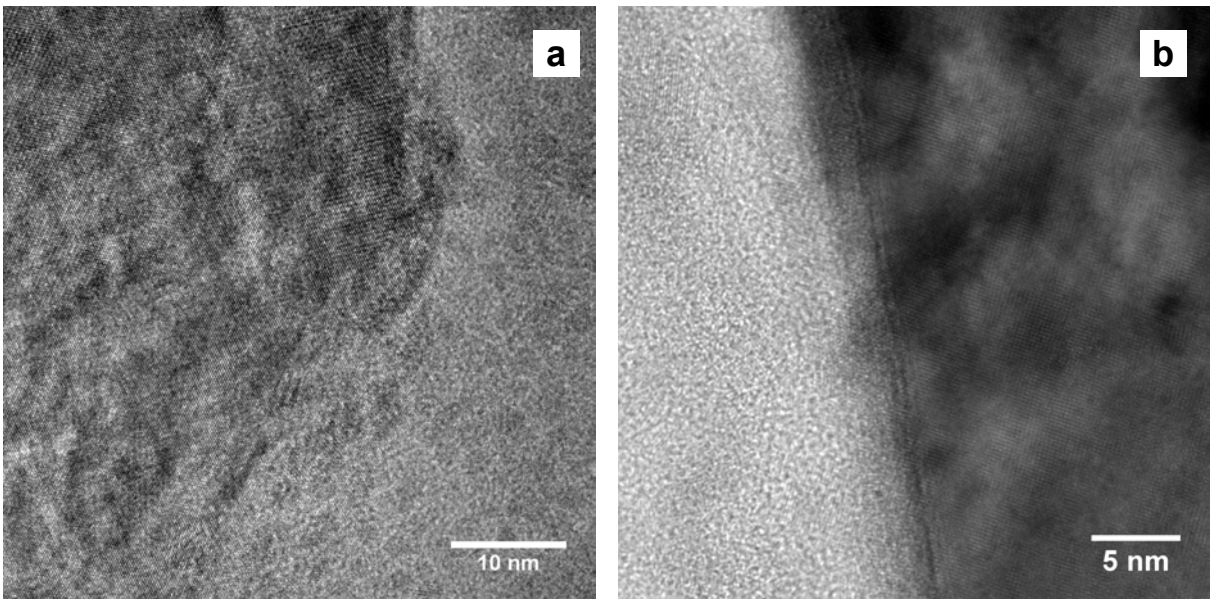

Figure 7-8: High resolution bright field TEM micrographs. a) The interface between the alumina particle to the left and the impurity phase to the right which is shown at lower magnification in Figure 7-3. b) The interface between the impurity phase shown in Figure 7-3 and the Ni particle.

S4: Re-deposited Ni in the impurity phase.

In the impurity phase shown in Figure 7-3 there are crystalline "islands" with a diameter of a few nanometer. A HAADF STEM (a) and bright field TEM (b) micrograph of this is shown in Figure 7-9. The crystalline "islands" appear bright in the HAADF STEM micrograph. These nanometer sized particles are Ni particles. This has been determined by point EDS in STEM mode. An EDS spectrum obtained on one of these crystalline particles is shown in Figure 7-10 (blue line) together with a spectrum recorded adjacent to it but in the amorphous impurity phase (red line). Clearly the spectrum (blue) obtained from one of the crystalline "islands" is enriched in Ni compared to the spectrum (red) obtained from the amorphous film. Three such pairs of spectra have been recorded and all illustrated that spectra obtained from the crystalline islands in the impurity phase were enriched with Ni as seen in the spectra in Figure 7-10. These nano-sized Ni particles are caused by re-deposition of material during FIB preparation of the TEM lamella. The nano-sized Ni particles cannot originate from the production of the cells as they would have agglomerated and grown to significantly larger Ni particles during sintering and subsequent testing of the SOC [108].

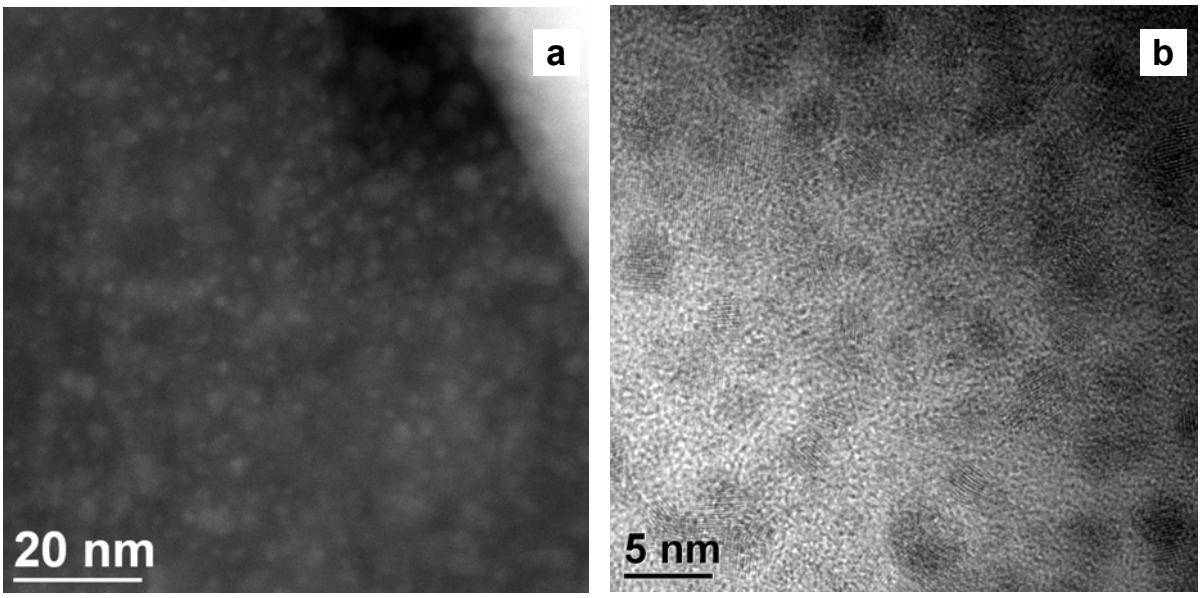

Figure 7-9: HAADF STEM micrograph (a) and bright field TEM micrograph (b) of crystalline "islands" on the impurity phase shown in Figure 7-3.

For the Ni K-line a count of 282±31 was obtained for the blue spectrum in Figure 7-10. For the three spectra recorded in the impurity phase as a part of the linescan shown in Figure 7-4 a maximum of 285 counts were obtained for Ni K-line. A count for the Ni K-line of 282 has been subtracted the first three spectra constituting the linescan for which the graph is shown in Figure 7-4, as the observed Ni counts in these spectra are not a part of the impurity phase but caused by re-deposited Ni from the FIB preparation of the lamella.

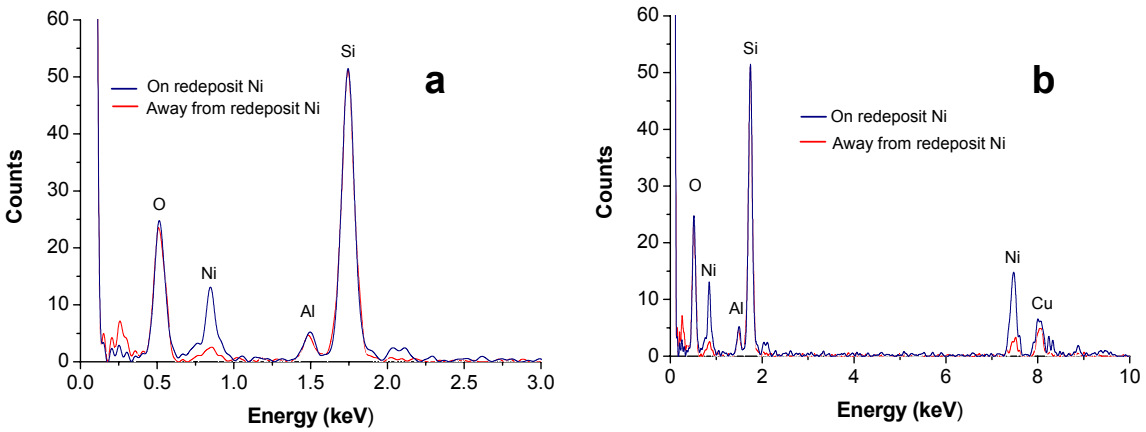

Figure 7-10: Energy dispersive X-ray spectra obtained on (blue) and away (red) from redeposit Ni on the impurity phase shown in Figure 7-3. a) Low-energy range of the spectra and b) the entire spectra.

S5: Redeposited material at the border of Ni and YSZ particles

Redeposited material has been observed in several regions of the TEM lamella. An example of redeposited material at the border of a Ni and YSZ particle is shown in TEM micrograph in Figure 7-11 together with EDS results from the Ni and YSZ particles and from the redeposited material at the border of these two particles. The area shown in Figure 7-11 is marked by the blue square closest to the electrolyte in Figure 7-2.

Note the differences in counts between the spectra obtained in the regions of redeposited material compared to the Ni and YSZ particles that are a part of the electrode structure. Furthermore, the regions of re-deposited material include both Ni and Zr. Cu is a background signal. The re-deposited material seems to be a thin film compared to the Ni and YSZ particles of the electrode.

S6: Average Al/Si ratio in the impurity phase in Figure 7-3 – EDS in STEM mode

The average Al/Si ratio in the impurity phase shown in Figure 7-3 was found by recording EDS in STEM mode over selected areas of the impurity phase. An example of such "area" EDS is shown in Figure 7-12 together with a TEM micrograph in which the selected area is marked by a red square.

S7: Estimated electron beam spread

For a thin specimen the beam spread can be estimated from [79]: $B=0.198\cdot(Z/E)\cdot(\rho/A)^{0.5}\cdot t^{1.5}$, where Z is the atomic number, A is the atomic weight, E is the electron energy (keV), ρ is the density of the specimen (g/cm^3) and t is the thickness (nm). Assuming that the impurity phase is a mixture of Al_2O_3 and SiO_2 then the average atomic number is 10, the average atomic weight is 20 and the average density is 2.75 g/cm^3. Applying the measured thickness of 54 nm (see S2) and the electron energy of 300 keV, a beam spread of 1.0 nm is obtained.

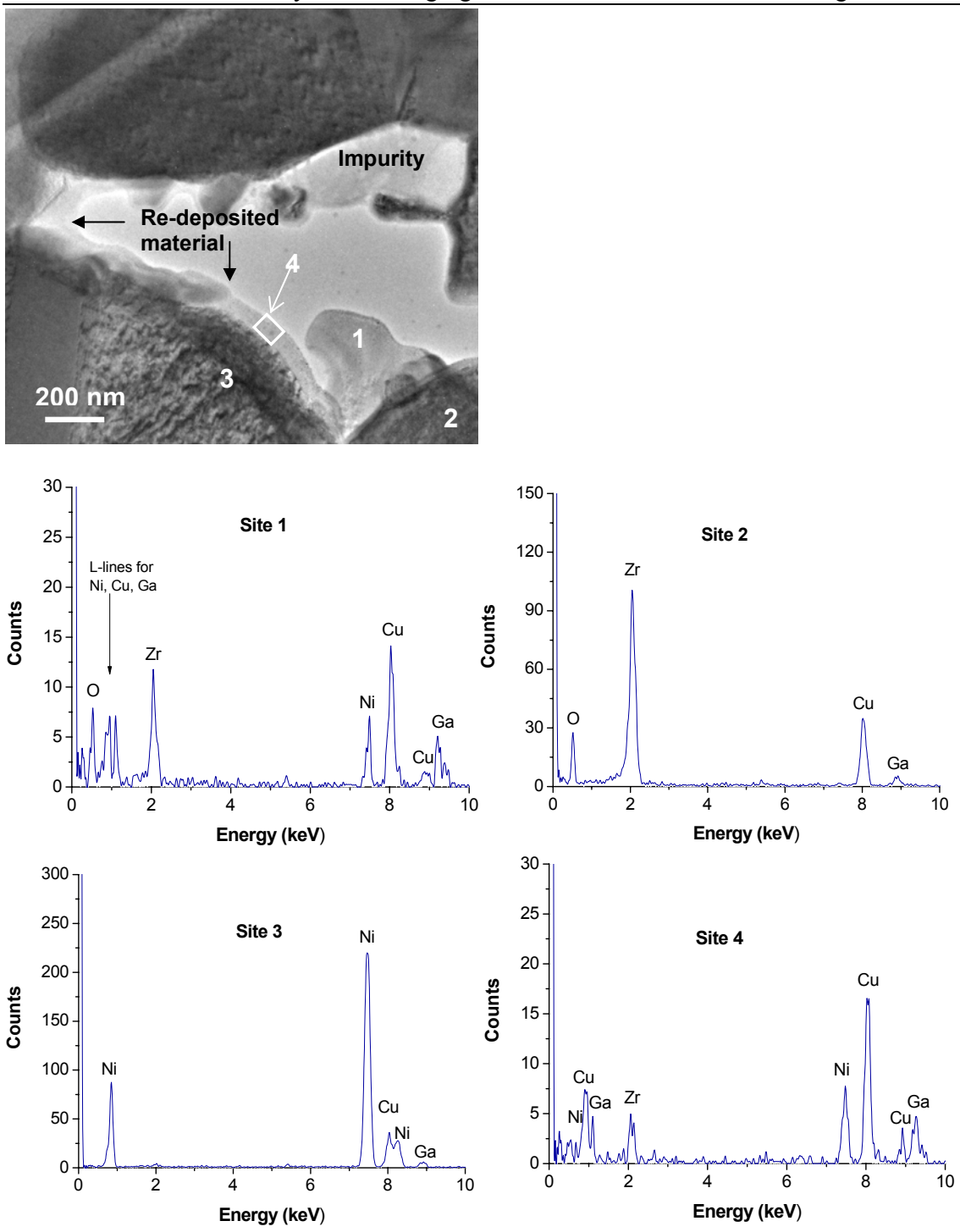

Figure 7-11: TEM micrograph of re-deposited material close to the impurity phase marked by the blue square closest to the electrolyte in Figure 7-2. The numbers in the TEM micrograph correspond to the numbers in the energy dispersive spectra, which were all recorded as "selected areas" in STEM mode with an acquisition time of 60 s for each spectrum. Site 1 and 4 are areas with re-deposited material.

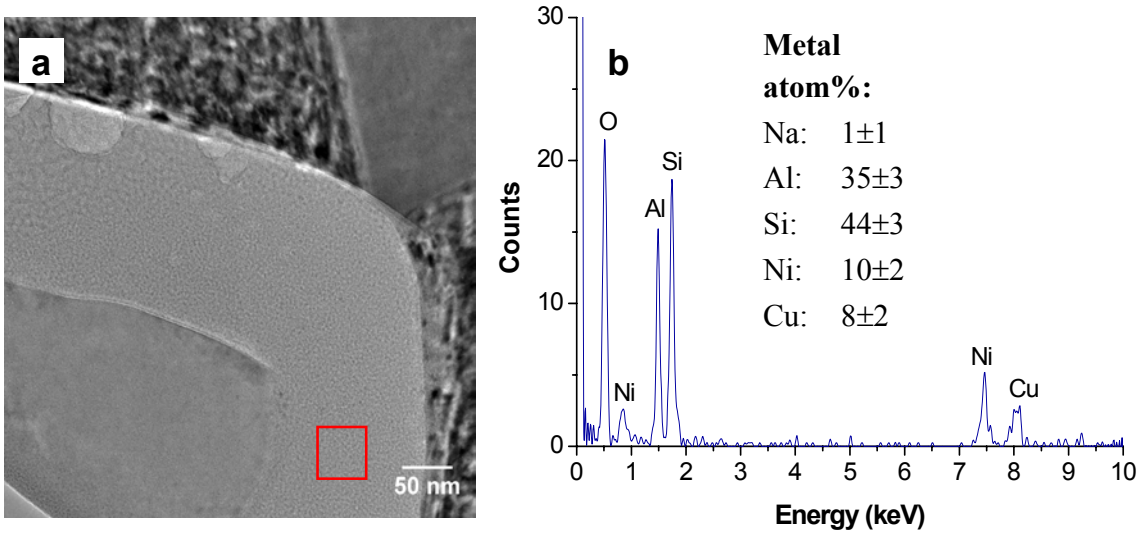

Figure 7-12: a) Bright field TEM micrograph of the impurity phase shown in Figure 7-3. The red square marks the selected area in which an energy dispersive X-ray spectrum was recorded in STEM mode. b) The spectrum obtained in the selected area of the impurity phase and the metal atom percentages obtained by standardless analysis using a Cliff-Lorimer correction.

S8: TEM micrograph of area for the EDS mapping in Figure 7-5.

A HAADF STEM micrograph and bright field TEM micrograph of the area for the EDS mapping in Figure 7-5 is given in Figure 7-13A and B, respectively.

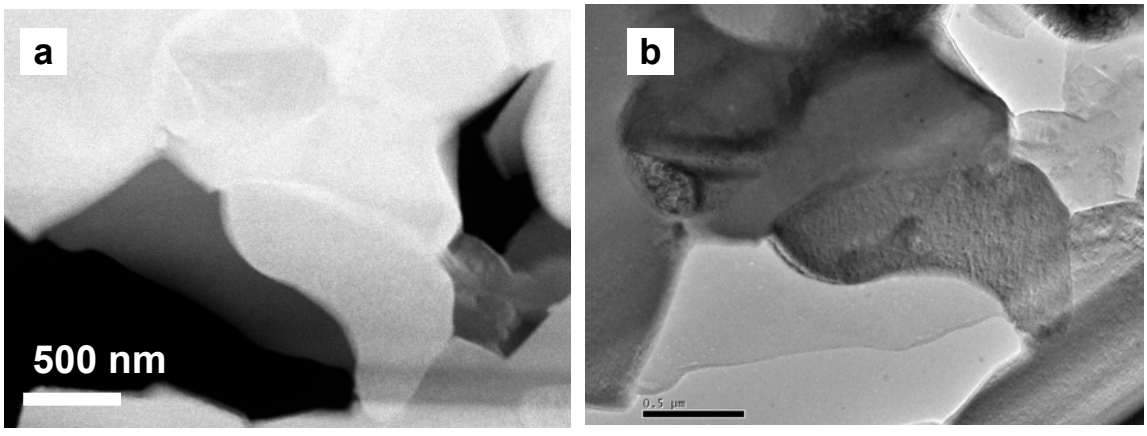

Figure 7-13: Micrographs of the area for the EDS mapping of the impurity phase shown in Figure 7-5. a) HAADF STEM micrograph and b) bright field TEM micrograph.

8. Effect of sealing and long-term durability of SOECs

8.1. Introduction

At present only few long-term tests on SOECs have been reported in literature. As for SOFCs, long-term durability is essential for SOECs in order to develop the SOECs from a potential and promising energy conversion technology to a commercially competitive and market mature technology. This PhD project has included galvanostatic SOEC tests of duration up to 1510 h and such long-term durability tests have shown that the SOECs experience a short-term passivation followed by an activation of the cell and a subsequent long-term degradation.

SOEC test results presented in chapter 3 and 4 showed that the electrolysis cells experience a short-term passivation over the first ~100-200 h and even though the main passivation is related to the H_2 electrode, it was shown in chapter 5 that Ni coarsening can only play a minor role in both the short-term passivation and the long-term degradation of the SOECs. SEM/EDS investigations presented in chapter 6 showed that there is most likely an "external" impurity source and that this could be the Si containing glass sealing used for the cell testing. The TEM/STEM/EDS results presented in chapter 7 showed accumulations of impurities of glassy phase aluminium-silicon oxides, sometimes also containing sodium, at the TPBs. These results have inspired to perform tests to investigate the effects of sealing material.

Furthermore, the long-term degradation is treated in more detail by using differential impedance spectroscopy. It is shown that the long-term degradation is most likely not an effect of the sealing material in the applied cell test set-up.

8.2. Experimental

The SOCs used for long-term electrolysis tests, the test set-up, test operation and procedure for data logging and recording impedance spectra was described in chapter 2. The operating conditions for the electrolysis tests described in this chapter are given in Table 8-1. Steam at a flow of 12 l/h was generated by combustion of hydrogen in oxygen. The five tests, 3test19, 3test30, 3test32, 3test33 and 3test36, were all exposed to one electrolysis test period each and operated long enough to have overcome the "initial" short-term passivation. 3test19, 3test30 and 3test32 were operated using the cell test set-up exactly as described in chapter 2. For 3test33 the glass sealing was pre-treated for 12 days at 950°C, 18 l/h H_2O and 2 l/h O_2 to the H_2 electrode and air to the O_2 electrode. This was done after sealing the cell by addition of a load of 8 kg, but prior to reduction of NiO in the H_2 electrode. For 3test36 pieces of gold foil were coiled and used as sealing together with platinum paste.

SOEC tests performed within this project have been compared to tests run at EIfER[15]. The SOECs tested at EIfER is produced as H_2 electrode supported cells at Risø. The cells are disc formed with an active electrode area of 47 cm^2 and the SOEC tests are performed using a sealing-less cell test set-up as described by Brissé et al. [145].

Table 8-1: Operating conditions during long-term galvanostatic electrolysis testing. Oxygen was passed over the O_2 electrode during electrolysis operation.

Test	Current density	Steam conv.	$p(H_2O)/p(H_2)$	Duration	Temp.
3test19	-0.25 A/cm^2	14%	0.7/0.3	767 h	850°C
3test30	-0.50 A/cm^2	28%	0.5/0.5	1316 h	850°C
3test32	-1.00 A/cm^2	53%	0.9/0.1	620 h	950°C
3test33	-0.50 A/cm^2	28%	0.5/0.5	1510 h	850°C
3test36	-0.50 A/cm^2	28%	0.5/0.5	694 h	850°C

Impedance spectra were recorded during electrolysis testing and used to characterise the cells during the long-term degradation. To improve the frequency resolution of these spectra, differential impedance spectra were calculated according to Jensen et al. [99]. The differential impedance spectra, $\partial Z'(f)/\partial \ln(f)$, were calculated from the real part of the experimental impedance, $Z'(f)$. Each point was calculated from equation (8-1) and to smoothen the differential impedance spectrum an average value of $\partial Z'(f_{n+1})/\partial \ln(f_{n+1})$, $\partial Z'(f_n)/\partial \ln(f_n)$ and $\partial Z'(f_{n-1})/\partial \ln(f_{n-1})$ was used when plotting $\partial Z'(f_n)/\partial \ln(f_n)$:

$$\frac{\partial Z'(f_n)}{\partial \ln(f_n)} \approx \frac{Z'(f_{n+1}) - Z'(f_{n-1})}{\ln f_{n+1} - \ln f_{n-1}} \tag{8-1}$$

It should be noted that "differentiating" by such three-point-average can lead to partly hiding of peaks or "shoulders" in the impedance plot. To avoid this more data points e.g. 12 points/decade should have been recorded than the 6 point/decade applied in this work, but the impedance spectra for these tests were obtained prior to the development of this differential treatment of impedance spectra.

To focus on the development of the impedance spectra during the long-term degradation, the difference ($\Delta_t \partial Z'(f)/\partial \ln(f)$) between the first spectrum recorded, where the long-term degradation is the dominating process, and the spectrum recorded at the time t_n has been calculated as:

$$\Delta_t \left(\frac{\partial Z'(f)}{\partial \ln f} \right) = \left[\frac{\partial Z'(f)}{\partial \ln f} \right]_{t=n} - \left[\frac{\partial Z'(f)}{\partial \ln f} \right]_{t=start} \tag{8-2}$$

[15] EIfER (European Institute for Energy Research, Karlsruhe, Germany) has, as a part of the 6th Framework EU project "Hi2H2", received and tested hydrogen electrode supported cells produced at Risø National Laboratory. These cells are produced as the cells tested in this PhD project.

8.3. Results

8.3.1. Long-term durability – albite glass sealing

The cell voltages versus time for three long-term tested SOECs are shown in Figure 8-1. For these three tests, 3test19, 3test30 and 3test32, the set-up described in chapter 2 was used including a stoichiometric albite glass as sealing material. 3test19 shows an initial passivation followed by a partial activation as described in [61]. This test was stopped before it could be judged whether a long-term degradation would take over after several hundred of hours, as observed for 3test30 after 600 h of electrolysis testing. The trend for 3test30 and 3test32 is a short-term passivation followed by activation and a long-term degradation that seems linear in time. For 3test32 the short-term passivation and long-term degradation are dominating as the activation of the cell only occurs from 127 h to 140 h of testing and only amounts to a few mV decrease in cell voltage. The initial activation of 3test32 has been previously observed for a test at 950°C (3test23) and can be due to improved contacting between layers. In consistency with the results presented in chapter 3, it is observed that the time for short-term passivation is decreased for the high p(H_2O) test, 3test32, compared to the low p(H_2O) test, 3test30. The long-term degradation for 3test30 is only 20 mV/1000 h (2%/1000 h) whereas the long-term degradation from t = 140 h and onwards is 65 mV/1000 h (6%/1000 h) for the high p(H_2O), high current density, high temperature test, 3test32. Notice, how 3test30 completely "recovers" from the short-term passivation.

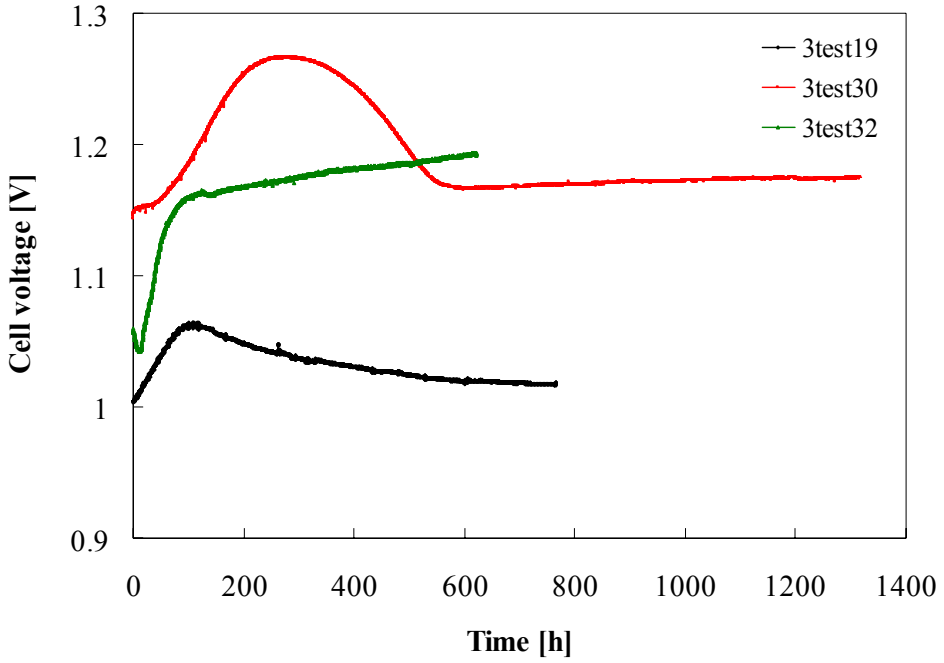

Figure 8-1: Cell voltages versus time for long-term durability test 3test19, 3test30 and 3test32 using an albite glass sealing as described in [61]. Electrolysis test conditions are given in Table 8-1.

The change in both the ohmic resistance (R_s) and polarisation resistance (R_p) during the long-term degradation of 3test30 and 3test32 is given in Table 8-2. The large ohmic resistance for 3test30 was caused by an imperfect Ni current collector foil. The relative increase in Rp is significantly larger than the relative increase in Rs for long-term degradation of both 3test30 and 3test32.

Table 8-2: Ohmic (R_s) and polarisation resistance (R_p) obtained from impedance spectra recorded just after the initial passivation/activation when the long-term degradation is the dominating process for 3test30 and 3test32, and at the end of electrolysis testing. Cell voltage curves for 3test30 and 3test32 are shown in Figure 8-1. The large R_s for 3test30 was caused by an imperfect Ni current collector foil.

Test	Time	R_s	R_p
3test30	599 h	0.182 Ωcm^2	0.256 Ωcm^2
3test30	1316 h	0.185 Ωcm^2	0.283 Ωcm^2
3test32	144 h	0.069 Ωcm^2	0.352 Ωcm^2
3test32	597 h	0.071 Ωcm^2	0.380 Ωcm^2

Differential impedance spectra were calculated by applying eq. 8-1 to the impedance spectra recorded during the long-term degradation for the two cells, that is after 599 h and 140 h for 3test30 and 3test32, respectively. To focus on the development of the impedance during the long-term degradation, and exclude the impedance development during the short-term passivation and activation, $(\Delta_t \partial Z'(f)/\partial \ln(f))$ was calculated from eq. 8-2 using t = 599 h and t = 140 h as a starting point for 3test30 and 3test32, respectively. The plot of $(\Delta_t \partial Z'(f)/\partial \ln(f))$ for 3test30 is shown in Figure 8-2 and for 3test32 in Figure 8-3. The peak developing the most in the plot of $(\Delta_t \partial Z'(f)/\partial \ln(f))$ for 3test30 (Figure 8-2) has a constant frequency around 2000 Hz and a "shoulder" can be observed at a frequency of ~200 Hz. It can be speculated whether the peak at 2000 Hz is actually a "double-peak" with frequencies of 1500 Hz and 2000 Hz, but the "double-peak" information could have been lost due to the three point average used for the calculation of $\partial Z'(f)/\partial \ln(f)$ (eq. 8-1). Furthermore, there seems to be a tendency for an increase in the $(\Delta_t \partial Z'(f)/\partial \ln(f))$ at a frequency of ~5 Hz (gas conversion arc). The peak developing the most in the plot of $(\Delta_t \partial Z'(f)/\partial \ln(f))$ for 3test32 (Figure 8-3) has a constant frequency of ~70 Hz and a decrease in the $(\Delta_t \partial Z'(f)/\partial \ln(f))$ at a frequency of ~5 Hz (gas conversion arc) is observed. Notice the difference of a factor of three for the $(\Delta_t \partial Z'(f)/\partial \ln(f))$ axis of Figure 8-2 and Figure 8-3.

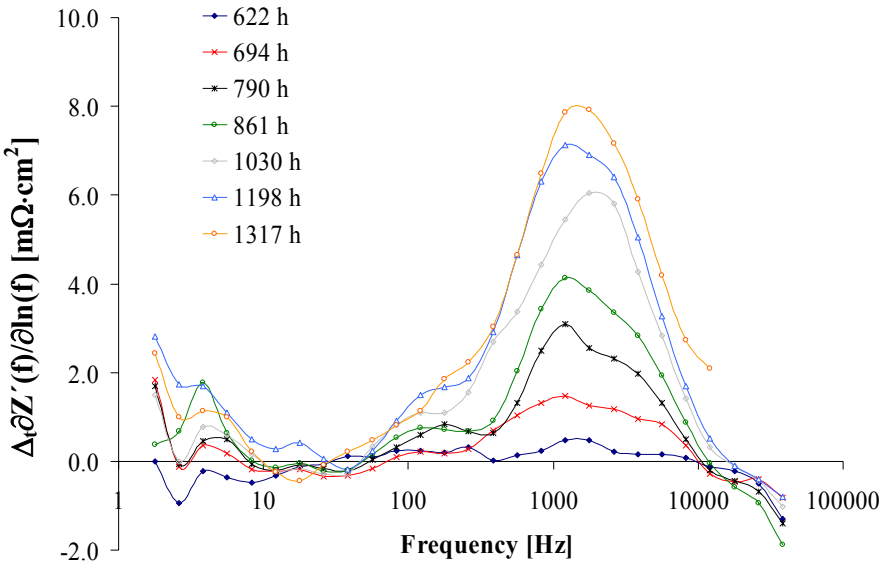

Figure 8-2: $\Delta_t\partial Z'(f)/\partial\ln(f)$ for the long-term degradation of 3test30, eq. 8-1 and 8-2. The differential impedance spectrum, $\partial Z'(f)/\partial\ln(f)$, after 599 h of electrolysis was used as reference spectrum and subtracted from each of the subsequent differential impedance spectra to form the $\Delta_t\partial Z'(f)/\partial\ln(f)$ shown in the graph. The electrolysis operating conditions are given in Table 8-1.

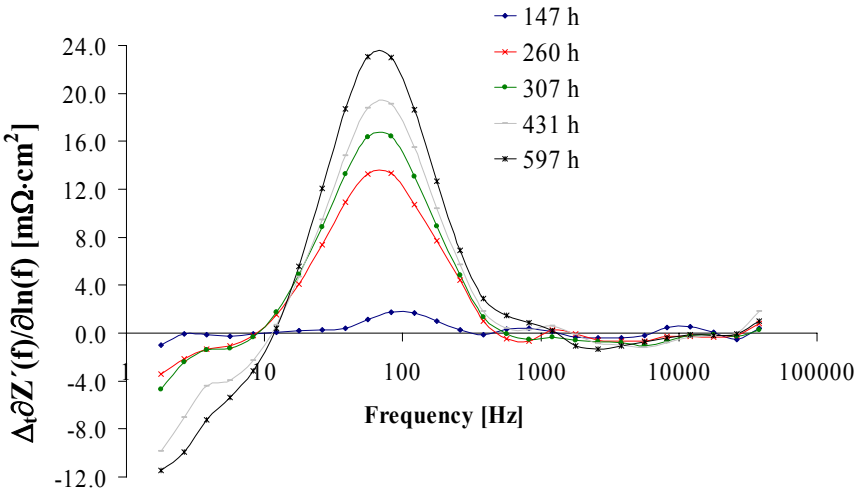

Figure 8-3: $\Delta_t\partial Z'(f)/\partial\ln(f)$ for the long-term degradation of 3test32, eq. 8-1 and 8-2. The differential impedance spectrum, $\partial Z'(f)/\partial\ln(f)$, after 144 h of electrolysis was used as reference spectrum and subtracted from each of the subsequent differential impedance spectra to form the $\Delta_t\partial Z'(f)/\partial\ln(f)$ shown in the graph. The electrolysis operating conditions are given in Table 8-1.

8.3.2 Long-term durability – pre-treated glass sealing

To investigate if evaporation of Si species from the glass sealing has an effect on the trends for the electrolysis test results, a test (3test33) was performed with a pre-treatment of the albite glass sealing. At 950°C and $p(H_2O)$ = 0.9 atm the maximum passivation caused by the short-term passivation was observed after six days of operation (3test32). Therefore 3test33 was pre-treated at 950°C and $p(H_2O)/p(O_2)$=0.9/0.1 for 12 days after sealing the test but prior to the reduction of the NiO. The intention with this pre-treatment was to evaporate Si species from the surface of the glass sealing. After this pre-treatment the usual start-up procedure and initial characterisation of the cell was performed and electrolysis testing was started for 3test33 at the same conditions as for 3test30, i.e. 850°C, $p(H_2O)$=0.5 atm and -0.5 A/cm^2. The results from the initial characterisation (iV curves and impedance spectra at OCV) for 3test33 were similar to other cells that had not been exposed to a pre-treatment of the glass sealing i.e. the pre-treatment did not seem to have effected the initial performance of the cell for 3test33.

The cell voltage versus time during electrolysis testing of 3test33 is shown in Figure 8-4, where it is compared with the cell voltage curve for 3test30 as these two tests were operated at the same electrolysis conditions (Table 8-1). The cell voltage curve for 3test33 is significantly different from 3test30. The cell voltage of 3test33 increase to 1122 mV within the first 173 hours of electrolysis testing and slowly decrease to 1108 mV over the following 896 hours of testing. The cell voltage increases ~28 mV/1000 h during the last 441 hours of 3test33 i.e. more than the long-term degradation rate for 3test30. The cell voltage curve of 3test33 is comparable with an electrolysis test performed at EIfER (Figure 8-5) as reported by Brissé et al. [145], where EIfERs sealing-less cell test set-up was used. The EIfER test was operated at a lower temperature (800°C), but on the other hand also at a lower current density (-0.3 A/cm^2), which in total lead to comparable cell voltages at the start of electrolysis testing for the two tests in Figure 8-5. There are differences in the time scale for the development of the cell voltages shown in Figure 8-5; nevertheless the development of the cell voltage curves shows similar trends.

Impedance spectra were recorded during 3test33 and representative spectra are shown in Figure 8-6. During the initial increase in impedance the frequency for the dominating arc decrease from 2000 Hz to reach 800 Hz after 141 hours of testing and this summit frequency returns to 2000 Hz during the subsequent activation of the cell. The summit frequency for this peak stays constant during the increase in impedance/cell voltage over the last 441 hours of electrolysis testing.

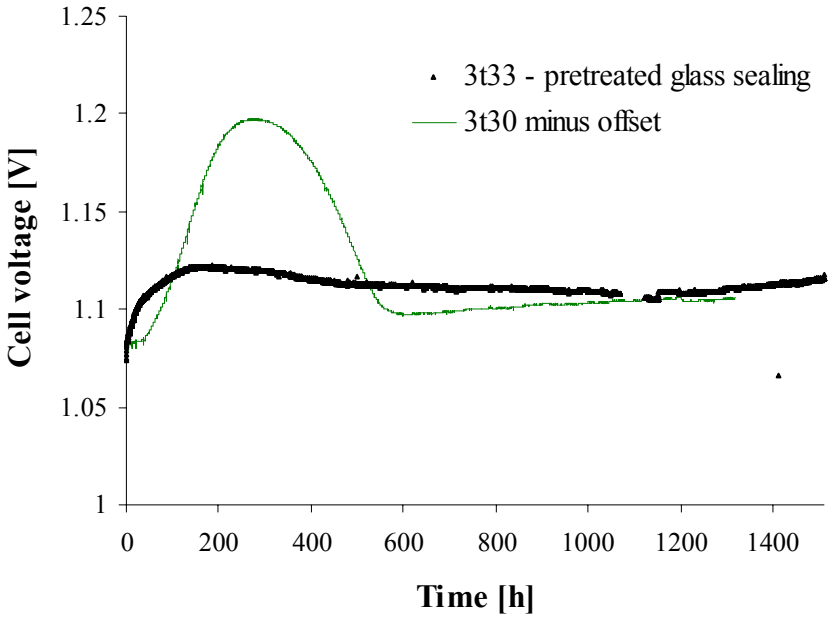

Figure 8-4: Cell voltage versus time for 3test33.The albite glass sealing used for 3test33 was pre-treated for 12 days at 950°C and p(H_2O) = 0.9 atm and p(O_2) = 0.1 atm. The cell voltage curve for 3test30 is shown for comparison. The difference in cell voltage at the start of electrolysis testing has been subtracted from the 3test30 cell voltage curve.

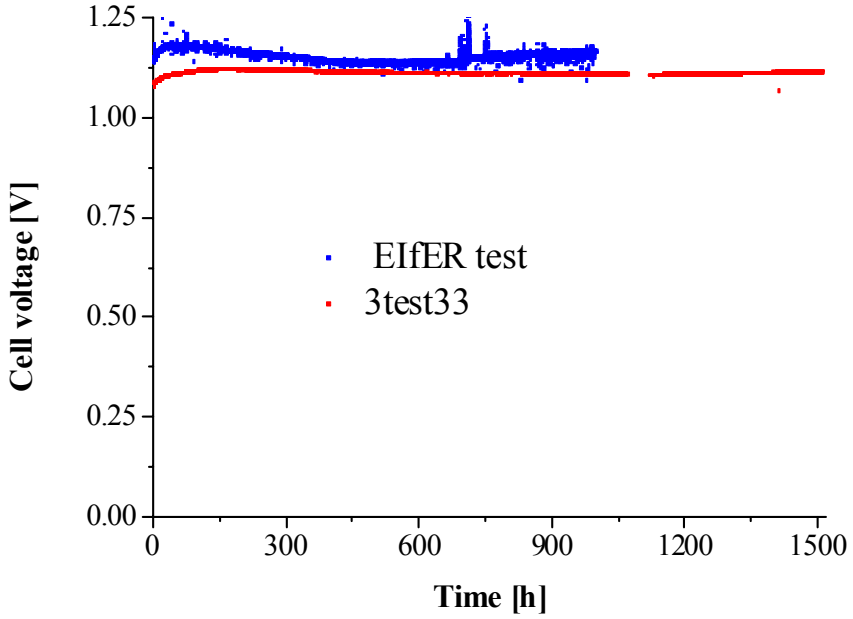

Figure 8-5: Cell voltage curve for 3test33 (red) compared to the cell voltage curve (blue) reported by A. Brisse et al. [145] obtained on a disk formed Risø cell in a sealing-less cell test setup at EIfER.

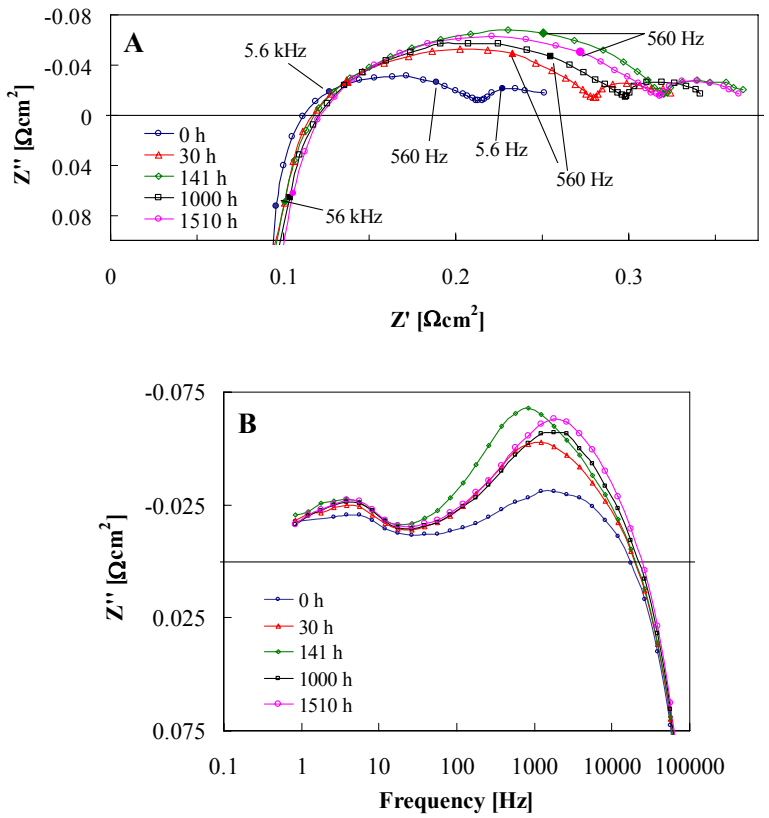

Figure 8-6: A) Impedance spectra recorded during 3test33 which had a pre-treated albite glass sealing, see "Experimental" and B) the imaginary part of the impedance spectra recorded during 3test33. The electrolysis operating conditions for 3test33 are given in Table 8-1

Differential impedance spectra were calculated by applying eq. 8-1 to the impedance spectra after 1050 h. To focus on the development of the impedance during the long-term degradation, and exclude the impedance development during short-term passivation and activation, $(\Delta_t \partial Z'(f)/\partial \ln(f))$ was calculated from eq. 8-2 using the spectrum recorded at t = 1050 h for 3test33. The plot of $(\Delta_t \partial Z'(f)/\partial \ln(f))$ for 3test33 is shown in Figure 8-7. The peak developing the most in the plot of $(\Delta_t \partial Z'(f)/\partial \ln(f))$ for 3test33 has a frequency around 3000 Hz. In this case it would have been favourable to have at least the double number of measurements per decade, as it appears that there might be a double peak (~800 Hz and ~3000 Hz) but this is not resolved properly in the plot of $\Delta_t \partial Z'(f)/\partial \ln(f)$ which is based on the three points average in eq. 8-1.

Gas shift experiments were performed at OCV and 750°C before and after electrolysis testing of 3test33 in the same manner as it was done for e.g. 3test30 and difference plots like the ones shown in Figure 4-5 were obtained. The relative change in the dominating

peak for the gas shift to the LSM electrode was only one third of the relative change of the dominating peak for the gas shift at the Ni/YSZ electrode.

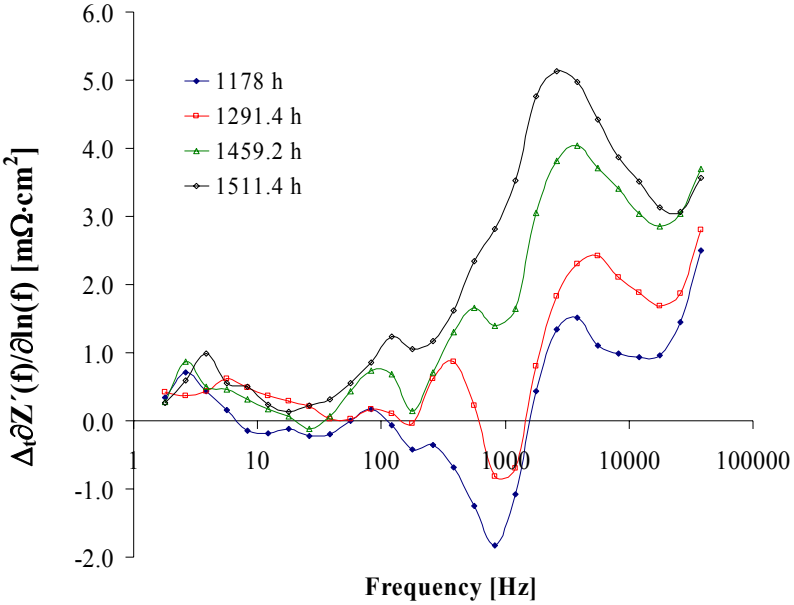

Figure 8-7: $\Delta_t\partial Z'(f)/\partial\ln(f)$ for the long-term degradation of 3test33, equation (8-1) and (8-2). The differential impedance spectrum, $\partial Z'(f)/\partial\ln(f)$, after 1050 h of electrolysis was used as reference spectrum and subtracted from each of the subsequent differential impedance spectra to form the $\Delta_t\partial Z'(f)/\partial\ln(f)$ shown in the graph. The electrolysis operating conditions are given in Table 8-1.

8.3.3 Long-term durability – gold as sealing material

To eliminate the effect of the albite glass sealing a test was set up using coiled gold foil and platinum paste as sealing material on both sides of the cell. This cell test, 3test36, was operated at the same electrolysis conditions as 3test30 and 3test33 (Table 8-1) and the cell voltage for 3test36 is shown as the red line in Figure 8-8. For comparison an EIfER-test[16] is shown by the blue dots in Figure 8-8. The EIfER test was run in a sealing-less cell test set-up at 800°C, 50% H_2O and -0.5 A/cm^2. The instability in the cell voltage of the EIfER test was caused by unstable steam supply. It was observed that the cell voltage curve for 3test36 is significantly different from the cell voltage curve of 3test30 where the albite glass sealing was used. 3test36 did not show the short-term passivation and activation as 3test30, but only a somewhat linear degradation. The cell voltage of 3test36 increases 56 mV/1000 h which is a factor of 2½ more than the long-term degradation of 3test30. Impedance spectra were recorded during electrolysis operation of 3test36. The ohmic resistance increased from 0.115 Ωcm^2 to 0.123 Ωcm^2 during the first 422 hours i.e. 17%/1000 h while the polarisation resistance increased from 0.273 Ωcm^2 to 0.376 Ωcm^2 i.e. 89%/1000 h.

[16] The cell voltage data for this ”EIfER-test” was kindly provided by Dr. Maria José Garcia, EIfER.

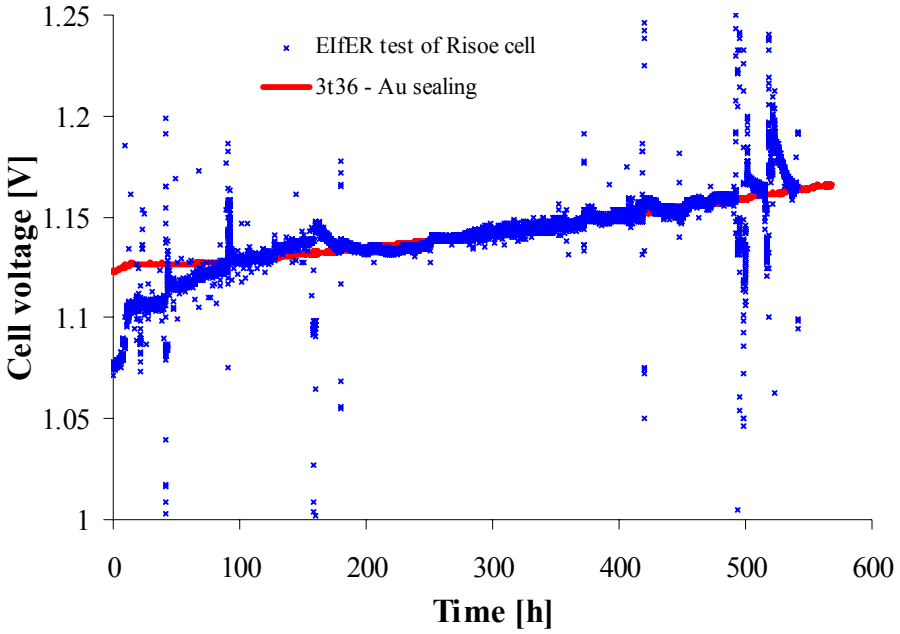

Figure 8-8: The red curve is the cell voltage versus time for 3test36 using a coiled gold foil and platinum paste as sealing. Electrolysis test conditions are given in Table 8-1. The blue curve is the cell voltage curve obtained by at EIfER on a disk formed Risø cell using a sealing-less cell test set-up. The operating conditions for the EIfER test were: -0.5 A/cm^2, p(H_2O) = 0.5 atm, 800°C and a steam conversion of ~70%.

Differential impedance spectra were calculated by applying eq. 8-1 to the impedance spectra recorded during 3test36 and the ($\Delta_t\partial Z'(f)/\partial\ln(f)$) was calculated from eq. 8-2 using the spectrum recorded at t = 0 h as reference spectrum. The plot of ($\Delta_t\partial Z'(f)/\partial\ln(f)$) for 3test36 is shown in Figure 8-9. Two peaks are observed to develop in the ($\Delta_t\partial Z'(f)/\partial\ln(f)$) plot in Figure 8-9, one with a summit frequency of 2000-4000 Hz, which is most likely related to Ni-YSZ charge transfer, and one at 3 Hz, which is a gas conversion peak. The high frequency peak seems to decrease in frequency over the first 422 hours of electrolysis operation of 3test36.

8.3.4 Thermochemical calculations for evaporation of Si species from glass sealing

The glass used for cell testing is a stoichiometric albite glass mixed with YSZ. This glass has the proper compressibility and viscosity at the temperature (950°C-1000°C) used when the SOCs are heated up and the reduction of the NiO in the Ni/YSZ is performed prior to cell testing. To investigate the possibility of contamination of the SOECs caused by the vapour pressure of Si-, Na- and Al-containing species over the albite glass at different operating conditions, the thermochemical data for Si-, Na-, and Al-gas species [146-148]

and the albite glass ($NaAlSi_3O_8$) [149] have been applied to the FactSage® program to calculate the partial pressure of Si-, Na-, and Al-containing species. The calculations show that the gas with the highest vapour pressure over the albite glass is $p(Si(OH)_4)$ at SOEC relevant conditions and the vapour pressures of NaOH and $Al(OH)_3$ are approximately an order of magnitude lower.

Examples of calculated $p(Si(OH)_4)$ at typical $p(H_2O)/p(H_2)$ and temperatures for both SOFC and SOEC operation of SOCs are given in Figure 8-10. The results shown in Figure 8-10 and Table 8-3 are based on open system calculations which describe a system with a continuous feed of H_2 and H_2O i.e. the activities of the inlet gasses are kept constant. If a closed system is assumed, the $p(Si(OH)_4)$ will be slightly higher e.g. $p(Si(OH)_4)$ is calculated to be $1.7 \cdot 10^{-7}$ atm for a closed system versus $1.4 \cdot 10^{-7}$ atm for an open system at 950°C and $p(H_2O)/p(H_2) = 0.9/0.1$.

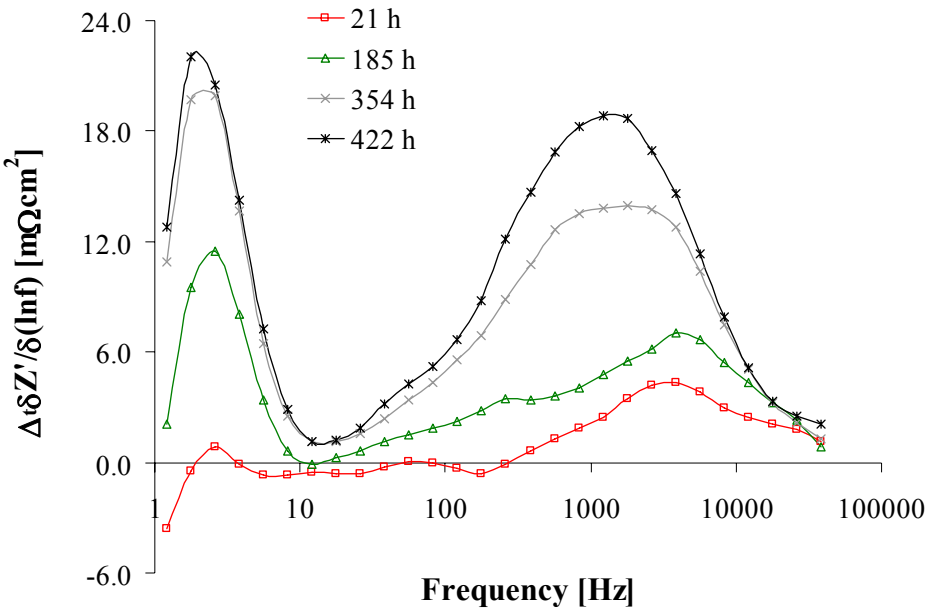

Figure 8-9: $\Delta_t \partial Z'(f)/\partial \ln(f)$ for the long-term degradation of 3test36, eq. 8-1 and 8-2. The differential impedance spectrum, $\partial Z'(f)/\partial \ln(f)$, at start of electrolysis was used as reference spectrum and subtracted from each of the subsequent differential impedance spectra to form the $\Delta_t \partial Z'(f)/\partial \ln(f)$ shown in the graph. The electrolysis operating conditions are given in Table 8-1.

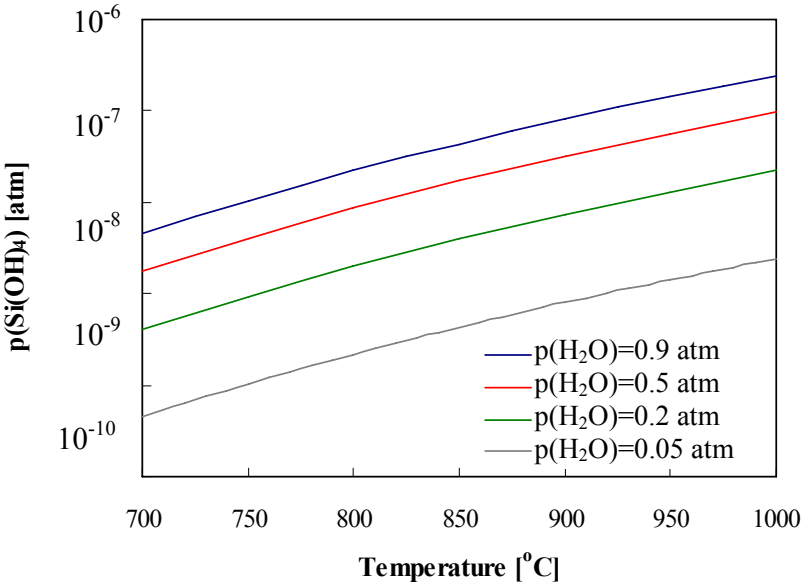

Figure 8-10: Calculated partial pressure of $Si(OH)_4$ over an albite glass sealing a different partial pressures of steam. Calculations are made using the program FactSage® and with an open system. Thermochemical data from [146-149] were used.

Table 8-3 gives an overview of the calculated $p(Si(OH)_4)$ for temperatures and gas compositions that are relevant for SOFC and SOEC respectively. Notice the factor of 10^2 in difference for the calculated $p(Si(OH)_4)$ at the same temperature but at typical SOFC gas composition ($p(H_2O)$=0.05 atm) and SOEC gas composition ($p(H_2O)$=0.90 atm).

Table 8-3: Calculated partial pressure of $Si(OH)_4$ over albite glass at typical temperatures and $p(H_2O)/p(H_2)$ ratios for SOFC and SOEC testing. The program Factsage® was used for the calculations in combination with data from [146-149].

	Temp. (°C)	$p(H_2O)/p(H_2)$	$p(Si(OH)_4)$ (atm)
SOFC	750	0.05/0.95	$1 \cdot 10^{-10}$
SOFC	750	0.20/0.80	$9 \cdot 10^{-10}$
SOFC	850	0.05/0.95	$4 \cdot 10^{-10}$
SOFC	850	0.20/0.80	$4 \cdot 10^{-09}$
SOEC/SOFC	850	0.50/0.50	$2 \cdot 10^{-08}$
SOEC	850	0.90/0.10	$4 \cdot 10^{-08}$
SOEC/SOFC	950	0.50/0.50	$6 \cdot 10^{-08}$
SOEC	950	0.90/0.10	$1 \cdot 10^{-07}$

8.4. Discussion

8.4.1. Effect of sealing material on SOEC tests

Comparing cell voltage curves for 3test30 and 3test33 (Figure 8-4) it is clear that the glass sealing plays a key role in the short-term passivation and activation phenomenon observed for SOEC tests in this project. For 3test33 the development over time for the initial passivation is significantly different from 3test30 and other tests performed using non-pre-treated albite glass sealing. There does not seem to be any "incubation time" for the increase in the cell voltage of 3test33 when compared to tests with non-pre-treated glass sealing. This could be explained by the fact that the pre-treatment of the glass sealing removed Si species from the surface of the glass but there may still be gaseous $Si(OH)_4$ available in the gas distribution layer, pores in the electrode etc. This will be available and reacted to SiO_2 near the electrolyte/electrode interface soon after the onset the electrolysis current load. For a non-treated glass sealing the evaporation of $Si(OH)_4$ will take place over a longer period of time after the onset of electrolysis testing, giving rise to the cell voltages develop as an "S"-shaped curve the first few hundred hours as observed for 3test30, whereas the initial increase of cell voltage for 3test33 is very pronounced within the first 175 h. If 3test33 is compared with an EIfER-test using a "sealing-less" set-up (Figure 8-5), it could be argued that the initial passivation of 3test33 is not related to the pre-treated glass sealing, but rather something inherent in the cell itself and it seems test set-up independent.

The impedance spectra for 3test33 (Figure 8-6) show the same general trend as for 3test30, though with smaller changes in the impedance. The trends are: 1) a decrease in frequency for the dominating arc from ~2000 Hz to ~800 Hz during short-term passivation, 2) an increase in the frequency for this arc during the subsequent activation and 3) the summit frequency for this arc stays constant at 2000 Hz during the long-term degradation. This development of the impedance spectra for 3test33 supports the hypothesis that even after pre-treatment of the glass sealing, it is mainly the Ni/YSZ electrode that passivates [95]. This was confirmed by the relative changes in the difference plot for changes in impedance spectra due to gas variations at OCV before and after electrolysis testing of 3test33.

The cell voltage curve for 3test36 provides the necessary data to conclude that the short-term passivation and subsequent activation for several SOEC tests in this project must have been an effect of the sealing material. Gold has been a successful sealing material from the point of view of testing the effect of sealing material on the SOEC tests, but in the long term gold is too expensive to be used as sealing material and further development of glass sealing for SOECs will be necessary. An application for a patent on a "scavenger-coating" of the glass sealing is in progress.

Even if we manage to eliminate or at least minimise the evaporation of Si, Al and Na species from the glass sealing, there is still a possibility of impurity contamination from the cell itself e.g. from impurities in the raw materials. Accumulation of impurities originating from the raw materials will most likely proceed via different routes (potential driven solid-state diffusion) compared to the contamination via gas phase impurities from "external" sources. This could lead to differences in the nanostructure and chemical composition of the impurities accumulated at the TPBs depending on which of the impurity sources are

responsible. To investigate this in detail, TEM/STEM micrographs and EDS analyses as those presented in chapter 7 are necessary for tested SOECs with no or at least a minimum contribution of impurities from "external" gas sources.

8.4.2. Long-term degradation SOECs

During the long-term degradation it is mainly the hydrogen electrode polarisation resistance that increases both for "low current density" tests (3test30, 3test33 and 3test36) and for the "high current density" tests. From a technological point of view degradation rates of 2%/1000 h at -0.5 A/cm^2 as for 3test30 and 6%/1000 h at -1.0 A/cm^2 as for 3test32 are unacceptable and these SOEC degradation rates are significantly higher than long-term fuel cell tests of similar cells. Especially at high current densities fuel cell tested cells have shown a much better long-term performance i.e. below 1%/1000 h at 1 A/cm^2 and 850°C, and below 2%/1000 h at 1.7 A/cm^2 and 950°C [32]. The higher degradation rate for 3test32 compared to 3test30 is not necessarily solely an effect of the higher current density but is possibly also caused by the increased steam utilisation for 3test32 resulting in larger concentration and polarisation gradients.

3test36 had a much higher degradation rate of ~5%/1000 h (Figure 8-8) than 3test30 even though the cell polarisation for 3test36 was only 22 mV higher than for 3test30 at the start of the two electrolysis tests[17]. The large increase in the impedance due to gas conversion (the arc at ~3 Hz in Figure 8-9) indicates that a significant change in the distribution of the current density occurs during electrolysis testing of 3test36. The reason for the similar degradation rate of the EIfER test shown in Figure 8-8 can be that they operate the cell a steam utilisation of ~70% and not 28% as for 3test36.

The $\Delta_t\partial Z'(f)/\partial\ln(f)$ for the long-term degradation of 3test30 (Figure 8-2), 3test33 (Figure 8-7) and 3test36 (Figure 8-9) all show - to a larger or smaller extent - a peak developing at ~2000 Hz. This points towards a degradation mechanism related to the charge transfer at the Ni-YSZ interface as reported by Barfod et al. [95]. According to the model by Barfod et al., an arc at a few hundred Hz can be ascribed to the oxygen electrode and an arc in this frequency range is visible in the impedance spectra of the long-term degradation for 3test30 (Figure 8-2). 3test32 was operated at a high temperature (950°C) and a higher frequency for the developing arc in the $\Delta_t\partial Z'(f)/\partial\ln(f)$ plot could be expected compared to tests at 850°C. The low frequency (~70 Hz) for the arc developing during the long-term degradation of 3test32 is due to the fact that the cell only re-activated slightly after the short-term passivation i.e. that the main peak was located at ~80 Hz when the long-term degradation is the dominating process during electrolysis testing.

The increasing arc in the impedance plots during long-term degradation has a constant summit frequency i.e. a decreasing capacitance. The arc due to gas conversion can be expected to be at a minimum at $p(H_2O)$=0.5 atm and increase for both higher and lower $p(H_2O)$ [9]. A decrease in the gas conversion volume at certain locations in the electrode microstructure will lead to an increase in the resistance, $R_{conv.}$, as observed for 3test30 and

[17] Effect of cell polarisation is described in chapter 3.

3test36 during long-term degradation, and a decrease in the capacitance, $C_{conv.}$, for the gas conversion impedance. It is more surprising that a decrease in $R_{conv.}$ was observed for the long-term degradation of 3test32 (Figure 8-3) indicating an improved distribution of the current density. This can be due to a partly activation of the cell after the short term passivation which is "hidden" by the long-term degradation.

For 3test30 the activation of the cell after the short-term passivation is complete and it could be expected that post-mortem analysis for this cell will show effects from the long-term degradation alone. As it was shown in chapter 7, it has been possible to find significant amounts of impurities of Al, Si and Na oxides at the TPBs in the hydrogen electrode of 3test30. Two different hypotheses – or a combination of them – can explain this: 1) The activation of the SOEC is not caused by evaporation of Si-species (originating from the $Si(OH)_4$ from the glass sealing) from the TPB, but rather a redistribution or crystallisation of the impurities which lead to a fewer number of blocked TPBs[18] or 2) The impurities found in the hydrogen electrode of 3test30 are not a "left-over" from the short-term "sealing" passivation phenomenon, but is caused by the long-term degradation where impurities from the raw materials accumulate at the TPBs.

The possible effect of impurity contamination can be expected to be at a minimum for 3test33. Preliminary SEM investigations of 3test 33 have been performed and no impurities have been found so far, but this does not necessarily mean that impurities are not present in the electrodes of 3test33. More thorough SEM/EDS work is necessary in combination with FIB/TEM/STEM/EDS work as presented in chapter 7 for 3test30. Cell pieces from 3test36 have not yet been subjected to post-mortem analyses.

8.4.3. Evaporation of $p(Si(OH)_4$ from the albite glass sealing

The albite glass sealing has proven to withstand hundreds of hours of fuel cell testing without any significant increase in leakage for the cell test set-up [75]. The typical steam content in the inlet gas for fuel cell testing is a few percentages and therefore very different conditions from electrolysis testing, where the applied partial pressure of steam can easily be 0.9 atm. It is the combination of two effects that gives the observed passivation problems when using albite glass sealing for SOEC tests: 1) The increased $p(H_2O)$ in the inlet gas for SOEC tests leads to a much higher $p(Si(OH)_4)$ over the glass sealing and 2) the reduction of H_2O at the electrode/electrolyte interface will push the equilibrium between silicon tetra hydroxide and silica (eq. 6-1) towards the formation of silica and this will not be the case for fuel cell testing of SOCs. The hypothesis that $p(Si(OH)_4)$ is the main impurity source causing the short-term passivation fits well with the fact that an electrolysis test that has been stopped at the maximum passivated state during the short-term passivation can be partly re-activated by fuel cell operation of the cell (see chapter 3).

The estimate for the amount of SiO_2 formed during a 500 h test given in the "Discussion" paragraph of chapter 6 was based on the calculations given in Table 8-3. As observed from Table 8-3 the $p(Si(OH)_4)$ varies from approximately $2 \cdot 10^{-8}$ to $1 \cdot 10^{-7}$ atm for typical SOEC

[18] For a more detailed description of the hypothesis describing the transient behaviour (passivation/activation) due to the evaporation of $Si(OH)_4$ species for these SOEC tests, see chapter 6 in [76].

test conditions, and SiO_2 contributions for a 500 h test can be expected to vary from below 1 mg to slightly above 3 mg. Besides the $p(Si(OH)_4)$ also $Al(OH)_3$ and NaOH evaporated from the albite sealing most likely contribute to - and alter the properties of - the impurities formed during the short-term passivation.
Impurity contamination caused by evaporated hydroxides from the glass sealing can be avoided when running CO_2 electrolysis tests with no addition of steam in the inlet gas. Two such tests have been run at Risø National Laboratory. Unfortunately other dominating passivation/degradation process(es) have made it difficult to illustrate that the passivation effect of the glass sealing has been avoided in these tests.

8.5. Conclusion

From the results presented in this chapter it can be concluded that:

- The short-term passivation and activation is closely related to the use of albite glass sealing in the cell test set-up.
- Comparison of tests performed at Risø and tests performed at EIfER (on Risø cells) using a sealing-less test set-up confirms that short-term passivation and activation is a test set-up based phenomenon.
- Pre-treating the albite glass sealing with a gas having a $p(H_2O) = 0.9$ atm at 950°C for 12 days prior to reduction of the NiO and cell testing significantly minimised the short-term passivation and activation phenomenon.
- Using a gold sealing led to an electrolysis test with no short-term passivation and activation, but only a degradation that is approximately linear in time.
- Thermochemical calculations of the partial pressure of $Si(OH)_4$ over the albite glass at SOEC relevant conditions resulted in $p(Si(OH)_4)$ of $2 \cdot 10^{-8}$ to $1 \cdot 10^{-7}$ atm and supported the hypothesis that the albite glass sealing can be a significant impurity source when operating the SOCs as electrolysis cells.
- For the best performing SOECs long-term degradation rates of 2%/1000 h at -0.5 A/cm^2, $p(H_2O) = 0.5$ atm and 850°C, and 6%/1000 h at -1.0 A/cm^2, $p(H_2O) = 0.9$ atm and 950°C were found.
- From the development of the impedance spectra during the long-term degradation it is believed that the main part of the degradation is related to processes in the Ni/YSZ electrode.

9. Overall discussion and summary

In this chapter a summary of the content of chapter 3-8 and an overall discussion is presented. This includes summary and discussions on issues such as initial performance of the SOECs, the short-term passivation/activation phenomenon and how it relates to an external impurity source from the sealing material, as well as the long-term degradation observed for the SOECs. As EIS results in chapter 4 and 8 have indicated as well as electron microscopy investigations in chapter 6 and 7 have given the evidence for, impurities in the H_2 electrode play an important role for the performance of the SOECs and some of the aspects of this issue are discussed in §9.5.
The weight on the different issues in this chapter does not directly reflect the effort and time spent on each various subjects during the project, but rather reflects what seem most important and necessary to focus on for the SOECs as it is viewed at the present moment.

9.1. Initial performance of SOECs

As reported in chapter 3 the initial electrolysis performance of the SOCs produced at Risø National Laboratory is excellent e.g. an ASR of 0.26 Ωcm^2 at 850°C when the chord of the iV curve from OCV to -0.75 A/cm^2 is used. From the initial characterisation of numerous of cells, it was observed that there was no discontinuity across OCV, and an iV curve in electrolysis mode at 850°C does not lead to any observable loss in performance. Furthermore, iV curves in electrolysis mode have shown that steam utilisation above 80% can be reached without notable steam starvation problems. This expresses an optimal microstructure of the H_2 electrode of the SOCs also for electrolysis operation. At EIfER initial electrolysis performances were recorded by iV curves on Risø cells. EIfERs measurements on a disc formed Risø cell resulted in an ASR of 0.53 Ωcm^2 at 800°C and no steam starvation was observed even for steam utilisations up to 63% at 800°C [145]. The ability for the SOECs to operate at high steam utilisation may not play at key role in these more fundamental studies of SOECs but in the perspective of future SOEC systems for commercialisation, a high steam utilisation and minimum recycling of gasses most likely become relevant issues.
Considering the initial electrolysis performance for these SOCs, it is worthwhile to attempt an optimisation of the cells even though the long-term degradation in electrolysis mode is significantly higher than for similar cells operated as fuel cells [32].

9.2. Short-term passivation and activation of the SOECs

The initial short-term passivation (~100-200 h) for the SOECs was related to a passivation of the hydrogen electrode. The EIS results strongly pointed towards an increased resistance due to surface and/or solid-state diffusion process(es). This corresponds well with the results of chapter 6, 7 and 8, i.e. that glassy phase impurities accumulate at the TPB and that the impurities originate from an external gaseous source which appears to vanish after a couple of hundred of hours.

As shown in chapter 3 and 8, a partial or complete activation of the SOECs after the short-term passivation can be obtained either by fuel cell operation of the cells or constant electrolysis conditions. The two ways of activating the passivated SOECs are believed to be due to different mechanisms. The fuel cell activation is most likely governed by the changed direction of the reaction at the TPB. The oxidation of hydrogen at the TPBs in the hydrogen electrode will shift the equilibrium:

$$SiO_2 + 2H_2O \rightleftharpoons Si(OH)_4 \qquad (9\text{-}1)$$

towards formation of gaseous silicon tetra hydroxide and liberate silica on the TPBs (see chapter 6). The activation of the SOECs during constant electrolysis conditions has to be either due to a slow evaporation of the Si species at the TPBs or a crystallisation or redistribution of the glassy phase impurities to cover fewer reactions sites. This is of course combined with a termination of the evaporation of impurities from the surface of the glass sealing

Much effort and time has been spent on the transient phenomenon and many of the SOEC test results have been dominated by this phenomenon. Nevertheless, seen in a broader perspective it is not the most crucial topic for the further development of the SOEC technology as it has been shown to be an effect of the sealing material i.e. a test set-up dependent phenomenon (chapter 8 and [145]). It is of course still necessary to develop appropriate sealing material and test these at a variety of operating conditions over hundreds of hours.

9.3. Effect of glass sealing material

The effect of modifying or changing sealing material on the passivation/activation phenomenon was evident from the results presented in chapter 8 and this confirmed the hypothesis given in the discussion section of chapter 6. It was the SEM/EDS findings of large amounts of Si containing impurities in tested SOECs that led to the belief that there was an external impurity source. Nevertheless, results already reported in literature could also have inspired consideration of the albite glass sealing as a potential impurity source, e.g. Jacobson et al. [129] found that the gas with the highest partial pressure, i.e. $Si(OH)_4$, over cristobalite (SiO_2) increases from $1.6 \cdot 10^{-8}$ atm to $9.9 \cdot 10^{-7}$ atm upon increasing $p(H_2O)$ in argon from 10% to 99% at 900°C.

Even though the albite glass sealing has caused troubles in the SOEC testing work, modified glasses should still be considered the most relevant option for sealing of the SOECs due to its physical properties (compressibility and viscosity) at SOC-temperatures and its cost competitiveness. The fact that similar problems in the use of albite glass sealing for SOFC tests have not been observed illustrates the different material demands and challenges for SOFCs and SOECs.

A long-term SOEC stack test has been performed at Risø National Laboratory with a stack design by the company Topsoe Fuel Cells. This means that a different glass composition was used and the glass area exposed to the inlet gas was significantly lower per active

electrode area than for single cell testing. This SOEC stack showed encouraging results. The average ASR per cell increased from 0.39 Ωcm^2 in electrolysis mode at 850°C prior to testing to 1.17 Ωcm^2 after 830 hours of electrolysis testing at 850°C, -0.25 A/cm^2, $p(H_2O)$ = 0.5 atm and a steam utilisation of ~28%. The four mid-cells out of a total of 6 cells were considered.

9.4. Long-term degradation of the SOECs

Some tests were operated long enough and/or used the proper set-up to provide information on the long-term degradation of the SOECs. This long-term degradation is indeed interesting in the longer perspective and important to investigate in relation to either an optimisation of the SOEC hydrogen electrode or even development of new electrodes as the long-term degradation rate is too high.

Gas shift impedance spectroscopy for 3test30 and 3test33 showed that the main passivation of the cells caused by the long-term degradation was related to process(es) in the H_2 electrode. This was supported by the summit frequency at ~2000 Hz for the arc with the increasing impedance during the long-term degradation. Jensen [76] suggested that this long-term degradation was caused by Ni coarsening but based on the results in chapter 5, this cannot be the case. The microscopy results presented in chapter 7 point more towards an impurity related long-term degradation mechanism (see next paragraph). It is noteworthy though that in contrast to the impedance spectra during the short-term passivation, the frequency is constant for the arc with the increasing impedance during the long-term degradation. This implies a decrease in the capacitance if a Cole-element is used to describe this impedance arc.

As there are only limited test results available on the long-term degradation, the dependency of the different operating parameters is still to be analysed.

9.5. Possible reaction mechanisms and impurities

A couple of the many aspects of reaction mechanisms and impurities in the hydrogen electrode of SOECs are discussed below. This includes a view on the possible electrochemical reactions at the TPBs in the H_2 electrode and how these can be affected by impurities, the origin of the impurities and considerations regarding modification of the impurity phases in order to minimise their effect on the performance of the SOEC.

Possible reaction mechanisms at the Ni-YSZ interface during cathodic operation

Details on the mechanisms for the electrode reactions in the hydrogen electrode during electrolysis testing cannot be deduced from the full cell tests performed within this project. Reaction mechanisms at the hydrogen electrode have been reported, modelled and discussed in literature [150-161] and the reported suggestions for the reaction mechanisms at the hydrogen electrode form the basis for the schematic illustration of different possible reaction mechanisms for the hydrogen electrode of an SOEC given in Figure 9-1.

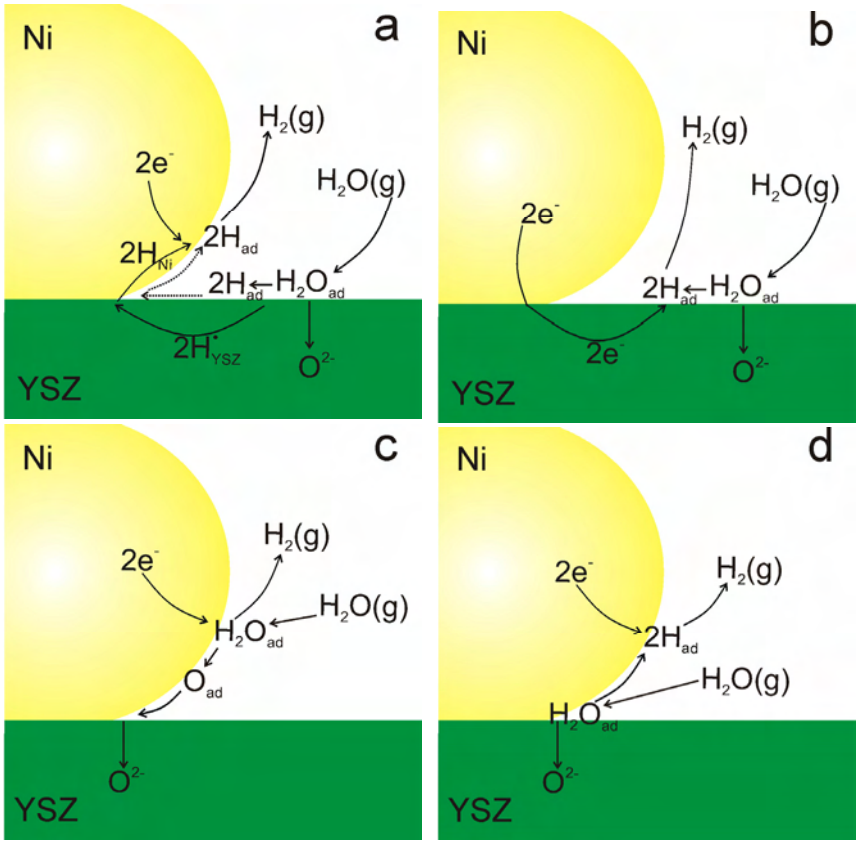

Figure 9-1: Schematic and simplified illustration of possible reaction mechanisms in the hydrogen electrode of an SOC. The suggested reaction mechanisms are based on mechanisms reported in literature [150-160]. A) Adsorption of H_2O on the YSZ surface and proton diffusion on the surface or in the bulk of YSZ. B) Adsorption of H_2O on the YSZ surface and electronic conductivity of YSZ assumed, C) Adsorption of H_2O on the Ni surface and diffusion of OH and oxygen on the Ni surface and D) H_2O adsorbed at the TPB and hydrogen diffusion on the Ni surface. Intermediate steps including adsorbed OH and vacancies are not shown in figure A, B and C.

In Figure 9-1 it is assumed that the inlet gas, mainly steam, has reached the region in the vicinity of the TPBs via the pores in the H_2 electrode structure. For simplicity of Figure 9-1 details such as intermediate steps including adsorbed OH, vacant surface adsorption sites, charge transfer for H/H^+ and vacancies ($V_O^{\bullet\bullet}$) in the YSZ are not shown. The inspiration for Figure 9-1A was found in discussions on the reaction mechanisms at anodic polarisation given by Mogensen et al. [157; 158] and Holtappels et al. [155]. In Figure 9-1A the electrode reaction proceeds via adsorption of H_2O on the YSZ surface in the vicinity of the TPB and hydrogen either dissolves in YSZ and diffuses through the bulk of YSZ and Ni to a vacant Ni site and $H_2(g)$ desorbs or hydrogen diffuses on the surface of the YSZ and Ni (dashed lines). The mechanisms can roughly be described by eq. 9-2 to 9-5. Alternatively,

eq. 9-6 and 9-7 describe hydrogen diffusion on the surface of YSZ and Ni (dashed line in Figure 9-1A). $\square_{ad}$ is a site vacant for adsorption. Intermediate steps including adsorbed OH and H like eq. 9-14 and 9-15 but on YSZ could be added in between eq. 9-2 and 9-3.

Figure 9-1A

$$H_2O(g) + \square_{ad,YSZ} \rightleftharpoons H_2O_{ad,YSZ} \quad (9\text{-}2)$$

$$H_2O_{ad,YSZ} + V_{O,YSZ}^{\bullet\bullet} \rightleftharpoons O_{O,YSZ}^{x} + 2H_{YSZ}^{\bullet} + \square_{ad,YSZ} \quad (9\text{-}3)$$

$$2e'_{Ni} + 2H_{YSZ}^{\bullet} \rightleftharpoons 2H_{Ni} \quad (9\text{-}4)$$

$$2H_{Ni} \rightleftharpoons H_2(g) \quad (9\text{-}5)$$

$$2H_{ad,YSZ} \rightleftharpoons 2H_{ad,TPB} \quad (9\text{-}6)$$

$$2H_{ad,TPB} \rightleftharpoons 2H_{ad,Ni} \quad (9\text{-}7)$$

Regarding proton diffusion in the electrolyte and electrode materials, it will be proton diffusion in YSZ (diffusion coefficient $D_{850°C} = 4 \cdot 10^{-7}$ cm^2/s [162]) that will contribute the most to the proton diffusion part of the polarisation resistance when compared to proton diffusion in the bulk of Ni ($D_{850°C} = 9 \cdot 10^{-5}$ cm^2/s [163]) or on a Ni surface ($D_{850°C} = 5 \cdot 10^{-4}$ cm^2/s [164]). Mogensen et al. [157] calculated a saturation concentration for protons in YSZ of $9.9 \cdot 10^{-7}$ mol/cm^3 at 986°C and a corresponding current density of $1.1 \cdot 10^{-4}$ A/cm^2, while they obtained a saturation concentration for protons in Ni of $1.0 \cdot 10^{-4}$ mol/cm^3 at 1000°C and this should enable that a considerable current density of 1.4 A/cm^2 can be sustained via bulk diffusion of protons in Ni.

Another possible reaction mechanism based on the assumption that H_2O will adsorb on the YSZ surface is given in Figure 9-1B and has recently been discussed by Mogensen et al. [161]. This mechanism involves conduction of electrons in the YSZ and can roughly be described by eq. 9-8 to 9-10. Again an intermediate step including adsorbed OH and H on YSZ could be added. Alternatively, the conduction of electrons in YSZ (eq. 9-10) can be replaced by surface diffusion of hydrogen from the YSZ to the TPB and electrons conducted in Ni to the TPB ie. eq. 9-11 and 9-12.

Figure 9-1B

$$H_2O(g) + \square_{ad,YSZ} \rightleftharpoons H_2O_{ad,YSZ} \quad (9\text{-}8)$$

$$\square_{ad,YSZ} + H_2O_{ad,YSZ} + V_{O,YSZ}^{\bullet\bullet} \rightleftharpoons O_{O,YSZ}^{x} + 2H_{ad,YSZ} \quad (9\text{-}9)$$

$$2e'_{YSZ} + 2H_{ad,YSZ} \rightleftharpoons H_2(g) + 2\square_{ad,YSZ} \quad (9\text{-}10)$$

$$2H_{ad,YSZ} \rightleftharpoons 2H_{ad,TPB} \quad (9\text{-}11)$$

$$2e'_{Ni} \rightleftharpoons H_2(g) + 2\square_{ad,TPB} \quad (9\text{-}12)$$

Figure 9-1C illustrates a mechanism with adsorption of H_2O on the Ni surface. This mechanism is based on the results reported by Mizusaki et al. [160] and was also sketched

in a slightly different form as one of the possible anodic reaction mechanisms by Holtappels et al. [155]. Mizusaki et al. [151] suggested, based on results obtained on Ni pattern electrodes on a single crystal YSZ, that the cathodic reaction mechanism should proceed via adsorbed OH and H species and that adsorbed oxygen should diffuse on the Ni surface to the TPB. They argued that the rate determining step was first order with respect to adsorbed hydrogen or surface diffusion of adsorbed hydrogen. Their suggestion for the cathodic reaction mechanism at the Ni/YSZ electrode can roughly be described by eq. 9-13 to 9-18.

Figure 9-1C

$$H_2O(g) + \square_{ad,Ni} \rightleftharpoons H_2O_{ad,Ni} \quad (9\text{-}13)$$

$$H_2O_{ad,Ni} + \square_{ad,Ni} \rightleftharpoons OH_{ad,Ni} + H_{ad,Ni} \quad (9\text{-}14)$$

$$OH_{ad,Ni} + \square_{ad,Ni} \rightleftharpoons O_{ad,Ni} + H_{ad,Ni} \quad (9\text{-}15)$$

$$2H_{ad,Ni} \rightleftharpoons H_2(g) + 2\square_{ad,Ni} \quad (9\text{-}16)$$

$$O_{ad,Ni} \rightleftharpoons O_{ad,TPB} \quad (9\text{-}17)$$

$$O_{ad,TPB} + 2e'_{Ni} + V^{\bullet\bullet}_{O,YSZ} \rightleftharpoons \square_{ad,Ni} + O^{x}_{O,YSZ} \quad (9\text{-}18)$$

In later work Mizusaki et al. [160] found that for both Ni pattern electrodes and for cermet electrodes, there appeared to be two different cathodic reaction paths depending on whether the data was obtained at low or high cathodic polarisation. For the low cathodic polarisation part they suggested that the slow diffusion of hydrogen i.e. $H_{ad,TPB} \rightarrow H_{ad,Ni}$ was rate determining, whereas they proposed that the reaction $2H_{ad,TPB} \rightarrow H_2$ (g) should be rate determining at high cathodic polarisation. Holtappels et al. [154] noted that the reaction mechanism during cathodic polarisation was less dependent on the charge transfer step than the anodic electrode reaction, and that the cathodic electrode reaction mechanism is complex and most probably involve various adsorbed species.

The mechanisms suggested by Mizusaki et al. [160] can be questionable for a couple of reasons: 1) In catalysis literature and as discussed by Skaarup et al. [164] adsorbed hydrogen is indeed very fast moving on Ni surfaces (see also Table 9-1) and it seems unlikely that diffusion of hydrogen adsorbed on the Ni surface should be rate determining and 2) most researchers report more than one, typically three, arcs in the impedance spectra obtained on Ni/YSZ cermets and the mechanism suggested by Mizusaki et al. does not seem to be able to account for this.

In Figure 9-1D a somewhat ideal situation is sketched. Here the H_2O is assumed to be adsorbed at the exact position of the TPB and only hydrogen has to diffuse on the Ni surface and desorps as H_2(g). In reality there are not an unlimited number of available TPBs and this will set a limit for the reaction mechanism sketched in Figure 9-1D, especially at high current densities.

Kawada et al. [165], Holtappels et al. [154] and Mizusaki et al. [151] included results and considerations on the electrode reaction mechanism for the H_2-H_2O-Ni-YSZ system at

cathodic polarisation. They all agreed that the rate determining steps under cathodic polarisation of the hydrogen electrode are not identical to the rate determining steps under anodic polarisation, but no consensus was obtained regarding the mechanism and rate determining steps under cathodic polarisation.
An important issue is not included in the above considerations on electrode reaction mechanism and typically it is not described or discussed in literature on the possible electrode reaction mechanisms either. It is the presence of impurities at the grain boundaries. Even cells that have not been used for long-term fuel cell or electrolysis testing most likely have nanoscale layers of impurities at the grain boundaries, e.g. silica impurities have been shown to segregate from the bulk of YSZ to the grain boundaries upon sintering [113; 137]. Levels of impurities in the raw materials and their chemical composition upon segregation to the grain boundaries may play an important role in the electrode reaction mechanism and be part of the discrepancy in the results reported on the reaction mechanisms for the H_2-H_2O-Ni-YSZ system.
Even in recent reviews (e.g. [161]) of the electrode reaction mechanism in the H_2-H_2O-Ni-YSZ system, where also new and relatively detailed modelling work was considered [152; 166], it seems that there does not exist a complete and well consolidated understanding of the electrode reaction mechanism at anodic polarisation for the H_2-H_2O-Ni-YSZ system, and even less is known about the reaction mechanism under cathodic polarisation.

Origin and accumulation of impurities at TPBs
As described in chapter 6, the raw materials used for the cells tested within this project contain impurities at ppm level. Typically the impurities are immiscible with the bulk phase and more stable at the free surfaces [139], and they will accumulate at the grain boundaries during sintering. In literature several examples can be found [78; 89; 100; 117; 127; 137; 139] reporting that impurities, mainly silica, segregate to the YSZ grain boundaries and Ni-YSZ interfaces and this affects the resistances and in particular the grain boundary resistance [78; 113; 127; 139]. Furthermore, it is worthwhile to emphasise that most of these studies were made in SOFC relevant atmospheres i.e. low $p(H_2O)/p(H_2)$ ratios. The higher $p(H_2O)/p(H_2)$ ratios for SOEC operation of the cells can be expected to cause a higher mobility and lower viscosity for the glassy phase impurities.
Both SEM/EDS in chapter 6 and especially the TEM/STEM/EDS results presented in chapter 7 gave evidence that glassy phase impurities accumulated at the TPBs in the hydrogen electrode of tested SOECs. Impurities were not detected in the two reference cells. This means that for reference cells impurities have not accumulated to the same extent as for tested SOECs. Nevertheless, FIB/TEM/STEM/EDS analysis of reference cells to verify if there are segregated impurities in a “few-nanometer-scale” at the grain boundaries still need to be performed. Considering the “opposite” inlet and outlet gas compositions for fuel cell and electrolysis operation and the shift in potential gradients for the two operation modes for SOCs, it appears logic that an activation of a passivated SOEC can be obtained by fuel cell operation of the cell by which impurities can be withdrawn from the reaction sites.

Effect of impurities

A schematic illustration of a TPB blocked by an impurity phase is shown in Figure 9-2. Some conductivity and diffusion coefficient data for silica and Na-Si glasses from literature is summarised in Table 9-1. To be able to compare data from literature only diffusion coefficients obtained on silica glasses have been included in Table 9-1, even though the EDS results in chapter 7 show that sodium containing alumina silicates should be considered as well, but data on a variety of glass compositions can be difficult to compare. Considering the data given in Table 9-1 a reaction path at a blocked TPB could proceed via diffusion of OH and H species in or on the glassy phase impurity, and it seems very unlikely that the reaction mechanism suggested by Mizusaki et al. [151] for cathodic operation i.e. via adsorbed oxygen will occur in this case as the diffusion coefficient for oxygen in silica is orders of magnitudes lower then for H, OH and H_2O diffusion in silica (Table 9-1).

Considering the simple sketch in Figure 9-2 reaction mechanisms that proceed via diffusion of species in the bulk of Ni and YSZ (Figure 9-1A and Figure 9-1B) can be relevant for electrolysis tested cells in which impurities have certainly accumulated at the TPBs. Nevertheless, it can only be suggestions for possible cathodic reaction mechanisms as long as the nature of cathodic electrode mechanism and rate determining steps are not even known for non-degraded SOECs. Furthermore, our knowledge on the exact geometrical shape (e.g. do the impurities stretch from the TPB and along the Ni and/or YSZ surface?) and chemical composition of the impurities is far too sporadic. It should be noted that properties such as diffusivity, viscosity (chapter 6) and conductivity (Table 9-1) can easily change orders of magnitudes when a glass modifier such as Na is present in the glass or few hundred ppm of H_2O are dissolved in the glass. Such changes in the properties of the glass phase impurities may easily affect the reaction mechanism at these sites.

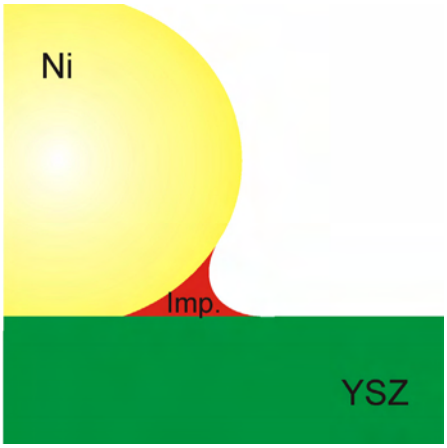

Figure 9-2: Sketch of a TPB in the hydrogen electrode blocked by an impurity phase. The size of the impurity phases in tested SOECs has been found to range from few tenths of nanometres up to a micron.

Table 9-1: Diffusion coefficients reported in literature for H, OH, O and H_2O in SiO_2, YSZ and Ni and conductivity for some Na-Si glasses.

Species	Diff. coef. (cm^2/s)	Temp. (°C)	Ref.	Note
O	$2 \cdot 10^{-23}$	850	[167]	SiO_2, bulk
O	$3 \cdot 10^{-23}$	850	[167]	SiO_2, surface
O	$6 \cdot 10^{-19}$	1000	[168]	SiO_2, bulk, 10 ppm H_2O in oxygen
OH	$3 \cdot 10^{-9}$	850	[169]	SiO_2, bulk
OH	$3 \cdot 10^{-9}$	850	[169]	SiO_2, bulk
H_2O	$1 \cdot 10^{-10}$	800	[170]	SiO_2, bulk
H_2O	$1 \cdot 10^{-10}$	850	[171]	SiO_2, bulk
H	$2 \cdot 10^{-7}$	850	[172]	SiO_2, bulk at $p(H_2) = 0.5$ atm.
H	$4 \cdot 10^{-7}$	850	[162]	YSZ, bulk
H	$9 \cdot 10^{-5}$	850	[163]	Ni, bulk
H	$5 \cdot 10^{-4}$	850	[164]	Ni, surface
Na/Si ratio	**Conductivity (S/cm)**	**Temp. (°C)**	**Ref.**	**Note**
0/100	$1 \cdot 10^{-6}$	400	[173]	Large ions (e.g. Ca and Mg) decrease the conductivity, while K and Na increase the conductivity.
15/85	$1 \cdot 10^{-4}$	400	[173]	
40/60	$7 \cdot 10^{-3}$	400	[173]	

It can be concluded that with the observed variation in the chemical composition and the lack of knowledge regarding the exact chemical composition and physical properties at SOEC operating conditions for the impurity phases observed at the TPBs after electrolysis testing, it is not possible to establish a well consolidated reaction mechanism for these sites at present.

Jensen [76] performed a detailed analysis and modelling of impedance spectra recorded during the short-term passivation. He concluded that this passivation could be due to an increased diffusion path length for hydrogen and oxygen at the TPBs, and this appear to fit well with an accumulation of impurities at the TPBs. Results from substituting the H_2/H_2O mixture with CO_2/CO revealed that diffusion of both hydrogen and oxygen containing species at the TPBs play a role and not just one of the species. It should be emphasized that the results presented by Jensen relate to the short-term passivation of the SOECs, and that the development in the impedance spectra during the long-term degradation (constant summit frequency for the arc with increasing impedance) do not resemble the development during the short-term passivation (decreasing summit frequency for the arc with increasing impedance). Further EIS analysis for the long-term degradation mechanism is necessary.

Modification of impurity phases

It is nearly impossible to completely avoid impurities in the SOCs without significantly increasing the cost of the SOCs. Therefore in the economical perspective for SOCs

modifications and attempts to control the impurities in the SOCs are of utmost importance. A solution can be the addition of an impurity scavenger in the hydrogen electrode.

One of the most well-known Si scavengers is alumina as reported by e.g. Lybye and Liu [117] and by Drennan and Butler [113; 174]. As shown in chapter 5, alumina is already present in the active hydrogen electrode prior to reduction of the NiO before the start of electrolysis testing. EDS results presented in chapter 7 indicate that alumina does act as Si scavenger in the SOEC, but not at all to a sufficient extent. If alumina is to be used as scavenger in these SOECs the amount of and distribution of alumina will need to be optimised.

Other well-known glass modifiers are K_2O [175] and vanadium (V^{3}+ and V^{4+}) [122; 175]. A preliminary attempt to impregnate a hydrogen electrode of an SOC was performed in this project by impregnation with V_2O_5. This was successful in the sense that the cell with the impregnated hydrogen electrode had a weight gain of 1% and SEM/EDS investigations of a non-reduced test piece impregnated in the exact same way as the cell for testing revealed that the impregnated vanadium was evenly distributed throughout the support layer and the active electrode (see Figure 9-3). Vanadium oxide particles in the size range of ~100-200 nm were found in the active Ni/YSZ layer. Unfortunately this impregnation was not successful in a SOEC test perspective as the impregnated cell had a cell voltage curve comparable with the cell voltage curve of the non-impregnated cell for 3test21 (see 3test21 and 3test28 in Appendix A).To develop cells with effective scavengers it is clearly necessary to both map the chemical composition and distributions/geometries of the accumulated impurities in the electrode structure, but also to control the amount and distribution of the potential scavenger in the active hydrogen electrode.

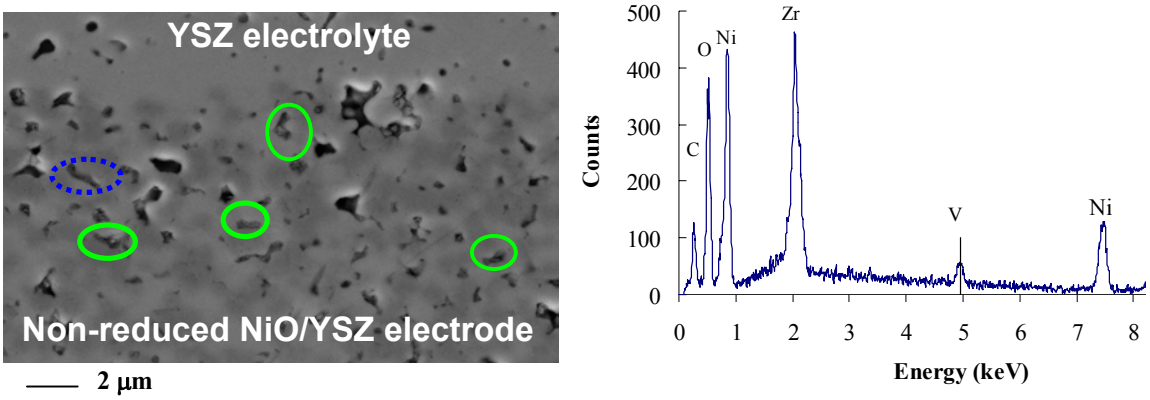

Figure 9-3: Hydrogen electrode impregnated with vanadium (V_2O_5 dissolved in citric acid). Circles in the SEM micrograph indicate where vanadium was detected using point EDS analysis. The location of the spectrum is marked by the dotted blue circle in the SEM micrograph.

10. Conclusions

From the results presented in the previous chapters the following main conclusions can be drawn:

- The SOCs produced at Risø National Laboratory have the best initial electrolysis performance reported in literature to date e.g. an area specific resistance (ASR) as low as 0.26 Ωcm^2 at 850°C and 0.17 Ωcm^2 at 950°C obtained from iV curves in electrolysis mode.
- The SOCs operate continuously across OCV; however the ASR in electrolysis mode was higher than in fuel cell mode.
- A short-term passivation occurs over the first 100-200 hours of electrolysis testing. The courses of cell voltage curves versus time were non-linear and with a characteristic "S"-shape. Tests applying different sealing materials revealed that the short-term passivation was an effect of the albite glass used as sealing material in the cell test set-up.
- The SOCs reactivated at constant electrolysis conditions after the short-term passivation. The ohmic resistances were unaffected by the short-term passivation/activation phenomenon while the polarisation resistances increased and decreased during this phenomenon.
- A quicker partial reactivation of an SOEC could be obtained by fuel cell operation of the cell after the short-term passivation.
- Long-term degradation of the SOECs showed a linear trend in time. Long-term degradation rates of 2%/1000 h at 850°C, $p(H_2O)$ = 0.5 atm and -0.5 A/cm^2 and 6%/1000 h at 950°C, $p(H_2O)$ = 0.9 atm and -1.0 A/cm^2 were obtained. This is significantly higher than for similar cells tested in fuel cell mode (below 2%/1000 h at 950°C and -1.7 A/cm^2).
- EIS results showed that the short-term passivation was due to an increase in the resistance for the diffusion of reacting species in the hydrogen electrode.
- EIS results showed that the long-term degradation was mainly caused by a loss in performance for the hydrogen electrode.
- SEM investigations of the Ni particle size distributions showed that the Ni size distributions for tested SOECs have changed compared to reference cells. Ni size distributions for SOEC tested cells were similar to distributions obtained on long-term fuel cell tested cells.
- The changes in the Ni particle size distribution for tested SOECs may contribute to the degradation of the SOECs; however this was not the main reason for the observed loss in performance for the SOECs.
- Silicon containing impurities have been observed by SEM/EDS to segregate to the innermost few microns of the hydrogen electrode closest to the electrolyte.

- The impurities were found as rims around the Ni particles i.e. a kind of surface layer in some of the SOCs and as discrete particles in more regular shapes in some SOCs.
- EDS results led to estimates of the total amount of impurities accumulated in the innermost few microns for a couple of tested cells. From these estimates it could be concluded that the detected impurities could not only originate from the raw materials but contributions from "external" impurity sources must be involved as well. It was later shown that the albite glass sealing contributed to the Si-contamination by the relative high (~10^{-7} atm) partial pressure of $Si(OH)_4$. Silicon tetra hydroxide will form silica according to the equation below, when the reduction of steam is started i.e. when the electrolysis current is applied:

$$Si(OH)_4 \rightleftharpoons SiO_2 + 2H_2O \qquad (10\text{-}1)$$

- The impurity phases always contained silicon oxide, and mostly also aluminium oxide. Furthermore, sodium was detected in some of the impurity phases. The typical ratio for Na/Al/Si was ~ 1/3/3. The Al oxides may originate from the alumina that was added as sintering aid during the production of the cells.
- The amorphous impurity phases reached an extent of several hundred nanometres in scale. These amorphous impurity phases appear to have embedded nanocrystalline particles embedded.
- The impurities that diffused to and accumulated at the TPBs of the hydrogen electrode of tested SOECs were believed to be the main reason for the loss in performance for the SOECs produced at Risø National Laboratory.

11. Outlook

After three years of work with SOEC testing, characterisation and post-mortem analysis there are still many areas that need to be explored further and where improvements are required. Some of these are listed below.

- An optimisation of glass sealing to avoid impurity contamination from the sealing material is necessary. A suggestion could be to apply a coating that works both as a physical barrier for the evaporation of Si, Al and Na hydroxides, but also as a chemical barrier by reacting with e.g. $Si(OH)_4$.
- Interconnect materials need to be optimised for SOECs application and tested both in single repeating units (SRU) and in stacks.
- Several long-term tests at varying operating conditions need to be performed where the impurity contamination from external sources such as the sealing material has been avoided. It is necessary to map the "set-up-independent" long-term degradation at various conditions in order to be able to optimise the SOC for electrolysis purposes.
- Combined FIB, TEM, STEM and EDS analysis of long-term tested SOECs from tests where the impurity contamination from the sealing material has been avoided. This is necessary to obtain an understanding of the processes leading to the loss in performance for the SOECs (the set-up independent loss in performance).
- For comparison, it will also be necessary with similar FIB, TEM, STEM and EDS analysis of reference cells and long-term fuel cell tested cells.
- Thorough electron microscopy and analysis to map the chemical composition and nanostrucuture of the impurities accumulating at the TPBs in order to obtain the knowledge to control these impurities e.g. by use of scavengers.
- As the SOCs produced at Risø National Laboratory have shown excellent initial electrolysis performance, it is worthwhile to try to develop scavengers in order to control the impurities and keep the TPBs free for the electrochemical reactions.
- Recently, preliminary tests of hydrogen electrodes based on niobium-doped strontium titanate for a model system showed promising initial performance also in electrolysis mode [176]. This has been up scaled up to full 5x5 cm^2 cells and now need to be tested at a variety of electrolysis test conditions.
- The potential for CO_2 electrolysis using SOECs should be investigated by tests and characterisation at various electrolysis test conditions followed by post-mortem analysis. Investigations of SOECs for combined electrolysis of CO_2 and H_2O for synthesis gas production should be performed to map the potential of using SOECs in the process of synthetic fuel production.

- SOEC tests should be performed on stack level at various test conditions to map potential problems and investigate limitations for SOEC stacks. In the long term such SOEC stack results should form the basis for analysis on how to design an optimal complete SOEC system (stacks, heat exchanger, gas supply etc.) which should be possible to integrate in larger energy systems e.g. in combination with surplus energy from wind turbines or in combination with nuclear power facilities.

Hopefully, a successful and rewarding completion of these suggested points - and probably many other points - within the field of SOECs could bring us closer to the answer for the ultimate question: How do we develop the SOEC technology in order for it to become a cost competitive, reliable and market mature technology for hydrogen and synthetic fuel production?

12. References

1. Minh, N.Q. and Takahashi, T. *Science and Technology of Ceramic Fuel Cells*, Elsevier Science B.V., Amsterdam (1995).

2. Singhal, S.C. and Kendall, K. *High Temperature solid Oxide Fuel Cells. Fundamentals, Design, and Applications*, Elsevier Ltd., Oxford, UK (2004).

3. Etsell, T. H. and Flengas, S. N. *Chemical Reviews*; **70** (3), p. 339 (1970).

4. Atkins, P.W. *Physical Chemistry*, Oxford University Press, Oxford (1998).

5. Bard, A.J. and Faulkner, L.R. *Electrochemical Methods. Fundamentals and Applications*, John Wiley & Sons Inc., New York (1980).

6. Ivers-Tiffée, E. and Virkar, A.V., in *High Temperature Solid Oxide Fuel Cells - Fundamentals, Design, and Applications*, edited by Singhal, S.C. and Kendall, K. p. 229-260. Elsevier Ltd., Oxford 2003.

7. Brown, M., Primdahl, S., and Mogensen, M. *Journal of the Electrochemical Society*; **147** (2), p. 475-485 (2000).

8. Mogensen M and Hendriksen PV, in *High temperature solid oxide fuel cells - Fundamentals, design and applications*, edited by Singhal, S.C. and Kendall, K. p. 261-289. Elsevier, London 2003.

9. Primdahl, S. and Mogensen, M. *Journal of the Electrochemical Society*; **145** (7), p. 2431-2438 (1998).

10. Primdahl, S. and Mogensen, M. *Journal of the Electrochemical Society*; **146** (8), p. 2827-2833 (1999).

11. Barfod, R., Hagen, A., Ramousse, S., Hendriksen, P. V., and Mogensen, M., *6th European Solid Oxide Fuel Cell Forum Proceedings*; p. 960-969, edited by Mogensen, M.; (2004)

12. Primdahl, S. and Mogensen, M. SOFC-VI, *Proceedings - The electrochemical Society*; **PV97-07**; p. 530-537, edited by Stimming, U., Singhal S.C., Takagi, H., and Leming, A.; (1997)

13. Barfod, R., Mogensen, M., Klemmensoe, T., Hagen, A., Liu, Y. L., and Hendriksen, P. V. SOFC-IX, *Proceedings - Electrochemical Society*; **PV2005-07**; p. 524-533, edited by Singhal, S.C. and Mizusaki, J.; (2005)

14. Appel, C. C., Bonanos, N., Horsewell, A., and Linderoth, S. *Journal of Materials Science*; **36**, p. 4493-4501 (2001).

15. Visco, S. J., Jacobson, C. P., Villareal, I., Leming, A., Matus, Y., and De J., Lutgard C. SOFC VIII, *Proceedings - Electrochemical Society*; **PV2003-7**; p. 1040-1050, edited by Singhal, S.C. and Dokiya, M; (2003)

16. van Berkel, F. P. F., van Heuveln, F. H., and Huijsmans, J. P. P. Proceedings of the Third International Symposium on Solid Oxide Fuel Cells, *Proceedings - Electrochemical Society*; **PV93-4**; p. 744-751, edited by Singhal, S.C. and Iwahara, H.; (1993)

17. Huijsmans, J. P. P., de Jong, J. P., van Heuveln, F. H., and van Berkel, F. P. F. SOFC-IV, *Proceedings - Electrochemical Society*; **PV95-1**; p. 94-99, edited by Dokiya, M., Yamamoto, O., Tagawa, and Singhal, S.C.; (1995)

18. Ouweltjes, J. P., van Berkel, F. P. F., Nammensma, P., and Christie, G. M. Solid Oxide Fuel Cells (SOFC VI), *Proceedings - Electrochemical Society*; **PV99-19**; p. 803-811, edited by Singhal, S.C. and Dokiya, M; (1999)

19. Singhal, S. C. EUR 13564, Proc. Int. Symp. Solid Oxide Fuel Cells, 2nd, *Comm.Eur.Communities, [Rep.] EUR*; p. 25-33, edited by Grosz, F., Zegers, P., Singhal, S.C., and Yamamoto, O.; (1991)

20. DiGiuseppe, G. SOFC-IX, *Proceedings - The Electrotrochemical Society*; **PV2005-07**; p. 322-333, edited by Singhal, S.C. and Mizusaki, J.; (2005)

21. Dönitz, W., Erdle, E., Schaefer, W., Schamm, R., and Spaeh, R. Proc. Int. Symp. Solid Oxide Fuel Cells, 2nd, *Comm.Eur.Communities, [Rep.] EUR*; p. 75-84, edited by Grosz, F., Zegers, P., Singhal, S.C., and Yamamoto, O.; (1991)

22. Stover, D., Diekmann, U., Flesch, U., Kabs, H., Quadakkers, W. J., Tietz, F., and Vinke, I. C. Solid Oxide Fuel Cells (SOFC VI), *Proceedings - Electrochemical Society*; **PV99-19**; p. 812-821, edited by Singhal, S.C. and Dokiya, M; (1999)

23. Becker, M., Mai, A., Ivers-Tiffée, E., and Tietz, F. SOFC-IX, *Proceedings - Electrochemical Society*; **PV2005-07**; p. 514-523, edited by Singhal, S.C. and Mizusaki, J.; (2005)

24. Khandkar, Ashok C., Stuffle, Kevin L., and Elangovan, S. Proc. Int. Symp. Solid Oxide Fuel Cells, 1st, *Proceedings - Electrochemical Society*; **PV89-11**; p. 377-383, edited by Singhal, S.C.; (1989)

25. Elangovan, S., Hartvigsen, J., and Khandkar, A. Solid Oxide Fuel Cells (SOFC-IV), *Proceedings - Electrochemical Society*; **PV95-1**; p. 146-152, edited by Dokiya, M., Yamamoto, O., Tagawa, and Singhal, S.C.; (1995)

26. Bakker, W., Milliken, C., Hartvigsen, J., Elangovan, S., and Khandkar, A. Solid Oxide Fuel Cells, *Proceedings - Electrochemical Society*; **PV97-40**; p. 254-263, edited by Stimming, U., Singhal, S.C., Takagi, H., and Leming, A.; (1997)

27. Dokiya, M, Sakai, N., Kawada, T., Yokokawa, H., Iwata, T., and Mori, M. Proc. Int. Symp. Solid Oxide Fuel Cells, 1st, *Proceedings - Electrochemical Society*; **PV89-11**; p. 325-336, edited by Singhal, S.C.; (1989)

28. Takagi, H., Kobayashi, S., Shiratori, A., Nishida, K., and Sakabe, Y. Proc. Int. Symp. Solid Oxide Fuel Cells, 2nd, *Comm.Eur.Communities, [Rep.] EUR*; p. 99-103, edited by Grosz, F., Zegers, P., Singhal, S.C., and Yamamoto, O.; (1991)

29. Hikita, T., Hishinuma, M., Kawashima, T., Yasuda, I., Koyama, T., and Matsuzaki, Y. Proceedings of the Third International Symposium on Solid Oxide Fuel Cells, *Proceedings - Electrochemical Society*; **PV93-4**; p. 714-723, edited by Singhal**,** S.C. and Iwahara, H.; (1993)

30. Sumi, H., Ukai, K., Hisada, K., Mizutani, Y., and Yamamoto, O. Solid Oxide Fuel Cells VIII (SOFC VIII), *Proceedings - Electrochemical Society*; **PV2003-7**; p. 995-1002, edited by Singhal, S.C. and Iwahara, H.; (2003)

31. Hagen, A., Menon, M., Barfod, R., Hendriksen, P. V., Ramousse, S., and Larsen, P. H. *Fuel Cells*; **6** (2), p. 146-150 (2006).

32. Hagen, A., Barfod, R., Hendriksen, P. V., Liu, Y. L., and Ramousse, S. *Journal of the Electrochemical Society*; **153** (6), p. A1165-A1171 (2006).

33. Wang, W. and Mogensen, M. *Solid State Ionics*; **176**, p. 457-462 (2005).

34. Blennow, P., Hansen, K. K., Wallenberg, R. L., and Mogensen, M. *Electrochimica Acta*; **52** (4), p. 1651-1661 (2006).

35. Christiansen, N., Kristensen, S., Holm-Larsen, H., Larsen, P. H., Mogensen, M., Hendriksen, P. V., and Linderoth, S. Solid Oxide Fuel Cells VIII (SOFC VIII),

Proceedings - Electrochemical Society; **PV2003-7**; p. 105-112, edited by Singhal, S.C. and Dokiya, M; (2003)

36. Larsen, PV, Mogensen, M, Linderoth, S., Hansen, K. K., and Wang, W. (Forskningscenter Risø, Den. **2005-DK379** (2005122300), p. 25 (2005). WO. 9-6-2005.

37. Bagger, C., Hennesoe, E., and Mogensen, M. Proceedings of the Third International Symposium on Solid Oxide Fuel Cells, 1993, *Proceedings - Electrochemical Society*; **PV93-4**; p. 756-765, edited by Singhal, S.C. and Iwahara, H.; (1993)

38. Primdahl, S., Jorgensen, M. J., Bagger, C., and Kindl, B. Solid Oxide Fuel Cells (SOFC VI), *Proceedings - Electrochemical Society*; **PV99-19**; p. 793, edited by Singhal**,** S.C. and Dokiya, M; (1999)

39. Bagger, C., Linderoth, S., Mogensen, M., Hendriksen, P. V., Kindl, B., Primdahl, S., Larsen, P. H., Poulsen, F. W., Bonanos, N., and Jorgensen, M. J. Solid Oxide Fuel Cells (SOFC VI), *Proceedings - Electrochemical Society*; **PV99-19**; p. 28-35, edited by Singhal, S.C. and Dokiya, M; (1999)

40. Larsen, P. H., Bagger, C., Linderoth, S., Mogensen, M., Primdahl, S., Jorgensen, M. J., Hendriksen, P. V., Kindl, B., Bonanos, N., Poulsen, F. W., and Maegaard, K. A. Solid Oxide Fuel Cells VII, *Proceedings - Electrochemical Society*; **PV2001-16**; p. 28-37, edited by Yokokawa, H. and Singhal, S.C.; (2001)

41. Primdahl, S., Hendriksen, P. V., Larsen, P. H., Kindl, B., and Mogensen, M. Solid Oxide Fuel Cells VII, *Proceedings - Electrochemical Society*; **PV 2001-16**; p. 932-941, edited by Yokokawa, H. and Singhal, S.C.; (2001)

42. Hagen, A., Barfod, R., Hendriksen, P. V., Liu, Y. L., and Ramousse, S. SOFC IX, *Proceedings - Electrochemical Society*; **PV 2005-07**; p. 503-512, edited by Singhal, S.C. and Mizusaki, J.; (2005)

43. Dönitz, W., Schmidberger, R., Steinheil, E., and Streicher, R. *International Journal of Hydrogen Energy*; **5** (1), p. 55-63 (1980).

44. Erdle, E., Dönitz, W., Schamm, R., and Koch, A. *International Journal of Hydrogen Energy*; **17** (10), p. 817-819 (1992).

45. Dönitz W, Erdle E and Streicher R, in *Electrochemical Hydrogen Technologies. Electrochemical Production and Combustion of Hydrogen*, edited by Wendt H. p. 213-259. Elsevier, 1990.

46. Dönitz, W. and Erdle, E. *International Journal of Hydrogen Energy*; **10** (5), p. 291-295 (1985).

47. Dönitz, W., Dietrich, G., Erdle, E., and Streicher, R. *International Journal of Hydrogen Energy*; **13** (5), p. 283-287 (1988).

48. Dönitz, W., Erdle, E., Schaumm, R., and Streicher, R. *Advances in Hydrogen Energy*; **6**, p. 65-73 (1988). 25-9-1988.

49. Isenberg, A. O. *Solid State Ionics*; **3-4**, p. 431-437 (1981).

50. O'Brien, J.E., Stoots, C. M., Herring, J. S., Lessing, P.A., Hartvigsen, J. and Elangovan, S., *Proceedings of ICONE12, 12th International Conference on Nuclear Engineering*, Virginia, USA; (2004)

51. Hartvigsen, J., Elangovan, S., O'Brien, J. E., Stoots, C. M., Herring, J. S., and Lessing, P., *Proceedings - 6th European Solid Oxide Fuel Cell Forum*; p. 378-387, edited by Mogensen, M.; (2004)

52. O'Brien, J. E., Stoots, C. M., Herring, J. S., and Hartvigsen, J. *Journal of Fuel Cell Science and Technology*; **3** (2), p. 213-219 (2006).

53. Marina, O. A. and L.R.Pederson, *Proceedings - 6th European Solid Oxide Fuel Cell Forum*; p. 388-391, edited by Mogensen, M.; (2004)

54. Wang, W. S., Huang, Y. Y., Jung, S. W., Vohs, J. M., and Gorte, R. J. *Journal of the Electrochemical Society*; **153** (11), p. A2066-A2070 (2006).

55. Utgikar, V. and Thiesen, T. *International Journal of Hydrogen Energy*; **31** (7), p. 939-944 (2006).

56. Uchida, H., Osada, N. N., and Watanabe, M. *Electrochemical and Solid-State Letters*; **7** (12), p. A500-A502 (2004).

57. Osada, N. N., Uchida, H., and Watanabe, M. *Journal of the Electrochemical Society*; **153** (5), p. A816-A820 (2006).

58. Hino, R., Haga, K., Aita, H., and Sekita, K. *Nuclear Engineering and Design*; **233** (1-3), p. 363-375 (2004).

59. Hong, H. S., Chae, U. S., Choo, S. T., and Lee, K. S. *Journal of Power Sources*; **149**, p. 84-89 (2005).

60. Zhu, B., Albinsson, I., Andersson, C., Borsand, K., Nilsson, M., and Mellander, B. E. *Electrochemistry Communications*; **8** (3), p. 495-498 (2006).

61. Hauch, A., Jensen, S. H., Mogensen, M., and Ramousse, S. *Journal of the Electrochemical Society*; **153** (9), p. A1741-A1747 (2006).

62. Hauch, A., Jensen, S. H., and Mogensen, M., *Solid State Electrochemistry, Proceedings of the 26th Risø International Symposium on Materials Science, Roskilde, Denmark*; p. 203-208, edited by Linderoth, S., Smith, A., Bonanos, N., Hagen, A., Mikkelsen, L., Hansen, K. K., Lybye, D., Hendriksen, P. V., Poulsen, F. W., Mogensen, M., and Wang, W.; (2005)

63. Jensen, S. H., Hauch, A., and Mogensen, M., *Solid State Electrochemistry, Proceedings of the 26th Risø International Symposium on Materials Science, Roskilde, Denmark*; p. 247-252, edited by Linderoth, S., Smith, A., Bonanos, N., Hagen, A., Mikkelsen, L., Hansen, K. K., Lybye, D., Hendriksen, P. V., Poulsen, F. W., Mogensen, M., and Wang, W.; (2005)

64. Lide DR. *Handbook of Chemistry and Physics*, (2004).

65. Yidiz, B. and Kazimi, M. S. *International Journal of Hydrogen Energy*; **31** (1), p. 77-92 (2006).

66. Mansilla, C., Sigurvinsson, J., Bontemps, A., Marechal, A., and Werkoff, F. *Energy*; **32** (4), p. 423-430 (2007).

67. Henriksen, N. From Petrol to REtrol (presented at Risø International Energy Conference 2005). *http://www.risoe.dk/rispubl/SYS/syspdf/energconf05/session4_henriksen_pre.pdf*; (2005).

68. Jensen, S. H., Høgh, J. T. V., Barfod, R. and Mogensen, M. *Proceedings of Risø International Energy Conference 19-21 May 2003*; p. 204-215, edited by Larsen, H. and Sønderberg Petersen, L; (2003)

69. Jensen, S. H., Hauch, A., and Mogensen, M., *HYPOTHESIS V*, Havana, Cuba; (2005)

70. Jensen, S. H., Larsen, P. H., and Mogensen, M. *International Journal of Hydrogen Energy* (In press) (2007).

71. Mogensen, M., Jensen, S. H., Hauch, A., Chorkendorf, I., and Jacobsen, T., *Proceedings of 32nd International Cocoa Beach Conference & Exposition on Advanced Ceramics and Composites*, The American Ceramic Society; (2007)

72. Bagger, C. in *Fuel Cell Seminar*; p. 241, edited by Pax, C. E. (1992)

73. Jørgensen, M. J. and Mogensen, M. *Journal of the Electrochemical Society*; **148** (5), p. A433-A442 (2001).

74. Hagen, A., Menon, M., Ramousse, S., Larsen, P. H., Barfod, R. and Hendriksen, P. V. *Proceedings of 6th European Solid Oxide Fuel Cell Forum Proceedings*; p. 930-939, edited by Mogensen, M. Luzerne, Switzerland (2004)

75. Barfod, R., Kock, S., Liu, Y. L., Larsen, P. H., Mogensen, M., and Hendriksen, P. V., *Proceedings - The Electrotrochemical Society (SOFC-VIII)*; **PV 2003-07**; p. 1158-1166, edited by Singhal, S.C. and Dokiya, M; (2003)

76. Jensen S.H. *Solid oxide electrolyser cell* (Thesis). Risø National Laboratory, Denmark, 2006.
ISBN 1399-2236

77. Macdonald, J. R. and Barsoukov, E. *Impedance Spectroscopy. Theory, Experiment, and Applications*, John Wiley & Sons, Inc., Hoboken, US (2005).

78. Liu, Y. L., Primdahl, S., and Mogensen, M. *Solid State Ionics*; **161** (1-2), p. 1-10 (2003).

79. Goodhew, P.J., Humphrey, J. and Beanland, R. *Electron Microscopy and Analysis*, Taylor & Francis, London (2001).

80. Hovington, P., Drouin, D., and Gauvin, R. *Scanning*; **19** (1), p. 1-14 (1997).

81. Mogensen, M., Larsen, P. H., Hendriksen, P. V., Kindl, B., Bagger, C. and Linderoth, S., Solid Oxide Fuel Cells (SOFC VI), *Proceedings - Electrochemical Society*; **PV99-19**; p. 904-915, edited by Singhal, S.C. and Dokiya, M. (1999)

82. Hauch, A., Jensen, S. H., Mogensen, M., and Bilde-Sørensen, J. B. *Journal of the Electrochemical Society*; **154** (7), p. A619-A626 (2007).

83. Dönitz, W. and Erdle, E. *International Journal of Hydrogen Energy,* **10**, p. 291-295 (1985).

84. Erdle, E., Dönitz, W., Schaumm, R. and Koch, A. *International Journal of Hydrogen Energy,* **17**, p. 817-819 (1992).

85. Eguchi, K., Hatagishi, T. and Arai, H. *Solid State Ionics,* **86-88**, p. 1245-1249 (1996).

86. Momma, A., Kato, T., Kaga, Y. and Nagata, S. *Journal of The Ceramic Society of Japan,* **105**, p. 369-373 (1997).

87. Herring, J. S., Lessing, P.A., O'Brien, J. E., Stoots, C. M., Hartvigsen, J., and Elangovan, S. *Second Information Exchange Meeting on Nuclear Production of Hydrogen*; p. 1-15 Argonne National Laboratory, Illinois, USA (2003).

88. O'Brien, J. E., Stoots, C. M., Herring, J. S., and Lessing, P. A. *Journal of Fuel Cell Science and Technology*; **2** (3), p. 156-163 (2005).

89. Jensen, K. V., Wallenberg, R., Chorkendorff, I., and Mogensen, M. *Solid State Ionics*; **160** (1-2), p. 27-37 (2003).

90. Liu, Y.-L. and Jiao, C. *Solid State Ionics*; **176**, p. 435-442 (2005).

91. Jensen, S. H., Hauch, A., Mogensen, M., Jacobsen, T., and Chorkendorff, I. *Journal of the Electrochemical Society* (submitted); (2006).

92. Primdahl, S. *Nickel/Yttria-Stabilised Zirconia Cermet Anodes for Solid Oxide Fuel Cells* (Thesis). Roskilde, Denmark: Risø National Laboratory, 1999.

93. Jensen, K.V. *The nickel-YSZ interface. Structure, composition and electrochemical properties at 1000 deg. C.* (Thesis). Risø National Laboratory, Technical University of Denmark, 2002.

94. Juhl Jørgensen, M. *Lanthanum manganate based cathodes for solid oxide fuel cells* (Thesis). Risø National Laboratory, Technical University of Denmark, 2001.

95. Barfod, R., Mogensen, M., Klemensø, T., Hagen, A., Liu, Y. L., and Hendriksen, P. V. *Journal of the Electrochemical Society*; **154** (4), p. B371-B378 (2007).

96. Jacobsen, T., Zachau-Chrisiansen, B., Bay, L., and Skaarup, S., *Proceedings of the 17th Risø International Symposium on Materials Science*; p. 29-40, edited by Poulsen, F. W., Bonanos, N., Linderoth, S., Mogensen, M., and Zachau-Christiansen, B., Roskilde, Denmark, Risø National Laboratory; (1996)

97. Jacobsen, T. and West, K. *Electrochimica Acta*; **40** (2), p. 255-262 (1995).

98. Johnson, D., Zview2.8, Scribner Associates, Inc.(2003)

99. Jensen, S. H., Hauch, A., Hendriksen, P.V., Mogensen, M., Bonanos, N., and Jacobsen, T. *Journal of the Electrochemical Society* (in press); (2007).

100. Vels Jensen, K., Primdahl, S., Chorkendorff, I., and Mogensen, M. *Solid State Ionics*; **144**, p. 197-209 (2001).

101. Vels Jensen, K., Wallenberg, R.L., Chorkendorff. I. and Mogensen, M. *Solid State Ionics,* **160**, p. 27-37 (2003).

102. Underwood, E. E. *American Society for Testing and Materials*; **504**, p. 3-38 (1972).

103. Thydén, K., Liu, Y.-L., and Bilde-Sørensen, J. B. *Solid State Ionics*; (submitted) (2007).

104. Phillips, B., Hutta, J. J., and Warshaw, I. *Journal of the American Ceramic Society*; **46** (12), p. 579-583 (1963).

105. NIST - National Institute of Standards and Technology. **Version 3.0** (2007). The American Ceramic Society.

106. Marina, O. A., Pederson, L. R., Williams, M. C., Coffey, G. W., Meinhardt, K. D., Nguyen, C. D., and Thomsen, E. C. *Journal of the Electrochemical Society*; **154** (5), p. B452-B459 (2007).

107. Brown, M., Primdahl, S., and Mogensen, M. *Journal of the Electrochemical Society*; **147** (2), p. 475-485 (2000).

108. Sehested J. *Catalysis Today,* **111**, p. 103-110 (2006).

109. Blennow, P., Hansen, K. K., Wallenberg, L. R., and Mogensen, M. *Journal of the European Ceramic Society*; **27** (13), p. 3609-3612 (2007).

110. Marina, O. A. and Stevenson, J. W. Solid State Ionic Devices III; **PV 2002-26**; p. 91, edited by Wachsman, E. D., Swider-Lyons, K., Carolan, M. F., Carzon, F. H., Liu, M., and Stetter, J. R., The Electrochemical Society Proceedings Series; (2002)

111. Tsukuma, K., Ueda, K., and Shimada, M. *Journal of the American Ceramic Society*; **68** (1), p. C4-C5 (1985).

112. Badwal, S. P. S. *Journal of Materials Science*; **18** (11), p. 3230-3242 (1983).

113. Butler, E. P. and Drennan, J. *Journal of the American Ceramic Society*; **65** (10), p. 474-478 (1982).

114. Verkerk, M. J., Winnubst, A. J. A., and Burggraaf, A. J. *Journal of Materials Science*; **17** (11), p. 3113-3122 (1982).

115. Feighery, A. J. and Irvine, J. T. S. *Solid State Ionics*; **121** (1-4), p. 209-216 (1999).

116. Butler, E.P. and Bonanos, N. *Materials Science and Engineering,* **71**, p. 49-56 (1985).

117. Lybye, D. and Liu, Y. L. *Journal of the European Ceramic Society*; **26** (4-5), p. 599-604 (2006).

118. Hansen, K. K., Larsen, P. H., Liu, Y. L., Kindl, B., and Mogensen, M., *5th European Solid Oxide Fuel Cell Forum*; p. 875, edited by Huijsmans, J., European Fuel Cell Forum, Lucerne, Switzerland; (2002)

119. Christiansen, N., Kristensen, S., Holm-Larsen, H., Larsen, P. H., and Mogensen, M., *5th European Solid Oxide European Fuel Cell Forum*; p. 34, edited by Huijsmans, J., European Solid Oxide European Fuel Cell Forum, Lucerne; Switzerland (2002)

120. Liu, Y. L., Thydén, K., Xing, Q., and Johnson, E., *Proceedings of the 26th Risø International Symposium on Materials Science: Solid State Electrochemistry*; p. 273-278, edited by Linderoth, S, Smith, A., Bonanos, N., Hagen, A., Mikkelsen, L., Kammer, K., Lybye, D., Hendriksen, P. V., Poulsen, F. W., Mogensen, M., and Wang, W., Roskilde, Denmark, Risø National Laboratory; (2005)

121. Anderson, J.C., Leaver, K.D., Rawlings, R.D. and Alexander, J.M. *Materials Science*, Chapmann & Hall, New York (1990).

122. Doremus, R. H. *Glass Science*, John Wiley & Sons, New York (1973).

123. Holland, L. *The Properties of Glass Surface*, Chapmann and Hall, London (1964).

124. Jewell, J. M., Spess, M. S., and Shelby, J. E. *Journal of the American Ceramic Society*; **73** (1), p. 132-135 (1990).

125. Jewell, J. M. and Shelby, J. E. *Journal of the American Ceramic Society*; **73** (5), p. 1446-1448 (1990).

126. Shelby, J. E. and Mcvay, G. L. *Journal of Non-Crystalline Solids*; **20** (3), p. 439-449 (1976).

127. Hughes, A. E. and Badwal, S. P. S. *Solid State Ionics*; **46** (3-4), p. 265-274 (1991).

128. Jacobson, N., Myers, D., Opila, E., and Copland, E. *Journal of Physics and Chemistry of Solids*; **66** (2-4), p. 471-478 (2005).

129. Jacobson, N. S., Opila, E. J., Myers, D. L., and Copland, E. H. *Journal of Chemical Thermodynamics*; **37** (10), p. 1130-1137 (2005).

130. Ried, R.C., Prausnitz, J.M. and Poling, B.E. *The properties of gasses and liquids*, McGraw-Hill Book Company, (1987).

131. Adler, S. B. *Chemical Reviews*; **104** (10), p. 4791-4843 (2003).

132. Boukamp B. *Nature Materials,* **5**, p. 517-518 (2006).

133. Wilson, J. R., Kobsiriphat, W., Mendoza, R., Chen, H.-Y., Miller, J. M., Miller, D. J., Thornton, K., Voorhees, P. W., Adler, S. B., and Barnett, S. A. *Nature Materials*; **5**, p. 541-544 (2006).

134. Holzer, L., Münch, B., Wegmann, M., Gasser, Ph., and Flatt, R. *Journal of the American Ceramic Society*; **89** (8), p. 2577-2585 (2006).

135. Østergard, M. J. L., Clausen, C., Bagger, C., and Mogensen, M. *Electrochimica Acta*; **40** (12), p. 1971-1981 (1995).

136. Deng, X. and Petric, A. *Journal of Power Sources*; **140** (2), p. 297-303 (2005).

137. de Ridder, M., van Welzenis, R. G., Brongersma, H. H., and Kreissig, U. *Solid State Ionics*; **158** (1-2), p. 67-77 (2003).

138. Jensen, K. V., Norman, K., and Mogensen, M. *Journal of Electrochemical Society*; **151** (9), p. 1436-1444 (2004).

139. Badwal, S. P. S. *Solid State Ionics*; **76** (1-2), p. 67-80 (1995).

140. Hwang, C. S. and Yu, C. H. *Surface & Coatings Technology*; **201** (12), p. 5954-5959 (2007).

141. Sholklapper, T. Z., Radmilovic, V., Jacobson, C. P., Visco, S. J., and De Jonghe, L. C. *Electrochemical and Solid State Letters*; **10** (4), p. B74-B76 (2007).

142. Piccardo, P., Chevalier, S., Molins, R., Viviani, M., Caboche, G., Barbucci, A., Sennour, M., and Amendola, R. *Surface & Coatings Technology*; **201** (7), p. 4471-4475 (2006).

143. Suzuki, S., Uchida, H., and Watanabe, M. *Solid State Ionics*; **177** (3-4), p. 359-365 (2006).

144. Giannuzzi, L. A. and Stevie, F. A .E. *Introduction to Focused Ion Beams. Instrumentation, Theory, Techniques and Practice*, p. 1-358, Springer Verlag, (2005).

145. Brisse, A., Schefold, J., Zahid, M., and Aslanides, A., *Proceedings of The 2nd World Hydrogen Technologies Convention*, Montecatini Terme, Italy; (2007)

146. Allendorf, M. D., Melius, C. F., Ho, P., and Zachariah, M. R. *Journal of Physical Chemistry*; **99** (41), p. 15285-15293 (1995).

147. Allendorf, M. D. and Spear, K. E. *Journal of the Electrochemical Society*; **148** (2), p. B59-B67 (2001).

148. Allendorf, M. D., Melius, C. F., Cosic, B., and Fontijn, A. *Journal of Physical Chemistry A*; **106** (11), p. 2629-2640 (2002).

149. Saxena, S.K., Chatterjee, N., Fei, Y. and Shen, G. *Thermodynamic Data on Oxides and Silicates*, Springer-Verlag, New York (1993).

150. Mizusaki, J., Tagawa, H., Saito, T., Kamitani, K., Yamamura, T., Hirano, K., Ehara, S., Takagi, T., Hikita, T., Ippommatsu, M., Nakagawa, S., and Hashimoto, K. *Journal of the Electrochemical Society*; **141** (8), p. 2129-2134 (1994).

151. Mizusaki, J., Tagawa, H., Saito, T., Yamamura, T., Kamitani, K., Hirano, K., Ehara, S., Takagi, T., Hikita, T., Ippommatsu, M., Nakagawa, S., and Hashimoto, K. *Solid State Ionics*; **70**, p. 52-58 (1994).

152. Bieberle, A. and Gauckler, L. J. *Solid State Ionics*; **146** (1-2), p. 23-41 (2002).

153. Mogensen, M. and Skaarup, S. *Solid State Ionics*; **86-88**, p. 1151-1160 (1996).

154. Holtappels, P., de Haart, L. G. J., and Stimming, U. *Journal of the Electrochemical Society*; **146** (5), p. 1620-1625 (1999).

155. Holtappels, P., Vinke, I. C., de Haart, L. G. J., and Stimming, U. *Journal of the Electrochemical Society*; **146** (8), p. 2976-2982 (1999).

156. Ihara, M., Kusano, T., and Yokoyama, C. *Journal of the Electrochemical Society*; **148** (3), p. A209-A219 (2001).

157. Mogensen, M., Sunde, S., and Primdahl, S., *Proceedings of the 17th Risø International Symposium on Materials Science: High Temperature Electrochemistry: Ceramics and Metals*; p. 77-100, edited by Poulsen, F. W., Bonanos, N., Linderoth, S., Mogensen, M., and Zachau-Chrisiansen, B., Roskilde, Denmark; (1996)

158. Mogensen, M. and Lindegaard, T., *Proceedings of the 3rd international symposium on solid oxide fuel cells (SOFC-III)*; **PV93-4**; p. 484-493, edited by Singhal, S.C. and Iwahara, H., Pennington, NJ, USA, The Electrochemical Society Inc.; (1993)

159. Kawada, T., Sakai, N., Yokokawa, H., Dokiya, M., Mori, M., and Iwata, T. *Solid State Ionics*; **40-1**, p. 402-406 (1990).

160. Mizusaki, J., Yamamura, T., Mori, M., Tagawa, H., Hirano, K., Ehara, S., Takagi, T., Hishinuma, M., Sasaki, H., Sogi, T., Nakamura, Y., and Hashimoto, K., *Proceedings of the 17th Risø International Symposium on Materials Science: High Temperature Electrochemistry: Ceramics and Metals*; p. 363-368, edited by Poulsen, F. W., Bonanos, N., Linderoth, S., Mogensen, M., and Zachau-Chrisiansen, B., Roskilde, Denmark; (1996)

161. Mogensen, M., Hansen, K. V., Høgh, J., and Jacobsen, T. *ECS Transactions*; **7** (1), p. 1329-1338 (2007).

162. Wagner, C. *Berichte der Bundsen-Gesellschaft für Physikalische Chemie*; **72**, p. 778 (1968).

163. Alefeld, G. and Voelkl, J. *Hydrogen in metals 1, Basic properties*, p. 325, Springer Verlag, New York (1978).

164. Skaarup, S. and Zachau-Christiansen, B. Jacobsen T., *Proceedings of the 17th Risø International Symposium on Materials Science, Roskilde, Denmark*; p. 423-430, edited by Poulsen, F. W., Bonanos, N., Linderoth, S., Mogensen, M., and Zachau-Chrisiansen, B.; Roskilde, Denmark; (1996)

165. Kawada, T., Sakai, N., Yokokawa, H., Dokiya, M., Mori, M., and Iwata, T. *Journal of the Electrochemical Society*; **137** (10), p. 3042-3047 (1990).

166. Bessler, W. G., Warnatz, J., and Goodwin, D. G. *Solid State Ionics*; **177** (39-40), p. 3371-3383 (2007).

167. Litton, D. A. and Garofalini, S. H. *Journal of Non-Crystalline Solids*; **217** (2-3), p. 250-263 (1997).

168. Doremus, R. H. *Journal of Non-Crystalline Solids*; **349**, p. 242-247 (2004).

169. Davis, K. M. and Tomozawa, M. *Journal of Non-Crystalline Solids*; **185** (3), p. 203-220 (1995).

170. Tian, L., Dieckmann, R., Hui, C. Y., Lin, Y. Y., and Couillard, J. G. *Journal of Non-Crystalline Solids*; **286** (3), p. 146-161 (2001).

171. Berger, S. and Tomozawa, M. *Journal of Non-Crystalline Solids*; **324** (3), p. 256-263 (2003).

172. Lou, V., Sato, R., and Tomozawa, M. *Journal of Non-Crystalline Solids*; **315** (1-2), p. 13-19 (2003).

173. Kingery, W.D., Bowen, H. K. and Uhlmann, D.R. *Introduction to ceramics*, John Wiley & Sons, New York (1976).

174. Drennan, J. and Butler, E. P., *Science of Ceramics 12*; p. 267-272, Facenzy, Italy; (1984)

175. Bansal, N.P. and Doremus, R.H. *Handbook of Glass properties*, Academic Press Inc., (1986).

176. Blennow, P. *Strontium Titante-based Anodes for Solid Oxide Fuel Cells* (Thesis). University of Lund, 2007.

List of publications

1. “Ni/YSZ electrodes in solid oxide electrolyser cells”, Hauch, A., Jensen, S. H., and Mogensen, M., in *Solid State Electrochemistry, Proceedings of the 26th Risø International Symposium on Materials Science, Roskilde, Denmark*; p. 203-208, edited by S. Linderoth et al. (2005).

2. “Ni/YSZ-electrode passivation at cathodic current”, Jensen, S. H., Hauch, A., and Mogensen, M., in *Solid State Electrochemistry, Proceedings of the 26th Risø International Symposium on Materials Science, Roskilde, Denmark*; p. 247-252; edited by S. Linderoth et al., (2005)

3. “The potential of the solid oxide electrolyser for the production of synthetic fuel”, Jensen, S. H., Hauch, A., and Mogensen, M., in *HYPOTHESIS V*, Havana, Cuba; (2005).

4. “Stability of solid oxide electrolyser cells”, Hauch, A., Jensen, S.H., Mogensen, M., Menon, M., in *Risø International Energy Conference 23-25 May 2005*, p. 216-230 edited by L. Sønderberg Petersen and H. Larsen, Roskilde, Denmark, Risø National Laboratory; (2005).

5. “Performance and Durability of Solid Oxide Electrolysis Cells”, Hauch, A., Jensen, S. H., Mogensen, M., and Ramousse, S., *Journal of the Electrochemical Society*; **153** (9), p. A1741-A1747 (2006).

6. “Performance of Reversible Solid Oxide Cells: A Review”, Mogensen, M., Jensen, S.H., Hauch, A., Chorkendorff, I., and Jacobsen, T., in *Proceedings 7th European SOFC Forum*, edited by U. Bossel, P0301, Lucerne; (2006).

7. “Silica segregation in the Ni/YSZ electrode”, Hauch, A., Jensen, S. H., Mogensen, M., and Bilde-Sørensen, J. B., *Journal of the Electrochemical Society*; **154** (7), p. A619-A626 (2007).

8. “Durability of Solid Oxide Electrolysis Cells for Hydrogen Production”, Hauch, A, Ebbesen, S. D., Jensen, S. H., and Mogensen, M.; *Risø International Energy Conference 2007*; p. 327-338, edited by L. Sønderberg Petersen and H. Larsen, Roskilde, Denmark, Risø National Laboratory; (2007).

9. "Reversible Solid Oxide Cells", Mogensen, M., Jensen, S. H., Hauch, A., Chorkendorf, I., and Jacobsen, T., *Proc. 32nd International Cocoa Beach Conference & Exposition on Advanced Ceramics and Composites*, The American Ceramic Society; (2007).

10. "A Method to Separate Process Contributions in Impedance Spectra by Variation of Test Conditions", Jensen, S. H., Hauch, A., Hendriksen, P.V., Mogensen, M., Bonanos, N., and Jacobsen, T., *J. Electrochem. Soc.*, in press (2007).

11. "Nanoscale Chemical Analysis and Imaging of Solid Oxide Cells", Hauch, A., Bowen, J., Theil Kuhn, L., and Mogensen, M., *Electrochem. & Solid-State Lett.*, submitted (2007).

Appendix A: Overview of electrolysis tests

Table A-1: Fingerprint results for electrolysis tested cells. The general operation conditions for the numbers given in the table are given in the notes below. Where the results are obtained at different conditions than those described below the table, it is described in the right most column. All resistances are given in Ωcm^2.

Test no	Production no	ASR[a] (FC)	ASR[b] (EL)	Rs[c]	Rp[c]	Rs[d]	Rp[d]	Rs[e]	Rp[e]	Note
3test12	PSC6412	-	0.25	0.072	0.182	0.155	0.714	-	-	b) $p(H_2O)$=0.98 atm , d) T = 850°C, $p(H_2O)$ = 0.98 atm.
3test13	PSC6413	-	-	-	-	-	-	-	-	Imperfect contacting – used as reference cell
3test14	PSC6414	0.16	-	0.063	0.154	0.120	0.258	0.065	0.336	d) T = 750°C, $p(H_2O)$ = 0.70 atm.
3test15	PSC6415	0.14	-	0.030	0.172	0.123	0.180	0.112	1.12	d) T = 750°C, $p(H_2O)$ = 0.70 atm.
3test18	PSC6418	0.25	-	0.066	0.192	0.734	1.07	-	-	d) T = 650°C, $p(H_2O)$ = 0.70 atm.
3test19	PSC6419	0.23	0.27	0.123	0.206	0.131	0.163	0.133	0.576	d) T = 850°C, $p(H_2O)$ = 0.70 atm.
3test21	PSC6421	0.33	0.29	0.110	0.228	0.108	0.158	0.172	0.661	d) T = 850°C, $p(H_2O)$ = 0.70 atm.
3test22	PSC6422	0.33	0.39	0.176	0.234	0.178	0.207	0.443	1.327	d) T = 850°C, $p(H_2O)$ = 0.70 atm.
3test23	PSC6423	0.19	0.21	0.085	0.168	0.007	0.076	0.095	0.307	d) T = 950°C, $p(H_2O)$ = 0.70 atm.
3test24	PSC12393-1	0.15	0.20	0.057	0.239	0.092	0.143	0.130	0.706	c,e) 950°C, $p(H_2O)$ = 0.05 atm, d) T = 850°C, $p(H_2O)$ = 0.90 atm
3test25	PSC6425	0.22	0.25	0.128	0.179	0.125	0.130	-	-	d) T = 850°C, $p(H_2O)$ = 0.50 atm.
3test26	PSC12279-1	0.22	0.28	0.138	0.184	0.142	0.252	0.149	0.417	d) T = 850°C, $p(H_2O)$ = 0.99 atm.

a) Fuel utilization corrected ASR from iV curves at 850°C with 20% H_2O to the hydrogen electrode and air to the oxygen electrode.
b) As a) but with 50% steam to the hydrogen electrode.
c) From EIS at OCV (not fitted data) at 850°C with 20% steam to the hydrogen electrode and air to the oxygen electrode.
d) From EIS (not fitted data) at -0.25 A/cm^2 when stepping from OCV to the chosen current density for the electrolysis testing.
e) As c) but at the ending finger-print.

Table A-1: Fingerprint results for electrolysis tested cells (continued)

Test no	Production no	ASR[a] (FC)	ASR[b] (EL)	Rs[c]	Rp[c]	Rs[d]	Rp[d]	Rs[e]	Rp[e]	Note
										d) T = 950°C, $p(H_2O)$ = 0.90 atm, e) at
3test27	PSC12259-1	0.37	0.42	0.224	0.240	0.140	0.137	0.848	0.505	950°C, start-up: R_s = 0.154 Ωcm^2, R_p = 0.159 Ωcm^2.
3test28	PSC12262-2	0.29	0.36	0.159	0.235	0.182	0.184	0.224	0.419	V impreg. H_2 electrode, d) T = 850°C, $p(H_2O)$ = 0.70 atm.
3test29	PSC12279-4	-	-	-	-	-	-	-	-	Imperfect contact – used as reference cell
3test30	PSC12298-1	0.29	0.35	0.166	0.234	0.171	0.172	0.190	0.269	d) T = 850°C, $p(H_2O)$ = 0.50 atm.
3test31	PSC12298-3	0.40	0.49	0.216	0.192	0.243	0.269	0.281	0.501	Mn impreg. H_2 electrode, d) T = 850°C, $p(H_2O)$ = 0.70 atm.
3test32	PSC12298-4	0.18	0.23	0.102	0.172	0.081	0.114	-	-	d) T = 950°C, $p(H_2O)$ = 0.90 atm.
3test33	PSC12326-2	0.17	0.24	0.098	0.175	0.098	0.143	0.099	0.239	d) T = 850°C, $p(H_2O)$ = 0.50 atm.
3test34	PSC12326-3	0.14	0.23	0.076	0.169	0.053	0.109	0.168	0.391	d) T = 850°C, $p(H_2O)$ = 0.50 atm.
3test35	PSC12335-1	0.33	0.37	0.188	0.243	0.195	0.194	0.198	0.426	Glass sealing covered by Au-foil d) T = 850°C, $p(H_2O)$ = 0.50 atm.
3test36	PSC12335-3	0.31	0.35	0.111	0.270	0.114	0.177	0.346	0.592	Sealing made of Au-foil. d) T = 850°C, $p(H_2O)$ = 0.50 atm.

Table A-2: Overview of electrolysis test results. 3test22 and 3test23 were both used for 3 electrolysis test periods applying different operation conditions. Two different electrolysis tests were performed using the cell for 3test24 and 3test34. Notice that the ΔU given is for the entire electrolysis test period and not normalized to 100 h or 1000 h.

Test no	T (°C)	i (A/cm^2)	$p(H_2O)$ (atm)	H_2O utili.%	Duration (h)	$R_{p,start}$ (Ωcm^2)	ΔR_p [a]	$R_{s,start}$ (Ωcm^2)	ΔR_s [a]	U_{start} (V)	ΔU [a]
3test12	850	-0.25	0.98	14	459	0.41	15%	0.15	8%	1.045	3%
3test14	750	-0.25	0.70	14	83	0.26	472%	0.12	2%	1.048	21%
3test15	750	-0.25	0.39	16	93 [b]	1.32	23%	0.11	2%	1.264	3%
3test18	650	-0.25	0.37	14	17	[c]	-	[c]	-	1.490	6%
3test19	850	-0.25	0.70	14	767	0.16	37%	0.13	-4%	1.004	1%
3test21	850	-0.50	0.70	28	140	0.18	181%	0.11	-2%	1.072	12%
	850	-1.0	0.70	53	353 [d]	0.60	58%	0.17	120%	1.442	24%
3test22	850	-0.50	0.3	34	43 [e]	0.97	-6%	0.34	21%	1.456	2%
	850	-0.50	0.70	22	93	0.68	29%	0.41	27%	1.440	7%
	850	-0.50	0.70	28	91 [e]	0.65	64%	0.34	51%	1.442	12%
	950	-0.50	0.70	28	135	0.08	13%	0.07	15%	0.971	2%
3test23	750	-0.25	0.30	17	83	1.20	26%	0.18	-4%	1.338	8%
	750	-0.25	0.70	11	35	1.34	0%	0.19	0%	1.352	1%
3test24	850	-0.50	0.90	14	168	0.31	86%	0.19	-5%	1.005	5%
	950	-1.0	0.67	79	474	0.72	49%	0.11	112%	1.138	19%

a) $\Delta R_p = (R_{p,end} - R_{p,start})/R_{p,start}*100$. ΔRs and ΔU are calculated in the same manor.

b) Was operated for 9 hours in electrolysis at $p(H_2O) = 0.7$ atm. Within these 9 hours the cell voltage increased from 1.185 V to 1.241 volt.

c) Impedance under current load not set-up for spectra recorded at 650°C

d) The results are obtained after 312 h of electrolysis operation. Hereafter gas change experiments were performed during electrolysis operation of the cell.

e) The cell was partly activated by operation in fuel cell mode at ½ A/cm^2 and $p(H_2O) = 0.05$ atm to the H_2 electrode.

Table A-2: Overview of electrolysis test results (continued).

Test no	T (°C)	i (A/cm^2)	$p(H_2O)$ (atm)	H_2O utili.%	Duration (h)	$R_{p,start}$ (Ωcm^2)	ΔR_p [a]	$R_{s,start}$ (Ωcm^2)	ΔR_s [a]	U_{start} (V)	ΔU [a]
3test25	850	-0.50	0.50	28	596	0.15	154%	0.13	-3%	1.098	7%
3test26	850	-0.50	0.99	28	300	0.19	303%	0.14	-2%	1.020	14%
3test27	950	-2.0	0.90	27	68	0.15	21%	0.33	200%	1.508	47%
3test28	850	-0.50	0.70	28	244	0.18	200%	0.21	-5%	1.250	11%
3test30	850	-0.50	0.50	28	1316	0.17	65%	0.17	8%	1.143	3%
3test31	850	-0.50	0.50	28	227	0.33	38%	0.24	13%	1.206	9%
3test32	950	-1.0	0.90	53	694	0.16	172%	0.09	-13%	1.075	13%
3test33	850	-0.50	0.50	28	1510	0.16	68%	0.09	9%	1.075	4%
3test34 [f]	950	-1.0	0.90	53	95	0.16	75%	0.06	9%	1.043	8%
	950	-1.0	0.90	53	157	0.31	7%	0.10	34%	1.176	8%
3test35	850	-0.50	0.50	28	735	0.222	147%	0.194	0%	1.135	13%
3test36 [g]	850	-0.50	0.50	28	568	0.273	38%	0.115	7%	1.121	3%

f) Unintended stop of electrolysis and switched automatically to OCV and 9% H_2 in N_2 to the H_2 electrode.

g) EIS data after 423 hours of electrolysis testing.

Table A-3: Development of cell voltage, ohmic resistance (R_s) and polarisation resistance (R_p) for electrolysis testing of H_2 electrode supported SOCs produced at Risø National Laboratory.

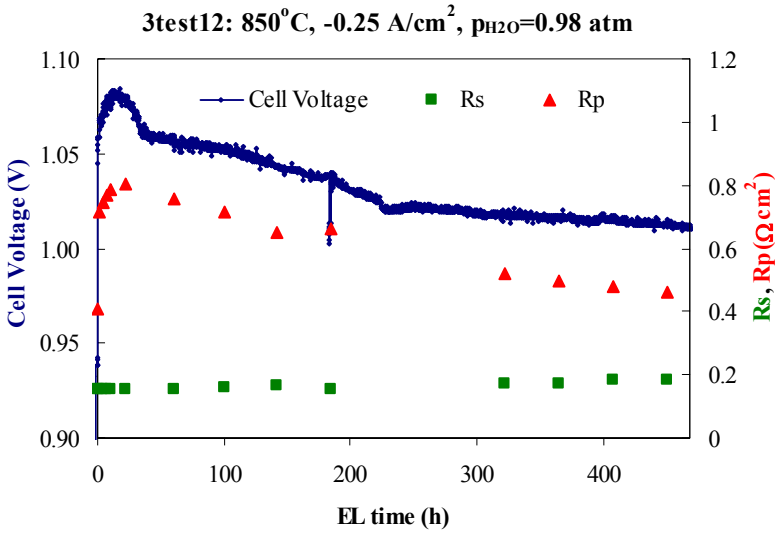

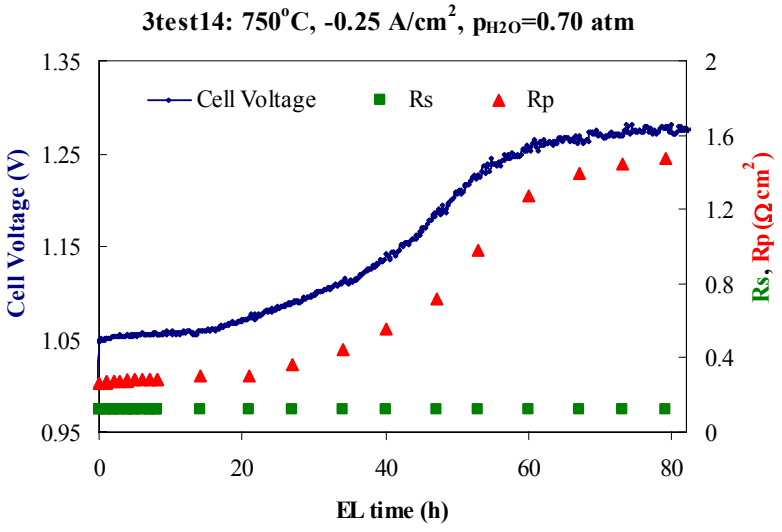

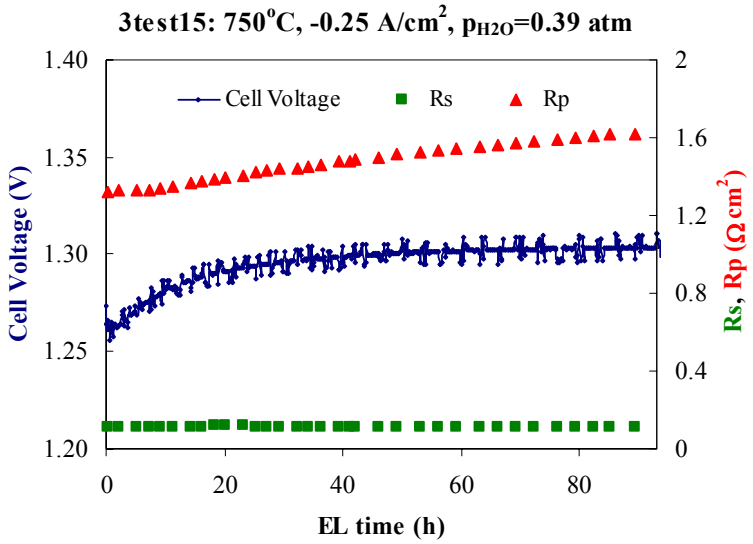
3test15: 750°C, -0.25 A/cm², pH2O=0.39 atm
Cell Voltage
Rs
Rp
Cell Voltage (V)
Rs, Rp (Ω cm²)
EL time (h)

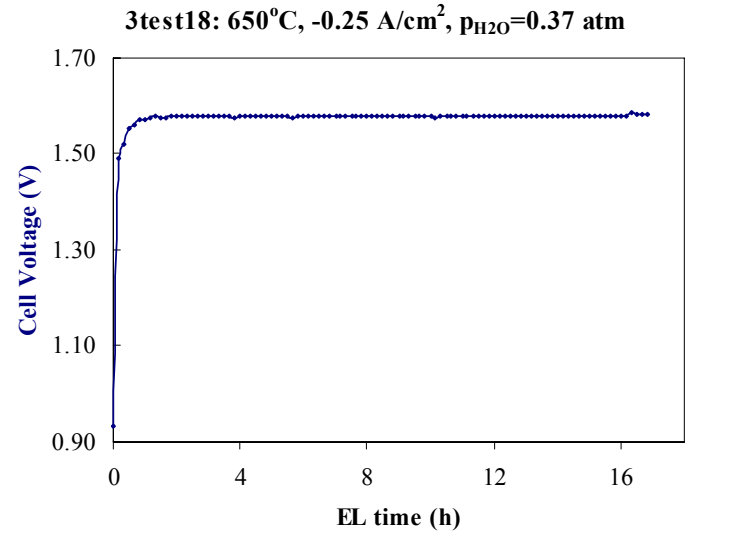
3test18: 650°C, -0.25 A/cm², pH2O=0.37 atm
Cell Voltage (V)
EL time (h)

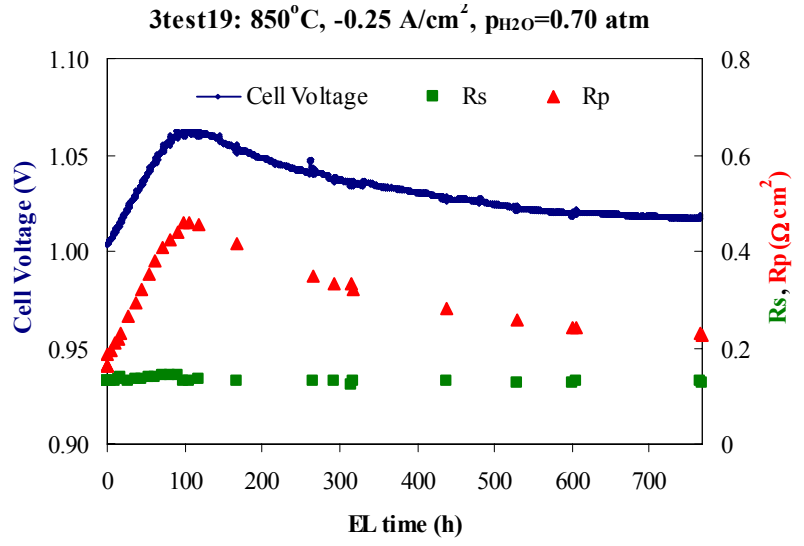
3test19: 850°C, -0.25 A/cm², pH2O=0.70 atm
Cell Voltage
Rs
Rp
Cell Voltage (V)
Rs, Rp (Ω cm²)
EL time (h)

3test21: 850°C, -0.50 A/cm², p_{H2O}=0.70 atm

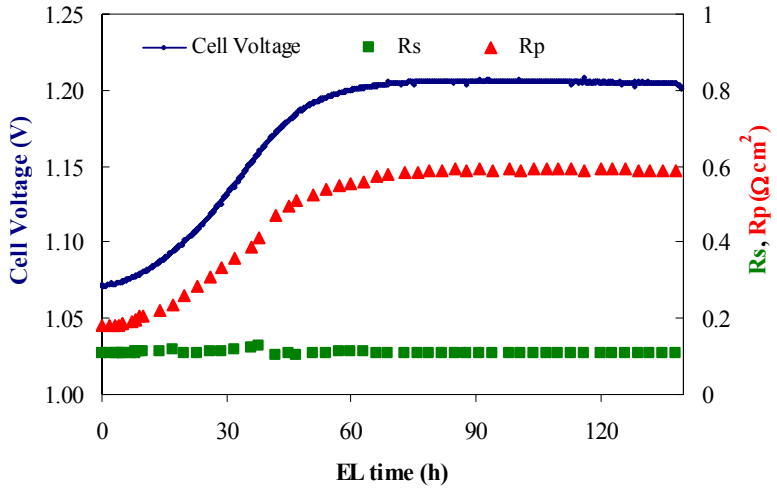

3t22: 850°C, -1.0 A/cm², p_{H2O}=0.70 atm (1st EL)

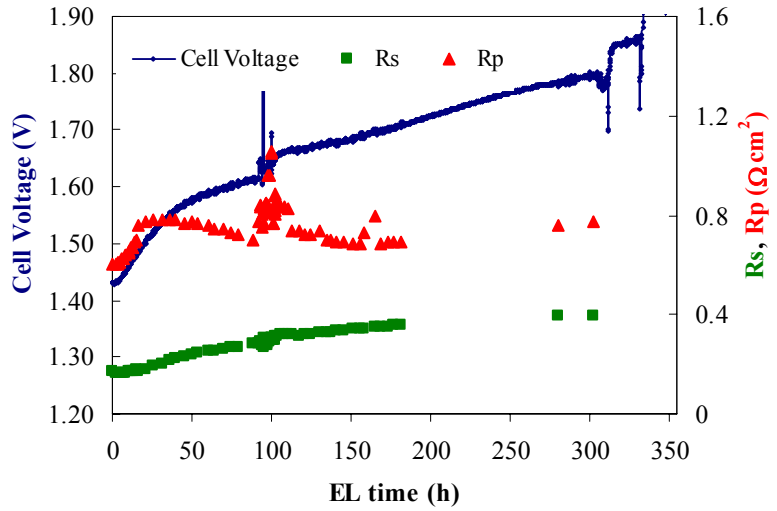

3t22: 850°C, -0.50 A/cm², p_{H2O}=0.30 atm (2nd EL)

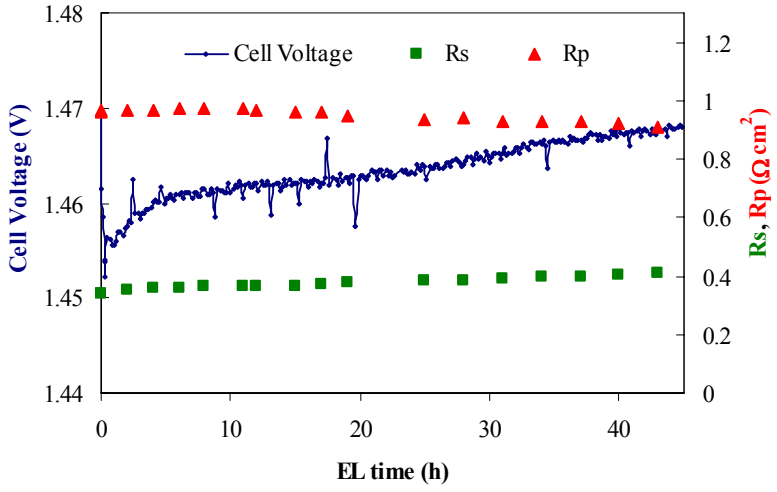

3t22: 850°C, -0.50 A/cm², p_{H2O}=0.70 atm (3rd EL)

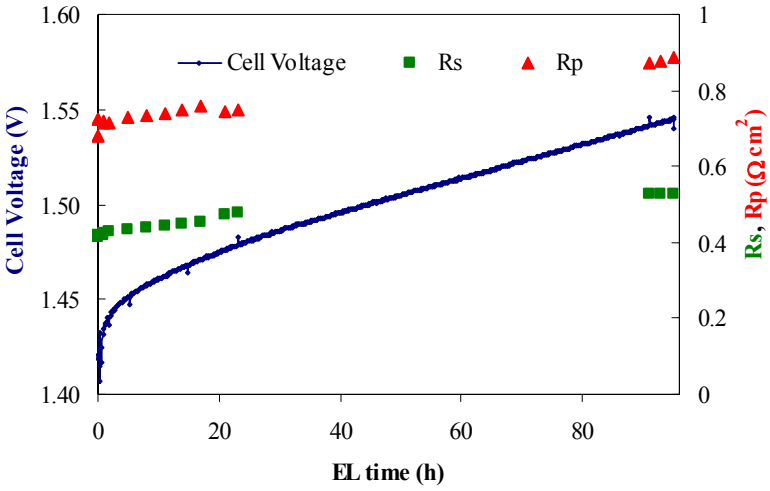

3t23: 950°C, -0.50 A/cm², p_{H2O}=0.70 atm (1st EL)

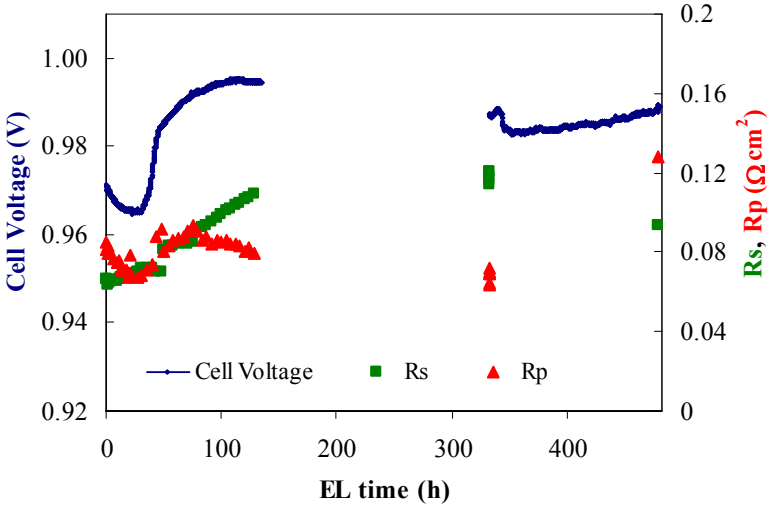

3t23: 750°C, -0.25 A/cm², p_{H2O}=0.30 atm (2nd EL)

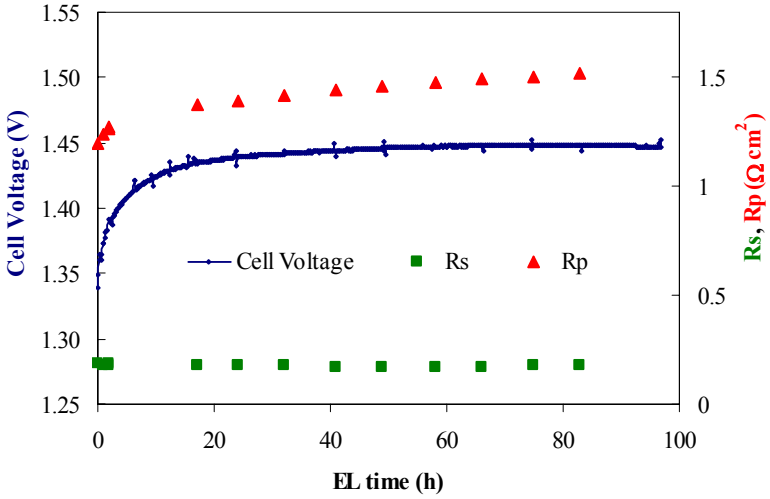

3t23: 750°C, -0.25 A/cm², p_{H2O}=0.70 atm (3rd EL)

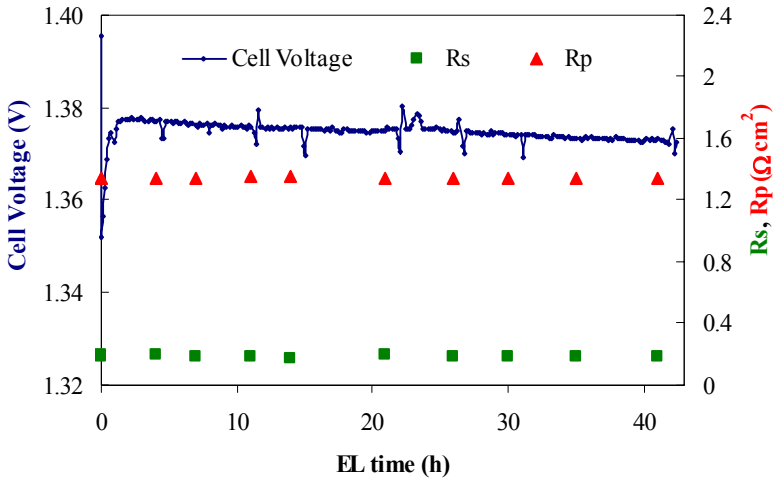

3t24: 850°C, -0.50 A/cm², p_{H2O}=0.90 atm (1st EL)

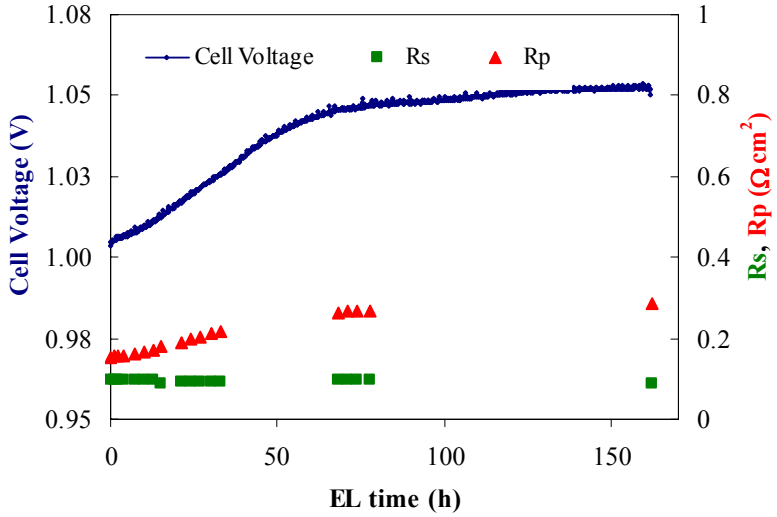

3t24 : 950°C, -1.0 A/cm², p_{H2O}=0.67 atm (2nd EL)

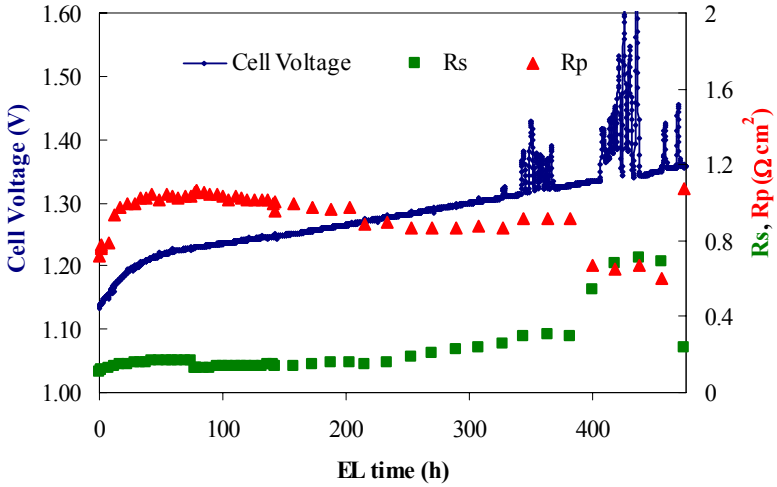

3test25: 850°C, -0.50 A/cm^2, p_{H2O}=0.50 atm

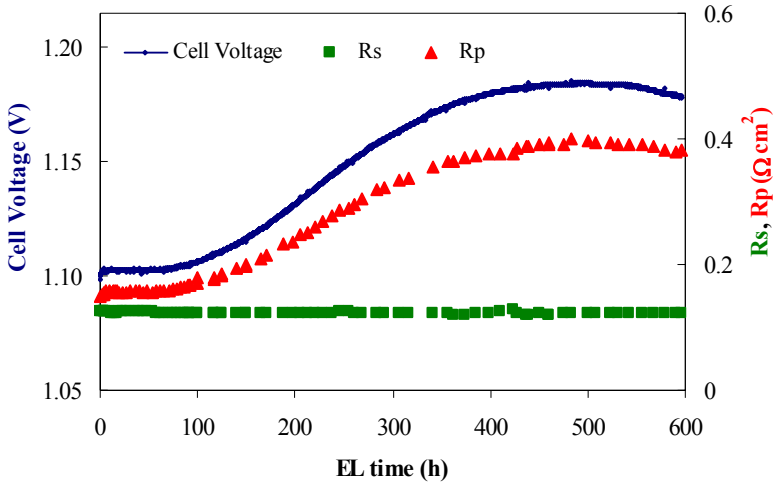

3test26: 850°C, -0.50 A/cm^2, p_{H2O}=0.99 atm

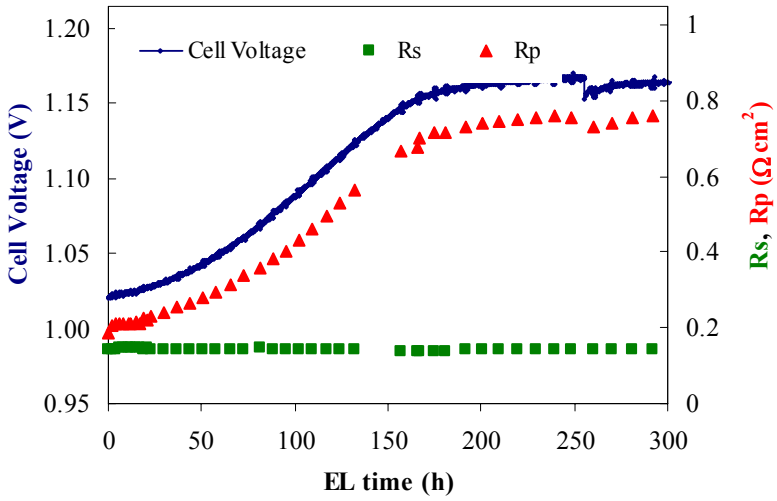

3test27: 950°C, -2.0 A/cm^2, p_{H2O}=0.90 atm

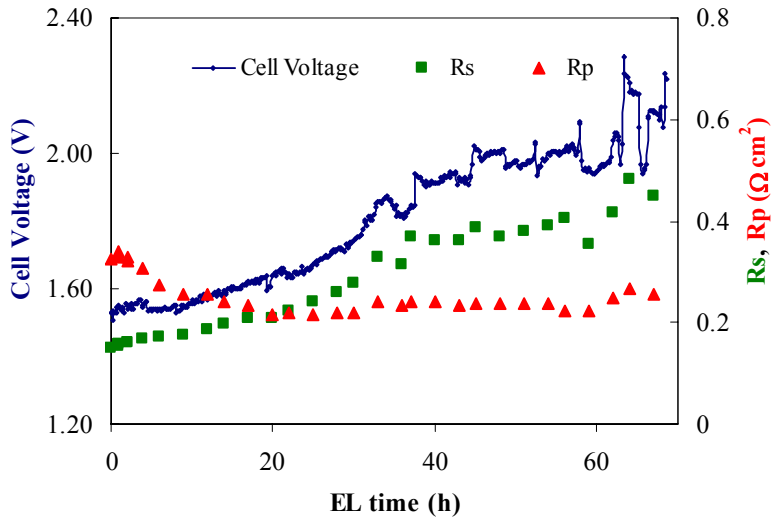

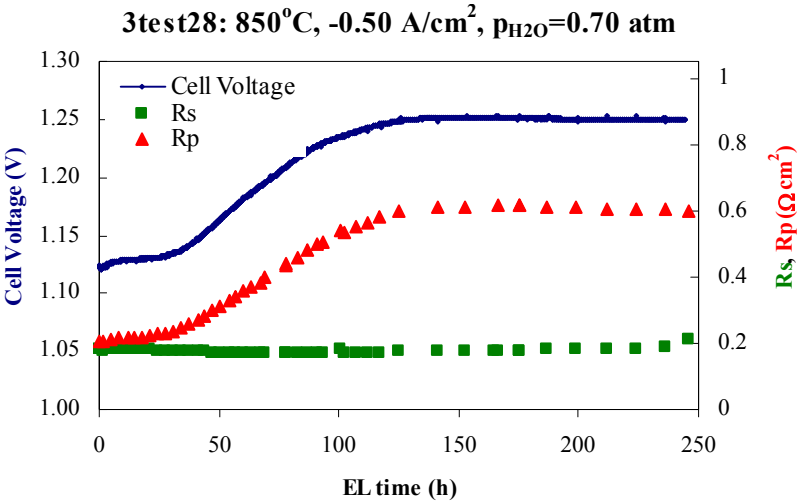
3test28: 850°C, -0.50 A/cm², pH2O=0.70 atm
Cell Voltage
Rs
Rp
Cell Voltage (V)
Rs, Rp (Ω cm²)
EL time (h)

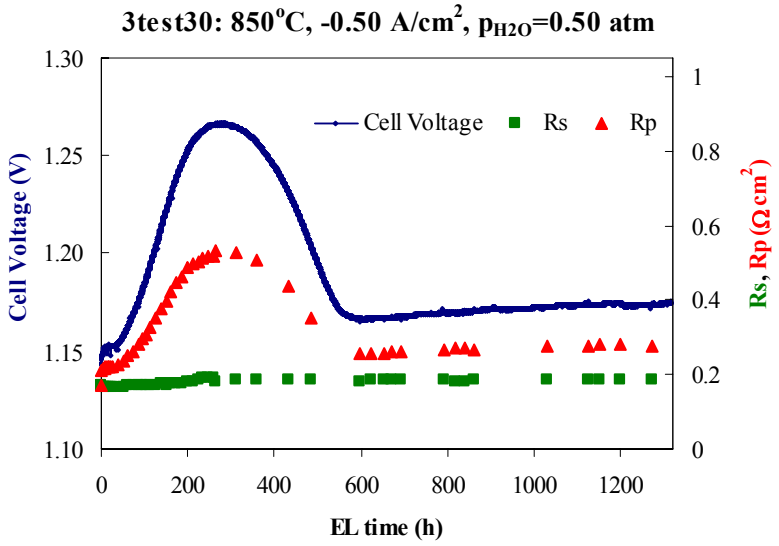
3test30: 850°C, -0.50 A/cm², pH2O=0.50 atm
Cell Voltage
Rs
Rp
Cell Voltage (V)
Rs, Rp (Ω cm²)
EL time (h)

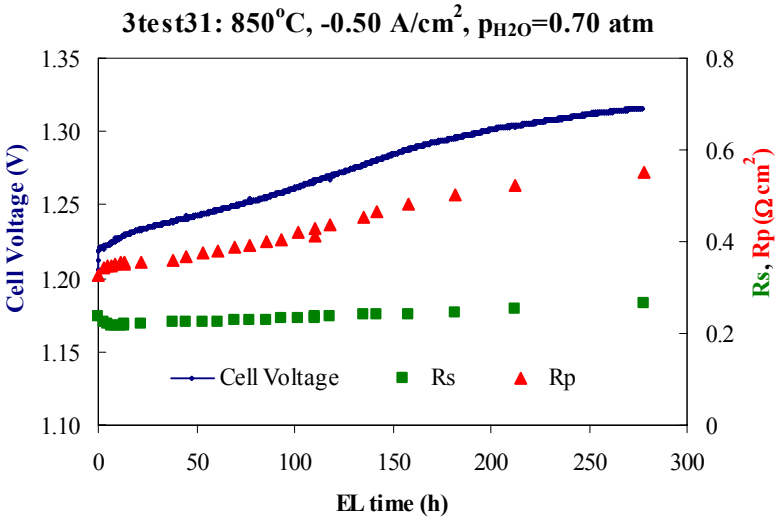
3test31: 850°C, -0.50 A/cm², pH2O=0.70 atm
Cell Voltage
Rs
Rp
Cell Voltage (V)
Rs, Rp (Ω cm²)
EL time (h)

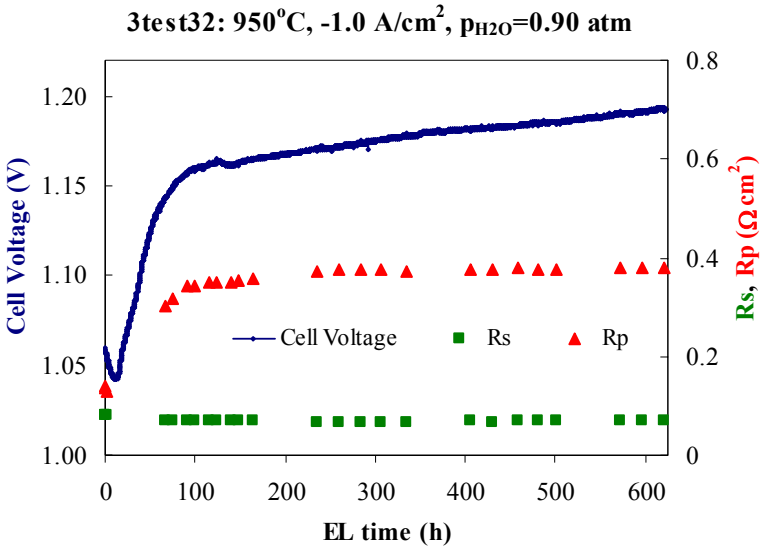
3test32: 950°C, -1.0 A/cm², pH2O=0.90 atm
Cell Voltage (V)
Rs, Rp (Ω cm²)
Cell Voltage
Rs
Rp
EL time (h)

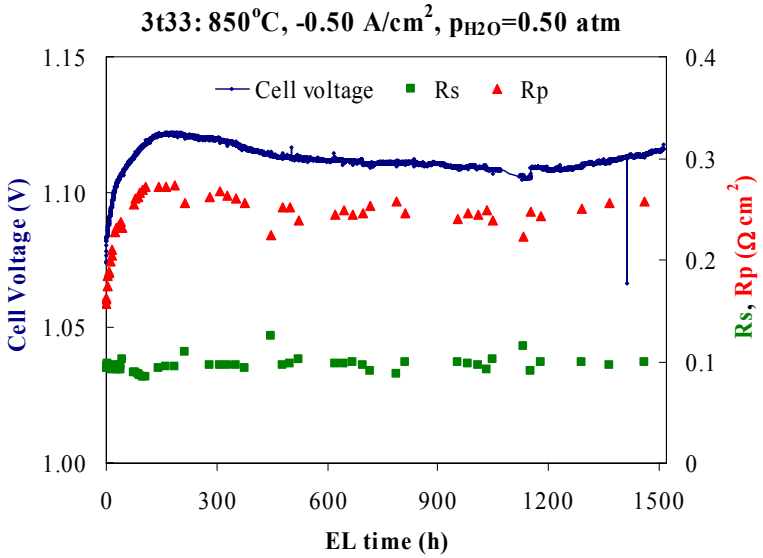
3t33: 850°C, -0.50 A/cm², pH2O=0.50 atm
Cell Voltage (V)
Rs, Rp (Ω cm²)
Cell voltage
Rs
Rp
EL time (h)

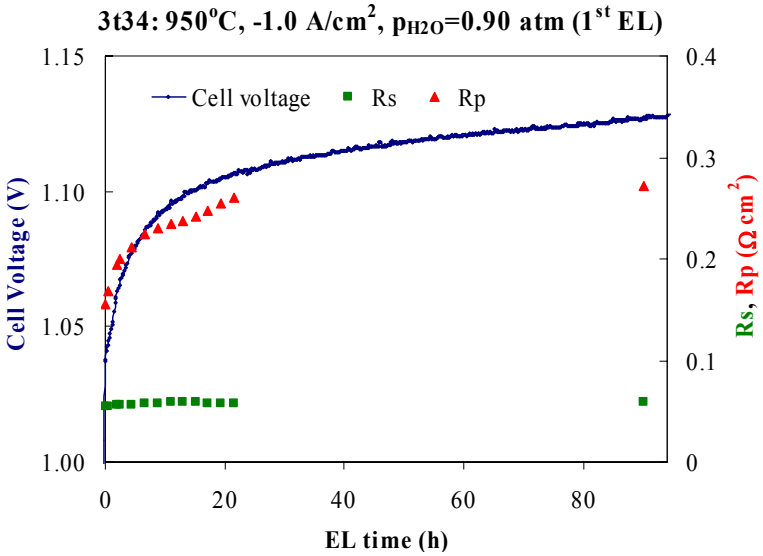
3t34: 950°C, -1.0 A/cm², pH2O=0.90 atm (1st EL)
Cell Voltage (V)
Rs, Rp (Ω cm²)
Cell voltage
Rs
Rp
EL time (h)

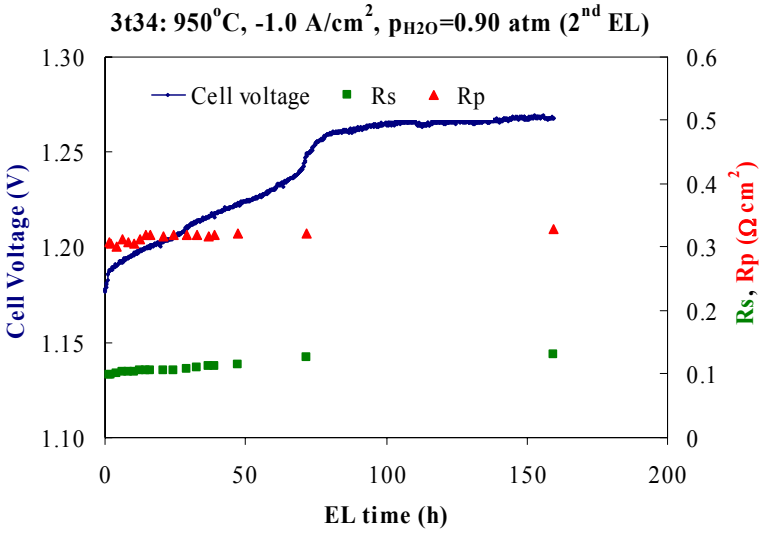
3t34: 950°C, -1.0 A/cm², pH2O=0.90 atm (2nd EL)
Cell voltage
Rs
Rp
Cell Voltage (V)
Rs, Rp (Ω cm²)
EL time (h)
1.30
1.25
1.20
1.15
1.10
0.6
0.5
0.4
0.3
0.2
0.1
0
0
50
100
150
200

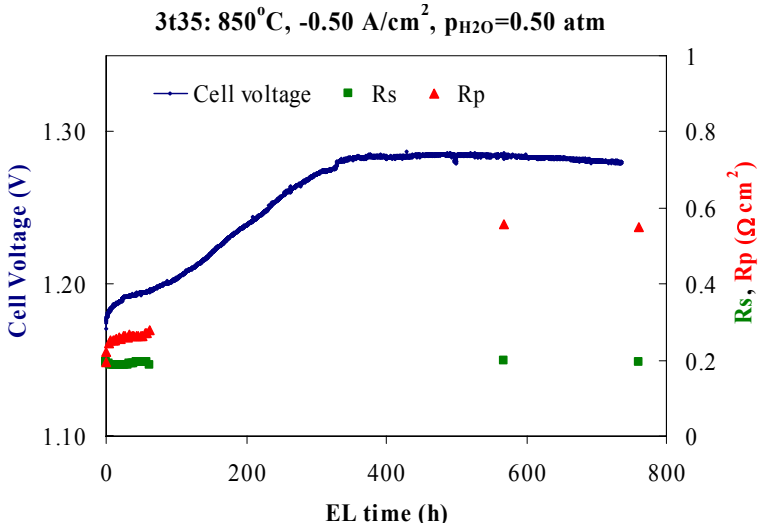
3t35: 850°C, -0.50 A/cm², pH2O=0.50 atm
Cell voltage
Rs
Rp
Cell Voltage (V)
Rs, Rp (Ω cm²)
EL time (h)
1.30
1.20
1.10
1
0.8
0.6
0.4
0.2
0
0
200
400
600
800

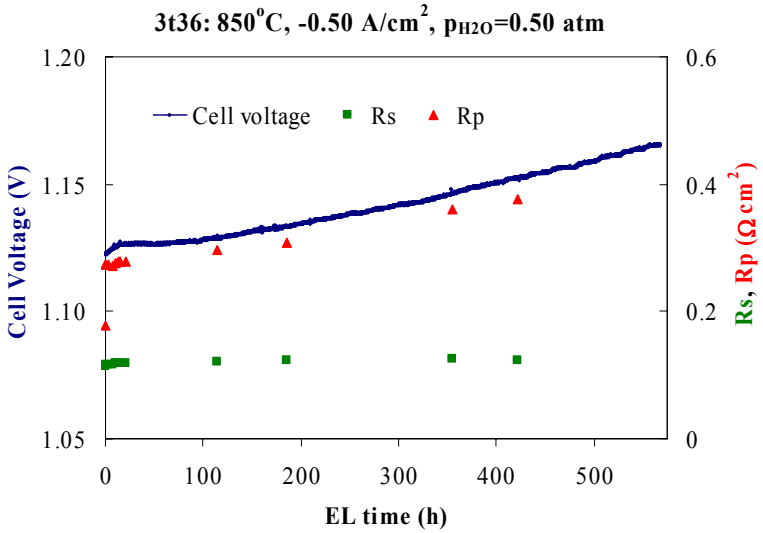
3t36: 850°C, -0.50 A/cm², pH2O=0.50 atm
Cell voltage
Rs
Rp
Cell Voltage (V)
Rs, Rp (Ω cm²)
EL time (h)
1.20
1.15
1.10
1.05
0.6
0.4
0.2
0
0
100
200
300
400
500